Okinawa Institute of Science and Technology
Graduate University

Thesis submitted for the degree

Doctor of Philosophy

Optical Nanofibers for Multiphoton Processes and Selective Mode Interactions with Rubidium

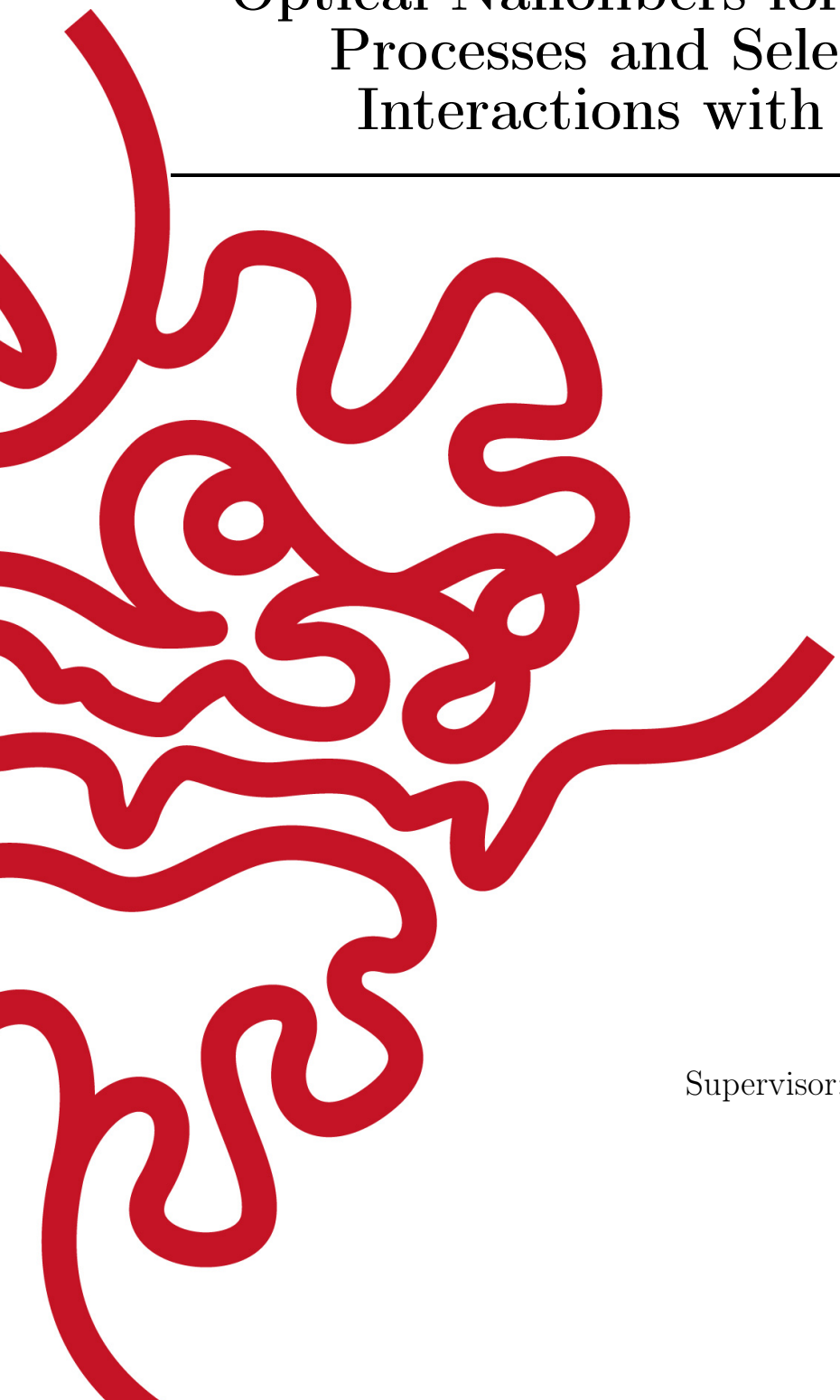

by

Thomas Nieddu

Supervisor: **Prof. Síle Nic Chormaic**

July, 2019

Declaration of Original and Sole Authorship

I, Thomas Nieddu, declare that this thesis entitled *Optical Nanofibers for Multiphoton Processes and Selective Mode Interactions with Rubidium* and the data presented in it are original and my own work.

I confirm that:

- No part of this work has previously been submitted for a degree at this or any other university.
- References to the work of others have been clearly acknowledged. Quotations from the work of others have been clearly indicated, and attributed to them.
- In cases where others have contributed to part of this work, such contribution has been clearly acknowledged and distinguished from my own work.
- None of this work has been previously published elsewhere, with the exception of the following:
  - T. Nieddu, T. Ray, K.S. Rajasree, R. Roy, S. Nic Chormaic, OE **27** 6528-6535 (2019)
  - F. Le Kien, T. Ray, T. Nieddu, T. Busch, S. Nic Chormaic, Phys. Rev. A **97** 013821 (2018)
  - T. Nieddu, V. Gokhroo, S. Nic Chormaic, J. Opt. **18** 053001 (2016)

Date: July, 2019
Signature:

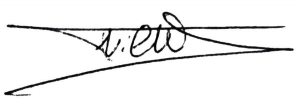

Abstract

Optical nanofibers (ONFs) interfaced with atoms have found numerous applications for the development of quantum technologies. They feature a strong evanescent field at their waist, thereby providing an intense and tightly focused beam over long distances. This can be used to achieve strong interactions between light and matter, enabling trapping, probing, and control of atoms along the waist. However, little experimental work has been done with the higher-order fiber guided modes (HOM). These feature inhomogeneous polarization distributions around the waist and some carry more than $\hbar$ of angular momentum (AM). Owing to the intense field gradient in their evanescent field, ONFs make excellent platforms to excite quadrupole-allowed transitions which could be used to store high-density information encoded on the AM of guided light. We predicted a transition probability up to 6 times stronger than for free-space beams using the fundamental mode and up to 4 times stronger using linearly polarized HOMs. We also studied a single-color, two-photon transition at 993 nm between the $5S_{1/2}$ and $6S_{1/2}$ atomic levels in a hot rubidium vapor and showed its suitability as a frequency reference. We experimentally verified the particular selection rules for this transition and showed that they may be used to characterize the polarization at the waist of an ONF embedded in a cloud of atoms formed by a magneto-optical trap. Finally, we developed a method to generate HOM-like beams in free-space, inject them into an ONF, and decompose the modal excitation at the output via transfer matrix calculation. This approach combined with absorption of guided-light by cold atoms may be used to infer the mode excitation at the waist and allow us to selectively excite HOMs.

Acknowledgment

This PhD has been quite the adventure and it would have been impossible to complete without the help of many people. I have intentionally used the pronoun "we" throughout this thesis in order to show that the work presented here was the result of combined efforts. Though I am the main actor in many of these projects, it could not have been achieved without help from my colleagues, or without moral support from my friends and family. I sincerely thank you all from the bottom of my heart.

The work reported here would not have even started were it not for my supervisor, Síle Nic Chormaic. She took me under her wing and made sure I was learning everything a researcher in experimental science needed to know, helping along the way with any issue I might have, professional or otherwise. I am deeply grateful for her support and her teachings, but most importantly for her patience during the PhD.

I would also like to thank all my colleagues, who were always friendly and always willing to have (heated but useful) scientific discussions. Thank you, Aili, Ali (Seer), Cindy, Domna, Fuchuan, Georgiy, Giang, Ivan (Gusachenko), Ivan (Toftul), Jean-Baptiste, Jesse, Jonathan, Kieran, Krishnapriya, Kristoffer, Maki, Marios, Mayuri, Metin, Peter, Priscilla, Ramgopal, Ratnesh, Ravi, Shou, Theo, Tridib, Yuta, and Vandna, for helping me progress. I'd like to particularly thank Dr. Kieran Deasy, and Dr. Vandna Gokhroo for providing me with proper training at the start of my PhD, making sure I would work diligently and precisely, and also Dr. Tridib Ray and Peter Mekhail for working closely with me throughout the PhD, always providing invaluable advice and support. Last but not least of all the group members, I'd like to thank Emi Nakamura, our research unit assistant, always cheering me up with chocolate and helping me go through administrative ordeals without ever complaining.

Outside of the unit, I would like to acknowledge the support of my mentor, Prof. Pinaki Chakraborty, who made sure I would choose a curriculum at the start of the PhD that would prepare me well for what was ahead, and who frequently inquired about the status of my PhD work. I am also grateful to Prof. Thomas Busch who always had the right words to cheer me up and who encouraged me to persevere when I was feeling down. I would like to express my gratitude to OIST and the Japanese government for funding my research during the entire PhD.

Many thanks also go to my parents, Sandro and Corinne, my brother Hugo, but also to my OIST family, known as the people from 224, Irina, Peter, Jiabao, Leonidas and Achilleas. Thank you very much for listening to my rants and making the OIST experience an enjoyable one. Also, if there ever was an award for most patient, most supportive, and most motivating person it would go without contest to my fiancee, Julia Janicki. Thank you for everything.

Abbreviations

4WM	Four-wave mixing
A-H	Anti-Helmholtz
AOM	Acousto-optic modulator
APD	Avalanche photo-diode
ATS	Autler-Townes splitting
BB	Beam blocker
BD	Beam displacer
BS	Beam splitter
CCD	Charge coupled device
CF flange	ConFlat flange
CM	Concave mirror
CMOS	Complementary metal-oxyde semiconductor
CVB	Cylindrical vector beam
CW	Continuous wave
DLCZ protocol	Duan-Lukin-Cirac-Zoller protocol
DM	Dichroic mirror
DSM	D-shaped mirror
ECDL	Extended cavity diode laser
EH	Electric hybrid
EIT	Electromagnetically induced transparency
EM	Electromagnetic
FBG	Fiber Bragg grating
FEM	Finite element method
FMF	Few-mode fiber
FIB	Focused ion beam
FPI	Fabry-Pérot interferometer
FS	Fiber splitter
HE	Hybrid electric
HEPA filter	High-efficiency particulate filter
HOM	Higher order modes
HWP	Half-wave plate
IDIOM	Interferometric decomposition into optical mode
IGBT	Insulated-gate bipolar transistor
IPA	Isopropyl-alcohol
LG beam	Laguerre-Gaussian beam
LP mode	Linearly polarized mode

MFC	Mass-flow controller
MMF	Multimode fiber
MOT	Magneto-optical trap
NA	Numerical aperture
NIR	Near infrared
OAM	Orbital angular momentum
ONF	Optical nanofiber
PBS	Polarizing beam-splitter
PCL	Plano-convex lens
PD	Photodiode
PDC	Phase discrepancy compensation
PID controller	Proportional integrate derivative controller
PM fiber	Polarization maintaining fiber
PMT	Photo-multiplier tube
PP	Polarization paddle
PVC	Polyvinyl chloride
QWP	Quarter-wave plate
RF	Radio-frequency
RMS	Root-mean square
SAM	Spin angular momentum
sCMOS	Scientific complementary metal oxide semiconductor
SEM	Scanning electron microscope
Sh	Shutter
SLM	Spatial light modulator
SPCM	Single-photon counting module
TE	Transverse electric
TM	Transverse magnetic
TOF	Time-of-flight
TRM	Transfer matrix
TSP	Titanium sublimation pump
UHV	Ultrahigh vacuum
UV	Ultraviolet

Nomenclature

n_1	Refractive index of the fiber core
n_2	Refractive index of the fiber cladding
n_{eff}	Effective refractive index
e	Elemental electric charge ($1.602\ 177 \times 10^{-19}$ C)
$\mathbf{r}$	Position vector
α	Damping coefficient
κ	Magnetic field gradient
ϵ_0	Free space permittivity ($8.854\ 188 \times 10^{-12}$ Fm^{-1})
χ_a	Scalar polarizability
$\mathbf{E}(\mathbf{r})$	Electric field
$U(r)$	Potential energy
Ω	Rabi frequency
$\bar{\Omega}$	Root-mean-square Rabi frequency
ω	Angular frequency
ω_0	Resonant angular frequency for a given transition
ω_L	Angular frequency of a laser beam
ω_D	Doppler shift
ω_{cool}	Cooling beam frequency
ω_{rep}	Repumping beam frequency
δ	Frequency detuning from resonance
λ	Wavelength
μ_B	Bohr magneton ($9.274\ 009 \times 10^{-24}$ J T^{-1})
$\mathbf{k}$	Wavevector of a light field
$\mathbf{k_0}$	Wavevector of a light field in vacuum
F	Force
B	Magnetic field amplitude
E_0	Amplitude of an electric field
U	Potential energy
Γ	Decay rate of the excited state
Γ_s	Scaterring rate
ρ_{ee}	Population in the excited state
β	Modal propagation constant inside an optical nanofiber
a	Fiber radius
$\nabla_{\mathrm{T,cyl}}$	Transverse Laplace operator
I	Intensity
I_{sat}	Saturation intensity

J_l	Bessel function of the first kind
Y_l	Bessel function of the second kind
I_l	Modified Bessel function of the first kind
K_l	Modified Bessel function of the second kind
$\mathcal{E}$	Spatial envelope of the electric field
$\mathcal{H}$	Spatial envelope of the magnetic field
Θ_z	Tapering angle
z_b	Beating length
W	Waist
K	Kinetic energy
T	Temperature
T_D	Doppler limited temperature
RSP	Detector's response
V_{meas}	Measured voltage
R_{load}	Load resistance
D	Distance between lens and MOT
k_B	Boltzmann constant ($1.3806\ 485 \times 10^{-23}$ $\mathrm{m}^2 Kgs^{-2}K^{-1}$)
v_{rms}	Root-mean-square velocity
M	Atomic mass
h	Planck constant ($6.626\ 070 \times 10^{-34}$ $\mathrm{m}^2 Kgs^{-1}$)
$\hbar$	Reduced Planck constant ($1.054\ 718 \times 10^{-34}$ $\mathrm{m}^2 Kgs^{-1}$)
Q_{ij}	Components of the electric quadrupole moment tensor
η_{osc}	Enhancement factor of the oscillator strength
P	Power
$\boldsymbol{S}$	Stokes vector
T	Mueller matrix for a transformation
E_{ref}	Electric field of the reference beam
I_{ref}	Intensity of the reference beam
E_{sig}	Electric field of the signal beam
I_{sig}	Intensity of the signal beam
I_{tot}	Intensity of the combined beams
k_{tilt}	Difference between the reference beam and signal beam wavevectors
d	Fiber diameter

"A mode is a mode, is a mode, is a mode."
J. P. Dowling (June 2017)

Contents

List of Figures

List of Tables

Chapter 1

Introduction to Optical Nanofibers[1]

The development of quantum-based devices is becoming increasingly necessary for future technological advances and, as a result, enormous effort is being made to find suitable experimental platforms, one of which is optical nanofibers (ONFs) interfaced with cold neutral atoms [1]. ONFs [2] are increasingly being used in cold atom experiments due to their versatility and the advantages they have when developing all-fibered systems for quantum technologies. They provide researchers with a method for overcoming the Rayleigh range for achieving high intensities in a tightly confined beam over a relatively long distance and can act as a noninvasive tool for probing cold atoms. These devices, as described in the following, have been used for atom probing [3–5], manipulation and trapping [6–8], the study of atom-dielectric surface interactions [9, 10], and the observation of nonlinear optics phenomena in atomic media [11, 12]. The functionality of ONFs in relation to the realization of atom-photon hybrid quantum systems [13–17] is also becoming more evident as some of the earlier technical challenges are surpassed.

In what follows, a comprehensive description of the state-of-the-art of the ONF-neutral atom field is presented. First, a description of the composition of a nanofiber is given and the methods available for its fabrication are briefly described. Some of the numerous advantages offered by such a device as compared to tightly focused, free-space beams are discussed. A summary of applications in which these fibers have been interfaced with hot atomic vapors and cold atomic systems are then presented. Very recent work on nonlinear optics phenomena is also discussed, such as electromagnetically induced transparency (EIT) and the associated slow light feature that led to the realization of ONF-based atomic memories. Finally, we provide some insight on work realized exploiting the higher order modes (HOM) of an optical nanofiber, an overlooked part of the field which is at the heart of this PhD thesis. The chapter ends with a conclusion section that clarifies the focus of the work presented here.

[1] This chapter was adapted from the work published in T. Nieddu, V. Gokhroo, and S. Nic Chormaic, *Optical nanofibers and neutral atoms,"* J. Opt. **18**, 053001 (2016) [1]. T. Nieddu wrote the review article under the supervision of V. Gokhroo and S. Nic Chormaic.

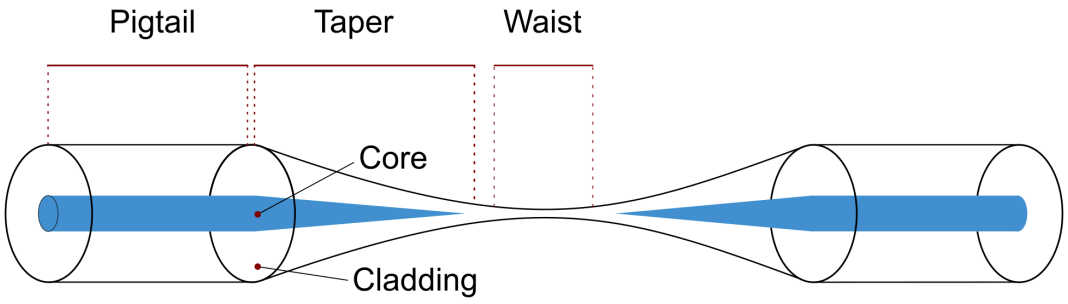

Figure 1.1: Schematic of an ONF. Three parts, indicated by the red dotted lines, can be distinguished: the pigtail, the taper, and the waist. The original core essentially vanishes at the waist where it is replaced by the former cladding.

1.1 Optical Nanofiber Basics

Fabrication of an ONF usually consists of heating a commercially available optical fiber, stripped of its acrylic coating, to a temperature close to the glass melting point (i.e., 1550°C for silica). Under these conditions, the stripped region of the fiber enters a plastic regime and can be elongated without breaking. As the pulling process is carried out, three regions appear: the pigtail, the taper, and the waist. The composition of an ONF is sketched in Fig. 1.1.

The pigtail consists of the unmodified part of the original optical fiber. In this region, the refractive index difference between the core and cladding is typically small; the core, with refractive index, $n_1 \approx 1.46$, is made from doped silica and has a slightly larger refractive index than that of the cladding, $n_2 \approx 1.45$, made out of silica, in order to ensure conditions for total internal reflection are met. In general, $n_1 - n_2 << 1$ and light guided in this region is said to be in the *weakly guiding regime*. The second region, called the taper, is a transition region in which the diameter of the original core reduces with the taper length, until it becomes so negligible it can be viewed as having vanished. At this point, the former cladding becomes the new core, thereby forming the third region or waist. The waist, with its core made out of the former cladding, i.e., silica, is clad by the surrounding medium, which is viewed as the vacuum throughout this PhD work. This medium needs to be of lower refractive index than silica in order to allow guided-light to propagate within the ONF, and we have $n_1 \approx 1.45$ and $n_2 = 1$. Due to the large refractive index difference between the core and cladding, light propagating in this region is said to be in the *strongly guiding regime*. Depending on the wavelength of the light launched into the fiber, and the diameter of the waist, a significant evanescent field can be generated [18]. This property finds a large range of applications which shall be discussed further in this chapter.

Several ONF fabrication methods have been reported in the scientific literature [19–26]. The choice of a specific method generally depends on one's needs, aims, and resources. For cold atom experiments, the so-called *flame-brushing technique* [20, 25] tends to be preferred over others as it offers fine control over both the taper shape and the waist size. Routinely, ONFs with waist diameters as small as 350 nm can be fabricated. Similar advantages were recently reported using a microheater-based fiber-pulling rig [27].

To avoid deterioration of the guiding properties of an ONF during the fabrication process, the so-called *adiabatic criterion* needs to be respected [28]. Previously, our group calculated the adiabatic criterion for fabrication of near-lossless nanofibers to permit the propagation of the first two families of modes, namely the linearly polarized (LP) modes, LP_{01} and LP_{11} [29], for the case of an 80 μm diameter pretapered fiber. The technique was later refined by Ravets *et al.*, using optical fibers with a 50 μm diameter cladding [30]. They obtained HOM propagation efficiency in the LP_{11} family up to 97.8%. Hoffman *et al.* subsequently reported fabrication of ultrahigh transmission ONFs for efficient support of both the fundamental mode and the first group of HOMs [31]. They observed the spatial evolution of HOMs in the LP_{11} group, over the whole fiber length, via Rayleigh scattering imaging [32]. With this method, they were able to identify and control modal propagation in the LP_{11} group. Nagai and Aoki proceeded to further optimize the tapering process by adjusting the tapering angle during the pull in order to closely match the adiabatic criterion for a given fiber diameter, reducing the overall length of the taper region [26]. This procedure was originally developed for fundamental mode nanofibers, but should, in principle, be easily extended to fabricate fibers for higher order modes. A more detailed description of adiabatic tapering will be presented in Chapter 2 specifically for a HOM-ONF that we fabricated and installed in the cold atom system used throughout this thesis work.

1.2 Probing Atoms using ONFs

ONFs have attracted considerable interest for particle trapping and manipulation and, more recently, for the development of atom-based quantum technologies. Such devices, being by design photonic waveguides, are particularly praised for their potential role as efficient and reliable photonic communication channels between distant quantum systems [33]. Atoms localized close to the waist's surface can emit light that couples preferentially to the guided modes of the fiber [3, 34, 35]. This, in turn, can enhance or inhibit the photon emission rate [36], depending on the orientation of the induced dipole, and can be engineered to generate a lateral translation-invariant force on the atoms [37]. The coupled photons in these modes are correlated in either a bunching or an anti-bunching fashion, as demonstrated experimentally by Nayak *et al.* [38]. Due to the significant evanescent field produced at the waist, the guided light can interact with atoms in its vicinity via absorption [39].

Extensive work on in-fiber spectroscopy of hot vapors [40–43] has also been done. However, introduction of an ONF into an atomic vapor often results in the atoms adsorbing to the fiber's surface, thereby reducing its efficiency as a probing tool. Several ways of dealing with this problem have been explored. For example, desorption of Rb atoms was demonstrated by coupling low power light that is blue-detuned from an atomic resonance into the ONF [41], or by placing the fiber on a flange-mounted heater [44]. Alternatively, it was also proposed to switch to a vapor of metastable xenon atoms [45], as the noble gas interacts less with the fiber. Saturated absorption at the nW level was shown in this system.

Due to the ultra-low pressures needed in cold atom experiments in contrast to vapor experiments, the problem of atom adsorption on the fiber does not occur to a detrimental

level. This makes the ONF an excellent tool to probe and characterize atom clouds created in a MOT [46, 47]. Our group was particularly active in this field of research [4, 5, 48], using an ONF embedded in a cold atomic system to measure the temperature of a cloud of ^{85}Rb atoms via several different techniques. In [5], temperature variations of the order of μK created by changes in the cooling lasers' alignment, intensities, or detuning, were detected by comparing the fluorescence signals coupling into the ONF throughout the different stages of a release-recapture process. A dark-MOT [48] of the same atomic species was also characterized using similar methods. Later, Grover *et al.* [49] performed temperature measurements in a MOT of ^{87}Rb atoms. The characterization method, although relying on fluorescence collected from an ONF, used a correlation function to extract the velocity of atoms surrounding the fiber and, hence, their temperature. It has also been proposed to use an ONF as position sensors of trapped atoms in an optical lattice [50].

The above-mentioned intense optical field at the waist can be created even for low input powers. This can be used for exploring nonlinear optics phenomena in atomic media, which is in stark contrast to the power requirements for similar experiments performed with free-space beams, i.e., typically a few mW, giving intensities of the order of ≈ 10 mW/cm^2 for tightly focused beams. Several years ago, our group made this evident by showing Autler-Townes splitting (ATS) of the $5S_{1/2} \rightarrow 5P_{3/2}$ transition, when probing the $5P_{3/2} \rightarrow 5D_{5/2}$ transition via a nanofiber-mediated two-photon process in laser-cooled ^{87}Rb atoms [11]. The ATS appeared for input powers as low as 20 nW and, in addition, frequency up-conversion from 776 nm to 420 nm was observed at powers as low as 0.2 nW, corresponding to intensities at the waist of the order of 10^4-10^5 mW/cm^2.

1.3 Nanofiber-Based Traps for Cold Atoms

The interaction of atoms with an evanescent light field has long been known [51–55]. In the 1990's, it was proposed [56], and later demonstrated [57], that atoms could be guided inside a hollow-core fiber using the optical dipole force resulting from the interaction with the guided light. Later, Ito *et al.* [58] designed a similar experiment using blue-detuned light to repel atoms from the fiber's inner surface and guide them along the center of the core. Loading atoms inside a fiber is nontrivial and, to overcome some of the limitations, Balykin *et al.* [59] proposed trapping ^{133}Cs atoms outside the ONF by propagating a red-detuned laser beam in the fundamental guided mode (i.e., HE$_{11}$). This mode creates a dipole force gradient within the evanescent field which attracts the surrounding atoms towards the fiber.

To understand how atoms can be trapped in the vicinity of an ONF's waist using a combination of beams detuned from resonance, it is necessary to identify the forces at play. Consider a single atom placed in an oscillating electric field, $\mathbf{E}(\mathbf{r})$, such that a dipole moment, $-e\mathbf{r}$, is induced in the atom. Mathematically, we have [60]

$$-e\mathbf{r} = \epsilon_0 \chi_a \mathbf{E}(\mathbf{r}), \tag{1.1}$$

where e is the fundamental electric charge, ϵ_0 is the electric permittivity in vacuum and χ_a is the scalar polarizability. The interaction between this dipole and the electric field yields a potential energy, $\mathrm{U}(\mathbf{r})$, given by

$$\mathrm{U}(\mathbf{r}) = \frac{1}{2} e\mathbf{r} \,.\, \mathbf{E}(\mathbf{r}), \tag{1.2}$$

where the factor of 1/2 arises due to the dipole moment being induced rather than permanent. Assume the electric field is a plane wave, propagating along the z-direction and polarized in the x-direction with angular frequency, ω, and wave number, k, with a field, $\mathbf{E}(\mathbf{r}) = E_0(\mathbf{r})\cos(\omega t - kz)\hat{\mathbf{e}}_x$. Then, the force acting on the atom in the z-direction is expressed as

$$\begin{aligned} \mathrm{F}_z &= \frac{-\partial \mathrm{U}}{\partial z} = -\frac{ex}{2}\frac{\partial E}{\partial z} \\ &= -\frac{ex}{2}\left[\frac{\partial E_0}{\partial z}\cos(\omega t - kz) + kE_0\sin(\omega t - kz)\right]. \end{aligned} \tag{1.3}$$

The expression in Eq. (1.3) can be written with the dipole moment expressed in terms of its components on the Bloch sphere and time-averaged to get the final expression for the forces as (see for example p.198 of [60] for a detailed development)

$$\begin{aligned} \bar{\mathrm{F}}_z = &-\frac{\hbar\delta}{2}\frac{\Omega}{\delta^2 + \Omega^2/2 + \Gamma^2/4}\frac{\partial\Omega}{\partial z} \\ &+ \frac{\hbar k\Gamma}{2}\frac{\Omega^2/2}{\delta^2 + \Omega^2/2 + \Gamma^2/4}, \end{aligned} \tag{1.4}$$

where Γ is the decay rate of the excited state, Ω is the Rabi frequency, and $\delta = \omega_L - \omega_0$ is the detuning between the laser frequency, ω_L, and the atomic transition resonant frequency, ω_0, of the considered transition. The first term of Eq. (1.4) describes the dipole force, whereas the second term is the scattering force, which plays a central role in laser cooling processes. It is important to note that the dipole force depends on the gradient of the electric field intensity and the frequency detuning. For negative detuning (i.e., a red-detuned beam), an atom placed in the vicinity of the ONF and interacting with its evanescent field will experience a force pointing in the same direction as the gradient of intensity, i.e., towards the fiber's center. For fibers with a waist diameter roughly half the light's wavelength, this force can be balanced by the centrifugal force acting on atoms revolving around the ONF [59] and, hence, can be used to trap them. However, the number of atoms that can be trapped using this scheme is restricted to those possessing an initial angular momentum along the fiber axis within an appropriate range. Le Kien *et al.* [61] proposed an improved version of the ONF trap, relying on a two-color scheme: a red-detuned beam to attract the atoms towards the ONF and a blue-detuned beam to repel and prevent them from sticking to its surface. In this case, the van der Waals potential created by the fiber [9, 10] acts together with the red-detuned beam to attract the atoms, while the blue-detuned beam prevents them from sicking to its surface.

The experimental achievement of the two-color trapping scheme was made in 2010 [6]. As depicted in Fig. 1.2, laser-cooled ^{133}Cs atoms were trapped around the waist of an ONF using the evanescent field resulting from the combination of a blue-detuned beam and two counter-propagating red-detuned beams with respect to the ^{133}Cs D_2 line. The trapping scheme was done in a collisional-blockade regime [62], which allows only one atom at most per trapping site at a time. Approximately 2,000 atoms were estimated to be trapped around the nanofiber. Atoms trapped in this configuration showed ground state coherence times on the order of milliseconds [63]. This trapping scheme was extended to create a conveyor belt [8] and led to the transportation of cold caesium atoms over a few mm along the ONF. Lee *et al.* later adapted the two-color scheme to trap ^{87}Rb atoms

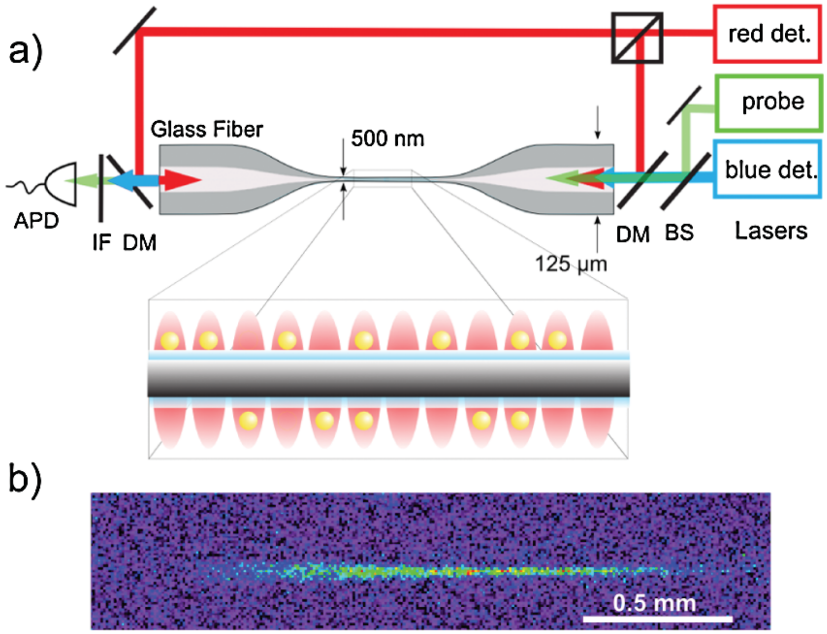

Figure 1.2: Principle behind the experimental implementation of the first ONF-mediated atom trap. a) Layout of the experimental set-up and schematic of the standing wave trapping sites. The counter-propagating red-detuned beams create trapping sites, while the blue-detuned beam prevents atoms from sticking to the surface of the fiber. b) Fluorescence image of trapped ^{133}Cs atoms in the evanescent field of an ONF. APD: Avalanche photodiode, BS: Beam-splitter, DM: Dichroic mirror, IF: Narrow-band infrared filter. Reproduced from [6].

[64]. They reported trapping of only 300 atoms, 7 times less than reported in [6] for ^{133}Cs atoms. This was attributed to the difference in atomic structure between ^{133}Cs and ^{87}Rb, the latter being subject to larger light shifts. It was also proposed to use the fictitious magnetic field generated by a nanofiber-guided light field in combination with an external magnetic bias field to create trapping potentials along the waist [65].

The above-mentioned light shifts can be problematic for the transfer of coherent information over long distances [66]. One solution is to use the so-called *magic wavelengths* [67]. When the trapping laser is operating at these specific wavelengths, hyperfine levels of interest undergo the same AC Stark shift, thus leaving the transition frequency unchanged. Several groups have been working on perfecting these state-insensitive traps, showing improved trap lifetimes and lower trapping powers in the two-color scheme for both rubidium and caesium atoms [7, 66, 68, 69]. Although extremely efficient, state-insensitive traps are restrictive as one is required to work with a specific trapping wavelength.

1.4 Collective Effects and Atomic Memories

Achievement of a fiber-based atom trap can be seen as a stepping-stone towards more complex experiments. With this tool at hand, researchers are able to study 1D-arrays of atoms periodically positioned in the vicinity of a nanofiber waist and associated collective

effects. For example, two groups demonstrated Bragg reflection from an atomic mirror created by means of an ONF-mediated atom trap [15, 16]. Note that collective effects have also been studied in systems which did not involve fiber-trapped atoms. Solano *et al.* recently demonstrated sub- and super-radiance in a MOT, showing that atoms in the vicinity of a nanofiber could interact over long distances by exchanging fluorescent photons coupled to the guided modes [17].

The development of an efficient quantum memory is fundamental to the creation of any quantum-based computing system. In a quantum network, a quantum memory acts as a node connecting quantum channels in which information is written, stored, and read out [70]. Quantum information is easily lost over long distances due to the lossy nature of photonic channels such as optical fibers. This problem can be resolved by setting quantum repeaters along a transmission channel [71]. These repeaters rely on heralding photons which can be detected to indicate a quantum system is entangled, all the while preventing the collapse of this entanglement when performing the measurement. Light-atom systems are good candidates for this purpose and extensive work on the implementation of optical quantum memories, reviewed in [72], has been done to date. Very recently, Corzo *et al.* [73] demonstrated heralded collective excitation in an atomic array, paving the way towards the implementation of an all-fibered DLCZ protocol[2] [71].

In particular, it has been proposed to store information carried by light in atoms, via EIT [74]. This effect, first demonstrated in 1990 with strontium atoms [75], relies, in its simplest form, on three atomic levels, which can be arranged in the so-called Λ-, ladder-, or V-configurations [76]. The three atomic levels, which we denote by $|1\rangle$, $|2\rangle$, and $|3\rangle$, need to be chosen such that the transitions $|1\rangle \rightarrow |2\rangle$ and $|2\rangle \rightarrow |3\rangle$ are allowed, but $|1\rangle \rightarrow |3\rangle$ is forbidden. If a weak probe field addresses $|1\rangle \rightarrow |2\rangle$ and a strong control field addresses $|2\rangle \rightarrow |3\rangle$, then, for a definite range of frequencies, the optical medium becomes transparent to the probe field. In addition to the induced transparency window, EIT also features a drastic reduction in the group velocity of the light beam passing through the material [77]. EIT, and the associated slow light feature, have been generated in atomic media using the evanescent field at the waist [78, 79]. Our group demonstrated a ladder-type EIT process in laser-cooled ^{87}Rb atoms [12], using powers below 1 μW in each of the required beams. Storage of guided light in a cold atomic system using the slow-light feature was also demonstrated [13, 14]. In [13], fiber-trapped ^{133}Cs atoms were used, following a trapping scheme similar to that presented in [6]. The probe pulse was stored and retrieved on demand, with a recovery efficiency of 3%. In [14], a similar experiment was carried out, this time using cold Cs atoms trapped in a MOT overlapping the waist of an ONF. The retrieval efficiency of the stored pulse was much better in this case and reached up to 10%.

[2]The implementation of the DLCZ protocol relies on three-level systems in atomic ensembles. Similar to the EIT Λ-configuration, the system has two ground states, $|1\rangle$ and $|3\rangle$, which can only be connected via an intermediate excited state, $|2\rangle$. An atomic ensemble is initially prepared in $|1\rangle$ and excited with a weak pulse detuned from the $|1\rangle \rightarrow |2\rangle$ transition. This probabilistically transfers one atom of the ensemble to the $|3\rangle$ state, emitting a heralding Stokes photon in the process. Two such atomic ensembles can be excited in a similar manner, for which detection of a Stokes photon in the far field heralds their entanglement.

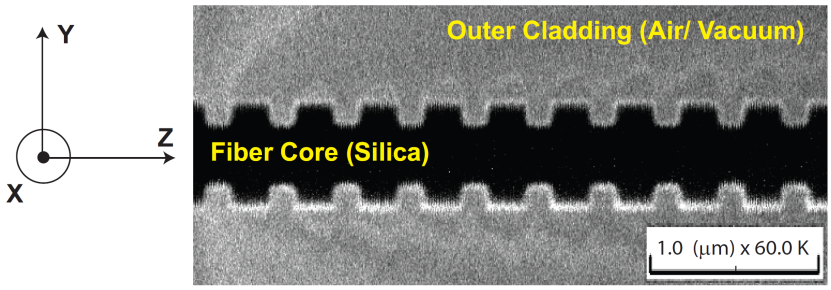

Figure 1.3: Scanning electron microscope image of a nanofiber Bragg grating fabricated via FIB milling. The fiber has a diameter of $\sim$ 560 nm and each slit is $\sim$ 150 nm wide and $\sim$ 100 nm deep. Two neighboring slits are separated by $\sim$360 nm. Reproduced from [89].

1.5 Fiber-Integrated Cavities

Strong coupling can be viewed as an essential requirement to devise quantum networks based on neutral atoms [70, 80, 81] and, until recently, free-space cavities were the most promising method for enabling an atomic system to enter this regime [82]. Although ONFs offer similar features to those of cavities, albeit in a more scalable manner, there is an interest to combine both in order to enhance the interaction between the light and matter. Some proposals have highlighted the advantages of creating a cavity network, in which each cavity is linked to others via fibers [83, 84]. Le Kien *et al.* have proposed an alternative solution, consisting of ONFs with a fiber Bragg grating (FBG) at either end of the waist [85–87]. The system combines both aspects in one and can be used to demonstrate the strong coupling regime with relatively low cavity finesse. Such devices could lead to improvements in the generation of EIT [85], or entangled photons [88], and thus pave the way to quantum information generation and storage in an all-fibered network. These proposals are experimentally achievable as Nayak *et al.* have reported fabrication of FBG-ONFs using a focused ion beam (FIB) milling technique [89], an image of which is presented in Fig. 1.3. Kato and Aoki [90] demonstrated strong coupling for a single trapped atom and an all-fibered optical cavity based on an ONF spliced between two fiber Bragg grating mirrors.

Another type of ONF-based cavity, the ring cavity, was recently developed [91]. The principle behind this type of cavity is fairly simple: an ONF is connected to both ends of a fiber-splitter in order to create a cavity. Using such a device, Ruddell *et al.* demonstrated collectively enhanced strong coupling between the guided-light and an ensemble of atoms trapped in a MOT [91], thereby further illustrating the potential offered by such devices for future quantum advances.

1.6 Exploiting Higher Order Fiber Modes

Waveguides, such as optical fibers, feature optical modes in which guided light can propagate. The capability of a step-index waveguide to guide light is determined by the value

of a dimensionless parameter called the V-number [92, 93], defined as

$$\mathrm{V} = \frac{\pi d}{\lambda}\sqrt{n_1^2 - n_2^2}, \tag{1.5}$$

where $d = 2a$ is the fiber waist diameter, λ is the wavelength of light, and n_1, n_2 are the refractive indices of the fiber core and cladding, respectively. A waveguide is said to be single-mode when $V < 2.405$. Modes that are permitted to propagate are characterized by their propagation constant, β [2]. Depending on the guiding regime, two families of modes can be distinguished: (i) the LP family and (ii) the true modes of the waveguide, namely transverse electric (TE), transverse magnetic (TM), hybrid electric (HE), and electric hybrid (EH) modes. We will loosely refer to the latter modes as HOMs in the following.

In standard optical fibers, the refractive index difference between the core and the cladding is typically small, on the order of 10^{-3}, leading to the aforementioned *weakly-guiding regime*. This leads to true modes of a particular LP family to be degenerate in β. Light propagating in these modes tends to excite combinations of HOMs, interfering to form the LP modes [92], a selected sample of which are plotted in Fig. 1.4. These families of modes have very distinct propagation constants. At the waist of ONFs, however, the refractive index difference between the core and the cladding is much larger, on the order of 10^{-1}, and light propagates in the *strongly-guiding regime*. The HOMs are analytic solutions to Maxwell's equations for a cylindrical, step-index, waveguide; they are no longer degenerate in β and can, in principle, be selectively excited. The transverse polarization profiles of the first few modes making the LP_{01} and LP_{11} groups are shown in Fig. 1.5. These modes were simulated for a waist diameter of 700 nm and a wavelength of 780 nm. Note that, even though four profiles are presented, the LP_{01} and LP_{11} families consist of six modes, as hybrid modes can exist in the so-called *even* or *odd* configuration[3].

Most experiments carried out so far with nanofibers embedded in atomic systems have focused solely on exploiting the fundamental modes, i.e., the HE_{11} modes. To date, our group has been the only one to report experimental work in which higher-order modes of an ONF have been shown to interact with cold atoms [94]. This scarcity in experimental work on HOMs and atoms is mainly due to the fact that, even though no longer degenerate, the β values for the HOMs within an LP family remain fairly close to that of other modes within the same LP group. In the example of the modes presented in Fig. 1.5, the β values are $[10.31,\ 8.78,\ 8.48,\ 8.26] \times 10^6$ m^{-1} for the modes $[\mathrm{HE}_{11}, \mathrm{TE}_{01}, \mathrm{TM}_{01}, \mathrm{HE}_{21}]$. As a consequence, light coupled to the HOMs of an LP family tends to cross-talk with other modes within the same LP family. This makes selective excitation an arduous task, especially when compared to the relative simple excitation of the fundamental fiber modes, HE_{11}.

1.6.1 Potential applications for HOMs in atomic systems

Despite the technical challenges associated with HOMs, a large amount of theoretical work has been carried out in the past few years. Le Kien *et al.* recently published a full theoretical characterization of a number of HOMs in an ONF [95]. These modes hold

[3]The suffix *even* and *odd* refers to the parity of the mode function defining the transverse electric field with respect to a given axis. The horizontal axis is chosen as the reference throughout the thesis.

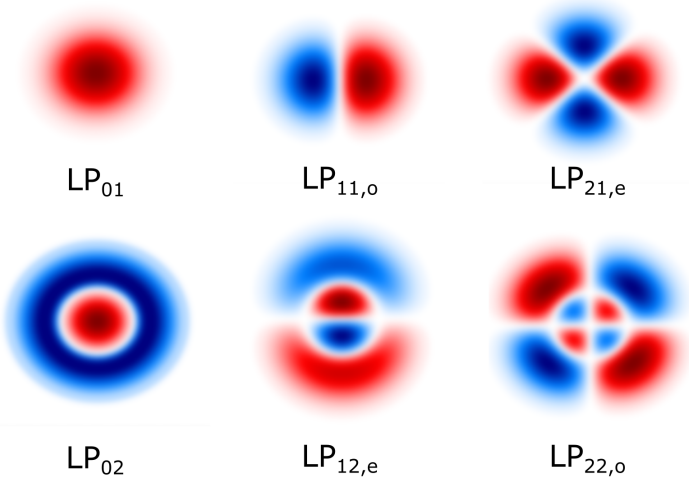

Figure 1.4: Electric field profiles of some LP modes. The red and blue colors indicate positive and negative amplitudes of the fields, respectively. Each mode, LP_{ij}, is characterized by two indices, with i indicating the number of pairs of lobes and j being the radial order. An additional index is used to indicate whether the mode is *even*, e, or *odd*, o.

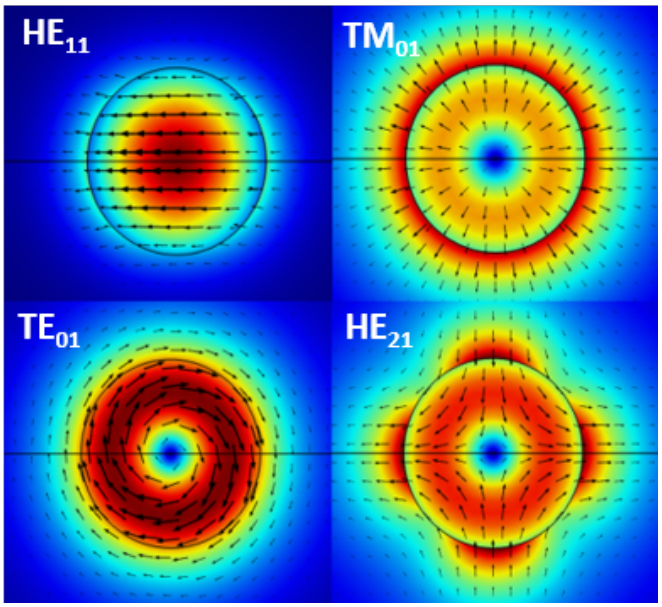

Figure 1.5: Polarization profiles of true-modes forming the first two LP groups. The hybrid electric, HE_{11}, mode is shown in its *odd* configuration and HE_{21} in its *even* configuration. Blue represents a low beam intensity and red a high beam intensity.

promise for a large range of applications. For example, they could be used to improve the probing of atomic systems [35, 96, 97]. An early theoretical study carried out by Masalov and Minogin found that fluorescent photons emitted from an excited ^{85}Rb atom close to the fiber's surface would preferentially couple to the higher order modes rather than the fundamental mode [35]. Le Kien *et al.* recently developed a more complex model of a similar system, using ^{87}Rb instead of ^{85}Rb [97], and found coupling values nearly three times lower than those predicted by the simple model used in [35]. In addition, Le Kien *et al.* showed that, for an atom close to the fiber waist, its spontaneous emission preferentially couples to the HE_{21} modes by up to 2 times more than for others modes. This behavior was valid for fiber radii relevant to the PhD work reported in this thesis. One issue this brings to light is that experiments limited to single-mode ONFs are effectively discarding a high percentage of light coupled into them from excited atoms. By using a HOM-ONF, signals should be increased, making detection of the low light levels typically involved in, for example, two photon processes, easier to detect.

Atom trapping using HOMs has also been proposed by several groups using different combinations of modes [98, 99]. Interference patterns resulting from the combination of two co-propagating, blue-detuned HOMs of LP_{11}, or one of the HOMs and the fundamental mode, should yield deeper trapping potentials at lower powers than what can be achieved in trapping schemes based solely on the fundamental mode [98]. A red-detuned version of this type of HOM + fundamental mode trap was also proposed by Fu *et al.* for a larger waist diameter [100]. Moreover, these modes offer the possibility of engineering trapping geometries that would allow for better control over the atom trap positions. This could also provide a mean to overcome limitations of fundamental mode fiber-based dipole traps that rely on a red-detuned, standing wave configuration yielding trapping sites separated by half a wavelength. With HOMs, the separation between each atom and their position relative to the fiber may be controlled by modifying the trapping beams' polarization [99, 101]. This is depicted in Fig. 1.6, which shows the trap geometries proposed in [99]. The method also relies on a two-color scheme in which counter-propagating red-detuned beams are in a HOM, while a blue-detuned beam is in the fundamental mode. One can choose from a periodically spaced ring, a periodic quadrupole, or a quadruple-helix trap geometry by fixing the red-detuned trapping beams' polarization to circular-circular with same handedness, linear-linear, or circular-circular with opposite handedness, respectively. Several ways of implementing a coherent tractor beam for cold atoms next to an HOM-ONF have also been proposed [102].

ONFs are highly valuable tools for the study of chiral systems due to the non-zero longitudinal field component at their waist [103]. In particular, the inhomogeneous polarization profiles that are a feature of HOMs makes them more chiral than the fundamental mode, and can even lead to *superchirality* (i.e., more chiral than circularly polarized light, thought initially to yield maximum chirality) [104]. This superchiral property is present along the whole length of the waist, a drastic difference from superchirality in free-space, only theorized until now to be found at the nodes of a standing wave made of circularly polarized beams [105].

Among the HOMs, hybrid modes (i.e., the HE and EH) are of particular interest for quantum information encoding. Indeed, in addition to spin-angular momentum (SAM), which is encoded on the polarization of the guided mode, these modes can also carry orbital angular momentum (OAM), which, in turn, can lead to a total angular momentum greater

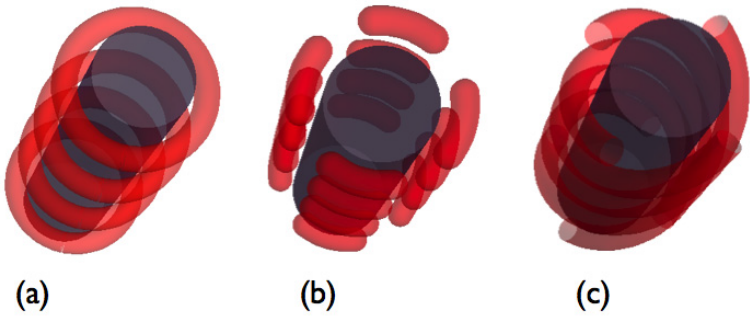

Figure 1.6: Various geometries achievable in two-color HOM trapping schemes. (a) Both of the red-detuned counter-propagating beams have circular polarization with identical handedness yielding periodic ring-like trapping potentials. (b) Both beams have linear polarization yielding periodic quadrupole-like potentials. (c) Both beams have circular polarization but with opposite handedness yielding a quadruple-helix trapping potential. Reproduced from [99].

than $\hbar$ [95] (see Fig. 1.7). Quantum information encoding using the OAM of light has seen tremendous development in the last few years (for a review see, for example, [106, 107]). The possibility to transfer high-density information encoded on both the SAM and OAM to a cold atomic system from an ONF is particularly interesting. This perspective is, in part, what motivated the theoretical work presented in Chapter. 4.

1.6.2 Selective excitation of HOMs

In most of the aforementioned applications, selective excitation of specific guided modes in the ONF is necessary. A first step towards mode selection comes from tailoring the value of the V-number. Figure 1.8 shows a plot of the effective refractive index of a mode, defined as $n_{\text{eff}} = \beta/k$, as a function of V. By monitoring the transmission of light injected into the optical fiber during the tapering process, the number of propagating modes can be directly tailored [28, 29, 31]. Note that the fundamental mode is always present.

Excitation of a specific LP family of modes in an optical fiber can be achieved by inducing birefringence in the fiber via mechanical stress [108], though it is difficult to do in a controlled manner. Alternatively, Laguerre-Gaussian beams (LG) with appropriate topological charge and radial order can be created in free-space and launched into the fiber to excite the same modes [109]. For example, an LG_{01} beam launched into an optical fiber will maximally overlap with the LP_{11} group, thus minimizing chances of cross-talk with other LP groups. Using a spatial light modulator (SLM) to combine two LG beams with unitary and opposite topological charge, namely LG_{01} and LG_{0-1}, leads to the creation of cylindrical vector beams (CVBs) [110], which can be regarded as the free-space equivalent of HOMs [111]. Previously, CVBs have been obtained after excitation of higher order modes in an optical fiber, either via control of the polarization [112] or the phase [113] of an input LG beam. In subsequent work, Fatemi and Beadie created similar beams using an optical fiber by first characterizing the mode mixing via interferometric decomposition of the fiber output and then correcting for it by applying mechanical stress at the input pigtail of the fiber [114]. Only two methods have been developed to characterize the

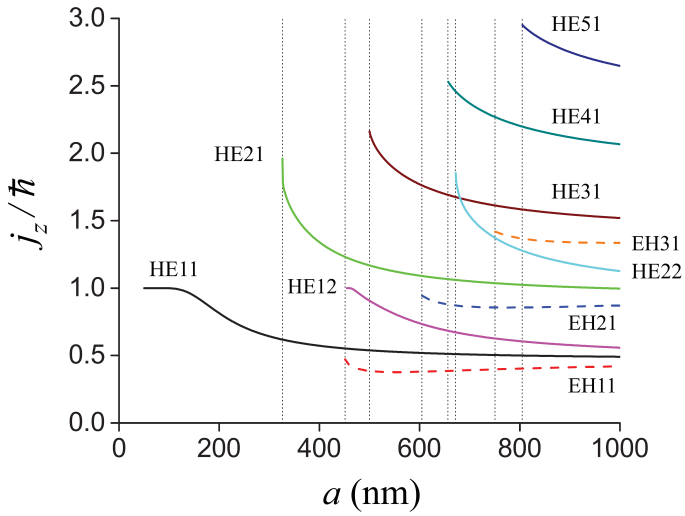

Figure 1.7: Capability of the hybrid modes to carry more than $\hbar$ of total angular momentum. The total angular momentum per photon, j_z, is plotted as a function of the fiber radius, a, for different circularly polarized hybrid modes. Reproduced from [95].

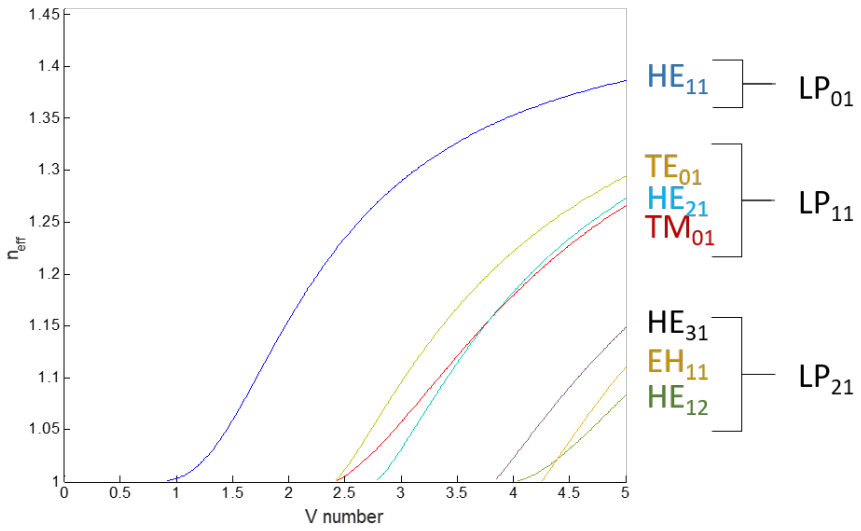

Figure 1.8: Effective refractive index as a function of the V-number for modes in the first three LP groups.

modes excited at the waist of an optical nanofiber; One uses Rayleigh scattering from imperfections at the waist [32], whereas the other uses near-field probing of the waist with another fiber [115, 116].

1.7 Conclusion

The main focus of this PhD work was to selectively excite the higher order modes in an optical nanofiber, with particular interest in the LP_{11} family to study interactions between atoms and HOMs. This research is of particular importance for applications such as novel trap geometries, OAM encoding, addressing quadrupole transitions, etc. The novel trap geometries could, for example, be used to move atoms further or closer to the waist surface than the conventional two-color dipole trap, thereby allowing one to tune the photon coupling strength into a guided mode. However, in order to achieve this goal it is essential to overcome a number of other experimental and technical challenges and these form the basis of the work presented here.

In Chapter 2, a brief mathematical description of the origin of HOMs in a nanofiber is provided, including the explicit expressions of their field components in polar coordinates. The chapter also provides a detailed explanation of the methodology used to fabricate a high transmission nanofiber supporting up to the first group of HOMs and to install it into a cold atom setup. Next, some basics behind laser cooling of neutral atoms are provided in Chapter 3 , along with a description of the cold atom setup used for most of this PhD work. The characterization of the MOT is additionally detailed.

In Chapter 4, a theory of a quadrupole interaction between a single atom and the evanescent field at the waist of a nanofiber is presented. The results show that ONFs form an excellent platform to mediate such transitions, as the transition probability is enhanced up to 6-fold when compared to free-space beams. The quadrupole excitation may also be driven by HOMs which leads to speculations about potential future applications for high-density quantum information encoding.

As the quadrupole excitation described in Chapter 4 could not be studied experimentally due to technical reasons, a similar system involving a single-color two-photon transition was studied. The results of experiments carried out in a hot vapor and with a nanofiber embedded in a MOT are presented in Chapter 5. Exploiting the selection rules for this transition, it may be possible to perform polarization tomography at the waist, which would be a valuable tool for the improvement of ONF-mediated atom trapping schemes. This could also prove useful for the development of methods to selectively excite HOMs at the fiber waist.

Chapter 6 presents initial results for interfacing HOMs with cold atoms in a MOT in order to determine the modes excited at the waist of a nanofiber. Details of the main technical challenges that were encountered are provided. This led to the development of an improved experimental setup, designed to generate HOM-like beams in free-space, to optimize their injection into the nanofiber, and to decompose the fiber output profiles in terms of its eigenmodes. Preliminary results obtained with the new setup are also presented.

Finally, Chapter 7 concludes this thesis, summarizing the work achieved so far and presenting some outlook on both the HOM and the two-photon projects, specifically in

the context of developing nanofiber-based quantum technologies.

Chapter 2

Optical Nanofibers: Higher Order Mode Propagation, Fabrication, and Integration with Cold Atoms

Technical challenges associated with selective modal excitation at the waist of an ONF have, so far, limited experimental work aimed at interfacing HOMs with atoms. However, as mentioned in Chapter 1, some higher order modes could potentially offer a series of advantages compared to the fundamental mode for atom probing [35, 97], trapping [98–100], or manipulation [102], and for the study of chiral systems [104]. This chapter first provides a brief mathematical description of the origin of HOMs in a step-index waveguide. Expressions for the mode profile function components in polar coordinates of both the electric and magnetic fields are introduced. Since the work presented herein focuses on the study of the first six true fiber guided modes, each mode type described hereafter is accompanied by an illustration of the appropriate intensity profile. The fabrication of a high transmission HOM-ONF is then explained in detail, followed by the description of its installation inside the ultrahigh vacuum (UHV) chamber that was used for most experiments presented in this thesis.

2.1 Guided Modes of a Step-Index Fiber

2.1.1 Eigenvalue equations

An ONF can be approximated as a perfectly cylindrical, step-index fiber in which the refractive index of the core, n_1, is larger than the refractive index of the cladding, n_2. Mathematically, the fiber is represented by the following index profile

$$n(r) = \begin{cases} n_1, \ 0 < r \leqslant a, \\ n_2, \ a < r < \infty, \end{cases} \tag{2.1}$$

where a denotes the core radius, r is the radial position from the fiber center, and it is assumed that the cladding radius is infinite. This assumption is common in fiber optics as the cladding radius is generally around 40 μm to 62.5 μm, which is an order of magnitude larger than the core radius of a few μm. If the fiber is assumed to be isotropic and source-free, Maxwell's equations for light propagating within this system can be reduced to the

following set of Helmholtz equations [92]

$$(\nabla^2_{\mathrm{T,cyl}} + n^2k^2 - \beta^2)\Psi_z = 0, \tag{2.2}$$

with $\nabla^2_{\mathrm{T,cyl}} = \nabla^2 - \partial^2/\partial z^2$ representing the transverse Laplace operator in cylindrical coordinates, $k = 2\pi/\lambda$ is the wave number, β is the modal propagation constant and $\Psi_z = \{E_z, H_z\}$ represents the z-component of either the electric or magnetic field of the input light wave, respectively. This equation is separable into its individual components [92, 93] and solutions may take the form

$$\Psi_z = \Psi(r)\exp(\pm il\phi), \tag{2.3}$$

with $\Psi(r)$ being the radial part and the exponential term representing the azimuthal part. Here, $l = 1, 2, 3, ...$, and z, r, and ϕ denote the longitudinal, radial, and azimuthal components of the field, respectively. Inserting this into Eq. (2.2) gives

$$\partial_r^2\Psi(r) + \frac{1}{r}\partial_r\Psi(r) + \left(n^2k^2 - \beta^2 - \frac{l^2}{r^2}\right)\Psi(r) = 0, \tag{2.4}$$

which is a Bessel differential equation, the solutions of which are Bessel functions of order l. Two cases can be distinguished, depending on the sign of $n^2k^2 - \beta^2$, and their general solutions can be calculated to yield [93]

$$\begin{aligned} \Psi(r) &= c_1 J_l(hr) + c_2 Y_l(hr) \ \text{ if } n^2k^2 - \beta^2 > 0, \\ \Psi(r) &= c_3 I_l(qr) + c_4 K_l(qr) \ \text{ if } n^2k^2 - \beta^2 < 0, \end{aligned} \tag{2.5}$$

where $h = \sqrt{n^2k^2 - \beta^2}$, $q = \sqrt{\beta^2 - n^2k^2}$, the c_i represent constants, J_l and Y_l are Bessel functions of order l of the first and second kind, respectively, and I_l and K_l are modified Bessel functions of order l of the first and second kind, respectively.

For confined propagation of light at the waist, the effective refractive index, β/k_0, should be larger than the cladding's refractive index; this leads to the case $n^2k^2 - \beta^2 < 0$. For $r \to \infty$, I_l diverges and leads to nonphysical solutions. Therefore, $c_3 = 0$ and we are left with the term $c_4K_l(qr)$ in the radial part of the field, see Eq. (2.3), describing the exponential decay of the evanescent field at the waist of the fiber.

Solving Eq. (2.2) for the fields in the core yields four eigenvalue equations, corresponding to the four possible guided modes inside a cylindrical optical fiber, namely the hybrid electric (HE), electric hybrid (EH), transverse electric (TE), and transverse magnetic (TM) modes. We list the analytical expressions for their eigenvalue equations here. The full mathematical development starting from Maxwell's equations can be found in Appendix A.

EH_{lm} modes:

$$\frac{J_{l+1}(ha)}{haJ_l(ha)} = \frac{n_1^2 + n_2^2}{2n_1^2}\frac{K_l'(qa)}{qaK_l(qa)} + \left(\frac{l}{(ha)^2} - R\right), \tag{2.6}$$

HE_{lm} modes:

$$\frac{J_{l+1}(ha)}{haJ_l(ha)} = -\left(\frac{n_1^2 + n_2^2}{2n_1^2}\right)\frac{K_l'(qa)}{qaK_l(qa)} + \left(\frac{l}{(ha)^2} - R\right), \tag{2.7}$$

TE_{0m} modes:

$$\frac{J_1(ha)}{haJ_0(ha)} = -\frac{K_1(qa)}{qaK_0(qa)}, \tag{2.8}$$

TM_{0m} modes:

$$\frac{J_1(ha)}{haJ_0(ha)} = -\frac{n_2^2 K_1(qa)}{qan_1^2 K_0(qa)}, \tag{2.9}$$

with

$$R = \left[\left(\frac{n_1^2 - n_2^2}{2n_1^2}\right)^2 \left(\frac{K_l'(qa)}{qaK_l(qa)}\right)^2 + \left(\frac{l\beta}{n_1 k_0}\right)^2 \left(\frac{1}{q^2a^2} + \frac{1}{h^2a^2}\right)^2\right]^{1/2}. \tag{2.10}$$

In these expressions, K_l' denotes $dK(qa)/d(qa)$.

2.2 Components of the Mode Profile Functions

From the mode conditions given in Eqs. (2.6), (2.7), (2.8), and (2.9), it is possible to get the full expression for the mode profile functions in cylindrical coordinates. In what follows, the formalism developed in [95] is used. We write the components of the electric and magnetic fields in the form

$$\begin{bmatrix}\mathbf{E}\\ \mathbf{H}\end{bmatrix} = \frac{1}{2}\begin{bmatrix}\mathcal{E}\\ \mathcal{H}\end{bmatrix}\exp(-i\omega t) + c.c, \tag{2.11}$$

where $\mathcal{E}$ and $\mathcal{H}$ are spatial envelopes which satisfy the Helmholtz equation. A guided mode with propagation constant, β, and azimuthal mode order, l, is described by

$$\begin{bmatrix}\mathcal{E}\\ \mathcal{H}\end{bmatrix} = \frac{1}{2}\begin{bmatrix}\mathbf{e}\\ \mathbf{h}\end{bmatrix}\exp[i(\beta z + l\varphi)], \tag{2.12}$$

where $\mathbf{e}$ and $\mathbf{h}$ are defined as the reduced mode profile functions. These functions can be decomposed in terms of their components in cylindrical coordinates. The notations $\hat{\mathbf{r}} = \hat{\mathbf{x}}\cos\varphi + \hat{\mathbf{y}}\sin\varphi$, $\hat{\boldsymbol{\varphi}} = -\hat{\mathbf{x}}\sin\varphi + \hat{\mathbf{y}}\cos\varphi$, and $\hat{\mathbf{z}}$ are chosen to represent the unit vectors in cylindrical coordinates $\{r, \varphi, z\}$, and link them with the Cartesian coordinates $\{x, y, z\}$. The next section gives the explicit expressions for the reduced mode profile functions in the cylindrical basis.

2.2.1 Hybrid modes

The hybrid modes, HE or EH, possess longitudinal and transverse components with respect to the ONF's axis for both the magnetic and electric fields. They are defined here for $l > 0$. In the first two LP families, namely LP_{01} and LP_{11}, four hybrid modes are found. The first pair of hybrid modes are the $HE_{11,e}$ and $HE_{11,o}$ modes, which are degenerate in β, and form the LP_{01} group in the weakly-guiding regime. These modes are also called *fundamental modes* as they are always present in a step-index ONF. The next pair of modes, the $HE_{21,e}$ and $HE_{21,o}$ modes, form part of the LP_{11} group and are also degenerate in β, even in the strongly-guiding regime. Each of these modes can be quasicircularly or quasilinearly polarized, the prefix "quasi" being used here to distinguish them from fields in free-space as these fiber modes have, in general, a nonzero component along the fiber axis. Explicit expressions for the mode functions in cylindrical coordinates are given for both polarizations below.

Quasicircularly polarized hybrid modes

For a quasicircularly polarized hybrid mode, expressions for the full mode functions are given by

$$\begin{aligned}\boldsymbol{\mathcal{E}}_{\text{circ}}^{(flp)} &= \mathbf{e}^{(flp)} e^{if\beta z + ipl\varphi} \\ \boldsymbol{\mathcal{H}}_{\text{circ}}^{(flp)} &= \mathbf{h}^{(flp)} e^{if\beta z + ipl\varphi},\end{aligned} \tag{2.13}$$

in which the reduced mode profile functions are given by

$$\begin{aligned}\mathbf{e}^{(flp)} &= e_r\hat{\mathbf{r}} + pe_\varphi\hat{\boldsymbol{\varphi}} + fe_z\hat{\mathbf{z}}, \\ \mathbf{h}^{(flp)} &= fp\hat{\mathbf{r}}h_r + f\hat{\boldsymbol{\varphi}}h_\varphi + p\hat{\mathbf{z}}h_z,\end{aligned} \tag{2.14}$$

where $f = \pm 1$ is the mode propagation direction, l is the azimuthal mode order, and $p = +$ or $-$ is defined as the phase circulation direction, essentially indicating the direction of rotation of a quasicircularly polarized mode.

As mentioned previously, in order to write the expressions for the components of the reduced mode functions, one needs to calculate the constants A, B, C, and D in Eq. (A.23) from the eigenvalue equations, and insert the result into Eqs. (A.21) and (A.22). However, prior to giving the explicit expressions for the components (e_r, e_φ, e_z) and (h_r, h_φ, h_z), it is useful to introduce the following parameters

$$\begin{aligned}s &= l\left(\frac{1}{h^2a^2} + \frac{1}{q^2a^2}\right)\left[\frac{J_l'(ha)}{haJ_l(ha)} + \frac{K_l'(qa)}{qaK_l(qa)}\right]^{-1}, \\ s_1 &= \frac{\beta^2}{k^2n_1^2}s, \\ s_2 &= \frac{\beta^2}{k^2n_2^2}s.\end{aligned} \tag{2.15}$$

Then, we find for $r < a$

$$\begin{aligned}e_r &= iA\frac{\beta}{2h}[(1-s)J_{l-1}(hr) - (1+s)J_{l+1}(hr)], \\ e_\varphi &= -A\frac{\beta}{2h}[(1-s)J_{l-1}(hr) + (1+s)J_{l+1}(hr)], \\ e_z &= AJ_l(hr),\end{aligned} \tag{2.16}$$

and

$$\begin{aligned}h_r &= A\frac{\omega\epsilon_0 n_1^2}{2h}[(1-s_1)J_{l-1}(hr) + (1+s_1)J_{l+1}(hr)], \\ h_\varphi &= iA\frac{\omega\epsilon_0 n_1^2}{2h}[(1-s_1)J_{l-1}(hr) - (1+s_1)J_{l+1}(hr)], \\ h_z &= iA\frac{\beta s}{\omega\mu_0}J_l(hr).\end{aligned} \tag{2.17}$$

For $r > a$

$$\begin{aligned} e_r &= iA\frac{\beta}{2q}\frac{J_l(ha)}{K_l(qa)}[(1-s)K_{l-1}(qr)+(1+s)K_{l+1}(qr)], \\ e_\varphi &= -A\frac{\beta}{2q}\frac{J_l(ha)}{K_l(qa)}[(1-s)K_{l-1}(qr)-(1+s)K_{l+1}(qr)], \\ e_z &= A\frac{J_l(ha)}{K_l(qa)}K_l(qr), \end{aligned} \tag{2.18}$$

and

$$\begin{aligned} h_r &= A\frac{\omega\epsilon_0 n_2^2}{2q}\frac{J_l(ha)}{K_l(qa)}[(1-s_2)K_{l-1}(qr)-(1+s_2)K_{l+1}(qr)], \\ h_\varphi &= iA\frac{\omega\epsilon_0 n_2^2}{2q}\frac{J_l(ha)}{K_l(qa)}[(1-s_2)K_{l-1}(qr)+(1+s_2)K_{l+1}(qr)], \\ h_z &= iA\frac{\beta s}{\omega\mu_0}\frac{J_l(ha)}{K_l(qa)}K_l(qr). \end{aligned} \tag{2.19}$$

The parameter A can be determined from the power in the guided mode. Examples of such modes are illustrated in Fig. 2.1, which shows the intensity profiles of quasicircularly polarized HE_{11} and HE_{21} modes for an ONF radius of $a = 350$ nm and a wavelength of $\lambda = 780$ nm. It is clear that, with these parameters, the evanescent field in the HE_{21} mode is much more intense than in the fundamental mode.

Quasilinearly polarized hybrid modes

Quasilinearly polarized hybrid modes can be described as the combination of a clockwise and a counter-clockwise quasicircularly polarized hybrid mode. As such, the full mode functions of such fields are given by [93, 95]

$$\begin{aligned} \boldsymbol{\mathcal{E}}_{\text{lin}}^{(fl\varphi_{\text{pol}})} &= \frac{1}{\sqrt{2}}(\boldsymbol{\mathcal{E}}_{\text{circ}}^{(fl+)}e^{-i\varphi_{\text{pol}}}+\boldsymbol{\mathcal{E}}_{\text{circ}}^{(fl-)}e^{i\varphi_{\text{pol}}}), \\ \boldsymbol{\mathcal{H}}_{\text{lin}}^{(fl\varphi_{\text{pol}})} &= \frac{1}{\sqrt{2}}(\boldsymbol{\mathcal{H}}_{\text{circ}}^{(fl+)}e^{-i\varphi_{\text{pol}}}+\boldsymbol{\mathcal{H}}_{\text{circ}}^{(fl-)}e^{i\varphi_{\text{pol}}}), \end{aligned} \tag{2.20}$$

where the angle, φ_{pol}, is the phase angle that determines the orientation of the symmetry axis of the mode profile in the plane transverse to the fiber. We can write

$$\begin{aligned} \boldsymbol{\mathcal{E}}_{\text{lin}}^{(fl\varphi_{\text{pol}})} &= \mathbf{e}^{(fl\varphi_{\text{pol}})}e^{if\beta z}, \\ \boldsymbol{\mathcal{H}}_{\text{lin}}^{(fl\varphi_{\text{pol}})} &= \mathbf{h}^{(fl\varphi_{\text{pol}})}e^{if\beta z}, \end{aligned} \tag{2.21}$$

where $\mathbf{e}^{(fl\varphi_{\text{pol}})}$ and $\mathbf{h}^{(fl\varphi_{\text{pol}})}$ are the reduced mode profile functions of quasilinearly polarized hybrid modes, expressed as

$$\begin{aligned} \mathbf{e}^{(fl\varphi_{\text{pol}})} &= \frac{1}{\sqrt{2}}(\mathbf{e}^{(fl+)}e^{i(l\varphi-\varphi_{\text{pol}})}+\mathbf{e}^{(fl-)}e^{-i(l\varphi-\varphi_{\text{pol}})}), \\ \mathbf{h}^{(fl\varphi_{\text{pol}})} &= \frac{1}{\sqrt{2}}(\mathbf{h}^{(fl+)}e^{i(l\varphi-\varphi_{\text{pol}})}+\mathbf{h}^{(fl-)}e^{-i(l\varphi-\varphi_{\text{pol}})}). \end{aligned} \tag{2.22}$$

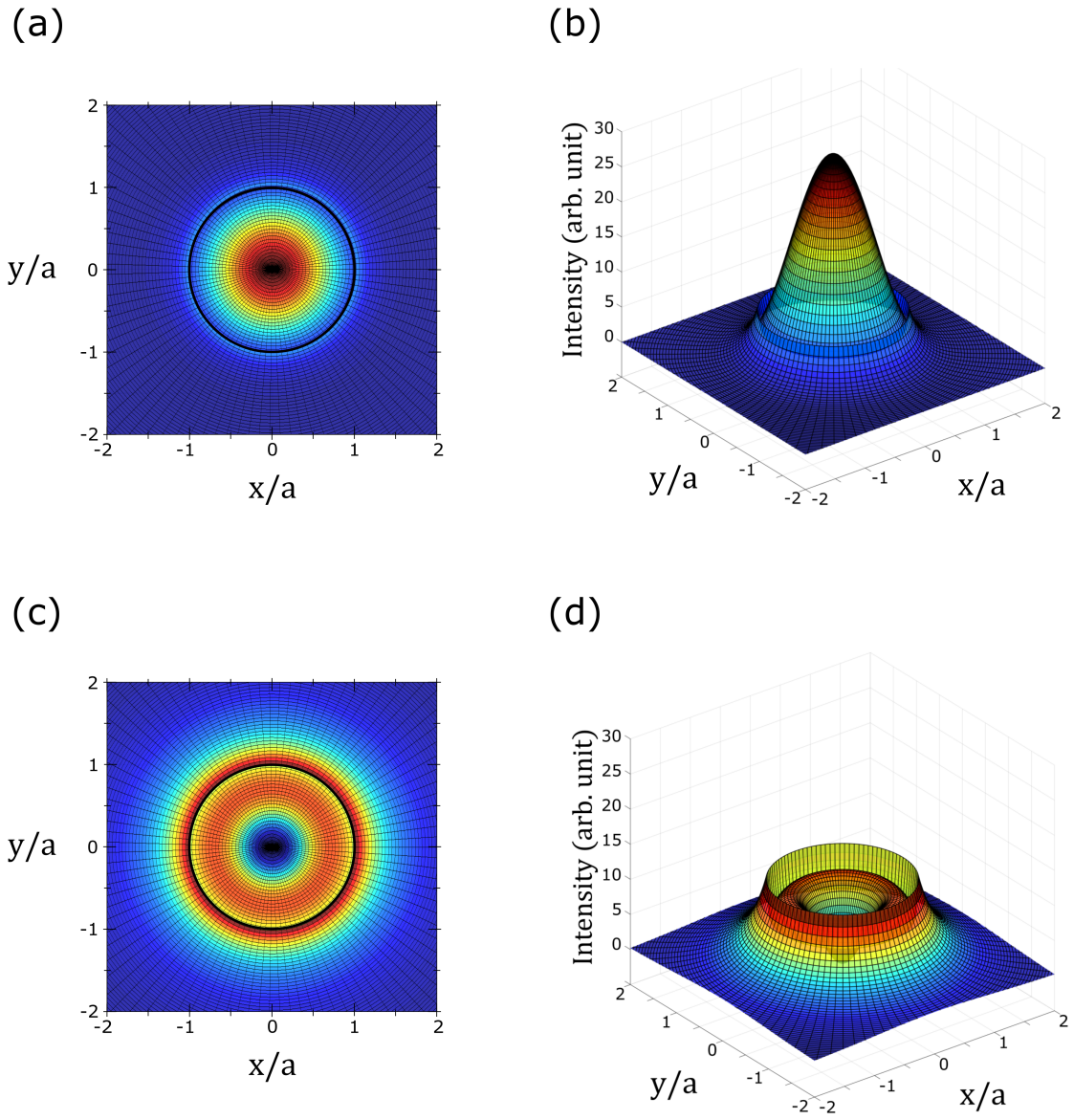

Figure 2.1: Intensity profiles of the first two HE modes with quasicircular polarization. (a) Top-down view of the quasicircularly polarized HE_{11} mode's intensity profile. (b) Same mode as in (a) viewed in 3-D. (c) Top-down view of the quasicircularly polarized HE_{21} mode's intensity profile. (d) Same mode as in (c) viewed in 3-D. In (a) and (c) the black circle at the center of the figure indicates the fiber surface. The ONF radius is $a = 350$ nm and the wavelength is $\lambda = 780$ nm.

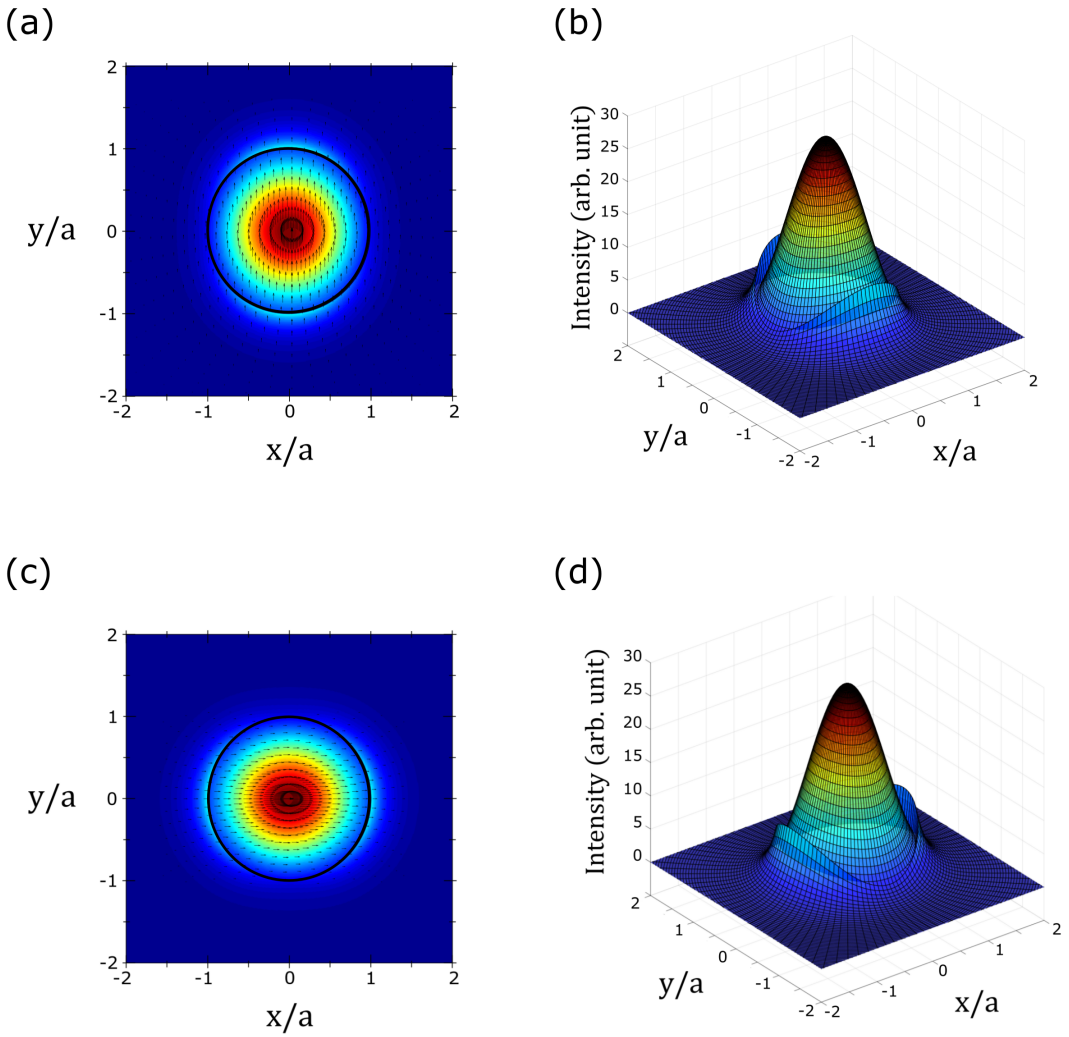

Figure 2.2: Intensity profiles of quasilinearly polarized HE_{11} modes and respective parities. (a) Top-down view of the mode's intensity profile with even parity. The black arrows represent local polarization vectors. (b) Same mode as in (a) viewed in 3-D. (c) Top-down view of the mode's intensity profile with odd parity. The arrows once again indicate the local polarization of the field. (d) Same mode as in (c) viewed in 3-D. In (a) and (c) the black circle at the center of the figure indicates the fiber surface. The ONF radius is $a = 350$ nm and the wavelength is $\lambda = 780$ nm.

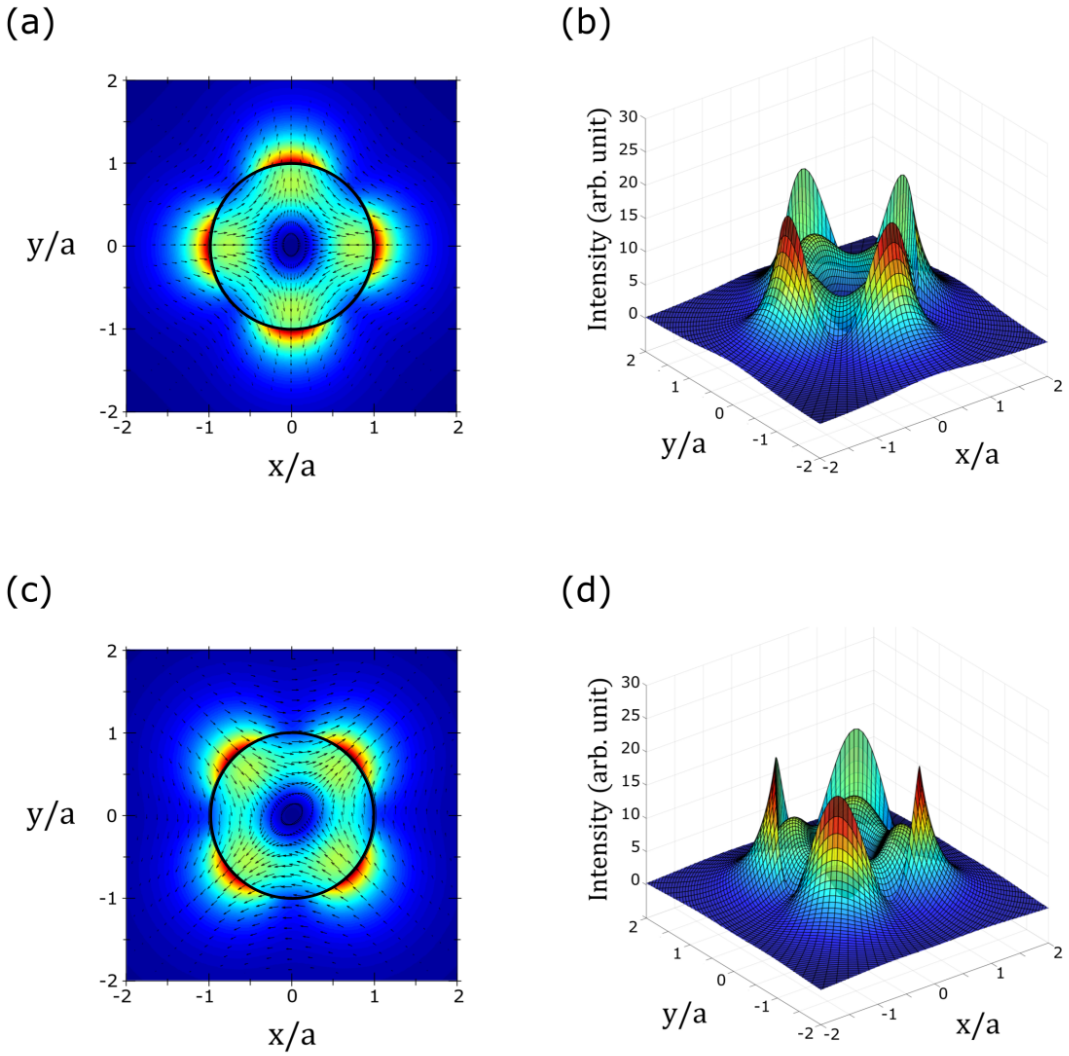

Figure 2.3: Intensity profiles of quasilinearly polarized HE_{21} modes and respective parities. (a) Top-down view of the mode's intensity profile with even parity. The black arrows represent local polarization vectors. (b) Same mode as in (a) viewed in 3-D. (c) Top-down view of the mode's intensity profile with odd parity. The arrows once again indicate the local polarization of the field. (d) Same mode as in (c) viewed in 3-D. In (a) and (c) the black circle at the center of the figure indicates the fiber surface. The ONF radius is $a = 350$ nm and the wavelength is $\lambda = 780$ nm.

Quasilinearly polarized hybrid modes are often labeled with a "parity" suffix [93], namely *even* or *odd*. The parity is determined by the value of φ and corresponds to the orientation of the mode in the transverse plane. Figure 2.2 shows the intensity of the field in the transverse plane of the ONF for both parities of the HE_{11} mode. Figure 2.3 is similar but for both parities of the HE_{21} mode.

2.2.2 TE modes

Transverse electric (TE) modes have nonzero components in cylindrical coordinates only for h_r, h_z, and e_φ (see Appendix A Section A.2 for a detailed mathematical development). This yields the full mode functions

$$\begin{aligned} \boldsymbol{\mathcal{E}}^{(f)} &= \mathbf{e}^{(f)} e^{if\beta z}, \\ \boldsymbol{\mathcal{H}}^{(f)} &= \mathbf{h}^{(f)} e^{if\beta z}, \end{aligned} \tag{2.23}$$

with the reduced mode profile functions

$$\begin{aligned} \mathbf{e}^{(f)} &= \hat{\boldsymbol{\varphi}} e_\varphi, \\ \mathbf{h}^{(f)} &= f\hat{\mathbf{r}} h_r + \hat{\mathbf{z}} h_z. \end{aligned} \tag{2.24}$$

The associated mode function components are given explicitly below. For the components of the electric field at $r < a$, we have

$$\begin{aligned} e_r &= 0, \\ e_\varphi &= i\frac{\omega\mu_0}{h} A J_1(hr), \\ e_z &= 0. \end{aligned} \tag{2.25}$$

For the magnetic field components we have,

$$\begin{aligned} h_r &= -i\frac{\beta}{h} A J_1(hr), \\ h_\varphi &= 0, \\ h_z &= A J_0(hr). \end{aligned} \tag{2.26}$$

Beyond the boundaries of the ONF, i.e., $r > a$, the electric field components are

$$\begin{aligned} e_r &= 0, \\ e_\varphi &= -i\frac{\omega\mu_0}{q}\frac{J_0(ha)}{K_0(qa)} A K_1(qr), \\ e_z &= 0, \end{aligned} \tag{2.27}$$

and the magnetic field components are given by

$$\begin{aligned} h_r &= i\frac{\beta}{q}\frac{J_0(ha)}{K_0(qa)} A K_1(qr), \\ h_\varphi &= 0, \\ h_z &= \frac{J_0(ha)}{K_0(qa)} A K_0(qr). \end{aligned} \tag{2.28}$$

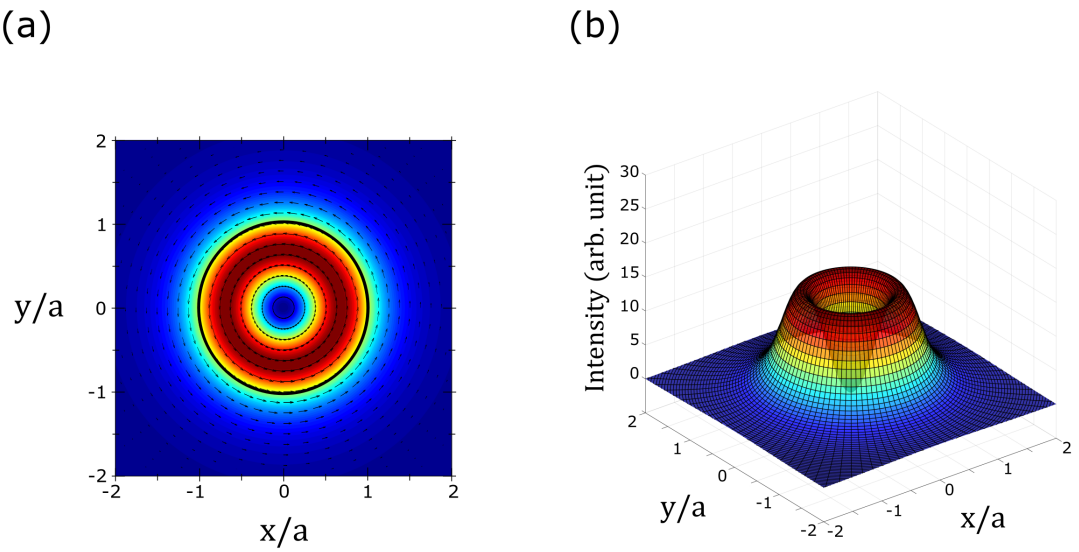

Figure 2.4: Intensity profile of a TE_{01} mode. (a) Top-down view of the mode's intensity profile. The black arrows represent local polarization vectors. (b) Same as in (a) viewed in 3-D. In (a) the black circle at the center of the figure indicates the fiber surface. The ONF radius is chosen to be $a = 350$ nm and the wavelength is $\lambda = 780$ nm.

The intensity profile of a TE_{01} mode, which belongs to the LP_{11} family in a weakly-guiding waveguide, is given in Fig. 2.4. For the used parameters, it can be noted that most of the field intensity is found in the evanescent field, outside the boundaries of the ONF. This contrasts with the intensity profiles for the HE_{11} mode (c.f. Fig. 2.2).

2.2.3 TM modes

In contrast to the TE case, transverse magnetic (TM) modes possess nonzero components only for e_r, e_z, and h_φ. The full mode functions are given by

$$\begin{aligned} \boldsymbol{\mathcal{E}}^{(f)} &= \mathbf{e}^{(f)} e^{if\beta z}, \\ \boldsymbol{\mathcal{H}}^{(f)} &= \mathbf{h}^{(f)} e^{if\beta z}, \end{aligned} \tag{2.29}$$

with the reduced mode profile functions given by

$$\begin{aligned} \mathbf{e}^{(f)} &= \hat{\mathbf{r}} e_r + f\hat{\mathbf{z}} e_z, \\ \mathbf{h}^{(f)} &= f\hat{\boldsymbol{\varphi}} h_\varphi. \end{aligned} \tag{2.30}$$

explicit expressions for each electric field component for $r < a$ are given by

$$\begin{aligned} e_r &= -i\frac{\beta}{h} A J_1(hr), \\ e_\varphi &= 0, \\ e_z &= A J_0(hr), \end{aligned} \tag{2.31}$$

and for each magnetic field component we have

$$\begin{aligned} h_r &= 0, \\ h_\varphi &= -i\frac{\omega\epsilon_0 n_1^2}{h} A J_1(hr), \\ h_z &= 0. \end{aligned} \tag{2.32}$$

When $r > a$, the electric field components are

$$\begin{aligned} e_r &= i\frac{\beta}{q}\frac{J_0(ha)}{K_0(qa)} A K_1(qr), \\ e_\varphi &= 0, \\ e_z &= \frac{J_0(ha)}{K_0(qa)} A K_0(qr), \end{aligned} \tag{2.33}$$

and the magnetic field components are

$$\begin{aligned} h_r &= 0, \\ h_\varphi &= i\frac{\omega\epsilon_0 n_2^2}{q}\frac{J_0(ha)}{K_0(qa)} A K_1(qr), \\ h_z &= 0. \end{aligned} \tag{2.34}$$

The intensity profile for the TM_{01} mode is shown in Fig. 2.5. This mode also belongs to the LP_{11} family in a weakly-guiding waveguide. In contrast with the TE_{01} mode shown previously, the field intensity is distributed between the outer and the inner part of the ONF. The evanescent field component is also larger than for an HE_{11} mode.

2.3 Practical Considerations for the Fabrication of a HOM Optical Nanofiber

As mentioned in Chapter 1, several methods to fabricate ONFs exist [25]. Fabrication of high-transmission HOM-ONFs is, in comparison, more challenging than the fabrication of fundamental mode optical nanofibers. This is a direct consequence of the difference in the adiabatic condition requirements for both types of fibers. For fundamental mode ONFs, an exponential taper profile is usually sufficient to achieve high transmission [31]. For a HOM-ONF, particular attention needs to be paid to the taper profile to ensure the fabrication parameters satisfy the adiabatic condition.

2.3.1 Adiabatic tapering

Reducing the size of an optical fiber and changing its overall shape inevitably induces modifications to its guiding properties. In order to prevent coupling from a given guided mode to any undesired mode, such as core or cladding modes, the optical fiber has to be adiabatically tapered down to the target diameter. The adiabatic condition sets a limit on the local taper angle, Θ_z, such that [117]

$$\Theta_z = \frac{a(z)}{z_b} = \frac{a(z)(\beta_1 - \beta_2)}{2\pi}, \tag{2.35}$$

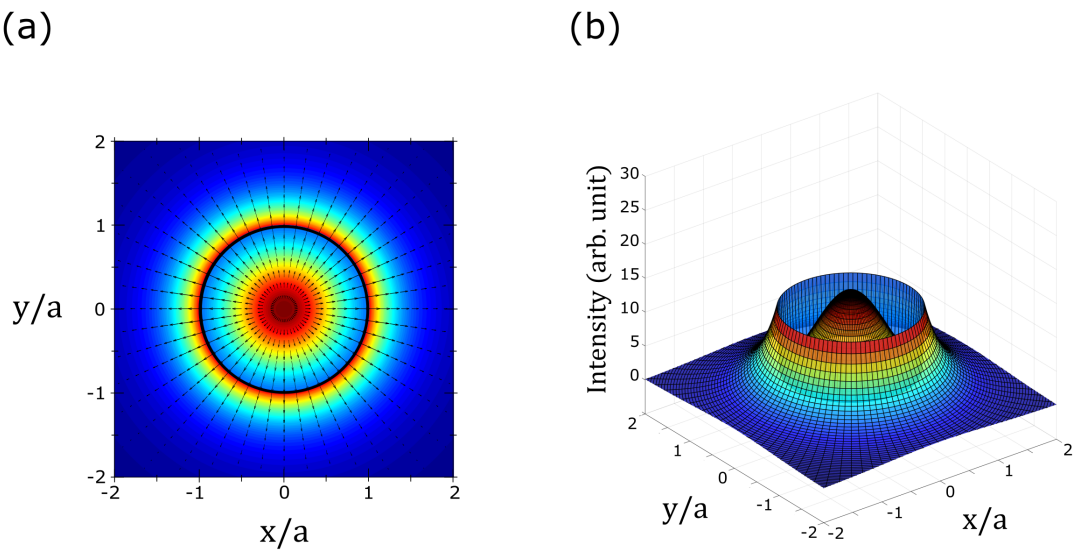

Figure 2.5: Intensity profile of a TM_{01} mode. (a) Top-down view of the mode's intensity profile. The black arrows represent local polarization vectors. (b) Same as in (a) viewed in 3-D. In (a) the black circle at the center of the figure indicates the fiber surface. The ONF radius is chosen to be $a = 350$ nm and the wavelength is $\lambda = 780$ nm.

where $a(z)$ is the ONF radius at a position, z, along the fiber axis and $z_b = (\beta_1 - \beta_2)/2\pi$ is defined as the beat length between two modes with propagation constants β_1 and β_2. Note that both β values are also functions of the local taper radius. If the local taper angle is larger than Θ_z, the guided mode starts beating with other modes and its transmission decreases. Previously, our group calculated the conditions required to adiabatically taper both fundamental mode and HOM-ONFs [28, 29]. From this work, we see that the limit on the tapering angle becomes smaller if modes in the LP_{11} family are to be supported in the fiber; this is a direct result of the propagation constants for neighboring modes being relatively close to each other. In particular, the authors of [28, 29] showed that the usual exponential taper profile used when fabricating fundamental-mode ONFs is not well-suited for HOM-ONFs.

The required shape of a taper can be determined by evaluating the reverse problem defined in [117]. For an exponential taper, for example, the fiber should be uniformly heated and stretched. In our case, for higher order mode propagation, we decided to adopt a tri-linear profile as it yields high transmission for the LP_{11} family. When making the fiber, we start with a small tapering angle (e.g. 0.064 mrad), which is increased twice (e.g. to 0.1 mrad and 0.2 mrad) before finishing the pulling process exponentially. This method, although not fully optimized (see [26] for optimization of the taper profile), keeps the taper length relatively short, typically ~ 5 cm, and respects the adiabatic criterion. It was also shown [29, 30] that starting with as small a cladding-to-core ratio as possible for the pretapered fiber improves the quality of the fabricated HOM-ONFs. Careful choice of the initial optical fiber is therefore crucial.

2.3.2 Choice of Initial Optical Fiber

For the HOM experiments reported in this thesis, we used a FiberCore SM1250(9/80) optical fiber, with a numerical aperture (NA) between 0.11 and 0.13 and a core diameter of ~ 5 μm. With a cladding diameter of 80 μm, the core-to-cladding ratio is smaller and better-suited for the fabrication of HOM-ONFs. Note that optical fibers with a 50 μm cladding have been used [30] and may be even more suitable. However, working with this fiber size would cause some difficulties in other aspects, such as splicing to standard fiber pigtails. The SM1250(9/80) fiber is single mode at a 1150 nm wavelength but becomes multimode below this value. At our working wavelength of 780 nm, the fiber allows the first four LP families, namely LP_{01}, LP_{11}, LP_{21}, and LP_{02}, to be guided. The fiber must be cut into sections of 50 cm in length prior to tapering, as coupling light through the whole fiber spool yields no light at the output. This is due to the fact that the fiber is not designed for multimode operation at 780 nm and any bend in the fiber results in the guided light leaking out. One end of this section of fiber is spliced with a SM1250(9/80) few-mode fiber (FMF), using a fusion splicer (Fujikura, Arc Fusion Splicer FSM60S) and connected using a bare fiber terminator (Thorlabs, BT1 + B30126A9 connector) to a coupling lens (Thorlabs, C220TMD-B) with a focal length of 11 mm and an NA of 0.25. The middle part of the fiber is clamped onto the fiber-pulling rig and prepared for tapering.

2.3.3 Importance of cleanliness

The fiber-pulling rig, which will be described hereafter, is operated by many members of the research unit for various projects. If an ONF is to be installed in an UHV chamber, cleanliness is of utmost importance. Contamination of components supporting the ONF and installed in the vacuum chamber will degas overtime and prevent the system from reaching the 10^{-9} mbar of pressure required to carry out cold atom experiments. In particular, contaminants, such as grease or dust, on the surface of the ONF are to be avoided at all costs as they not only prevent good transmission of the guided light, but eventually result in the nanofiber melting and breaking once a few mW of power is launched into it under vacuum. Any dust particle on the fiber creates a local "hot spot" when light propagates through it; light in the evanescent field is then scattered at this hot spot, rather than guided through the fiber. With no possibility of heat dissipation in the quasi free-hanging nanofiber, it heats up, melts, and subsequently breaks.

A first step towards ensuring the ONF remains spotless, is to create a clean fabrication environment. The fiber-pulling rig is installed in a clean-box in which a top-bottom laminar air flow is created by a vent continuously kept on, except for when an ONF is being fabricated. The air entering the clean-box is first passed through high-efficiency particulate (HEPA) filters and the positive pressure difference it creates between the inside and the outside of the box ensures that contaminants cannot diffuse inwards. In addition, anyone operating the rig is instructed to wear a lab coat and nitrile gloves, whether working towards installing an ONF in vacuum or not. Finally, at the start of every day, the whole rig system, its surroundings, and the inside of the clean box are wiped with Isopropyl alcohol (IPA).

The fiber to be tapered is initially stripped of its acrylic coating over a $\sim$10 cm region,

long enough to accommodate the maximum hot-zone[1] width. The stripped region is then wiped once dry, once with IPA, once with acetone, and once more with IPA. The fiber is then clamped onto the pulling rig using V-groove fiber clamps and its cleanliness analyzed by imaging the stripped region using a camera equipped with a microscope objective. If the cleanliness is deemed unsatisfactory, the fiber is discarded and a new one is prepared for pulling.

2.3.4 Oxy-Hydrogen fiber-pulling rig

The fiber-pulling rig used to fabricate our HOM-ONF was designed by several members of the group over the years and has been described in detail elsewhere [21, 25]. Here, we only give a brief description of its method of operation. A picture of the fiber-pulling rig is presented in Fig 2.6. The heat source is a clean oxy-hydrogen torch that heats up the fiber to a temperature between 1200°C and 1500°C. At this temperature, the fiber enters a plastic regime which allows it to be extended without breaking. The torch is mounted on a 2D-translation stage with one axis perpendicular to the fiber axis and the other parallel to it, allowing the flame to move in towards the fiber and brush it once positioned under it. A mass-flow controller (MFC), not shown in the picture, precisely controls the gas flow rate of the oxygen-hydrogen mix. We use a volumetric hydrogen to oxygen ratio of 2:1 to ensure complete combustion of the gas, the byproduct being water. The fiber pigtail is clamped onto motorized translation stages by means of a series of clamps. The motion of every translation stage involved in the fabrication process is controlled via an XPS-Q4 controller interfaced through LabVIEW. For the HOM-ONF, pre-calculated stage velocities, accelerations, and flame positions are loaded into the program and then communicated to the relevant translation stage. Compared to what was discussed in [21, 25], we have an improved version of the fiber-rig, specifically built for the cold atom group. This allows for the fabrication of high transmission and defect-free ONFs.

2.4 Fabrication of a High Transmission HOM-ONF

In the work reported by Hoffman *et al.* [32], transmission of the whole LP_{11} family was monitored to determine the quality of a HOM-ONF during fabrication. Here, the method of fabrication slightly differs, in that the transmission of a single mode, i.e., HE_{21}, is monitored at the output of the fiber. We believe this gives more information about the quality of the taper profile. For example, a loss of transmission in the HE_{21} mode gives a good estimation of the waist diameter of the ONF which can serve as a valuable tool to iteratively calibrate the pulling parameters and produce HOM-ONFs with as small a diameter as possible while still allowing propagation of every mode in the LP_{11} family. In addition, we use a flame brushing method in which the pulling stages move away from each other at a constant speed rather than the oscillating stage method reported in [32].

[1] We define the hot-zone as the region of the fiber brushed by the flame during the pulling process.

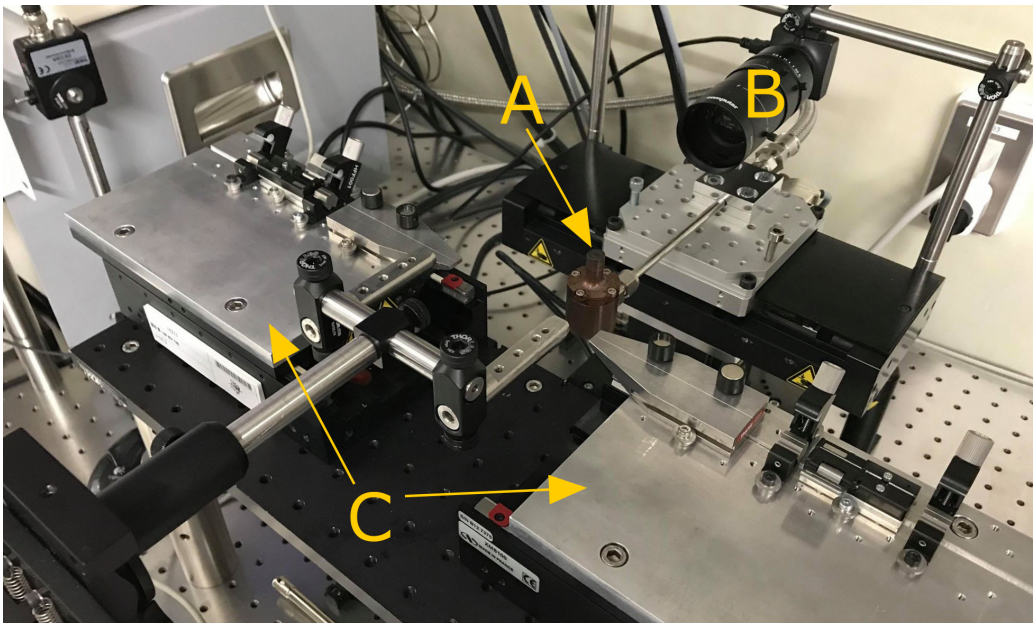

Figure 2.6: Picture of the fiber-pulling rig. (A) flame nozzle, (B) front camera, (C) primary pulling stages. Various clamping methods, such as magnets and V-grooves, are used to hold the fiber in place during the pulling process.

2.4.1 Tapering the fiber

A schematic of the ONF fabrication setup is presented in Fig. 2.7. A 780 nm beam originating from a fibered laser is collimated and reflected off a spatial-light modulator (SLM) (Meadowlark, 512 × 512 pixels Analog SLM) to generate an LG_{01} beam in free-space. This beam is launched into the free end of the FMF which, as we mentioned previously, was spliced to the fiber to be pulled. The LG_{01} beam excites the whole LP_{11} family of modes and a two-lobed profile is observed at the output if no further modification is made to the system. To observe the desired HE_{21} mode at the output of the fiber clamped on the pulling-rig, the FMF is looped through three polarization paddles (PPs) which, by way of a rotation-induced twist, allow us to change its birefringence properties, thereby adjusting the mode excitation. On the other side of the pulling-rig, the output pigtail is connected to a coupling lens (Thorlabs, C240TMD-B) allowing free-space propagation of the beam. This beam passes through a 50/50 beam-splitter (BS); the transmitted beam then goes through a polarizer and onto a CMOS camera (Thorlabs, DCC1545M), whereas the reflected beam strikes an avalanche photodetector (APD) (Thorlabs, InGaS APD110C). Rotation of the polarizer while monitoring the beam profile allows us to estimate which HOM has been excited. As mentioned previously, we try to excite one of the HE_{21} modes as their cutoff indicates that the fabricated ONF has a diameter which is too small to support the whole LP_{11} family of modes. Transmission in the selected mode is also monitored during the pulling process using the same APD. A typical transmission profile is shown in Fig. 2.8. Another CMOS camera (Thorlabs, DCC3240N) allows us to image the flame-brushing process and detect any impurity on the surface of the fiber. In case of contamination of the fiber or observation of defects on its surface, the pulling process is stopped and the optical fiber is replaced.

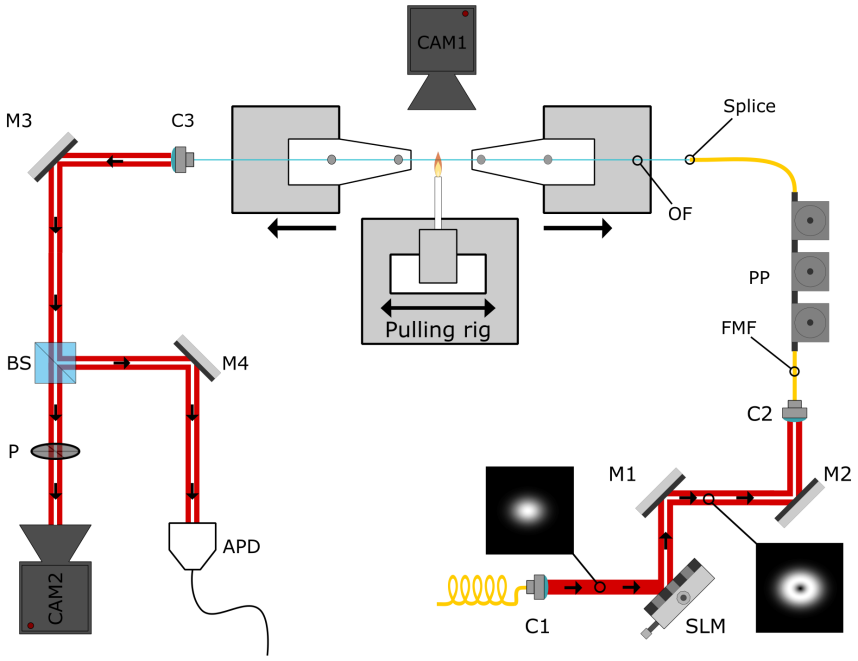

Figure 2.7: Layout of the HOM-ONF fabrication setup. Excitation of the whole LP_{11} family is realized by injection of an LG_{01} beam at 780 nm into a patch cord FMF to which the fiber to be tapered is spliced. The specific mode excited is determined via rotation of a linear polarizer placed in front of CAM2 and transmission is monitored on an APD. CAM1 images the flame-brushing to ensure no defect is created. C1-C3: Coupling lenses, SLM: Spatial-light modulator, M1-M4: Mirrors, FMF: Few-mode fiber, PP: Polarization paddles, OF: optical fiber, CAM1-CAM2: CMOS cameras, BS: Beam-splitter, P: Linear polarizer, APD: Avalanche photodetector.

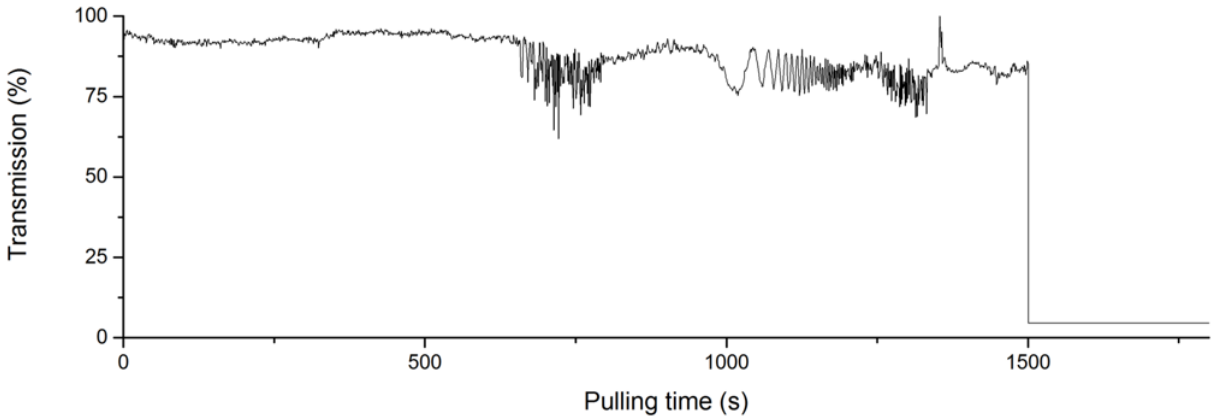

Figure 2.8: Transmission of a HE_{21} mode monitored during the fabrication of a HOM-ONF. The fabrication process takes ∼25 min, after which the fiber is disconnected from the APD, resulting in the abrupt transmission drop observed at the end of the plot.

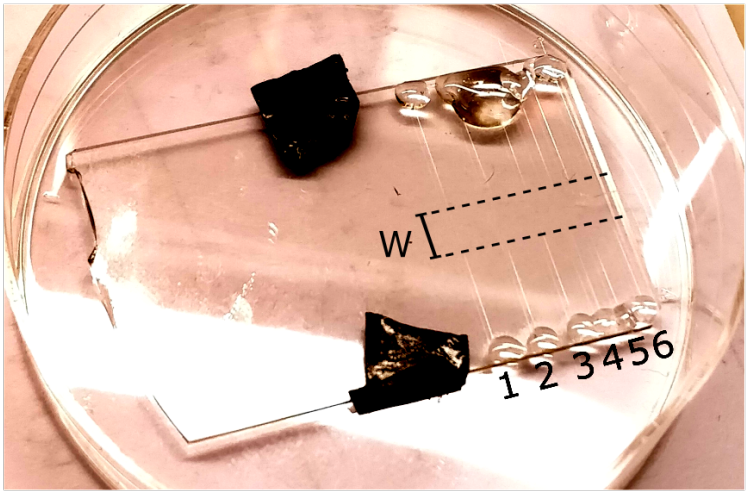

Figure 2.9: Two batches of three HOM-ONFs fabricated using tri-linear tapering. The fibers have been prepared for SEM imaging of the waist diameter to calibrate the pulling process. The region labeled "W" indicates the approximate position of the waist for each ONF. Fibers 1-3 were fabricated with pulling parameters calculated to yield a final waist diameter of 700 nm. Fibers 4-6 were fabricated with an aimed final waist diameter of 750 nm.

Pulling parameters, such as the pulling speed and variation of the hot-zone width during the pulling, are first calculated from the *reverse problem* detailed in [117]. Several such programs are publicly available but, in the work presented here, we used a MATLAB script written in-house by Dr. K. Karlson. Discrepancies between computed and experimental parameters may exist, yielding waist diameters that differ from those we would expect. Calibration of the fabrication process is therefore required prior to installing a HOM-ONF into a cold atom system.

Direct imaging of the fiber waist during the pulling process would require a sub-diffraction microscopy apparatus to be incorporated into the pulling rig. This being technically challenging, we decided to fabricate test HOM-ONFs and measure their waist diameter using a scanning electron microscope (SEM). The accuracy of our pulling process is statistically determined by fabricating batches of HOM-ONFs with identical pulling parameters and comparing their final waist diameters. Each batch contains three HOM-ONFs, which is, in general, sufficient to give a good indication of the pulling process accuracy. If transmission drops while pulling a fiber, or if some scattering indicating the presence of a contaminant is observed on the camera facing the pulling rig, the fabrication is stopped and the optical fiber is discarded. After successful fabrication, a small section of the ONF containing the waist is cut and then glued onto a microscope slide, which is then coated with a 3 nm conductive layer of Pt-Pd by ion sputtering. SEM imaging becomes possible at this point. An example of test HOM-ONF batches prepared for SEM imaging is shown in Fig. 2.9.

Here, two separate batches of three HOM-ONFs each were used to calibrate the pulling

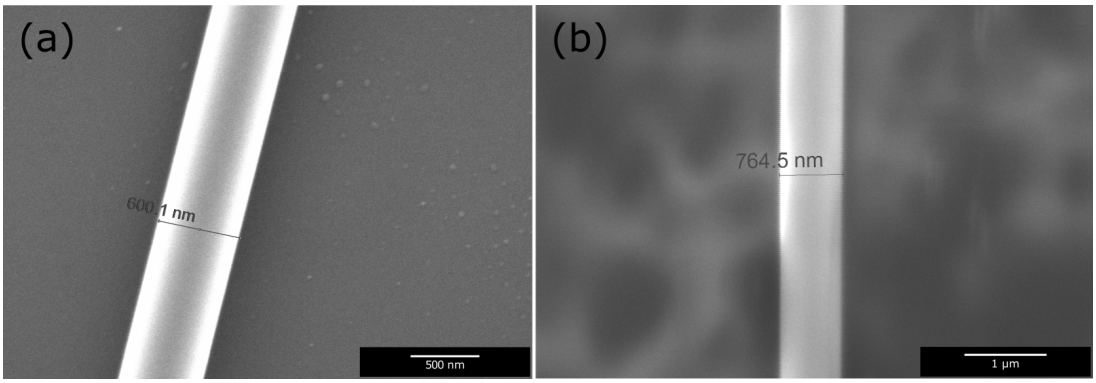

Figure 2.10: SEM images of two HOM-ONFs with different waist diameters. (a) SEM image and measured diameter of ONF 1 in Fig. 2.9. This fiber waist diameter is too small to support the HE_{21} mode. (b) SEM image and measured diameter of ONF 5 in Fig. 2.9. This fiber would be suitable for our cold atom experiment.

parameters calculated by our MATLAB program. The first batch, ONFs 1 to 3, was fabricated with pulling parameters calculated to yield a final waist diameter of 700 nm. For ONFs 1 and 2, a change in the output profile from a two-lobed pattern to a perfect Gaussian beam was observed and this coincided with a major drop in transmission of the HE_{21} mode. These observations hinted that the waist diameter of these fibers was too small to support the HE_{21} mode and that the resulting weakly transmitted Gaussian beam was a consequence of imperfect coupling at the input to the original FMF. This was confirmed by SEM imaging, from which a waist diameter of 600 nm was measured (Fig. 2.10(a)). This value is smaller than the cut-off diameter of 657 nm for a 780 nm wavelength. The second batch, ONFs 4 to 6, were fabricated with a target final diameter of 750 nm. These ONFs were found to be suitable for our cold atom experiment as the waist diameters were measured to be 698 nm, 747 nm and 764 nm. An example of measurement via SEM imaging is shown for ONF 5 in Fig. 2.10(b).

2.4.2 Mounting the fiber

Once pulling parameters have been established to yield a consistent waist diameter, they are used to pull a new HOM-ONF that can be installed inside the UHV chamber. If the fiber shows more than 85% transmission in the HE_{21} mode and if no defect is observed on its surface, it is deemed to be good. A U-shaped mount, that facilitates the fiber installation into the vacuum chamber (see Fig. 2.11(a)), is first brought below the HOM-ONF using a 3-axis translation stage and precisely adjusted so that it is oriented parallel to the fiber axis. The entire mounting process takes place in the clean-box with the HEPA filters on to ensure a contaminant-free environment. We then use a UV-cured polymer (Norland Optical Adhesive 61), chosen for its high-viscosity and its fast curing time, to glue the pigtails of the tapered fiber onto the U-mount. Note that the polymer has not been observed to degas, even under UHV conditions, thus further motivating our choice.

The U-shaped mount is specifically designed so that both ends of the tapered fiber's pigtails are in contact with it in a manner that maximizes the guiding properties of the fiber. Transmission is nevertheless monitored at all time to ensure the HOM-ONF

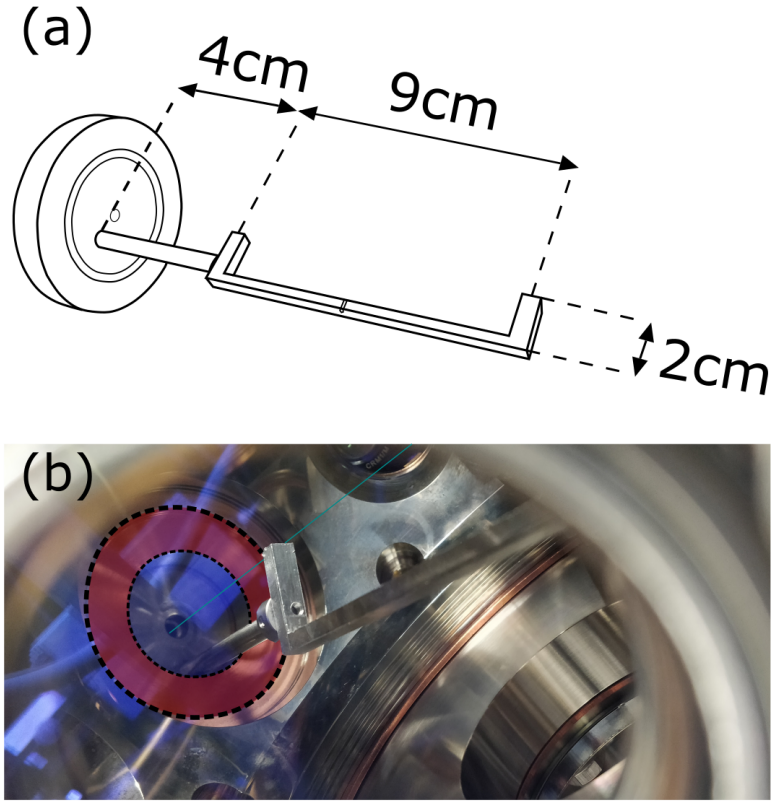

Figure 2.11: (a) Sketch of the U-mount connected to the feed-through flange. (b) Photo of the HOM-ONF installed in the vacuum chamber. The red area between the dotted lines shows part of the hollow blank flange. The fiber has been highlighted in cyan.

remains unaffected by the gluing process. Once mounted, the fiber is cut to leave ~ 15 cm of pigtail on either side. One side is passed through a large, specially grooved blank CF flange, which is itself connected to a smaller feed-through vacuum flange used to close the vacuum chamber. The U-mount is connected to a rod sticking out of the flange (see Fig. 2.11(b)). The mount has a length of 9 cm and a height of 2 cm. Its base is 0.3 cm thick and each "pillar" surface is 0.5 cm by 0.5 cm. The rod connecting the fiber mount to the flange is chosen to be 4 cm in length such that, once the fiber is installed, the middle of the waist aligns with the center of the science chamber. Prior to its installation, the HOM-ONF is shielded by a PVC sleeve, one end of which has been modified to tightly fit inside the groove of the above-mentioned blank flange.

2.5 Installation of the Fiber in the Vacuum Chamber

Cold atom experiments are conducted under UHV conditions, which typically require pressures around 10^{-8} or 10^{-9} mbar, and thus need careful preparation of the vacuum system that hosts them. Contaminants such as dust, water and oils, or trapped air between screws, for example, can lead to *outgassing*, which prevents the creation of a

vacuum suitable for experiments. A common practice to deal with these problems is to clean the vacuum system components in an ultrasonic bath (i.e., sonicate them) and then proceed to a bake-out of the vacuum chamber at temperatures higher than 100°C while pumping the pressure down. However, baking out the chamber to such temperatures can damage, and sometimes destroy, a nanofiber installed in the chamber. To avoid this issue, we prepare the vacuum chamber a few days before installing the HOM-ONF.

2.5.1 Preparation of the vacuum system

Once calibration of the pulling process has been achieved and HOM-ONFs can be produced with the desired waist diameter in a reproducible manner, the vacuum system is prepared. The first step of the preparation consists in wiping any part that will either seal the vacuum chamber, or be inside of it, with acetone using dust-free lens tissues. Each component is handled with nitrile gloves to avoid deposition of oil from contact with the skin. Components to be installed inside the vacuum chamber (e.g. U-mount, connecting rod, Teflon ferrules, etc.) are successively sonicated in hot baths of soapy water, deionized water, acetone, and finally IPA, for 15 minutes in each case. These components are then wrapped in aluminium[2] foil and stored in a clean-box where a low vacuum ($\sim 10^{-2}$ mbar) is created. The vacuum chamber is sealed and a vacuum pump (HiCube 80 Eco Turbo Pump), which combines both a diaphragm pump and a turbo pump, is switched on.

A schematic of the closed vacuum system is depicted in Fig. 2.12, where three regions (A, B, and C) have been identified. Region A consists of the main science chamber (Kimball Physics 8 Multi-CF Spherical Square) in which the U-mount with the HOM-ONF will be installed and where the rubidium atoms are laser-cooled and trapped in a MOT. The distance between the feed-through flanges, F1 and F2, is 24 cm. Region B, which connects A and C together, is equipped with rubidium dispensers (SAES Rb getters). These are replaced before the vacuum system is closed when the need arises. Finally, region C consists of a six-way cross connecting together a pressure gauge (Agilent FRG-720/730 Pirani Bayard-Alpert gauge), a titanium-sublimation pump (TSP) (Agilent TSP Filament Cartridge), an ion pump (Agilent 4UHV VacIon Plus Starcell 75) and a viewport. The sixth port is connected to a T-valve, itself connected to the vacuum pump, which can be opened or closed as desired. The ion pump is kept far enough away from the main chamber to prevent its magnetic field from affecting the cloud of cold atoms. The whole vacuum system is made out of stainless steel, with CF connectors. Copper gaskets are inserted between the knife edges of the flanges and, once compressed, seal the system.

Once the pressure in the vacuum chamber has reached 10^{-6} mbar, we proceed with the second step of the preparation process, a bake-out. Each region is wrapped with 20 mm-wide heating tapes (AS ONE ribbon heaters) and then covered in aluminium foil to make the heating as uniform as possible and prevent heat dissipation during the baking process. Along with thermocouples that monitor the temperature in each region, the heating tapes are connected to a home-made PID system that controls the temperature. The temperature is gradually increased to 130°C by increments of 10°C every hour. This allows for homogeneous heating of the whole system. Note that the vacuum pump is kept on during the entire bake-out process. This temperature is maintained overnight.

[2]All chemical elements will be written using the UK spelling.

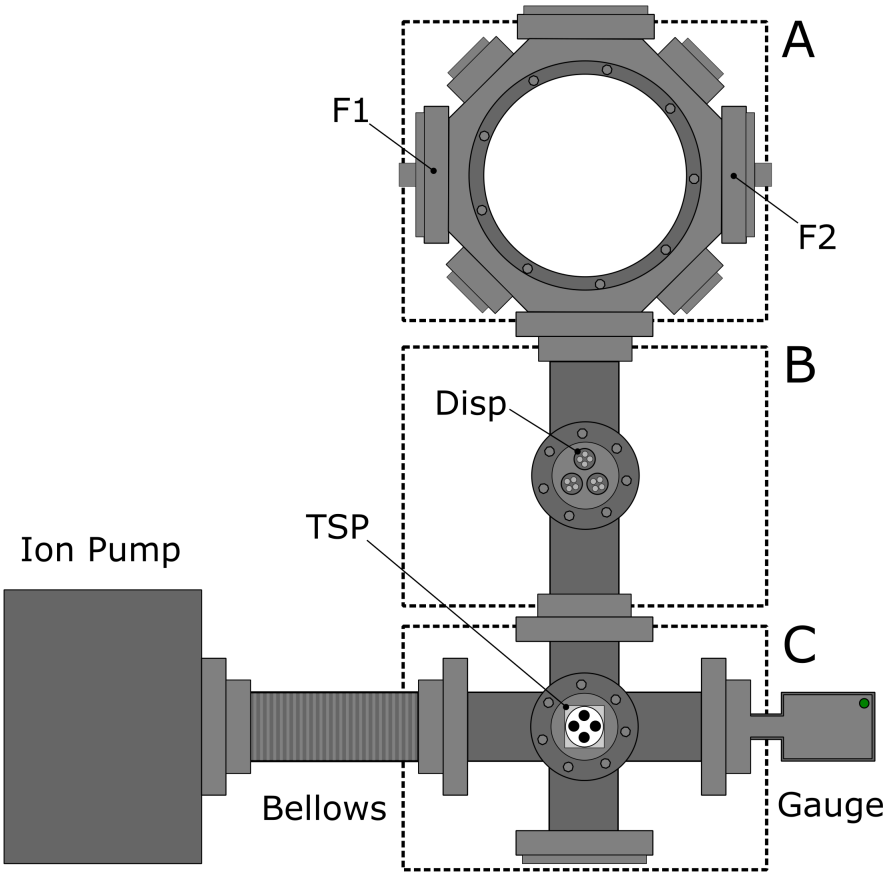

Figure 2.12: Schematic of the vacuum system used for the cold atom experiments. (A) Science chamber in which the cold atom cloud is created and trapped; (B) Connecting region with Rb dispensers; (C) Six-way cross which connects the pressure gauge, the titanium sublimation pump (TSP) and the ion pump bellows. The port at the bottom of the figure is a viewport and the last port (not shown) connects via a bellows to a turbo pump.

Figure 2.13: Characteristic pearl-necklace pattern resulting from contamination of an ONF by particles. No more than 1 μW of power was launched into the fiber to take this picture. Increasing the power beyond this point broke it.

We start the next day by slowly reducing the temperature of the system, here too by increments of 10°C every hour. After reaching room temperature, the aluminium foil and heating tapes are removed. Once a HOM-ONF has been successfully fabricated and mounted on the U-mount in the fabrication room, the vacuum pump is turned off, disconnected, and the freed port is connected to a nitrogen supply. As the T-valve is opened, the vacuum fills with nitrogen until atmospheric pressure has been reached. At this point, we remove the flanges on either side of the science chamber (F1 and F2 in Fig. 2.12). The constant supply of nitrogen maintains a positive pressure difference between the inside of the vacuum chamber and the outside. The chamber is open and ready for the installation of the HOM-ONF.

2.5.2 Transport from the fabrication room to the cold atom lab and installation

Early attempts at transporting a tapered fiber from the fabrication room to the vacuum chamber resulted in high contamination of its surface. This was made evident by the presence of scattering points, such as those depicted in Fig. 2.13, appearing along the length of the fiber once light was coupled into it. Carrying the HOM-ONF in a shielded container and opening it at the last minute before installation inside the vacuum chamber resulted in less contamination, but it remained significant nonetheless. It was, thus, decided that the strategy to adopt was to keep the fiber shielded even as it was being installed inside the vacuum chamber.

In Section 2.4, we detailed the fabrication method of a high-transmission HOM-ONF, and its subsequent mounting on the U-mount. We mentioned a PVC sleeve used to shield the assembled components during their transportation to the vacuum chamber, a picture of which is shown in Fig. 2.14. The sleeve is a 32 cm long PVC tube, chosen to be much longer than the distance of 24 cm between the two feed-through flanges of the science chamber so that it could be removed on one side after the HOM-ONF installation. One end was bored down to a smaller cylinder with an inner diameter of 6 cm and an outer

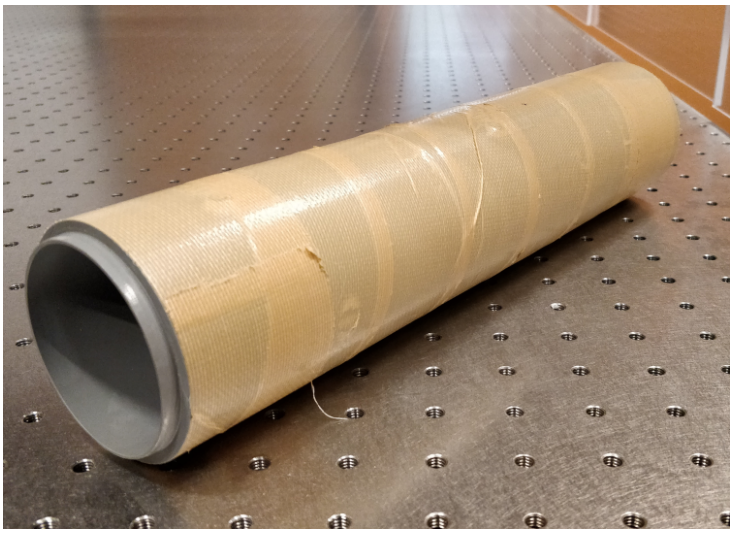

Figure 2.14: Protective sleeve used to transport the HOM-ONF to the vacuum chamber. The front end has been bored into a cylinder that tightly fits inside the circular groove carved in a blank flange. The sleeve's length is chosen such that it is longer than the distance between the two relevant ports of the vacuum chamber during installation of the HOM-ONF.

diameter of 6.9 cm, over a 2 cm length. This part is designed to tightly fit inside a blank flange in which a 2 cm deep, 7 cm wide circular groove was carved.

With the sleeve shielding it, the mounted HOM-ONF is transported to the open, nitrogen-filled, vacuum chamber. All the parts are inserted inside the science chamber, except for the feed-through and flanges that seal one side of the chamber. Once the components are screwed in place, the PVC sleeve is carefully removed from the opposite side, and another feed-through flange is used to close the system.

2.5.3 Sealing the chamber and making vacuum

The vacuum chamber is now mostly closed, with only the feed-through part of flanges F1 and F2 remaining to be put in place. First, the HOM-ONF's two pigtails are wiped with IPA using a lens tissue. The pigtails are passed through a pre-drilled Teflon ferrule, seen in Fig. 2.15(a), which is inserted in the feed-through port of the flange. A Swagelok© nut is threaded through the pigtail and screwed onto the feed-through port, Fig. 2.15(b), squeezing the Teflon ferrule in the process, thereby sealing the system. This technique is used in most ONF experiments [118]. The Teflon ferrules were fabricated by the OIST machine shop, using precision machining to drill perpendicularly and at the center of the ferrules (schematized in Fig. 2.15(c)), in order to minimize twisting of the tapered fiber's pigtails when tightening the Swagelok© nut.

Next, the nitrogen supply is gradually switched off and eventually disconnected once the vacuum chamber is sealed. The bellows of the vacuum pump is connected back onto the T-valve and the pump is switched on. Pressure in the vacuum chamber is first brought down from atmosphere to $\sim 10^{-3}$ mbar by the diaphragm pump, after which the turbo pump kicks in. The system is left to run overnight, typically bringing the pressure to

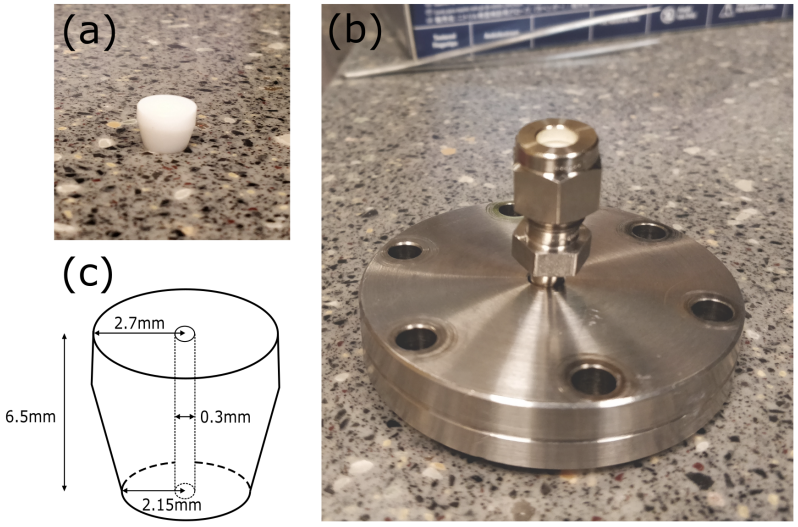

Figure 2.15: Final elements sealing the vacuum system at the HOM-ONF's pigtails. (a) Picture of a blank 1/4 inch Teflon ferrule. (b) Assembled feed-through flange, Teflon ferrule, and Swagelok© nut. (c) Schematic of the hole drilled in a Teflon ferrule which allows us to thread a fiber pigtail through it.

10^{-8} mbar. If, at this point, the pressure is still considered too high, a leak test is carried out by squirting small quantities of methanol in the CF flanges' notches, designed for this very purpose, while monitoring the pressure. Once the leak has been fixed, the pressure quickly goes down to the value mentioned above.

Taking advantage of the high pumping rate of the turbo pump, we now burn off the protective coating from the rubidium dispensers. These are placed far enough away from the center of the science chamber (see Fig. 2.12) to avoid collisions between hot atoms and the cold atoms, once the latter have been trapped in a MOT. Each dispenser consists of a slotted metallic case containing rubidium, covered in a protective chromate mixture. The metallic case is electrically connected to copper wires, sealed with ceramic feed-throughs, shown in Fig. 2.16, through which a current can be passed. The metallic case heats up by the Joule effect, along with the protective layer which evaporates. Current through the dispensers is slowly increased by increments of 0.5 A every 30 minutes, up to 4 A, after which only rubidium evaporates out of the slot in the metallic casing. The incremental method ensures that the protective coating is progressively pumped out and that the pressure inside the UHV chamber does not increase too quickly. Once burnt off, the dispensers are turned off and the pressure goes back down to values in the low 10^{-7} or high 10^{-8} mbar. If the pressure is not in this range, an additional step involving the TSP is required. A pneumatic valve isolates the six-way cross from the rest of the system, while the TSP undergoes a complete sublimation cycle via periodic injection of a high current through its coated filaments. The pneumatic valve is then reopened and, once the pressure has settled in the low 10^{-8} mbar, the T-valve is closed, and the turbo pump is turned off and disconnected. The ion pump now takes over and keeps pumping the system down to 10^{-9} mbar at which cold atom experiments can be done.

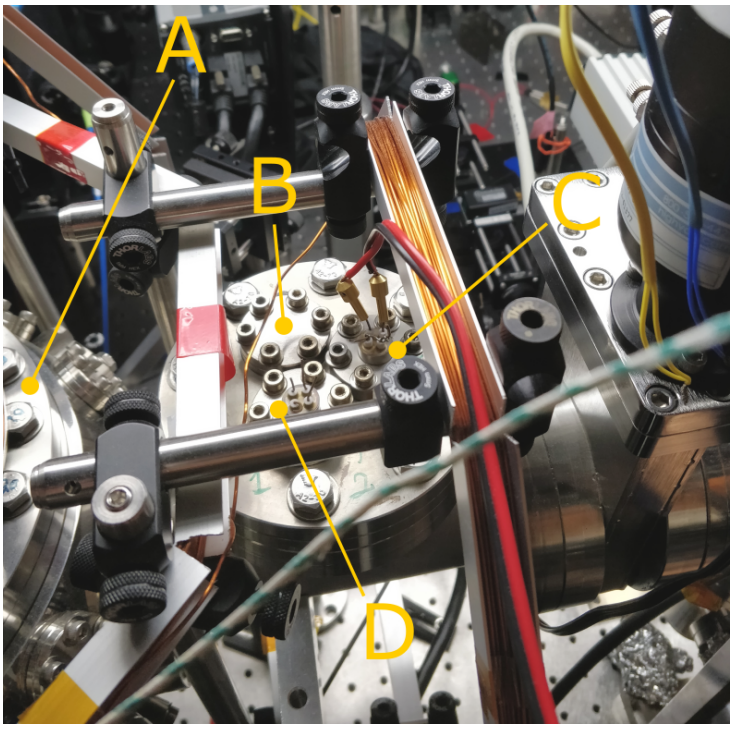

Figure 2.16: Electrical feed-through of the Rb dispensers. (A) Science chamber; (B) Blank flange; (C) Pair of electrical feed-through connected to Rb dispensers, one of which is currently in use; (D) Spare pair of dispensers.

2.5.4 Robustness test in vacuum

Upon reaching the UHV regime, no further baking is necessary. The robustness of the HOM-ONF when injected with high laser power now needs to be tested. A good power benchmark for these fibers lies in the range of 80 to 150 mW, as these values would be sufficient to generate deep trapping potentials for cold atoms around the waist, even for light guided in the fundamental mode[3]. While no fiber-mediated trapping was done in this work, we have designed the system so that it could be implemented if necessary. We found that the HOM-ONFs installed following the method described in the previous sections can reliably take up to 120 mW of power at 780 nm, over extended periods of time (at least two to four hours). This is likely due to the cleanliness of the fiber as barely any scattering can be detected on a camera image (see Fig. 2.17).

The fiber diameter is then evaluated by injecting a 1064 nm beam into it. The incidence angle to the fiber surface leads to coupling in all the modes available. As no mode other than the fundamental mode was observed at the output of this HOM-ONF, an upper limit on the waist diameter could be evaluated. As we also know that the HE_{21} mode can propagate at 780 nm, this sets a lower limit on the waist diameter. We find that the waist of our HOM-ONF lies between 664 nm and 775 nm.

[3]Higher power is required here to generate fiber-mediated trapping potentials when using the fundamental mode as our HOM-ONF is larger than in other ONF-based experiments. For example, compare our waist diameter of 700 nm with the 400 nm waist diameter of the ONF used in [6].

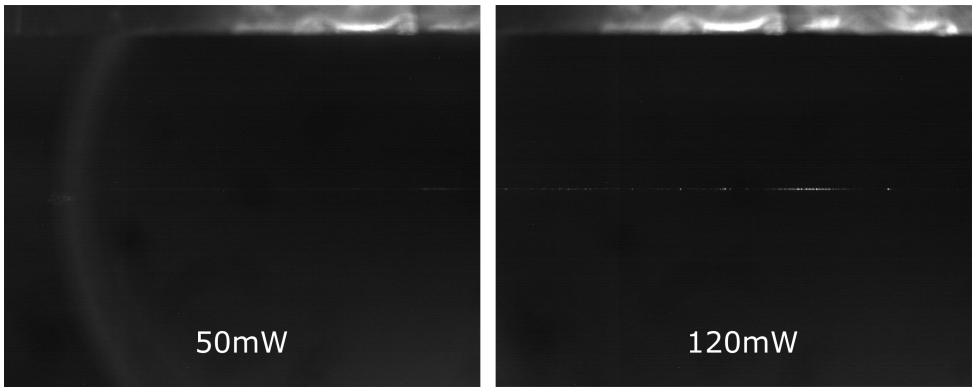

Figure 2.17: HOM-ONF installed in the chamber, injected with (left) 50 mW and (right) 120 mW of power at 780 nm. No major contamination is observed, although fiber defects become apparent at the higher power. Cleanliness is key for high transmission HOM-ONFs in vacuum.

2.5.5 Installation of two fibers at once

In an earlier version of the project, we installed two ONFs at once in the vacuum chamber (see Fig. 2.18). The first ONF was tailored to only allow the fundamental mode to propagate at 780 nm, while the second was a HOM-ONF, fabricated as described in Section 2.4. The installation procedure was similar to that described previously, the only difference being that the two ONFs were mounted on the same U-mount prior to their installation in the vacuum chamber. This presented several issues that ultimately forced us to focus solely on interfacing a HOM-ONF with a cloud of cold atoms. For example, the quality of the vacuum achieved when two ONFs were simultaneously installed was worse than with a single fiber. This was likely due to having two holes drilled in the Teflon ferrules. Contamination of one of the fibers was also more likely in this case, as the first ONF was made some time before the second one. Finally, alternatively overlapping the MOT with each ONF was a challenging task as the cooling beams had to be aligned differently for both cases. This led to different MOT profiles (i.e., difference in atom number, temperature, cloud diameter, density, etc.), preventing any significant comparisons to be made between experiments performed with either fiber. We temporarily fixed this issue by attaching the U-mount onto ultrahigh vacuum compatible 3D-stages (SmarAct SLC-1730 positioners), which allowed us to move both fibers through the cloud as opposed to the alternative. This proved very useful for working with the fundamental mode ONF, but induced drastic mode mixing for the HOM-ONF as the pigtails on either side were stretched during the motion or vibration of the stages.

2.6 Conclusion

This chapter provided a mathematical description of the origin of HOMs in strongly guiding waveguides, along with their explicit expressions in cylindrical coordinates. The fabrication of HOM-ONFs used throughout this thesis work was described in detail, putting emphasis on the degree of cleanliness required when installing such fibers in a UHV en-

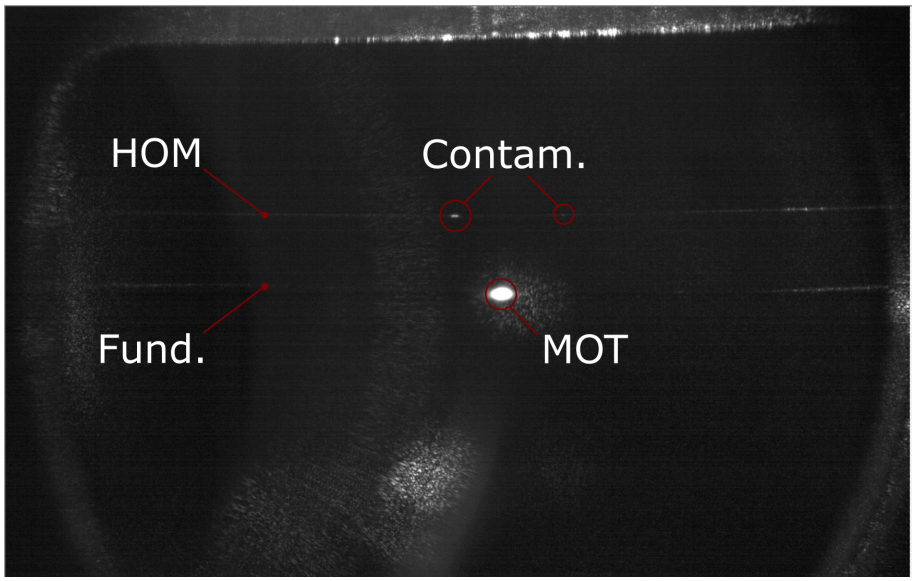

Figure 2.18: Two ONFs installed in the vacuum chamber. The top ONF is tailored to guide up to the LP_{11} family of modes at 780 nm and exhibits some contamination. The bottom ONF can only guide the fundamental mode at the same wavelength. Only a very small MOT could be overlapped with this ONF due to the required misalignment of the cooling beams.

vironment. Monitoring the transmission of one of the HE_{21} modes, excited at the output of the fiber to be tapered, during the pulling process allowed us to fabricate HOM-ONFs with a diameter close to the cut-off condition for a wavelength of 780 nm. The installation of this fiber inside the vacuum chamber was also described, along with the thorough procedure needed to ensure pressures suitable for cold atom experiments could be reached. We developed a way to completely shield the tapered fiber both before and during its installation inside the chamber to avoid contamination of its surface. This would deteriorate its transmission and prevent us from injecting enough power to generate a fiber-mediated atom trap in the future. The setup and procedures outlined here led to the fabrication of a HOM-ONF and its installation in a UHV system; this was used for the experimental work discussed in Chapter 6.

Chapter 3

Laser-Cooling and Trapping of Rubidium Atoms

Most of the work reported in this thesis revolves around interfacing the guided modes of an ONF with cold atoms trapped in a MOT. In Chapter 2, the fabrication and installation of the HOM-ONF inside the UHV chamber were described. Here, the focus is put on the second component essential for this type of experiment, namely the laser-cooling of neutral atoms. This chapter first gives some theoretical background and includes a description of the experimental setup that is used in the remainder of this work to create, control, and characterize a cloud of cold ^{87}Rb atoms trapped in a MOT.

3.1 Laser-Cooling of Neutral Atoms

The fundamental idea behind laser-cooling is that electromagnetic (EM) radiation from a laser source can affect the kinetic energy of an atom by, for example, reducing it, subsequently reducing its temperature. Considering an atomic gas with a well-defined velocity distribution, one can relate the average kinetic energy of the gas, $< K >$, to the notion of temperature, T. In 1D, this is expressed as

$$< K > = \frac{k_B T}{2}, \tag{3.1}$$

with k_B being the Boltzmann constant. This is easily expanded to 3D and the relationship between the root mean square (rms) velocity[1], v_{rms}, and temperature is established via

$$v_{rms} = \sqrt{\frac{3k_B T}{M}}, \tag{3.2}$$

where M is the mass of an atom in the sample considered. Atomic samples with ultralow temperatures are highly valuable for applications in fundamental research, and, in particular, for the study of quantum physics, as cancellation of the thermal motion in matter allows one to access its quantum properties more easily. The importance of such technological advance was highlighted by the award of the physics Nobel Prize in 1997 to

[1]The root mean square velocity of a freely expanding gas is defined as the square root of the mean square, or, more explicitly, the square root of the average of the square of the velocity.

S. Chu, C. Cohen-Tannoudji and W.D. Phillips *"for the development of methods to cool and trap atoms with laser light"*. This field of research eventually led to the experimental demonstration of Bose-Einstein condensation [119]. In what follows, the description of laser-cooling of neutral atoms considers the simple case of a two-level atom. The reader interested in more detailed theoretical considerations can see, for example, the books by Foot [60] or Metcalf and van der Straten [120].

3.1.1 The scattering force

In Chapter 1, Eq. (1.4) contains the mathematical expression for the forces acting on a single atom placed in an electric field derived from first principles. Two terms were identified, corresponding to two different forces: the dipole force and the scattering force. The dipole force is directly proportional to δ, the detuning of the laser frequency with respect to the atomic transition considered. For resonant light, or light reasonably close to resonance (i.e., a few MHz away from the transition), the contribution from this force is negligible compared to the scattering force. Since this regime is generally adopted to slow and cool atoms, we set the dipole force to zero in what follows.

The scattering force stems from an exchange of momentum between a photon and a moving atom with which it interacts. Consider the situation depicted in Fig. 3.1. A single atom is traveling with a velocity, v, towards a laser beam which bombards it with photons. During each absorption process, a photon transfers its energy to the atom by exciting it to a higher energy level. There is also a momentum effect, whereby the atom receives a kick in the direction of the incoming photon; for laser detuning below atomic resonance, this is preferentially against the direction of the atom's motion. The atom decays back to its ground state via spontaneous emission, thereby recoiling in the direction opposite to the photon emission. The average recoil after many such cycles is null, as the spontaneous emission process is isotropic. The only contribution felt by the atom is that of the initial kick received after a photon is absorbed, thus resulting in a net force on the atom opposite to its direction of motion. The atom is, therefore, slowed down over time.

Mathematically, the magnitude of the scattering force is the product of a photon's momentum, $\hbar\mathbf{k}$ where $\mathbf{k}$ is the wave vector of the photon, and a scattering rate, Γ_S, characteristic of the absorption-emission process:

$$\mathbf{F_{scatt}} = \hbar\mathbf{k}\Gamma_S. \tag{3.3}$$

The scattering rate is defined as [60]

$$\Gamma_S = \Gamma\rho_{ee}, \tag{3.4}$$

where Γ is the decay rate of the excited state and ρ_{ee} is the population in the excited state. By considering the full expression of ρ_{ee} and incorporating it in the previous expressions, we get

$$\mathbf{F_{scatt}} = \hbar\mathbf{k} \quad \frac{\Gamma}{2}\frac{\Omega^2/2}{(\delta+\omega_D)^2+\Omega^2/2+\Gamma^2/4}, \tag{3.5}$$

which gives a similar expression to Eq. (1.4), with the notable addition of the term $\omega_D = \mathbf{k}.\mathbf{v}$, or a Doppler shift in frequency that accounts for the motion of the atom. This

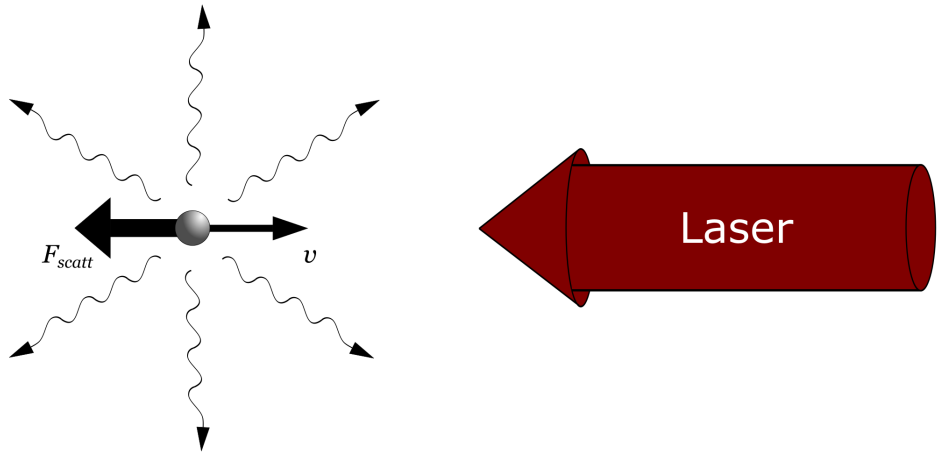

Figure 3.1: Slowing of an atom via the scattering force. The atom is moving along a unique direction with a velocity v. Transfer of momentum from the photons impinging onto the atoms generates a force that opposes the atom motion, slowing it in the process.

expression can be rewritten in a more experimentally appropriate form by considering the link between the Rabi frequency, Ω, and the saturation intensity, I_{sat}, such that $I/I_{sat} = 2\Omega^2/\Gamma^2$, which gives

$$\mathbf{F_{scatt}} = \hbar\mathbf{k}\,\frac{\Gamma}{2}\frac{I/I_{sat}}{1 + (I/I_{sat}) + (2(\delta + \omega_D)/\Gamma)^2}. \tag{3.6}$$

This expression reaches a maximum when $I \to \infty$ at which $\mathbf{F_{scatt}} = \hbar\mathbf{k}\Gamma/2$. As atoms are decelerated, the Doppler shift decreases and the slowing laser beam goes out of resonance. To keep $\delta + \omega_D$ constant over time, either the laser frequency or the atomic resonance frequency has to be adjusted. The latter case is in general preferred in atom cooling experiments and its implementation relies on the creation of an inhomogeneous magnetic field that induces a spatially-dependent Zeeman splitting of the energy levels. This consideration eventually led to the development of the MOT, which will be explained in Section 3.1.3.

3.1.2 Optical molasses

A direct expansion to the cooling scheme detailed above is to add another cooling beam, co-propogating with the atom's original direction of motion, as a single beam eventually pushes the atom backwards. From there, this counter-propagating beam configuration can be expanded to 3D (i.e., using six beams), as illustrated in Fig. 3.2, in order to ensure efficient cooling of a freely expanding atomic gas.

In such a system, an atom experiences a force in each direction resulting from the contribution of each beam. Again, the Doppler effect must be taken into account. For simplicity, let us assume once more that the atom's motion is confined to a unique dimension, with a pair of counter-propagating beams acting upon it, slightly red-detuned from

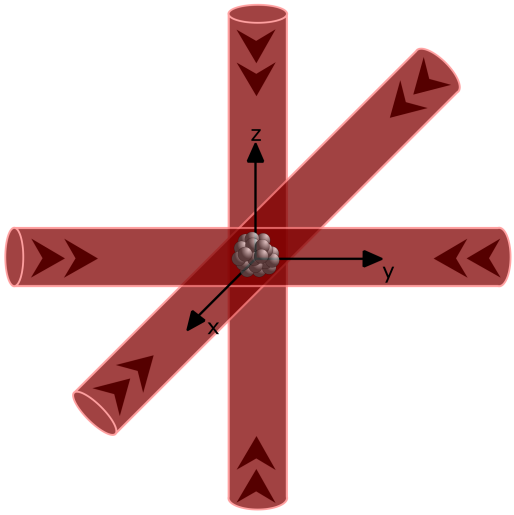

Figure 3.2: Principle of an optical molasses. Pairs of counter-propagating, red-detuned beams in the three directions of space create an "optically viscous" medium for a sample of atoms placed at the intersecting region of all the beams.

the transition frequency ($\delta < 0$). The total force felt by an atom in this case is

$$\mathbf{F}_{tot} = \hbar\mathbf{k}\frac{\Gamma}{2}\left[\frac{I/I_{sat}}{1+I/I_{sat}+(2(\delta+\omega_D)/\Gamma)^2} - \frac{I/I_{sat}}{1+I/I_{sat}+(2(\delta-\omega_D)/\Gamma)^2}\right]. \tag{3.7}$$

In the limit of small velocities, $\mathbf{k}.\mathbf{v} \ll \Gamma$, and after expanding in series we have

$$\mathbf{F}_{tot} \approx \frac{I}{I_{sat}}\,\frac{8\hbar k^2\delta\mathbf{v}}{\Gamma\left[1+(2\delta/\Gamma)^2\right]} \equiv -\alpha\mathbf{v}, \tag{3.8}$$

where we have introduced α, the damping coefficient. By using red-detuned beams, an atom evolving in this system will absorb more photons from the beam opposing its motion due to the compensation of the Doppler shift, whereas the co-propagating beam, being Doppler shifted further away from resonance, has a lower probability to be absorbed. Consequently, the atom experiences a damping force in the direction opposite to its motion and is cooled. In 3D, the beams create an optically viscous medium around the atom, thus justifying the term of *optical molasses*.

3.1.3 Magneto-optical trapping

We mentioned earlier that one way to compensate for the reducing Doppler shift when the atom is slowed down is to generate an inhomogeneous magnetic field to create a spatially-dependent Zeeman shift of the atomic energy levels. This situation is schematized in Fig. 3.3 and describes the mechanism for the cooling and trapping of atoms in a MOT. In Fig. 3.3(a), we show the required elements to generate the trap: (i) a pair of coils in an anti-Helmholtz configuration, which generates the inhomogeneous magnetic field, and (ii) three pairs of counter-propagating beams with orthogonal circular polarizations (labeled σ^+ and σ^-) that overlap at the center of the trap. Note that the same scheme

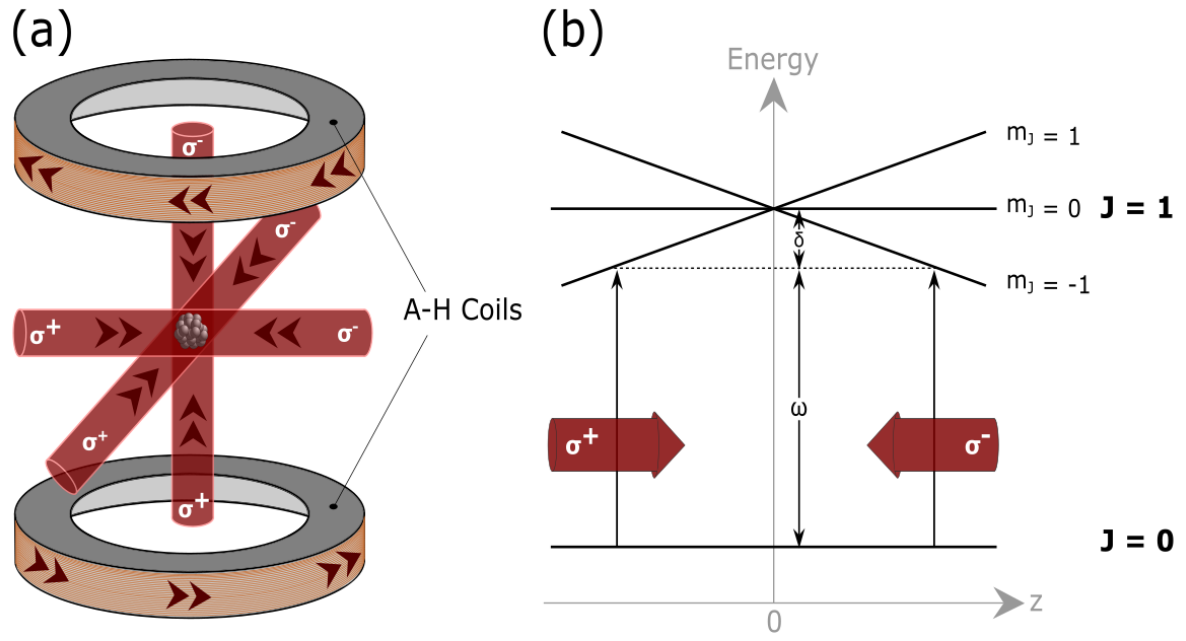

Figure 3.3: Principle of a MOT. (a) A pair of coils in an anti-Helmholtz (A-H) configuration generates a magnetic field gradient and 3 pairs of counter-propagating beams with orthogonal circular polarizations (σ^+ and σ^-) cool and trap atoms at the center of the system. (b) Mechanism of the MOT for an atom with a $J = 0$ to $J = 1$ transition. The spatially-dependent Zeeman splitting and the selection rules for dipole transitions cause atoms to absorb more photons from a beam propagating in a direction opposite to that of their motion.

can be achieved by using three retro-reflected beams instead, placing a quarter-wave plate (QWP) just before reflection to ensure that the reflected beam is also circularly polarized but with opposite handedness.

The active mechanism for trapping an atom in a MOT for a $J = 0$ to $J = 1$ transition is sketched in Fig. 3.3(b). We consider a one-dimensional model for simplicity, assuming the atom can only propagate along the z-axis. In this case, the quadrupole magnetic field generated by the anti-Helmholtz coils induces a Zeeman shift of the atom's energy levels of the form κz, where z is the position of the atom (taken to be 0 at the center of the trap) and κ is the magnetic field gradient. In the region where $z > 0$, the $m_J = 1$ level is shifted up, while the $m_J = -1$ is shifted down. For values of $z < 0$, the opposite situation occurs. Selection rules in a dipole-allowed transition impose that absorption of a σ^+-polarized photon excites the transition $|J = 0, m_J = 0\rangle \rightarrow |J' = 1, m_J = 1\rangle$ whereas a σ^--polarized photon excites $|J = 0, M_J = 0\rangle \rightarrow |J' = 1, m_J = -1\rangle$. By detuning the laser frequency appropriately, such that its frequency corresponds to that of a shifted level, atoms preferentially absorb photons from beams opposing their motion; an atom leaving the center of the trap will more likely absorb photons from the σ^--beam if moving towards the $z > 0$ region, and vice-versa, thereby pushing it back to the center in either case.

Mathematically, this situation is analogous to that of a damped harmonic oscillator, which is similar to Eq. (3.8) aside from the incorporation of a restoring term. Explicitly,

we have:

$$\mathbf{F}_{MOT} = -\alpha\mathbf{v} - \frac{\alpha\kappa}{k}\mathbf{z}, \tag{3.9}$$

with the same α as in Eq. (3.8), and $\kappa = (\mu_B\hbar)/(dB/dz)$, with μ_B being the Bohr magneton, and B the magnetic field.

3.2 Experimental Setup for the MOT

The formalism adopted in the previous section was intentionally kept simple in order to make the theoretical description straightforward. Creating a MOT experimentally requires further considerations than what was presented here. For example, an additional beam, the so-called *repump* beam, is in general used to ensure atoms remain in the cooling cycle. Beam intensities, quality of the vacuum, and the magnetic field gradient have to be carefully adjusted in order to create a cloud of atoms as cold and dense as possible. It is these parameters that shall be discussed in this section. We provide details about the experimental apparatus used to achieve laser cooling and trapping of ^{87}Rb atoms in a MOT. The cloud of atoms was overlapped with an HOM-ONF to carry out some of the experiments described in Chapter 6. Note that a similar experimental setup involving a fundamental mode ONF is also located on the optical table. This latter setup was used for some of the experiments presented in Chapter 5, but is not described in what follows, as the system was assembled by other members of the group and is very similar to what is described here.

3.2.1 Choice of atom

Alkali metals are in general favored for cold atom experiments for several reasons. First, these atoms have all of their electronic shells completely filled, except for the outermost one which contains a single valence electron. As such, the atom behaves as if it were made of a positive nucleus and a single electron. This makes predictions on its behavior when placed in an EM field much easier. Second, laser diodes addressing the desired cooling transitions are commercially available. Finally, and most importantly, these atoms offer cyclic transitions, which allow the implementation of a closed cooling scheme. Our experiments use ^{87}Rb, for which some physical properties are presented in Table 3.1. In Fig. 3.4, the energy levels that are used in the projects presented in later chapters of this thesis are shown: The quadrupole project is described in Chapter 4, the single-color, two-photon project in Chapter 5, and the HOM project in Chapter 6. The energy levels relevant to the cooling of ^{87}Rb atoms are described hereafter.

The fine structure of ^{87}Rb has two main spectroscopic lines: The D_1-line, addressable at a wavelength of 795 nm, and the D_2-line at 780 nm. We work with the D_2-line, which, using the Russel-Saunders notation, is between the ground state, $5S_{1/2}$, and the excited state, $5P_{3/2}$. Table 3.2 shows some relevant optical properties of the transition.

Each level in the fine structure possesses a hyperfine structure, which results from the interaction between the nuclear spin, I, and the total angular momentum of the valence electron, J. A hyperfine level is in general labeled F in most atomic physics textbooks, and its value is dictated by the condition $|J - I| \leq F \leq J + I$. We adopt the same notation here. The energy levels of the ^{87}Rb D_2-line and the transitions involved in the

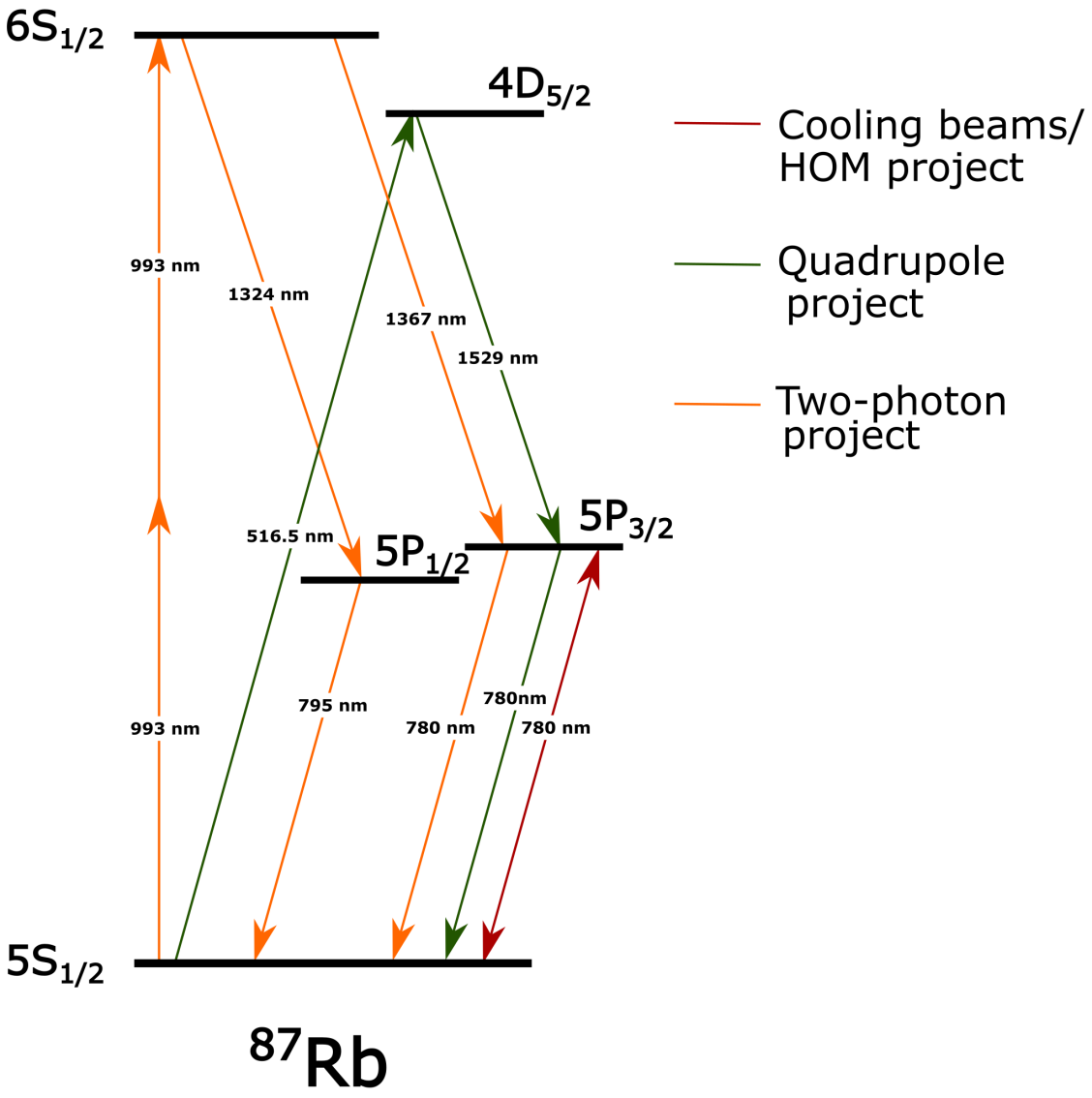

Figure 3.4: Energy levels of ^{87}Rb used in the projects presented in this thesis.

Table 3.1: Physical properties of ^{87}Rb

Atomic number	37
Total nucleons	87
Nuclear spin	3/2
Relative natural abundance	27.83 %
Atomic mass	1.44316065×10^{-25} kg

cooling process are shown in Fig. 3.5. The ground state possesses two hyperfine levels, $F = 1$ and $F = 2$, while the excited state has four, namely $F' = 0, 1, 2, 3$. The cooling beam is tuned to a frequency, ω_{cool}, that drives the $5S_{1/2}F = 2 \rightarrow 5P_{3/2}F' = 3$ transition. This transition is a *cycling transition*; selection rules for a dipole transition only allow $\Delta F = 0, \pm 1$ transitions, allowing a photon from the cooling beam to be absorbed but preventing the atom excited in the $F' = 3$ hyperfine state from decaying back to any other state than the $F = 2$ ground state. Subsequent absorption of a photon from the cooling beam resets the cycle. However, the cooling beam has a non-zero probability to drive the $F = 2 \rightarrow F' = 2$ transition. This pushes all of the atoms in a sample out of the aforementioned loop after a few thousand cycles. A repumping beam tuned to a frequency, ω_{rep}, drives the $F = 1 \rightarrow F' = 2$ transition, thus ensuring atoms are always brought back to the cooling cycle.

3.2.2 Creation and control of the magnetic fields

The anti-Helmholtz coils are made in-house to fit around the top and bottom viewports of the science chamber, placing them at a distance of 130 mm from each other. Each coil is 160 mm in diameter with 200 winds of enameled copper wire. In each coil, the inductance is measured to be 28 mH and the total resistance is 6 Ω. Two outputs of a three-channel power supply (GW Instek, PST-Series 3-channel Power Supply) provide the currents. These can be tuned relative to each other, giving us some leeway in adjusting the magnetic trap to correct for any misalignment of the coils and other experimental imperfections. This system gives a field gradient of 9.6 G/cm with 4 A of current in each coil. In addition, the coils are individually connected to an insulated gate bipolar transistor (IGBT) switch, which allows the magnetic field to be turned off in 3.4 μs. When

Table 3.2: Optical properties of the D_2 line in ^{87}Rb ($5S_{1/2} \rightarrow 5P_{3/2}$).

Frequency	$2\pi \times 384.2305$ THz
Wavelength (vacuum)	780.2412 nm
Wavelength (air)	780.0320 nm
Lifetime	26.24 ns
Natural linewidth (FWHM)	$2\pi \times 6.065$ MHz
Atomic mass	1.44316065×10^{-25} kg
Recoil energy	$2\pi \times 3.7710$ kHz
Doppler temperature	146 μK
Saturation intensity ($\sigma^{\pm}$ polarization)	1.669 mW/cm^2

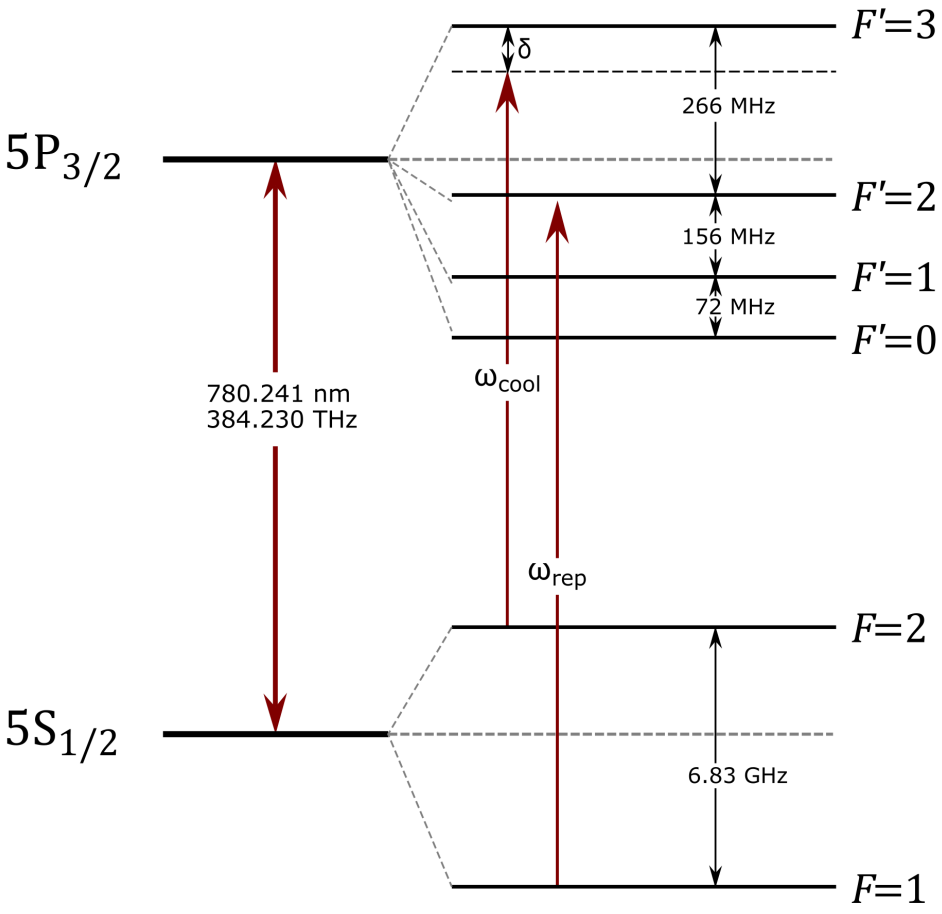

Figure 3.5: Energy levels of the D_2 line of ^{87}Rb showing the cooling transitions. The cooling laser is tuned to a frequency ω_{cool}, red-detuned by δ from the $F = 2 \rightarrow F' = 3$ transition. A repump beam, tuned to ω_{rep}, drives the $F = 1 \rightarrow F' = 2$ transition and ensures atoms are kept in the cooling cycle.

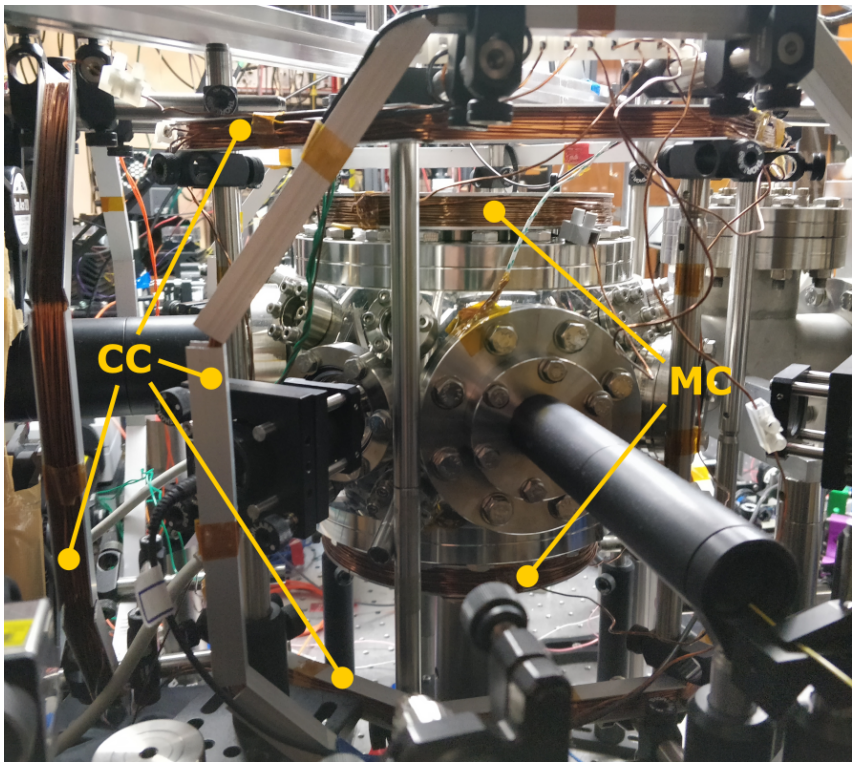

Figure 3.6: Picture of the magnetic coils on the experimental setup. The two main magnetic coils (MC), in an anti-Helmholtz configuration, are positioned around the top and bottom viewports of the vacuum chamber. Four of the six compensation coils (CC), in a Helmholtz configuration, can also be seen.

short-circuited, the inductively generated current in the coils is preferentially discharged into resistors instead of circulating through the coils backwards. A picture of the setup featuring the positioning of the coils is presented in Fig. 3.6.

Three additional pairs of coils, positioned along the three directions of space, are also used, each pair set in a Helmholtz configuration. This allows the magnetic center of the trap to be shifted, and, by extension, provides us with a way to optimize the overlap of the MOT with the HOM-ONF. This is done by measuring the coupling of fluorescent photons from atoms into the guided modes of the nanofiber using a single-photon counting module (SPCM) (Excelitas, SPCM-AQRH).

3.2.3 Cooling and repump laser systems

As mentioned previously, the cooling of ^{87}Rb atoms in a MOT is done by tuning a laser to a frequency which is slightly red-detuned from that of the $5S_{1/2}F = 2 \rightarrow 5P_{3/2}F' = 3$ transition. This detuning, chosen to be $\delta = 14$ MHz, is adjusted using an acousto-optic modulator (AOM) (IntraAction ATM-602DA2B) with a central frequency of 60 MHz in a double-pass configuration. In addition to the frequency shift it provides, the AOM also acts as a fast switch, allowing us to turn off the cooling beams on demand. The frequency and amplitude modulation of the AOM are controlled by a data acquisition card (National Instruments, DAQ) using a LabVIEW program. The repump beam is also

passed through an AOM (IntraAction AOM-802AF3) with a central frequency of 80 MHz, but its frequency is, in general, not shifted from that of the $5S_{1/2}F = 1 \rightarrow 5P_{3/2}F' = 2$ transition.

A schematic of the experimental setup for both the cooling and repump beams is given in Fig. 3.7. The cooling beam is provided by an external cavity diode laser (ECDL) system within a commercial tapered amplifier system (Toptica TA Pro). The repump beam is provided by another ECDL, with no further power amplification component (Toptica DL100 Pro). Both lasers are tuned to a wavelength of 780.2 nm, with a typical linewidth of the order of a few 100 kHz. For the cooling beam, two fiber-coupled ports are available for use. First, a back port provides a small fraction of the total power ($\sim$1 mW) and connects to a compact saturation spectroscopy system (Toptica CoSy), the output of which is fed to a computer-controlled, laser-locking module (Toptica DigiLock110). Scanning the laser frequency provides hyperfine spectroscopic peaks from which the DigiLock110 can generate error signals and, subsequently, enables us to lock the laser onto a specific peak. The remaining port is connected via a polarization-maintaining (PM) fiber to a collimating lens (C1) providing a free-space beam with up to 400 mW of power at its output. The free-space beam is sent through a half-wave plate (HWP1) and a polarizing beam-splitter (PBS1), allowing us to control the power ratio between the reflected and transmitted paths of PBS1 by rotating HWP1. Here, the reflected beam is blocked while the transmitted beam is allowed to propagate. Since two experiments share the same optical table, we use HWP2 and PBS2 to divide the power equally among both experiments. A third such combination is used before the double-pass AOM, again in order to control the total power used in the experiment. This time the transmitted beam is blocked and the reflected beam passes through the AOM. This beam and its diffracted orders exit the AOM and pass through a quarter-wave plate (QWP), a plano-convex lens (PCL) with focal length $f = 100$ mm, and an iris that transmits only the first diffracted order. The QWP is tuned appropriately to ensure total transmission through PBS3 after retro-reflection, and the PCL is placed one focal length away from the AOM such that the diffracted beams are parallel, thus facilitating the selection of the first order when using the iris. The resulting beam is retro-reflected and passed once again through the AOM, after which the first order is selected, resulting in a beam shifted in frequency by 120 MHz. The beam power is divided equally and coupled to three PM fibers, giving close to 12 mW per cooling beam in each direction. We lock the laser to the $5S_{1/2}F = 2 \rightarrow 5P_{3/2}F' = (2,3)_{co}$ peak, which appears at half the frequency difference between the hyperfine levels $F' = 2$ and $F' = 3$, that is at 133 MHz (see Fig. 3.5). Efficient cooling is, in general, achieved for a red-detuning of 14 MHz $\approx 2\Gamma/2\pi$; this requires the locked cooling beam to be frequency shifted by 119 MHz, which is easily adjusted from the 120 MHz shift mentioned previously.

The repump beam is not shared with the other experiment and, consequently, follows a less convoluted optical path. Moreover, if locked to the $5S_{1/2}F = 1 \rightarrow 5P_{3/2}F' = (1,2)_{co}$ peak, the laser must be frequency shifted by only 78 MHz and a single-pass through an AOM with a central frequency of 80 MHz is sufficient. After the AOM, the beam power is divided equally in three and coupled to the same aforementioned PM fibers, giving close to 1 mW per MOT beam. Both cooling and repump beams are in all directions to increase the effect of repumping.

To produce the MOT beams, each PM fiber is connected to a cage-mounted fiber-collimator, in front of which is placed a QWP adjusted to give the desired circular polar-

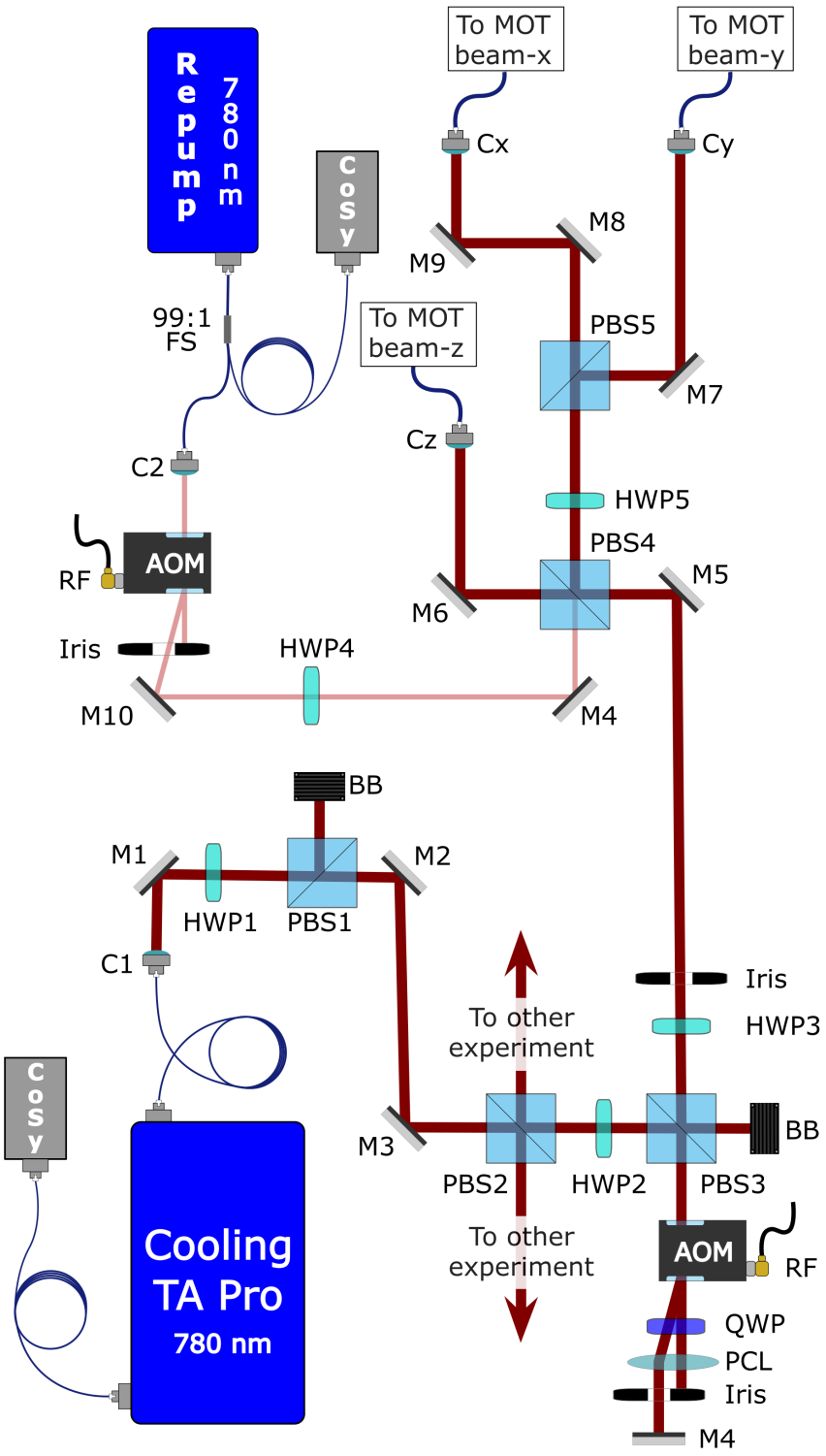

Figure 3.7: Detailed schematic of the optics in the control and frequency tuning of the cooling and repumping beams. Both beams are utlimately fiber-coupled to generate beams in each direction of space (Cx, Cy, and Cz). BB: Beam blocker, C1-C2: Collimating lenses, FS: Fiber-splitter, HWP1-HWP5: Half-wave plates, M1-M10: Mirrors, QWP: Quarter-wave plate, PBS1-PBS5: Polarizing beam-splitters, PCL: Plano-convex lens, RF: Radio-frequency modulating signal.

ization. Beams of 1.5 cm in diameter are produced resulting in a cooling beam intensity of ≈ 6.8 mW/cm^2, well above the saturation intensity (see Table. 3.2) and a repump intensity of 0.5 mW/cm^2. Each fiber-collimator faces a viewport, sending the beams into the science chamber. A cage-mounted assembly composed of a mirror and a QWP is placed in front of a viewport directly opposite to each one of the fiber-collimators such that the cooling beams are retro-reflected with opposite circular polarization. Irises can be mounted on the cage system in front of the mirror and the fiber-collimator for alignment purposes.

3.2.4 Characterization of the cold atom cloud

After alignment of the beams and locking of the laser frequencies to the respective repump and cooling transitions, a first, non-optimal MOT, is generally obtained. Further optimization requires fine tuning of the magnetic fields and better alignment of the laser beams. These parameters are adjusted based on the fluorescence emitted by the cold atomic cloud, while maintaining a pressure in the low 10^{-9} mbar for an optimal MOT. In our system, the pressure generally starts from 9.8×10^{-10} mbar when the dispensers are off and settles to around 3 $\times10^{-9}$ mbar when the experiment is running.

Once the MOT is optimal, it has to be fully characterized. For this, we estimate the average atom temperature via time-of-flight (TOF) measurements and the atom density by detection of fluorescent photons. Note that, for these measurements, the atom cloud is moved a short distance away from the HOM-ONF using the compensation coils. The images taken during one such TOF experiment are shown in Fig. 3.8. A triggerable CMOS camera (Thorlabs DCC3240N) is placed facing the front viewport of the vacuum chamber and images the cloud of atoms in the MOT. The main magnetic coils, the repump, and cooling beams are all turned off at the same time and the cloud is left to expand. After an arbitrary period of time, typically a few milliseconds, the cooling beams are briefly turned on to "flash" the cloud and generate fluorescence. The camera is triggered at the same time and a picture of the expanded cloud is taken. By measuring the cloud diameter every millisecond, the expansion rate can be determined and directly correlated to the temperature of the cloud, T_{cloud}, via the relation

$$T_{cloud} = \frac{M\Delta\tau}{k_B}, \tag{3.10}$$

where M is the mass of a ^{87}Rb atom, k_B is the Boltzmann constant, and $\Delta\tau$ is the rate of expansion squared, measured from the slope of the curve obtained when plotting the diameter of the cloud squared as a function of the expansion time squared. This value can be compared to the Doppler limited cooling temperature for ^{87}Rb, $T_D = 146$ μK, calculated from the expression

$$T_D = \frac{\hbar\Gamma}{2k_B}, \tag{3.11}$$

with $\hbar$ being the reduced Planck's constant and Γ being the decay rate of the excited state. The TOF experiment presented here yielded a temperature of $\sim$117 μK, showing that we have achieved sub-Doppler cooling.

In order to estimate the atom density in the MOT, we need to first evaluate the diameter of the cloud and the number of atoms trapped in it. Determining the diameter

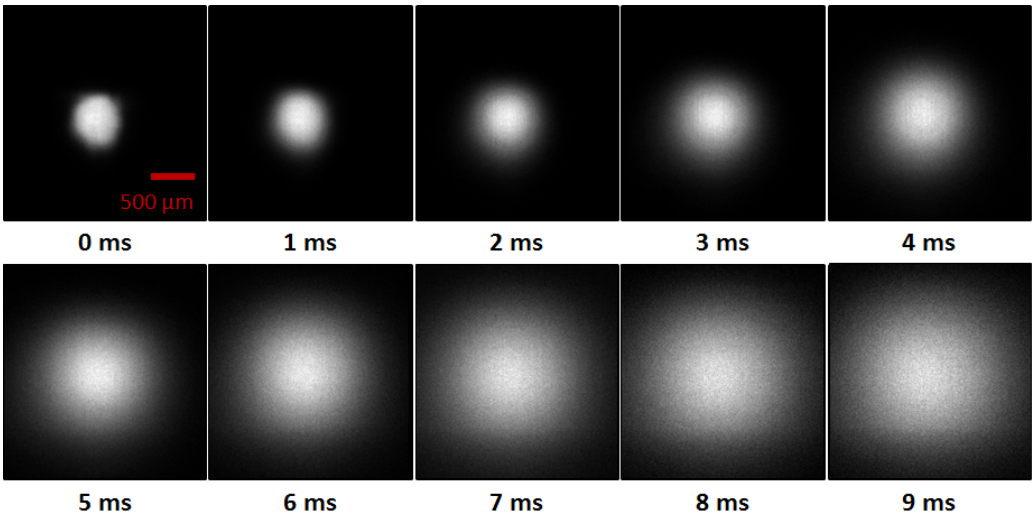

Figure 3.8: MOT temperature measurement via time-of-flight. The value under each picture indicates the amount of time for which the cloud was left to expand before taking the picture.

is straightforward, as it simply requires an image of the MOT that we then compare with an image of a known object captured with the same optical apparatus (i.e., the camera and zoom-lens with unchanged focus). Evaluation of the number of trapped atoms requires collecting fluorescent photons emitted by atoms in the MOT onto an APD in front of which we place a plano-convex lens. We compare the measured signal with the background signal when the magnetic coils are switched off. From the obtained voltage on the APD one can calculate the transmitted power from

$$\text{Power} = \frac{V_{\text{meas}}}{\text{RSP}\, R_{\text{load}}}, \tag{3.12}$$

where V_{meas} is the measured voltage, RSP is the detector's response, or the photon-electron conversion efficiency at a given wavelength, here 780 nm, and R_{load} is the 1 MΩ load resistance for the oscilloscope. The power can be used to get an approximation of the number of atoms in the trap using

$$\text{Power} = N\, h\omega_{cool}\, \frac{\pi r^2 \Gamma}{8\pi D^2}, \tag{3.13}$$

where N is the number of trapped atoms, h is Planck's constant, ω_{cool} is the cooling transition frequency, $r = 1.25$ cm is the radius of the lens, $\Gamma = 6$ MHz is the decay rate of the excited state, and $D = 15$ cm is the distance from the MOT center to the lens. We typically measure close to 10^7 atoms trapped in our MOT, with an average density in the range of 10^{10} to 10^{11} cm^{-3}.

3.3 Conclusion

In this chapter, we have provided a brief theoretical description of laser-cooling of neutral atoms and detailed the experimental setup used throughout this thesis work to create,

control, and characterize a MOT of cold ^{87}Rb atoms. We explained the origin of, and provided the mathematical expressions for, the forces acting on neutral atoms when they are cooled via optical molasses or trapped in a MOT. We then described the experimental setup allowing us to tune the frequency and lock the frequencies of the cooling and repump beams before they are used to create a MOT. We calculated an average temperature of $\sim$117 μK for the trapped atoms, which is found to be below the Doppler limited cooling temperature of 146 μK for ^{87}Rb

Chapter 4

Enhancement of a Quadrupole-Allowed Transition Mediated by an Optical Nanofiber[1]

This chapter outlines some of the results obtained from our theoretical work on optical nanofiber-mediated quadrupole interactions with a single atom and is based on the work published in [121]. Here, however, we only present the results that are relevant to an experimental implementation of this work. The detailed mathematical derivations used to form the theoretical model, along with some of the plots, which were either not produced by the author of this thesis or judged irrelevant for experimental work, can be found in Appendix B.

The chapter starts with an introduction, where the relevance of the work in the context of high-density quantum information encoding using the orbital angular momentum of light (OAM) is shown. The theoretical model describing a quadrupole interaction between a ^{87}Rb atom and fiber-guided light is then briefly described, before presenting the results of numerical simulations for the example of the $5S_{1/2} \rightarrow 4D_{5/2}$ quadrupole-allowed transition in ^{87}Rb at 516.5 nm.

4.1 Introduction

Atoms and photons are excellent building blocks for the realization of quantum networks [70]. Information can be encoded on the quantum state of a photon, then coherently mapped onto an atomic excitation, where the information can be either stored or processed, before being mapped back to a photonic state. Among the degrees-of-freedom onto which information can be encoded in a photon, orbital angular momentum (OAM) states have recently received particular attention [106, 122, 123]. OAM modes form a discrete and orthogonal basis that can be used to define an infinite-dimensional Hilbert space

[1]This chapter is adapted from the work published in F. Le Kien, T. Ray, T. Nieddu, T. Busch, S. Nic Chormaic, Phys. Rev. A **97**, 013821 (2018) [121]. T. Nieddu participated in the writing of the research article and was involved in the numerical calculations for quadrupole excitation via the HOMs of the ONF. These calculations were based on analytic expressions for the quadrupole moment, Rabi frequency, oscillator strength, and enhancement factors derived analytically by F. Le Kien.

[124]. Such modes can be created in free-space using Laguerre-Gaussian (LG) beams, also called vortex- or donut-beams, which carry $l\hbar$ of OAM per photon, l being the azimuthal mode order [125]. This new degree-of-freedom has been used to demonstrate, for example, entanglement of OAM at the single-photon level [126], the violation of Bell inequalities in the case of high-dimensional entanglement of photonic states [127], the uncertainty principle between the angular position and the OAM [128], and high-security quantum cryptography protocols [129].

Experiments listed above have focused on the first key ingredient in the design of a quantum network, namely, the photon. However, beyond its importance in the verification of fundamental principles of quantum physics, the OAM of light also holds the potential to develop high data capacity for applications such as quantum networks [130]. For this very purpose, efficient OAM interfaces with matter have to be developed. Cold atomic ensembles make an excellent storage platform in this context. Storage and retrieval of OAM-states in such systems have been shown, using coherent population oscillation [131], high-order wave-mixing [132], and electromagnetically induced transparency (EIT) [133]. In addition to storing information encoded on the OAM degree-of-freedom of photons, the storage of entangled OAM- states in a cold atomic ensemble has also been recently demonstrated [134].

Despite the much larger signal-to-noise-ratio provided by cold atomic ensembles, interaction at the single atom level is of particular importance both for the fundamental understanding of interaction mechanisms and in the framework of quantum information for establishing reliable and efficient encoding protocols. To directly map high-dimension qubits encoded on the OAM of a photon onto a single atom state, multipole transitions are required. This was recently experimentally achieved with trapped ions by Schmiegelow *et al.* [135], in which both the SAM and OAM of a tightly focused LG_{01} beam in free-space were used to excite a quadrupole-allowed transition in a single $^{40}Ca^{+}$ ion. Contrary to dipole-allowed transitions, quadrupole-allowed transitions do not rely on the electric field intensity, but instead are more likely to occur in a high field gradient. For example, an atom positioned at the center of a circularly polarized LG_{01} beam is in a region of zero field intensity, but experiences a very high field gradient, thereby increasing the likelihood of driving a quadrupole-allowed transition.

Given the technological advances promised by OAM in free-space, its development for fibered systems, such as ONFs, for example, is a natural extension of what has been achieved so far. In Section 1.6.1, we already hinted that OAM could be carried by specific HOMs; some of the hybrid modes, specifically the HE and EH modes, can carry more than $\hbar$ of total angular momentum [95]. This feature could be exploited in systems that interface the guided modes of an ONF with cold atoms to reproduce results obtained in free-space experiments. Research during this PhD project was largely concerned with exploiting the HOMs of an ONF as an additional degree-of-freedom to encode quantum information and, potentially, transfer it to cold atoms. Motivated by the work reported in [135] on the use of OAM-carrying beams to drive quadrupole-allowed transitions in a single ion, we developed a theoretical model to establish the capability of an ONF to drive such transitions in a single atom for both the fundamental mode and the first group of HOMs [121]. This has, as a perspective, the development of an ONF-based platform suitable for high-density information encoding.

Techniques to investigate non-dipole transitions have been explored theoretically and

experimentally for atoms in free-space [19, 135–142], in evanescent fields [143–145], near a dielectric microsphere [146], near an ideally conducting cylinder [147], and near plasmonic nanostructures [148, 149]. However, the difficulty in achieving large electric field gradients over a long distance makes the study of quadrupole transitions in an extended medium a challenging task. ONFs allow tightly radially confined light to propagate over a relatively long distance [1, 150, 151], typically a few millimeters. As shown hereafter, despite being driven by the gradient of the field, a quadrupole transition has a higher probability of occurring if the field intensity is strong enough. This poses a problem for experiments using free-space beams. However, for ONFs, in addition to a high field intensity, the evanescent field also offers a large intensity gradient in the radial direction [152, 153]. Furthermore, the HOMs of an ONF [94, 95, 104] may also offer an azimuthal phase gradient.

4.2 Theoretical Model: Quadrupole Interaction of an Atom with Guided Light

The basics of the theoretical model used to study the quadrupole interaction of an alkali-metal atom with guided light in the fundamental and HOMs of a vacuum-clad ONF are presented here. The detailed mathematical development leading to the analytical expressions for the quadrupole Rabi frequency, the quadrupole oscillator strength, and their enhancement factors for the general case, i.e., interaction with an arbitrary light field, is contained in Appendix B. Here, we highlight the features needed for a general understanding of the theory.

We first consider an atom placed in an arbitrary electric field, $\boldsymbol{\mathcal{E}}$. Let $|e\rangle$ and $|g\rangle$ be upper and lower states of the atom, with energies $\hbar\omega_e$ and $\hbar\omega_g$, respectively. The Rabi frequency for the quadrupole transition between the two states, Ω_{ge}, is given by

$$\Omega_{ge} = \frac{1}{12\hbar}\sum_{ij}\langle e|Q_{ij}|g\rangle\frac{\partial\mathcal{E}_j}{\partial x_i} \tag{4.1}$$

where the Q_{ij} are the components of the electric quadrupole moment tensor, calculated using Eq. (B.31). For an alkali atom, the transition is degenerate due to the presence of magnetic sublevels, i.e., $|g\rangle = |nFM\rangle$ and $|e\rangle = |n'F'M'\rangle$, see Fig. B.1(b). Here, n denotes the principal quantum number and all additional quantum numbers not shown explicitly, F is the quantum number for the total angular momentum of the atom, and M is the magnetic quantum number. The expression for the quadrupole Rabi frequency, $\Omega_{FMF'M'}$, is given by Eq. (B.38) and yields the selection rules $|F'-F| \leq 2 \leq F'+F$ and $|M'-M| \leq 2$. It can be shown (see Eqs B.36-B.37) that these selection rules can be expanded to the quantum numbers for the total angular momentum, J, and the orbital angular momentum, L, of the electron. The selection rules are then $|J'-J| \leq 2 \leq J'+J$ and $|L'-L| = 0, 2$.

It is now possible to define the root-mean-square (rms) Rabi frequency, $\bar{\Omega}_{FF'}$, which is given by summing over all M and M' values [154]

$$\bar{\Omega}^2_{FF'} = \sum_{MM'}|\Omega_{FMF'M'}|^2. \tag{4.2}$$

This value is used to get an expression for the oscillator strength, $f_{FF'}$, obtained using the relation [154]

$$\bar{\Omega}_{FF'}^2 = \frac{e^2|\mathcal{E}|^2}{8\hbar m_e \omega_0}(2F+1)f_{FF'}, \tag{4.3}$$

where m_e is the mass of an electron. The full expression for $f_{FF'}$ is given by Eq. (B.43). It is a measure that characterizes the proportionality of $\bar{\Omega}_{FF'}$ to the field magnitude, $\mathcal{E}$, through Eq. (4.3). This measure depends not only on the quadrupole of the atom, but also on the normalized gradients of the field components. We note that, for atoms in free-space, the oscillator strength can be interpreted as the ratio between the quantum mechanical transition rate and the classical absorption rate of a single electron oscillator with the same frequency [154, 155]. However, this interpretation may not be valid for atoms in the vicinity of an object because the modifications of the transition rate are much more complicated than for the Rabi frequency.

We now define the enhancement factors for the rms Rabi frequency, η_{Rabi}, and for the oscillator strength, η_{osc}, in arbitrary light as

$$\begin{aligned} \eta_{\text{Rabi}} &= \frac{\bar{\Omega}_{FF'}}{\bar{\Omega}_{FF'}^{(0)}}, \\ \eta_{\text{osc}} &= \frac{f_{FF'}}{f_{FF'}^{(0)}}, \end{aligned} \tag{4.4}$$

where $\bar{\Omega}_{FF'}^{(0)}$ and $f_{FF'}^{(0)}$ are the rms Rabi frequency and oscillator strength of an atom interacting with a plane wave light field in free-space via an electric quadrupole transition. Their respective analytical expressions are given by Eq. (B.44) and Eq. (B.45). We find the relation

$$\eta_{\text{osc}} = \eta_{\text{Rabi}}^2 = \frac{2}{k_0^2|\mathcal{E}|^2}\sum_q \Big|\sum_{ij} u_{ij}^{(q)} \frac{\partial \mathcal{E}_j}{\partial x_i}\Big|^2, \tag{4.5}$$

where the matrices $u_{ij}^{(q)}$ with $q = -2, -1, 0, 1, 2$ are given by Eqs. (B.28). It is clear from Eq. (4.5) that η_{Rabi} and η_{osc} are independent of the quantum numbers F and F'. Moreover, these factors do not depend on any characteristics of the atomic states except for the atomic transition frequency, ω_0. They are determined by the normalized spatial variations of the mode profile function, $\mathcal{E}$, at the frequency, ω_0.

We consider the electric quadrupole interaction between the atom and a guided light field of a vacuum-clad ONF (see Fig. B.1(c)). Assume that the fiber is a dielectric cylinder of radius, a, and refractive index, n_1, and is surrounded by an infinite background medium of refractive index, n_2, where $n_2 < n_1$. We use Cartesian coordinates $\{x, y, z\}$, where z is the coordinate along the fiber axis, and also cylindrical coordinates $\{r, \varphi, z\}$, where r and φ are the polar coordinates in the fiber transverse plane xy. The relations between the Cartesian-coordinate vector components $\mathcal{E}_x$ and $\mathcal{E}_y$ and the cylindrical-coordinate vector components $\mathcal{E}_r$ and $\mathcal{E}_\varphi$ are $\mathcal{E}_x = \mathcal{E}_r\cos\varphi - \mathcal{E}_\varphi\sin\varphi$ and $\mathcal{E}_y = \mathcal{E}_r\sin\varphi + \mathcal{E}_\varphi\cos\varphi$. We note that our model consists of a fiber and a single atom; though this may not be very experimentally realistic it will provide us with useful characterization parameters for the system. When the atom is very close to the surface, the energy levels and the transition rates of the atom are modified. However, for simplicity, we neglect the effect of the fiber on the atom. Because of this approximation, the results for the case where the atom is placed

on the fiber surface is considered as the limiting situation for cases where the atom is close to, but not exactly on, the fiber surface, thence the approximations are valid. The fiber supports the fundamental modes, HE_{11}, and the next four HOMs, namely TE_{01}, TM_{01}, and the two HE_{21}, in a finite bandwidth around the central frequency $\omega_0 = \omega_e - \omega_g$ of the atom to match experimental conditions. Expressions for the electric field of each of these modes has already been given in Section 2.2, but we rewrite them here for convenience.

For a quasicircularly polarized, hybrid, HE_{lm}, mode with propagation direction, f, and phase circulation direction, p, the full mode function is given by

$$\boldsymbol{\mathcal{E}}_{\text{circ}} = (e_r\hat{\mathbf{r}} + pe_\varphi\hat{\boldsymbol{\varphi}} + fe_z\hat{\mathbf{z}})e^{if\beta z + ipl\varphi}, \tag{4.6}$$

where e_r, e_φ, and e_z are given by Eqs. (2.18), for $\beta > 0$ and $l > 0$.

Quasilinearly polarized, hybrid modes are linear superpositions of counterclockwise and clockwise quasicircularly polarized, hybrid modes. The full mode function of the guided field in a quasilinearly polarized, hybrid mode can be written in the form

$$\boldsymbol{\mathcal{E}}_{\text{lin}} = \sqrt{2}[\hat{\mathbf{r}}e_r\cos(l\varphi - \varphi_{pol}) + i\hat{\varphi}e_\varphi\sin(l\varphi - \varphi_{pol}) + f\hat{\mathbf{z}}e_z\cos(l\varphi - \varphi_{pol})]e^{if\beta z}, \tag{4.7}$$

where the e_r, e_φ, and e_z components are the same as before and the phase angle, φ_{pol}, determines the orientation of the symmetry axes of the mode profile in the fiber transverse plane. In particular, the specific phase angle values, $\varphi_{pol} = 0$ and $\varphi_{pol} = \pi/2$, define two orthogonal polarization profiles in the fiber transverse plane, xy.

For a TE_{0m} mode with a propagation direction f, the full mode function is given by

$$\boldsymbol{\mathcal{E}} = e_\varphi\hat{\varphi}e^{if\beta z}, \tag{4.8}$$

where the only nonzero, cylindrical component, e_φ, is given by Eq. (2.27).

Finally, for a TM_{0m} mode with propagation direction, f, the full mode function is

$$\boldsymbol{\mathcal{E}} = (e_r\hat{\mathbf{r}} + fe_z\hat{\mathbf{z}})e^{if\beta z}, \tag{4.9}$$

where the components e_r and e_z are given in Eq. (2.33)

We now derive an analytical expression for the enhancement factor, η_{osc}, for quasicircularly polarized HE, TE, and TM modes. We assume that the atom is positioned on the positive side of the x axis, i.e., we set $\varphi = z = 0$. Then, for quasicircularly polarized HE, TE, or TM modes, we have

$$\begin{aligned}
&\frac{\partial\mathcal{E}_1}{\partial x_1} = e_r', \quad \frac{\partial\mathcal{E}_2}{\partial x_1} = pe_\varphi', \quad \frac{\partial\mathcal{E}_3}{\partial x_1} = fe_z',\\
&\frac{\partial\mathcal{E}_1}{\partial x_2} = \frac{p}{r}(ile_r - e_\varphi), \frac{\partial\mathcal{E}_2}{\partial x_2} = \frac{1}{r}(ile_\varphi + e_r), \frac{\partial\mathcal{E}_3}{\partial x_2} = \frac{fp}{r}ile_z,\\
&\frac{\partial\mathcal{E}_1}{\partial x_3} = if\beta e_r, \quad \frac{\partial\mathcal{E}_2}{\partial x_3} = ifp\beta e_\varphi, \quad \frac{\partial\mathcal{E}_3}{\partial x_3} = i\beta e_z,
\end{aligned} \tag{4.10}$$

where $e_{r,\varphi,z}' = \partial e_{r,\varphi,z}/\partial r$. When we insert Eqs. (4.10) into the expression for the enhancement factor, Eq. (B.47), and use Eqs. (B.28), we find

$$\begin{aligned}
\eta_{\text{osc}} \;=\; &\frac{1}{k_0^2|\mathbf{e}|^2}\Bigg[\left|e_r' - \frac{1}{r}(ile_\varphi + e_r)\right|^2 + \left|e_\varphi' + \frac{1}{r}(ile_r - e_\varphi)\right|^2\\
&+ |e_z' + i\beta_0 e_r|^2 + \left|\frac{l}{r}e_z + \beta_0 e_\varphi\right|^2\\
&+ \frac{1}{3}\left|e_r' - 2i\beta_0 e_z + \frac{1}{r}(ile_\varphi + e_r)\right|^2\Bigg],
\end{aligned} \tag{4.11}$$

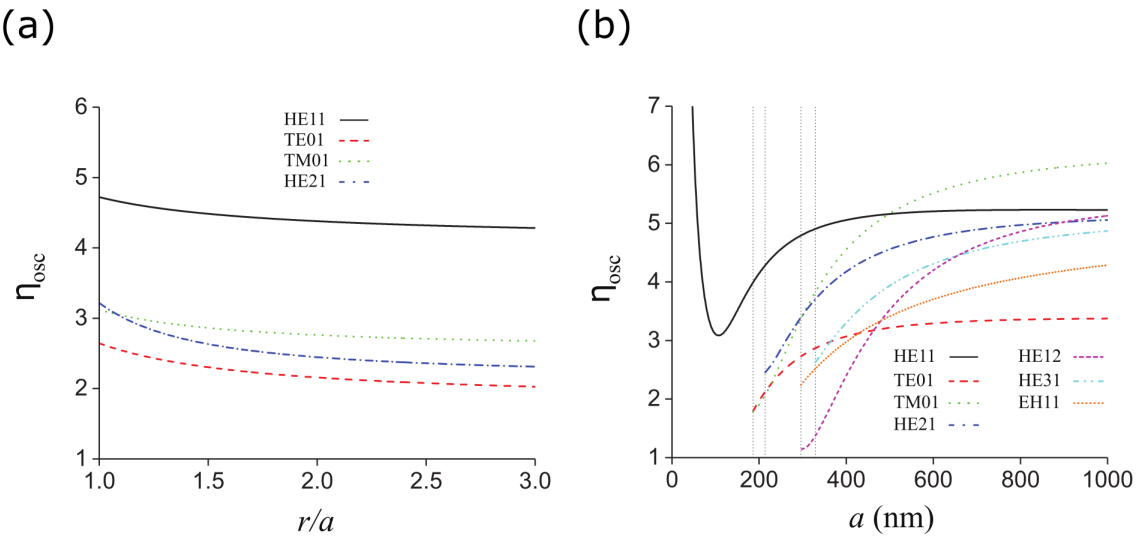

Figure 4.1: Oscillator strength enhancement factor, η_{osc}, for different guided modes. (a) Radial dependencies of η_{osc} for different guided modes. The fiber radius is $a = 280$ nm and has refractive indices of $n_1 = 1.4615$ and $n_2 = 1$ for the fiber core and vacuum cladding, respectively. (b) η_{osc} as a function of a for different guided modes. The atom is positioned on the fiber surface. The hybrid modes are quasicircularly polarized and the quantization axis is arbitrary. The 516.5 nm guided light is simulated at a power of 10 nW. These figures were reproduced from [121] and made by Dr. Le Kien.

where $\beta_0 = \beta(\omega_0)$. In Eq. (4.11), the mode functions and their spatial derivatives must be evaluated at the atomic transition frequency, ω_0, before inserting them into the expression for η_{osc}.

4.3 Numerical results

Here, we present some of the results obtained for the oscillator strength enhancement factor, as this quantity is of particular interest for experiments. The numerical calculations have been done for the electric quadrupole transition between the ground state, $5S_{1/2}$, and the excited state, $4D_{5/2}$, of a ^{87}Rb atom. This transition occurs at 516.5 nm and is accessible by the commercial Ti:Saphire laser system (Msquared, SolsTiS), equipped with a frequency doubler (Msquared ECD-X), recently acquired by the group. For this transition, we have $L' = 2$, $J' = 5/2$, $L = 0$, $J = 1/2$, $S = 1/2$, and $I = 3/2$. The experimentally measured oscillator strength of the transition $5S_{1/2} \to 4D_{5/2}$ in free-space is 8.06×10^{-7} [137]. In our numerical calculations, we assume that the field is at exact resonance with the atom i.e., $\omega = \omega_0$. We note that, despite the choice of a specific quadrupole transition in a specific atom, our numerical results are relatively general, as η_{osc} does not depend on any intrinsic properties of the atom except for the atomic transition frequency (see Appendix B for details).

In Fig. 4.1(a), we plot the radial dependencies of η_{osc} for different guided modes. We see that η_{osc} achieves its largest values at $r/a = 1$, that is when the atom is close to the

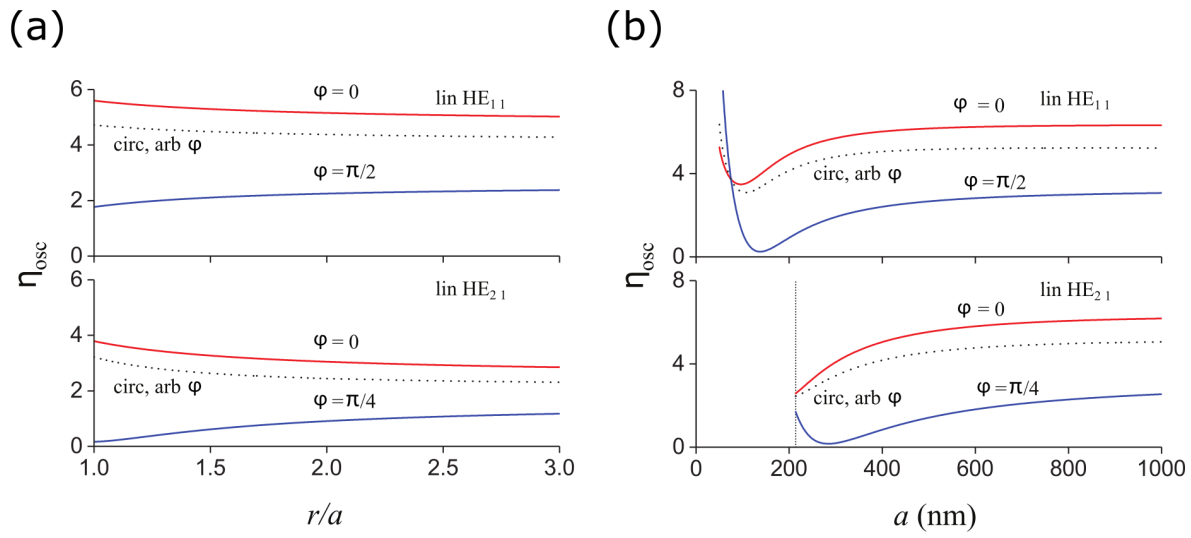

Figure 4.2: Oscillator-strength enhancement factors, η_{osc}, for the quasilinear, HE_{11} and HE_{21}, modes. (a) Dependence on the radial distance, r, at different azimuthal angles, φ. The orientation angle of the quasilinear polarization axis is $\varphi_{\mathrm{pol}} = 0$ and the quantization axis is arbitrary. Other parameters are as for Fig. 4.1. For comparison, the results for the corresponding quasicircular, hybrid modes are shown by the dotted black curves. (b) Dependence on the fiber radius, a. The atom is positioned on the fiber surface at different azimuthal angles, φ. The orientation angle of the quasilinear polarization axis is $\varphi_{\mathrm{pol}} = 0$ and the quantization axis is arbitrary. Other parameters are as for Fig. 4.1. The vertical dotted line indicates the position of the cutoff for the HE_{21} mode. For comparison, the results for the corresponding quasicircularly polarized, hybrid modes are shown by the dotted black curves.

fiber surface and that it reduces slowly with increasing radial distance, r. This means that, despite the evanescent field behavior, η_{osc} can be significant even when the atom is far from the fiber, since the oscillator strength, $f_{FF'}$, and, hence, η_{osc} are determined not by the field amplitude but the ratio between the field gradient and the field amplitude. In Fig. 4.1(b) we study the dependence of η_{osc} on the fiber radius, a, for different guided modes. As for the oscillator strength, $f_{FF'}$, (see Fig. B.11), η_{osc} has a local minimum at a fiber radius $a \simeq 107$ nm for the fundamental mode, HE_{11}, and is larger for higher order modes in the region $a < 498.2$ nm. ONFs fabricated for cold atom experiments have a typical fiber radius ranging from 200 to 400 nm, which is within this region. The fundamental mode has, therefore, always a higher probability to drive the quadrupole-allowed transition compared to other modes if the atom is close to the fiber surface.

Due to the summation over transitions with different magnetic quantum numbers and the cylindrical symmetry of the field in a quasicircularly polarized hybrid mode, the $f_{FF'}$ and the η_{osc} do not depend on φ. For the field in a quasilinearly polarized, hybrid mode the cylindrical symmetry is broken and $f_{FF'}$ and η_{osc} vary with varying φ. In Figs. 4.2(a) and 4.2(b), we plot the dependencies of η_{osc} for the quasilinearly polarized, HE_{11} and HE_{21}, modes on r and a for different φ. We observe that, depending on φ, the factor η_{osc}

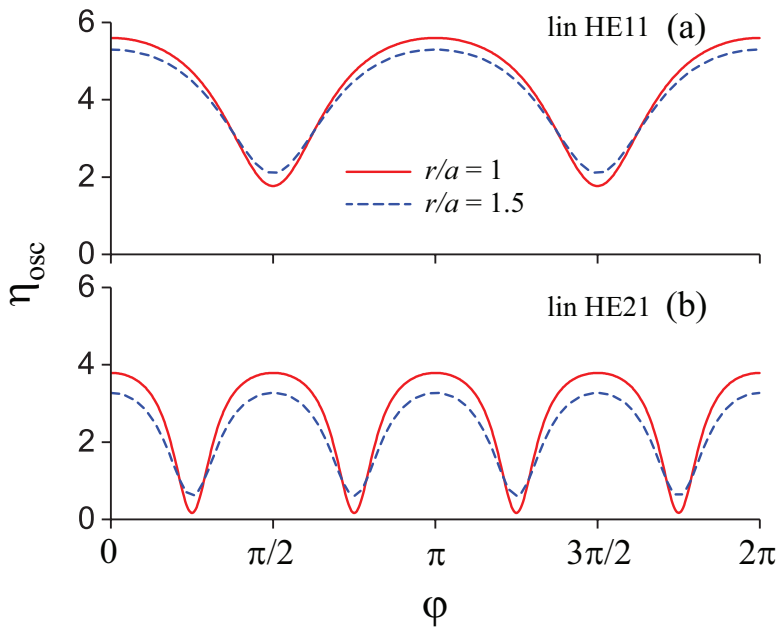

Figure 4.3: Oscillator-strength enhancement factors, $\eta_{\rm osc}$, for the quasilinearly polarized, HE_{11} and HE_{21}, modes as functions of the azimuthal angle, φ, for the position of the atom in the fiber cross-sectional plane. The orientation angle of the quasilinear polarization axis is $\varphi_{\rm pol} = 0$ and the quantization axis is arbitrary. Other parameters are as for Fig. 4.1.

may decrease or increase with increasing r, may be larger or smaller than that for the corresponding quasicircular hybrid mode, and may have a minimum in the dependence on a. Figure 4.2(a) shows that $\eta_{\rm osc}$ varies slowly in the radial direction. Comparison between the curves for different azimuthal angles in Figs. 4.2(a) and 4.2(b) indicates that $\eta_{\rm osc}$ for quasilinear modes varies significantly in the azimuthal direction.

In order to get a better view of the spatial profiles of the enhancement factor, $\eta_{\rm osc}$, for quasilinearly polarized, hybrid modes, in Figs. 4.3 and 4.4 we plot this factor as a function of the azimuthal angle, φ, and the Cartesian coordinates, x and y, of the position of the atom in the fiber cross-sectional plane. The figures show that $\eta_{\rm osc}$ for quasilinearly polarized, hybrid modes varies significantly in the azimuthal direction, but only slightly in the radial direction, and is relatively large or small along the major or minor symmetry axes of the modes, respectively.

Our results on the enhancement factor of the oscillator strength can be compared with the work of S. Tojo *et al.*, in which an evanescent field was generated via total internal reflection in a prism and made to interact with a Cs vapor [144, 145]. Although our results match their theoretical findings [145], both qualitatively and quantitatively, optical nanofibers offer several advantages compared to prisms. For example, a nanofiber can directly be embedded in an atomic vapor, essentially non-destructively, allowing interactions between the guided-light and the atoms in all three directions of space. In contrast, prisms only allow interactions in the vicinity of their reflecting surface. Moreover, in [145], a maximum enhancement factor of 6 is predicted for a p-wave with incidence angle of $\pi/2$. These conditions are challenging to meet experimentally, as clear from their experimental work [144], in which the maximum enhancement factor obtained was 2.5 for a p-wave

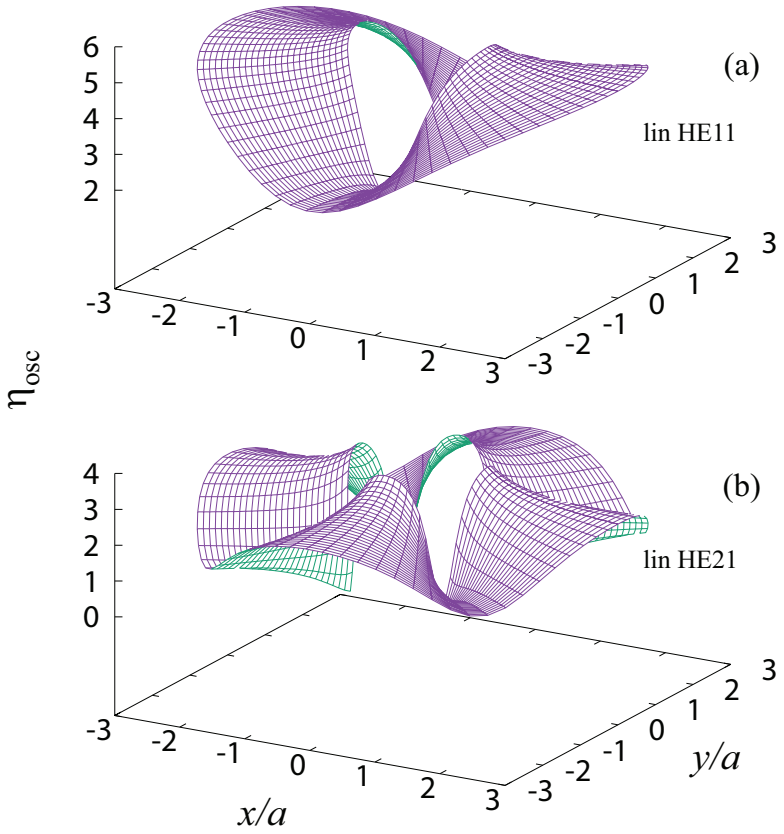

Figure 4.4: Oscillator-strength enhancement factors, η_{osc}, for the quasilinearly polarized, HE_{11} and HE_{21}, modes as functions of the position of the atom in the fiber cross-sectional plane. The orientation angle of the quasilinear polarization axis is $\varphi_{\mathrm{pol}} = 0$ and the quantization axis is arbitrary. Other parameters are as for Fig. 4.1.

with incident angle close to $\pi/4$. This constraint does not apply to nanofibers for which a maximum enhancement factor of 6 is also predicted when the atom is positioned close to the fiber surface. This condition can be reproduced experimentally, in particular when working with cold atom ensembles for which the highest density of atoms can be created in the vicinity of the ONF's surface [17].

4.4 Conclusion

In this chapter, we have motivated the use of HOMs as a way to encode high-density information on their total angular momentum. Furthermore, we have theoretically studied the electric quadrupole interaction of a ^{87}Rb atom with guided light in the fundamental and HOMs of an ONF, in order to demonstrate the potential of such a platform for the storage of information carried by the guided modes. This is illustrated by the fact that the quadrupole oscillator strength[2] is enhanced by the effect of the fiber on the gradient of the field amplitude, thus increasing the chances to drive a quadrupole-allowed transition compared to what could be achieved with free-space beams. The enhancement factors of the rms Rabi frequency and the oscillator strength do not depend on any characteristics of the internal atomic states except for the atomic transition frequency. These factors are determined by the normalized spatial variations of the mode profile function at the atomic transition frequency. Like the oscillator strength, its enhancement factor, η_{osc}, varies slowly with increasing distance from the atom to the fiber surface. Hence, η_{osc} can be significant even when the atom is far away from the fiber.

[2]The rms Rabi frequency is also enhanced in this system. This is shown in Appendix B.

Chapter 5

Single-Color Two-Photon Excitation[1]

Following the theoretical results on the ONF-mediated enhancement of quadrupole-allowed transitions that were presented in Chapter 4, we decided to address experimentally the relevant $5S_{1/2} \rightarrow 4D_{5/2}$ transition in Rb atoms at a 516.5 nm wavelength via a single-color two-photon excitation at 1033 nm. This wavelength is within the specified range of a Ti:Sapphire laser (Coherent MBR10), acquired by the group a few years ago. The two-photon transition facilitates the access to spectroscopic peaks that can later be used as frequency references for laser-locking. Unfortunately, the laser being close to its wavelength limit yielded insufficient power at 1033 nm to run the experiment. We decided nonetheless to carry on with our original plan to perform ONF-mediated two-photon experiments with cold atoms, albeit by exploiting the $5S_{1/2} \rightarrow 6S_{1/2}$ transition at 993 nm, in order to gain valuable knowledge on such an experiment. This could be later used once a laser at 1033 nm would become available.

This chapter first gives an introduction to two-photon processes. Next, the spectroscopic study carried out exploiting the $5S_{1/2} \rightarrow 6S_{1/2}$ two-photon transition in a hot Rb atom vapor, using a single-frequency laser beam is described. The preliminary results obtained when a similar experiment was performed using a fundamental mode ONF embedded in a cold atom cloud are then presented. In this system, we observed an energy level splitting from the two-photon excitation mediated by the tapered fiber, suggesting that the atoms are strongly-coupled to its guided-modes. We also exploited the specific selection rules associated with the transition to show that polarization tomography at the waist of the ONF may be achievable. This latter feature acts as a stepping-stone towards selective optical mode excitation at the waist of a HOM-ONF. We emphasize, however, that the results obtained with the cold atom experiments are ongoing, preventing us from giving a complete theoretical description of the physics involved. The chapter ends with a summary and provides perspectives on future experiments to be done within the research group.

[1]This chapter was adapted from the work published by T. Nieddu, T. Ray, K.S. Rajasree, R. Roy, S. Nic Chormaic, Opt. Express **27**, 6528-6535 (2019) [156]. T. Nieddu did the experiments and drafted most of the paper.

5.1 Introduction

The $5S_{1/2} \rightarrow 6S_{1/2}$ two-photon transition is dipole-forbidden in the single-photon regime, but dipole-allowed in the two-photon regime [157]. Two-photon processes in atomic systems have several distinct advantages over single-photon processes. When the two photons are derived from two counter-propagating beams, a judicious choice of the polarizations can yield background-less, Doppler-free spectra [158, 159]. Two-photon transition frequencies for $S \rightarrow S$ transitions are insensitive to magnetic fields below the Pacshen-Back domain [160], while two-photon transitions to metastable states have extremely narrow linewidths compared to those for single-photon processes [161, 162]. These unique features make two-photon spectroscopy a powerful tool for precision measurements. Following the first observation of a two-photon transition in an atomic system containing caesium [163], numerous different atomic transitions have been investigated [164–170]. The technique has been extensively used for metrology and the accurate determination of fundamental constants [171, 172], as a frequency reference [173], and in quantum telecommunications [174].

5.2 Two-Photon Spectroscopy in Rubidium Vapor

The spectroscopy experiment reported in this section was initially designed as a stepping-stone towards more elaborate experiments employing the ONF and cold atoms. It turned out, however, that the excitation of the $5S_{1/2} \rightarrow 6S_{1/2}$ transition using a one-color, two-photon excitation had never been observed before. We, therefore, decided to explore the dependency of the spectroscopy signal on (i) the intensity and (ii) the polarization of the pump beam to confirm the two-photon character of the transition. As shall be seen, we observed a quadratic dependency on the intensity of the pump laser which is a signature of the two-photon transition. We also show that the pump laser frequency can be stabilized to the observed spectroscopic peaks, thereby illustrating that the transition could be used as a frequency reference. This section also discusses some possible applications for precision measurements and quantum telecommunications.

5.2.1 Energy levels of the $5S_{1/2} \rightarrow 6S_{1/2}$ transition

The energy level diagram for the Rb $5S_{1/2} \rightarrow 6S_{1/2}$ transition is shown in Fig. 5.1. Atoms are excited from the $5S_{1/2}$ ground state, via a virtual state, to the $6S_{1/2}$ state using a two-photon process at 993 nm. The atoms can decay back to the ground state via two possible channels characterized by an intermediate state; this can either be (i) the $5P_{1/2}$ level on emission of a pair of photons with wavelengths 1324 nm and 795 nm (i.e., the D_1 transition), or (ii) the $5P_{3/2}$ level on emission of a pair of photons with wavelengths 1367 nm and 780 nm (i.e., the D_2 transition). The photons at 1324 nm and 1367 nm fall beyond the range of the detectors available for this experiment. Hence, for the work reported hereafter, we only detect the 780 nm and 795 nm light.

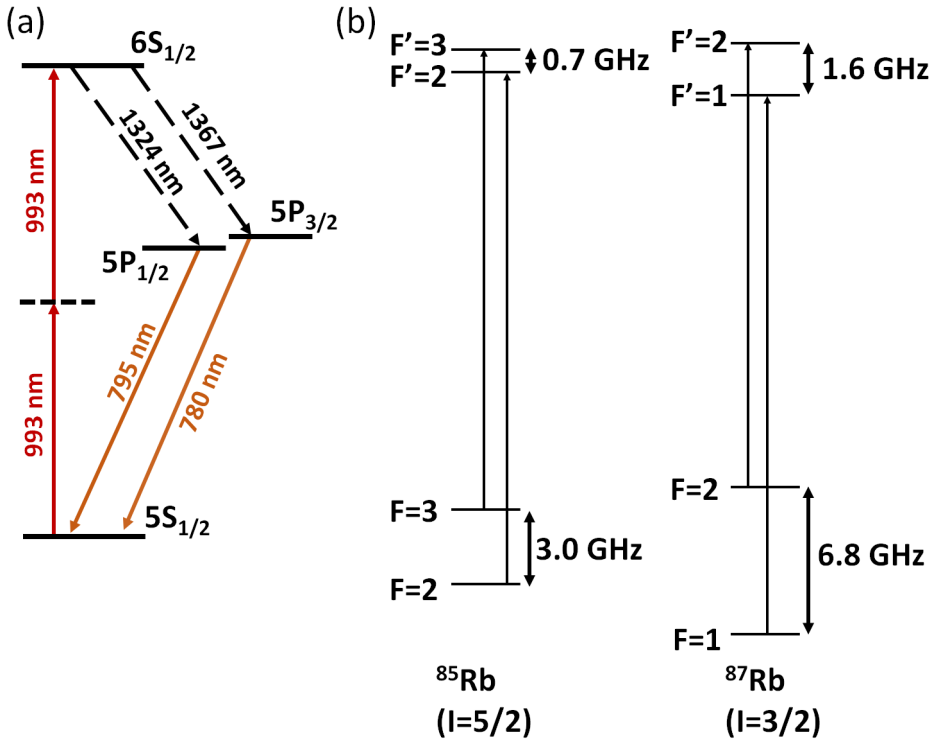

Figure 5.1: (a) Energy level diagram for Rb. A beam at 993 nm excites atoms from $5S_{1/2}$ to $6S_{1/2}$ via single-color, two-photon excitation. The intermediate virtual state is represented as a dashed line. The atoms decay back to $5S_{1/2}$ via $5P_{1/2}$ or $5P_{3/2}$, with photons emitted at 795 nm and 780 nm (orange arrows in the figure); (b) Hyperfine level diagrams for the two Rb isotopes. Two-photon transitions allowed by the selection rule, $\Delta F = 0$, $\Delta m_F = 0$, are shown, along with the frequencies of the hyperfine splittings.

5.2.2 Doppler-free spectroscopy

Two-photon spectroscopy in a counter-propagating configuration can yield a Doppler-free spectrum, which stems from the very nature of the two-photon process itself. In order to understand this feature, let us consider the case of a sample of two-level atoms in a gas. Each atom in the sample travels in space with a velocity $\mathbf{v} = (v_x, v_y, v_z)$. Two counter-propagating beams traveling along the $x-$direction with identical frequency, ω, are shone onto the sample and absorbed by the moving atoms. In the frame of reference of a single atom, the two beams are seen as Doppler-shifted in frequency such that [175]

$$\omega_{LB} = \omega\left(1 - \frac{v_x}{c}\right), \tag{5.1}$$

$$\omega_{RB} = \omega\left(1 + \frac{v_x}{c}\right), \tag{5.2}$$

where c denotes the speed of light in vacuum, and ω_{LB} and ω_{RB} are the frequencies of the beam as seen from the atom's perspective, for the left and right beams, respectively. The resonance condition to excite the atom from its ground state energy, E_g, to its excited state energy, E_e, is given by

$$E_e - E_g = \hbar(\omega_{LB} + \omega_{RB}) = \hbar\omega\left(1 - \frac{v_x}{c}\right) + \hbar\omega\left(1 + \frac{v_x}{c}\right), \tag{5.3}$$

which simplifies to

$$E_e - E_g = 2\hbar\omega. \tag{5.4}$$

This final expression is devoid of any velocity term. This implies that each atom in the sample interacting with the counter-propagating beams, and for which the resonance condition Eq. (5.4) is satisfied, contributes to the spectroscopic signal, regardless of its velocity. This contrasts with usual spectroscopy methods, such as saturated absorption spectroscopy, for example, since only atoms with velocity classes close to $v_x = 0$ contribute to the spectroscopic signal.

Due to the fact that the transition takes place between two S-levels (i.e., L = 0), conservation of the total angular momentum in the electric dipole-allowed, two-photon transitions imposes $\Delta F = 0$ and $\Delta m_F = 0$ [176]. On the one hand, these selection rules lead to a reduced number of allowed transitions, i.e., only two transitions per isotope: ^{87}Rb $F = 2 \leftrightarrow F' = 2$, ^{85}Rb $F = 3 \leftrightarrow F' = 3$, ^{85}Rb $F = 2 \leftrightarrow F' = 2$, and ^{87}Rb $F = 1 \leftrightarrow F' = 1$. On the other hand, this also restricts the possible combinations of polarizations for the laser beams which excite the transition, since the net angular momentum transfer to the atom has to be null. As we will see in Section 5.3.2, this may be used for the development of polarization tomography at the waist of an ONF.

The absorption probability of two photons from a single beam is equal to that of absorbing a single photon from each of the two counter-propagating beams [175]. This generally leads to a single-color, two-photon spectroscopic signal featuring an intense, narrow, and Doppler-free peak at resonance, superimposed on a Doppler-broadened baseline. However, for the particular case of S to S transitions, this baseline can be completely removed via appropriate choice of the polarizations of the counter-propagating beams. If the counter-propagating beams have orthogonal circular polarizations, absorption of two photons from a single beam is forbidden as the net angular momentum transfer to

the atomic state would be nonzero. Thus, one photon from each beam has to be absorbed, yielding a background-less, Doppler-free spectroscopic signal. The experimental verification of this claim is presented in Section 5.2.4.

5.2.3 Spectroscopy setup

The experimental setup is illustrated in Fig. 5.2. The experiment takes place in a glass cell filled with Rb in its natural isotopic abundances, maintained at a temperature of 130°C. The 993 nm beam used to drive the two-photon transition is provided by a continuous wave (CW) Ti:Sapphire laser (Coherent MBR 110), locked to a scanning reference cavity yielding a spectral linewidth of 100 kHz. The laser frequency can be scanned by changing the length of the reference cavity. The combination of a half-wave plate (HWP) and a polarizing beam-splitter (PBS) at the output of the laser allows us to control the powers in the reflected (R) and transmitted (T) beams from the PBS. Most of the optical power, typically >90%, is in T and passes through the vapor cell for the two-photon spectroscopy studies. The remaining light, in R, is fiber-coupled and further split so that 99% goes to a Fabry-Pérot cavity (Toptica FPI-100) and 1% to a wavemeter (HighFinesse WS-6). The wavemeter has two purposes; it allows us to tune the laser to the desired wavelength and to monitor the frequency scanning. The Fabry-Pérot cavity has a free-spectral range of 1 GHz and is used to monitor the linearity of the frequency scan.

An optical isolator is placed in front of the vapor cell to avoid reflections back into the laser. A plano-convex lens (L1), with focal length $f_1 = 150$ mm, is placed after the optical isolator to focus the beam in the cell. The $1/e^2$ beam diameter is measured to be 128 μm using a beam profiler (Thorlabs BC106VIS). A concave mirror (CM), with focal length $f_{CM} = 75$ mm, and placed $2f_{CM} = 150$ mm away from the focal plane of L1 ensures retro-reflection of the beam back to the focal point. Quarter-wave plates (QWP) can be inserted in the beam path before L1 and CM to generate a circularly polarized beam. We detect both the 795 nm and 780 nm decay photons using a photomultiplier tube (PMT) (Hamamatsu R636-10). A short-pass filter with a cut-off wavelength of 800 nm is placed in front of the PMT to prevent any scattered light from the 993 nm pump from being detected. We use a pair of lenses, L2 and L3, with focal lengths of $f_2 = f_3 = 50$ mm, in front of the PMT in a telescope configuration for efficient collection of the light. The quantum efficiencies of the PMT at 780 nm and 795 nm are 9% and 8%, respectively. The obtained current is amplified by a pre-amplifier with a gain of 10^5 and dropped across a 50 Ω resistor on an oscilloscope.

5.2.4 Results

A typical spectrum is shown in Fig. 5.3(a). Here, excitation to the $6S_{1/2}$ level is obtained by scanning the frequency of the 993 nm laser and using the same linear polarization for the forward and retro-reflected beams. Note that the simple setup presented here does not measure the absolute frequency of the transition. The hyperfine splitting of the $6S_{1/2}$ level is 717.54 Mhz for ^{85}Rb and 1615.32 MHz for ^{87}Rb, using a resonant intermediate level [177]. The relative frequency difference is obtained by setting the frequency of the first peak, i.e., the ^{87}Rb $5S_{1/2}, F = 2 \rightarrow 6S_{1/2}, F' = 2$ transition, to zero. A linear frequency scaling obtained by using fringe interpolation of the Fabry-Pérot peaks, which

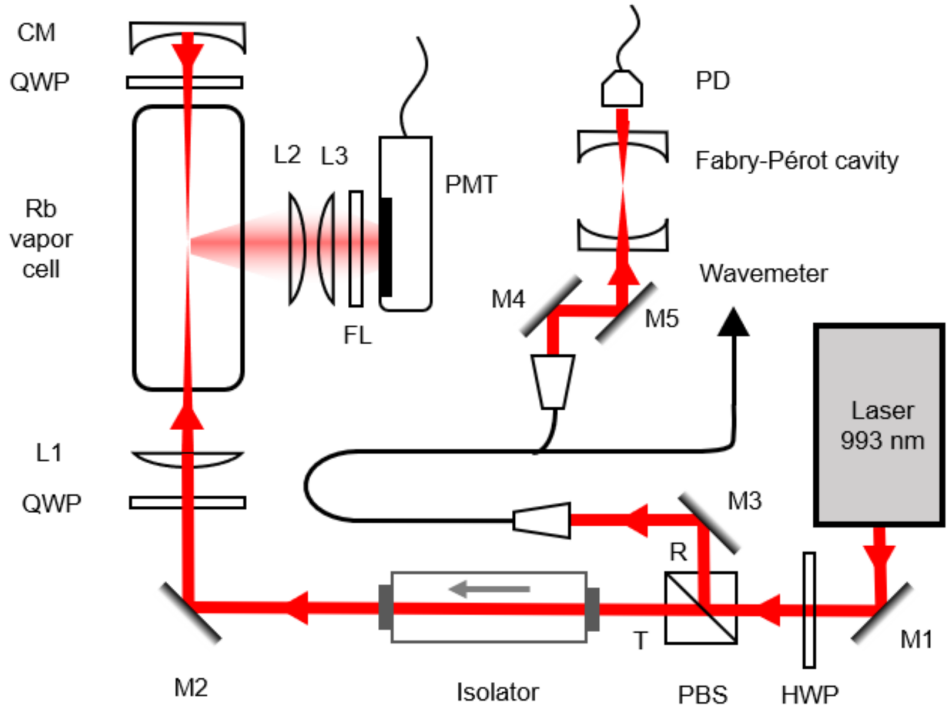

Figure 5.2: Schematic of the experimental setup. Light from a tunable 993 nm laser is used for two-photon excitation in a Rb vapor cell using a retro-reflected configuration. The resulting atomic fluorescence is detected by a PMT. The polarizations of the forward and retro-reflected beams are controlled using QWPs. A small amount (<10%) of the 993 nm beam is coupled to a Fabry-Pérot cavity and a wavemeter to monitor the laser frequency. M1-M5: Mirrors, L1-L3 Plano-convex lens, HWP: Half-wave plate, QWP: Quarter-wave plate, PBS: Polarizing beam-splitter, CM: Concave mirror, PMT: Photomultiplier tube, FL: Short-pass optical filter, PD: Photodiode.

are 1 GHz apart, yields a similar result. Due to the two-photon process, the relative frequency differences of the peaks are half the actual energy differences of the atomic levels.

Power variation

The relative height and width of each peak in Fig. 5.3(a) is shown in Fig. 5.3(b). For a particular Rb isotope, the intensities of the transitions from the ground hyperfine levels are proportional to the statistical weights of the atomic population in those hyperfine levels [178]. However, since the difference in energy between the hyperfine levels is negligible compared to the transition energy, the weight factor is equivalent to the degeneracy $(2F + 1)$ of the hyperfine levels. These values are $5 : 3$ and $7 : 5$ for ^{87}Rb and ^{85}Rb, respectively. The variation of peak height as a function of the square of the laser power is shown in Fig. 5.3(c). The peak heights show a quadratic dependence on the total beam power, P (i.e., the sum of the powers in the forward and retro-reflected beams); this is a signature of the two-photon process [179]. The ratios of the slopes of the fitted straight lines are 1.667 for ^{87}Rb and 1.387 for ^{85}Rb, i.e., close to the expected ratios of $5 : 3$ and $7 : 5$, respectively. The width of the peaks does not change as a function of power, at least within the standard deviation of the measurements. We measure a Lorentzian full-width-at-half-maximum (FWHM) of 2.60 ± 0.07 MHz, 2.44 ± 0.09 MHz, 2.49 ± 0.04 MHz and 2.43 ± 0.04 MHz for the ^{87}Rb $F = 2 - F' = 2$,^{87}Rb $F = 1 - F' = 1$, ^{85}Rb $F = 3 - F' = 3$ and ^{85}Rb $F = 2 - F' = 2$ peaks, respectively.

Laser frequency stabilization to spectroscopic peaks

To establish the viability of the transition as a frequency reference, we demonstrate frequency locking of the pump laser to the spectroscopic peaks. This is implemented by integrating a TEM LaseLock® module with the Ti:Sapphire laser. First, the reference cavity is bypassed and the laser frequency is scanned by directly varying its cavity length. A 10 kHz modulation is applied to one of the piezo-driven mirrors to generate frequency sidebands. The modulated spectroscopic signal is fed into a lock-in amplifier and an error signal is generated. An example of a modulated signal and a derived error signal are shown in Fig. 5.3(d). The laser cavity and, hence, the frequency can be stabilized to each of these error signals.

Polarization variation

We next explore the effect of changing the polarization of the counter-propagating beams on the spectroscopic signal. As shown in Fig. 5.2, a quarter-wave plate at either end of the vapor cell can be used to generate identical, or orthogonal, circularly polarized forward and retro-reflected beams. Let us denote linear and circular polarizations as π and σ, respectively, and their orthogonal polarizations as π' and σ', respectively. As mentioned, the two-photon transition selection rules between the S levels are $\Delta F = 0$ and $\Delta m_F = 0$, hence the total angular momentum of two photons absorbed by an atom during the excitation process must be zero.

First we study the case of linear polarizations. By blocking the retro-reflected beam, a π configuration is created, see Fig. 5.4(a). We observe a Doppler-broadened signal since

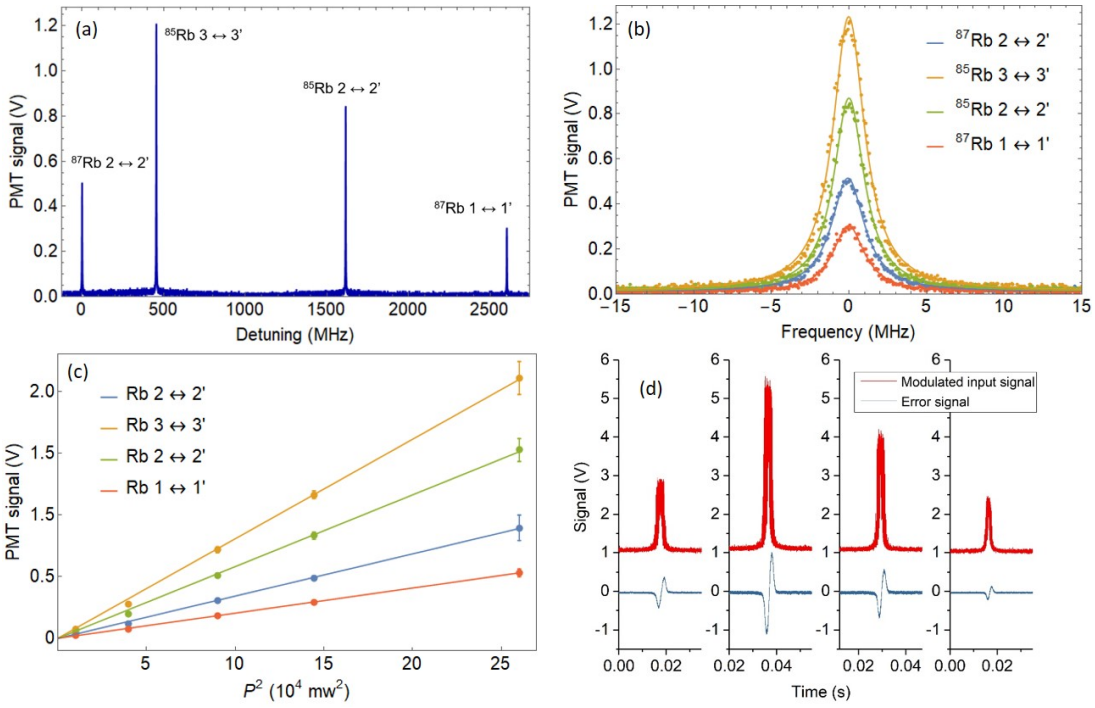

Figure 5.3: (a) Typical spectroscopic signal obtained by scanning the frequency of the 993 nm pump beam and recording the signal on the PMT. Each peak indicates a hyperfine transition as labeled. (b) Comparison of the individual peak intensities and linewidths from (a). (c) Linear dependence of the peak height as a function of the total pump power, P, squared. (d) Modulated signals and the generated error signals for each peak to which the laser can be locked. For clarity, a 1 V offset is added to the modulated signal.

both photons are derived from the forward beam. Next, by introducing a retro-reflected beam, a $\pi - \pi$ configuration is created, see Fig. 5.4(b). Here, we obtain a narrow, Doppler-free spectrum on top of a small Doppler-broadened baseline. The Doppler-free spectrum arises when the two photons are absorbed from counter-propagating beams, whereas the Doppler-broadened signal results from the two photons being absorbed from the same (forward or retro-reflected) beam. Next, the addition of a QWP after the vapor cell, aligned at 45° with respect to the forward beam's polarization axis, creates a retro-reflected beam, with orthogonal linear polarization to the forward beam, resulting in a $\pi - \pi'$ configuration, see Fig. 5.4(c). The two photons can only be absorbed from either the forward or the retro-reflected beam, i.e., they cannot be absorbed simultaneously from both beams. The signal on the PMT results in the sum of two Doppler-broadened spectra, one from each beam, yielding double the amplitude of the π configuration. One can note an increase in the noise level between Figs. 5.4(a) and (c). This is likely attributed to the PMT being positioned such that it collects more scattered photons from the retro-reflected beam than from the forward beam. Note that a similar observation can also be made when comparing the next two figures (i.e., Figs. 5.4(d) and (e)).

We next move to the case where the beams have circular polarizations. By inserting a QWP at 45° before the vapor cell and blocking the retro-reflected beam, a σ configuration is created, see Fig. 5.4(d). In this case, the transition is forbidden (the sum of the angular momenta of two photons in the forward beam is non-zero), hence there is no signal recorded on the PMT. The $\sigma - \sigma$ configuration is created by allowing the retro-reflected beam to propagate inside the vapor cell, see Fig. 5.4(e). This transition is also forbidden as, once more, the sum of the angular momenta of the two photons from the counter-propagating beams ($2\hbar$) is non-zero. However, due to experimental imperfections, a weak signal can be observed. This is likely explained by the fact that the QWP's retardance is not exactly 0.25 at 993 nm (it is designed for 980 nm) and because the incident beams' polarizations can be slightly elliptical if they do not enter the vapor cell orthogonally. Finally, inserting a QWP before the retro-reflecting mirror forms a $\sigma - \sigma'$ configuration. The orientation of the waveplate's axis is irrelevant. The two photons that drive the transition can only be absorbed from the counter-propagating beams. As a result, a background-less, Doppler-free spectrum is obtained, shown in Fig. 5.4(f). The peak heights are half those obtained for the $\pi - \pi$ configuration as the probability to absorb two-photons with opposite spin angular momentum is less in this case. For completeness, we show in Fig. 5.4(g) that the other orthogonal circular polarization configuration yields a similar result.

5.2.5 Discussion

Ab-initio calculations of the electronic wavefunction close to the nucleus rely on an accurate measurement of the hyperfine splitting of the atomic energy level [180]. To date, the $6S_{1/2}$ level in Rb has been accessed via a two-color, two-photon excitation scheme at 795 nm and 1324 nm for measuring its lifetime [177] and hyperfine splitting [181]. Accessing the $6S_{1/2}$ level via the one-color, two-photon method presented here should enhance the accuracy and precision of such measurements since only a single laser is necessary for the excitation. Additionally, the two-photon transition could be used for the measurement of parity nonconservation [182, 183] in alkali atoms.

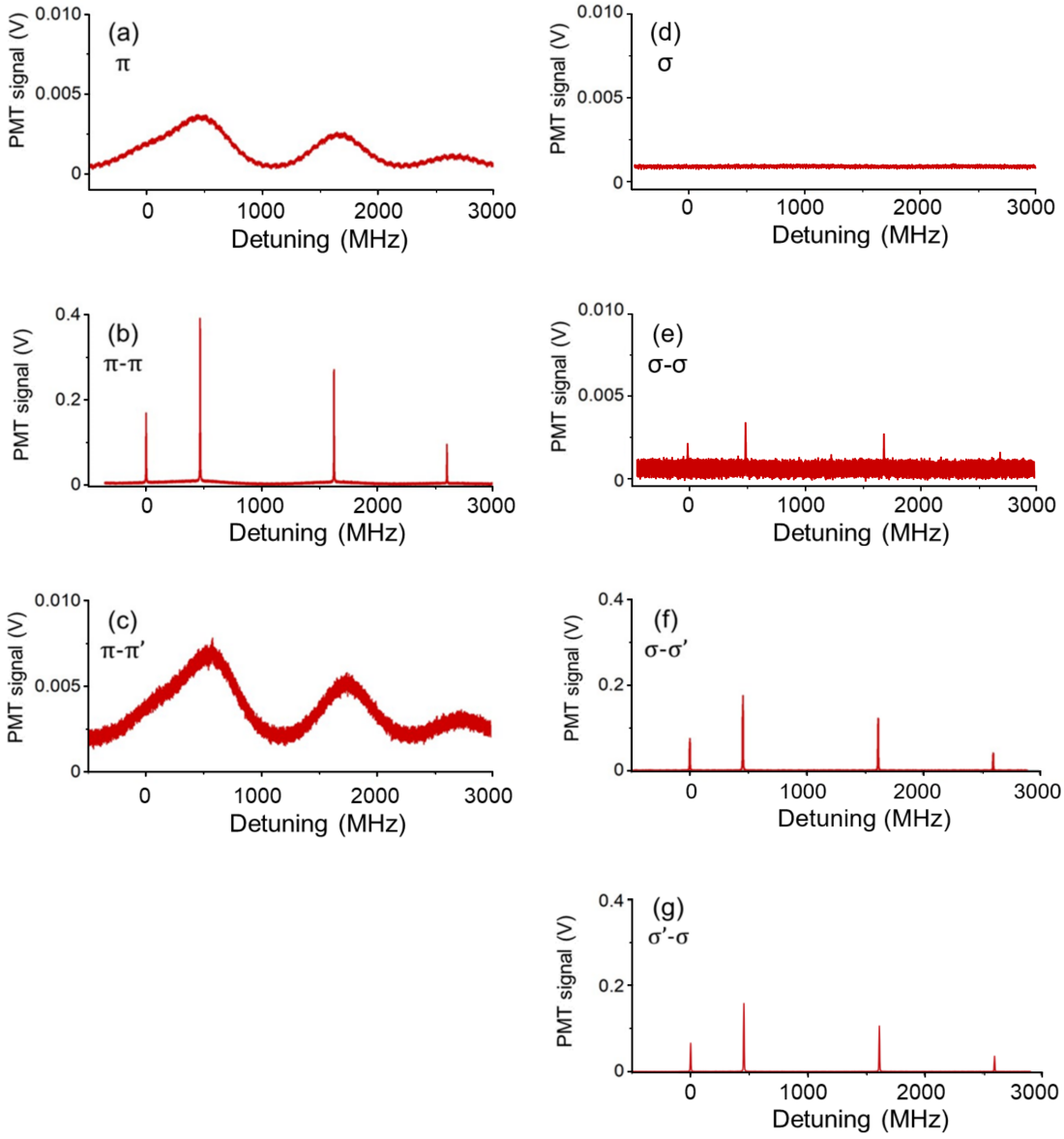

Figure 5.4: Effect of beam polarization on the two-photon excitation as recorded by the PMT. As in Fig. 5.3(a), the relative frequency is obtained by setting the frequency of the $5S_{1/2}, F = 2$ - $6S_{1/2}, F' = 2$ peak to zero. The power of the 993 nm beam is fixed at 250 mW and its frequency is scanned. The polarization of the beam is changed using QWPs. (a) Doppler-broadened spectrum with a single, linearly polarized beam. (b) Linearly polarized counter-propagating beams reveal the Doppler-free peaks and a small Doppler-broadened base. (c) Counter-propagating beams with orthogonal linear polarizations yield a Doppler-broadened spectrum of twice the amplitude of that in (a). (d) A single, circularly polarized beam does not yield a signal. This configuration is forbidden, according to the selection rules. (e) Due to experimental imperfections, counter-propagating beams with identical circular polarizations yield a signal with intensity comparable to that of the noise. This transition is forbidden for the same reason as in (d). (f) Counter-propagating beams with orthogonal circular polarizations yield a background-less Doppler-free spectrum. Here, the total angular momentum for the transition is zero. (g) Same polarization combination as in (f) but inverted, showing a similar signal.

The excitation scheme presented herein enables the conversion of two near-infrared photons at 993 nm into a telecommunication O-band photon, at either 1324 nm or 1367 nm, and another near-infrared photon, at 795 nm or 780 nm, respectively. Chanelière *et al.* [174] proposed a method for building quantum repeaters using cascaded atomic transitions, whereas Willis *et al.* [184] generated time-correlated photon-pairs between a near-infrared photon and an O-band photon using a four-wave mixing (4WM) process in a Rb vapor. The 4WM scheme made use of the $6S_{1/2}$ level, accessed via a two-color, two-photon excitation. Our scheme is compatible with these results, as driving the $5S_{1/2}$ to $6S_{1/2}$ two-photon transition would permit us to exploit both O-band photons as signal photons, and the corresponding NIR photons as idlers mapped onto an atomic quantum memory. In particular, the 993 nm photons could be coupled to atoms interacting with the evanescent field at the waist of an optical nanofiber embedded in a cold atomic ensemble [1] to make the process more efficient [185].

The first order Zeeman shifts experienced by the same hyperfine states of the $5S_{1/2}$ and $6S_{1/2}$ levels are identical since they have the same hyperfine Landé g-factors. This feature renders the frequency of the $5S_{1/2}$ to $6S_{1/2}$ transition insensitive to stray magnetic fields. The transition frequency is also less sensitive to electric fields compared to transitions to nonzero angular momentum states (where $l > 0$). These features make the transition an attractive choice for a frequency reference.

5.3 Nanofiber-Mediated Two-Photon Excitation in Cold Atoms

After successfully establishing a spectroscopy setup on which the 993 nm beam could be locked, we decided to proceed with the cold atom experiment. Approximately 20 mW of power are taken directly from the output of the Ti:Sapphire laser and coupled to a single-mode patch cable at 993 nm (Thorlabs SM980-5.8-125) to deliver light to the cold atom setup, while the rest is used in the spectroscopy setup. The beam at the output of the patch cable is further divided into two paths, sending one half of the power towards either end of an ONF embedded in a MOT. The cold atom experimental setup is identical to that described in Chapter 3, except for the ONF itself, which was fabricated using an exponential taper. In addition, the diameter at the waist of this ONF is 400 nm, making it single-mode for 780 nm. Both pigtails of the ONF are spliced to patch-cables (Thorlabs SM 800-125), which are single-mode at all the wavelengths used.

A schematic of the relevant components in the experiment is given in Fig. 5.5. The excitation scheme and energy levels are identical to those in Fig. 5.1. Any photon emitted by atoms decaying back to their ground state can couple to the guided modes of the ONF, irrespective of the decay channel chosen, and are detected by single photon counting modules (SPCM) (Excelitas, SPCM-AQRH-FC) after the patch-cable. By contrast with the vapor experiment, in which we detected both the 780 nm and 795 nm photons simultaneously, here we detect 795 nm and 780 nm photons separately, at either end of the ONF. Experimental data are analyzed based on signals collected from photons at 795 nm, whereas signals at 780 nm are used for completeness and to confirm the two-photon excitation. This choice is motivated by two main practical factors, namely, (i) the $6S_{1/2} \rightarrow 5P_{1/2}$ decay channel has a higher occurrence probability compared with the

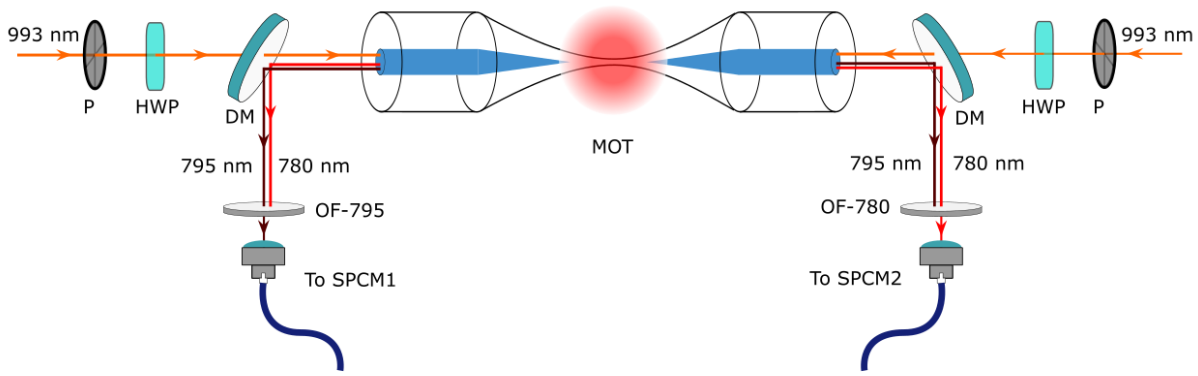

Figure 5.5: Schematic of the experimental setup used for the cold atom experiments. Two counter-propagating beams at 993 nm are injected into either end of an ONF whose waist is embedded in a MOT. Fluorescent photons at 780 nm and 795 nm couple to the guided modes of the fiber and are detected at both outputs of the ONF by two SPCMs. P: Linear polarizer, HWP: Half-wave plate, DM: Dichroic mirror, SPCM: Single photon counting module, OF: Optical bandpass filter.

$6S_{1/2} \rightarrow 5P_{3/2}$ channel, resulting in a larger number of detectable photons, and (ii) this wavelength can be isolated from the fluorescent photons at 780 nm emitted by the MOT. On one end of the patch-cable, a dichroic mirror (DM) (Thorlabs DMLP900) transmits the 993 nm seed light which is injected into the ONF, and reflects 780 nm and 795 nm photons towards a fiber coupler connected to an SPCM. A similar optical setup is used on the other side of the patch-cable. The polarization of the 993 nm beam is kept linear and is adjusted by rotation of a linear polarizer (P) and a half-wave plate (HWP) through which the beam is passed prior to its injection into the patch-cable. We choose to work with linear polarization as this maximizes the chances of driving the two-photon transition and, thus, leads to a better signal (see Fig. 5.4 for the polarization analysis in a vapor). Narrow-band filters (Alluxa 794.9-1 OD4, and Thorlabs FB780-10) placed in front of the fiber-couplers selectively allow one of the wavelengths of interest to be transmitted to the SPCM. Here, we label SPCM1 the detector for 795 nm photons and SPCM2 the detector for 780 nm photons.

After loading and overlapping a MOT of ^{87}Rb atoms with the waist of the ONF, we scan the frequency of the 993 nm laser in a $\pm$100 MHz range around resonance with the ^{87}Rb $F = 2 \leftrightarrow F' = 2$ transition, over the course of 1 s. The atomic population in the MOT cycles mainly between the $5S_{1/2}$ $(F = 2)$ and $5P_{3/2}$ $(F' = 3)$ levels, leaving the $5S_{1/2}$ $(F = 1)$ ground state largely depleted of its population. Consequently, a two-photon excitation between the $5S_{1/2}$ $(F = 1)$ and $6S_{1/2}$ $(F' = 1)$ levels leads to a weak signal which we are unable to detect in our experiments. The results reported here are obtained by driving the $5S_{1/2}$ $(F = 2) \rightarrow 6S_{1/2}$ $(F' = 2)$ two-photon transition.

In Fig. 5.6, we show a typical set of signals observed when scanning the 993 nm laser frequency. The input power in each beam is 400 μW, and each signal results from an average of data collected over 20 scans. Signals at 795 nm and 780 nm are detected by SPCM1 and SPCM2, respectively, with a gate time of 10 ms. The vapor cell spectroscopic signal is simultaneously recorded as a reference. Detection of a peak close to resonance

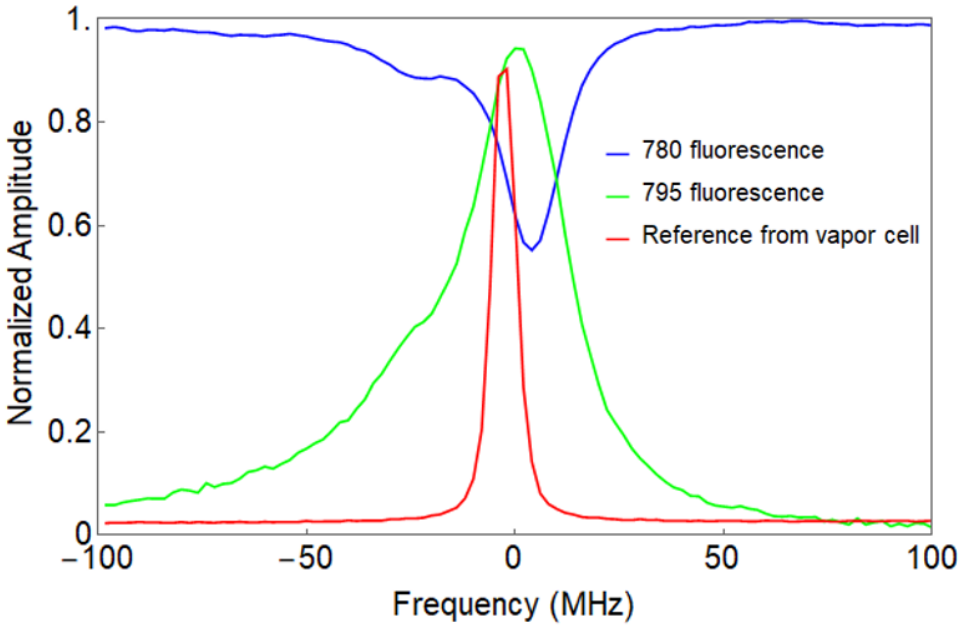

Figure 5.6: Evidence of ONF-mediated, two-photon excitation in cold atoms. The seed laser at 993 nm is scanned in frequency and launched into the ONF with 400 μW of power in each beam. Data are normalized to the baseline of the 780 nm signal.

at 795 nm indicates that the two-photon transition was successfully mediated by the evanescent field at the ONF waist. This is further confirmed by the dip in the 780 nm signal, occurring at the same frequency as the 795 nm peak. This dip likely results from a transfer of atomic population from the MOT cooling-cycle to the two-photon transition. Both peaks are frequency-shifted compared to the vapor cell signal. This shift has been observed in other experiments involving nanofibers embedded in cold atom clouds and can be attributed to either van der Waals interactions between atoms and the ONF surface [3, 186], or light-shifts induced by the intense field of the 993 nm beams at the nanofiber waist [6, 64].

5.3.1 Evidence of strong-coupling

Using the setup described above, we studied the influence of the 993 nm beam power on the single-color, two-photon transition, see Fig. 5.7 (a). Individual plots show the fluorescence signal at 795 nm detected by SPCM1 as a function of the frequency detuning from resonance with the $5S_{1/2}$ $(F = 2) \rightarrow 6S_{1/2}$ $(F' = 2)$ transition, for a given power of a single 993 nm beam. For powers between 0.2 to 0.8 mW per beam (i.e., 0.4 to 1.6 mW of total power), the signal broadens with increasing power. Beyond this range of power, two peaks can be distinguished, their separation increasing with the power. This splitting is a likely signature of strong-coupling[2] between the guided-modes of the ONF and atoms surrounding it. Our group previously demonstrated Autler-Townes splitting in cold atoms

[2]Interaction between an atom and a field is said to take place in the strong-coupling regime when the atom-field coupling, characterized by the Rabi frequency, Ω, is much larger than the excited state decay rate, Γ, i.e., $\Omega \gg \Gamma$.

surrounding an ONF [11], but a third level had to be used in a ladder excitation scheme to probe the splitting of the intermediate level. To the best of our knowledge, this is the first time strong-coupling is experimentally observed in a two-level system. Further evidence of the occurrence of strong-coupling in our system can be concluded from Fig. 5.7 (b), where we plot the peak separation as a function of the power per pump beam, P_{pump}. The peak splitting is found to be linearly dependent on P_{pump}. This contrasts with the usual square-root signature of a strong-coupling regime in single-photon transitions, but is consistent with a single-color, two-photon excitation. This phenomenon has already been highlighted in Fig. 5.3 when we plotted the peak height as a function of the pump beam power squared in the vapor experiment to see the linear relationship. A full picture of the physics behind our observations has yet to be developed before drawing any definite conclusion. We are currently developing a theoretical model of the system under consideration, which will help us determine the specific nature of the strong-coupling behavior (e.g. Autler-Townes splitting, Mollow triplet, ...).

5.3.2 Polarization tomography at the ONF waist

Polarization at the waist of a tapered fiber is a valuable, yet difficult to access, piece of information for the design of ONF-atom interfaces. In most experiments involving ONFs and cold atoms, the polarization at the waist is either adjusted by direct imaging of the waist via Rayleigh scattering [7, 14], or simply by modifying the polarization of the input beam until the interaction between the evanescent field and the cold atoms is deemed optimal [64]. Taking advantage of the polarization restrictions imposed on the pump beams by the two-photon selection rules between two S-levels, we decided to test the capability of atoms to act as probes of the polarization at the waist. As the ONF used here supports only the fundamental mode, probing the polarization at the waist using atoms provides a good test-bed before moving to more complex experiments involving the HOMs.

We slightly modify the experimental setup in Section 5.3 (see Fig. 5.5) in order to control the input beam polarization and measure the polarization state of both the input and output beams. A schematic of the modified experimental setup is provided in Fig. 5.8. The two-photon transition is driven by a single beam at 993 nm, passed through a QWP, allowing us to modify its polarization state continuously from linear to circular polarization. The beam is then launched into the ONF, the waist of which can be overlapped with the MOT as desired. At the output pigtail, the 993 nm beam is transmitted through a DM and its polarization state characterized by a polarization analyzer (Schäfter + Kirchhoff SK010PA). The isotropic nature of the fluorescence at 795 nm allows us to collect these photons from either side of the ONF and we choose SPCM1.

We want to study the change in the polarization of light, whether guided by the ONF or propagating in free-space. A convenient way to describe a light beam's polarization is using the Stokes vectors, $\boldsymbol{S} = (S_0, S_1, S_2, S_3)$. For a monochromatic plane-wave with electric field, $\boldsymbol{E}(\boldsymbol{x}, t)$, described as $\boldsymbol{E}(\boldsymbol{x}, t) = (\boldsymbol{\varepsilon_1} E_1 + \boldsymbol{\varepsilon_2} E_2) e^{i(\boldsymbol{k}.\boldsymbol{x} - \omega t)}$, where the $\boldsymbol{\varepsilon}_i$ are orthogonal unit vectors in the cartesian frame of reference, $E_1 = a_1 e^{i\delta_1}$ and $E_2 = a_2 e^{i\delta_2}$,

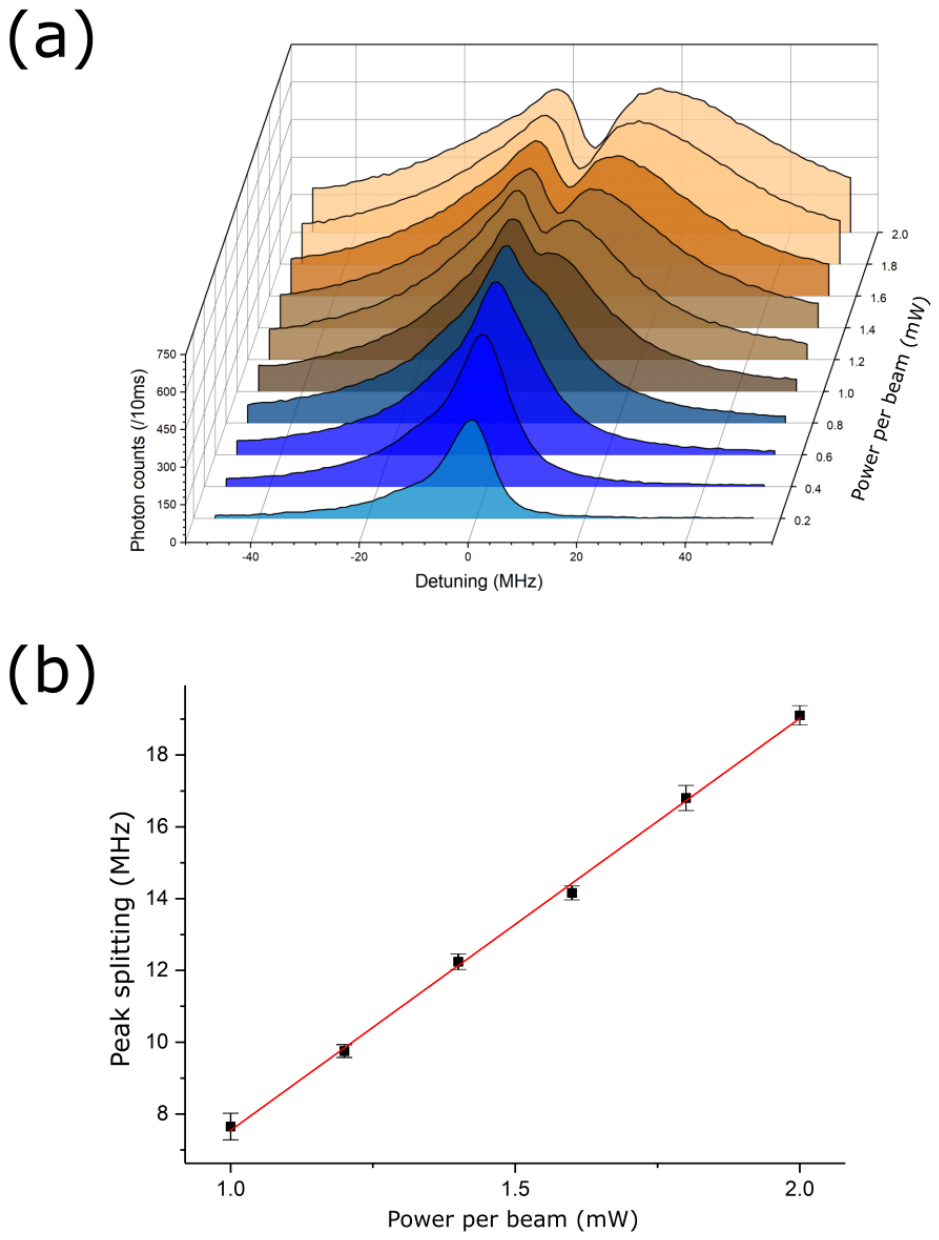

Figure 5.7: Experimental observation of strong-coupling. (a) Cascaded plot showing the increase in splitting of the $6S_{1/2}$ ($F' = 2$) level as the power per 993 nm beam is increased. Each signal is observed through collection of fluorescent photons at 795 nm when the frequency of the 993 nm beam is scanned around resonance. (b) Linear dependence of the separation between the split peaks on the power per beam. The red line represents a linear fit. Data obtained for powers below 1 mW per beam do not show any peak splitting.

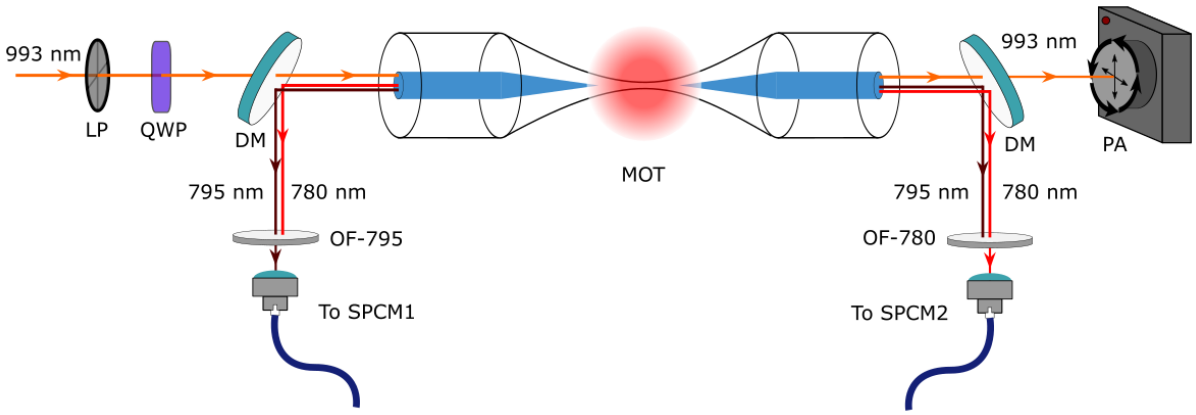

Figure 5.8: Modified experimental setup used in the polarization tomography experiment. Here, a single beam at 993 nm is launched into the ONF after passing through a quarter-wave plate (QWP) that allows us to continuously vary the polarization of the input beam from linear to circular. A polarization analyzer (PA) can either be placed in front of the input beam or in front of the output beams in order to measure the Stokes components.

the components of the Stokes vectors are defined as follows [155]:

$$\begin{aligned} S_0 &= |\boldsymbol{\varepsilon_1}.\boldsymbol{E}|^2 + |\boldsymbol{\varepsilon_2}.\boldsymbol{E}|^2 &&= a_1^2 + a_2^2, \\ S_1 &= |\boldsymbol{\varepsilon_1}.\boldsymbol{E}|^2 - |\boldsymbol{\varepsilon_2}.\boldsymbol{E}|^2 &&= a_1^2 - a_2^2, \\ S_2 &= 2\,\mathrm{Re}[(\boldsymbol{\varepsilon_1}.\boldsymbol{E})^*(\boldsymbol{\varepsilon_2}.\boldsymbol{E})] &&= 2a_1a_2\cos(\delta_2 - \delta_1), \\ S_3 &= 2\,\mathrm{Im}[(\boldsymbol{\varepsilon_1}.\boldsymbol{E})^*(\boldsymbol{\varepsilon_2}.\boldsymbol{E})] &&= 2a_1a_2\sin(\delta_2 - \delta_1). \end{aligned} \tag{5.5}$$

The S_0 component gives the intensity of the field, S_1 indicates the degree of linear polarization, i.e., whether the field has a horizontal ($S_1 > 0$) or a vertical ($S_1 < 0$) linear polarization component, while S_2 and S_3 give information about the relative phases of the field along the directions $\boldsymbol{\varepsilon_1}$ and $\boldsymbol{\varepsilon_2}$. After normalizing $\boldsymbol{S}$ to S_0, the other three components can be used to define a point on the surface of a unit sphere, called the Poincaré sphere, whose axes are formed by $(\boldsymbol{S_1}, \boldsymbol{S_2}, \boldsymbol{S_3})$. Specific polarization states can be distinguished on this sphere. We have $H = (1, 1, 0, 0)$, $V = (1, -1, 0, 0)$, $D = (1, 0, 1, 0)$, $A = (1, 0, -1, 0)$, $R = (1, 0, 0, 1)$, $L = (1, 0, 0, -1)$, respectively denoting linear-horizontal, linear-vertical, linear-diagonal, linear-antidiagonal, circular-right, and circular-left polarization.

As schematized in Fig. 5.9(a), light traveling through the ONF undergoes a transformation, $\mathrm{T_{tot}}$. This transformation is the result of a combination of two other transformations; one between the input of the ONF and its waist, $\mathrm{T_1}$, and one between the waist and the output of the ONF, $\mathrm{T_2}$. These transformations can be expressed as matrices using the Mueller-formalism [187], and we can write the relations

$$\boldsymbol{S_{waist}} = \mathrm{T_1}\boldsymbol{S_{in}} \tag{5.6}$$

$$\boldsymbol{S_{out}} = \mathrm{T_2}\boldsymbol{S_{waist}} \tag{5.7}$$

$$\boldsymbol{S_{out}} = \mathrm{T_2T_1}\boldsymbol{S_{in}} = \mathrm{T_{tot}}\boldsymbol{S_{in}} \tag{5.8}$$

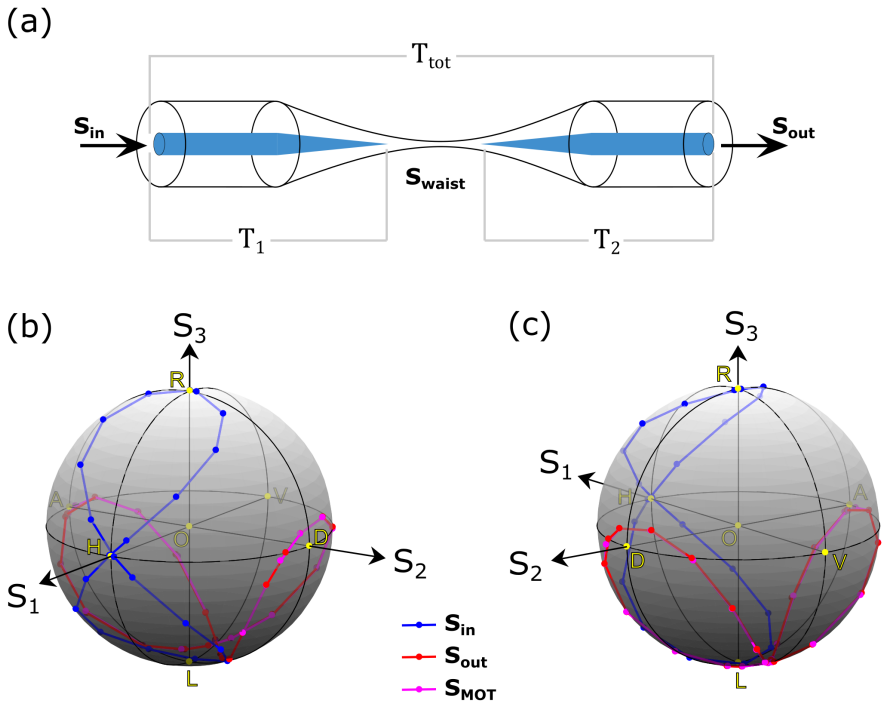

Figure 5.9: Characterization of the ONF-induced transformation of the input light's Stokes components. (a) System under consideration and associated transformations. The input light can be characterized by a Stokes vector, $\mathbf{S_{in}}$, which undergoes two transformations, T_1 and T_2, while traveling from the ONF input to the waist and from the waist to the output, respectively. We label the Stokes vectors at the waist and output of the ONF $\boldsymbol{S}_{\mathbf{waist}}$ and $\boldsymbol{S}_{\mathbf{out}}$, respectively. The combination of T_1 and T_2 form the overall transformation T_{tot}. (b) Experimental data obtained by measuring the Stokes components of the input, $\mathbf{S_{in}}$, and output beams, $\mathbf{S_{out}}$, represented on the Poincaré sphere. The vector $\mathbf{S_{MOT}}$ denotes data obtained from measuring $\mathbf{S_{out}}$ while the MOT was overlapping the ONF waist. (c) Same as (b) but with principal axes S_1 and S_2 rotated by 90° around the S_3 axis for clarity.

We measure the Stokes components of the 993 nm input beam, both before and after launching it into the ONF. The polarization of the input beam is incrementally changed from linear to circular by rotation of the QWP in front of the ONF. The data for 22 orientations of the QWP are presented in Fig. 5.9(b) and Fig. 5.9(c) for polarization measurements at the input ($\boldsymbol{S}_{\mathbf{in}}$) and the output ($\boldsymbol{S}_{\mathbf{out}}$) with no atoms around the waist. It appears that the overall transformation, T_{tot}, has as effect a rotation of the input beam trajectory on the Poincaré sphere twice, with respect to two different axes. We additionally evaluate the influence of the MOT atoms on the overall polarization state transformation. For this, we repeat the measurements for $\boldsymbol{S}_{\mathbf{out}}$ while overlapping the MOT with the ONF waist. This corresponds to the magenta trajectory in Fig. 5.9(b) and Fig. 5.9(c), labeled $\boldsymbol{S}_{\mathbf{MOT}}$, which does not seem to deviate much from the measured trajectory of $\boldsymbol{S}_{\mathbf{out}}$. We thus conclude that atoms in the MOT have no significant effect on the change of polarization observed between $\boldsymbol{S}_{\mathbf{in}}$ and $\boldsymbol{S}_{\mathbf{out}}$.

We now need to evaluate $\boldsymbol{S}_{\mathbf{waist}}$ by overlapping the cold atoms with the waist of

the ONF and measuring the evolution of the absorption at 993 nm for different input polarization states. The emission of 795 nm photons should be directly proportional to the absorption of the 993 nm pump beam. In the ideal case of pure circular polarization, the pump beam cannot drive the two-photon transition, yielding no emission at 795 nm (i.e., no absorption at 993 nm, see Section 5.2.4 for details). In contrast, for the ideal case of pure linear polarization, a maximum emission at 795 nm (i.e., maximum absorption at 993 nm) should be observed. Due to the presence of a nonzero longitudinal component of the electric field in an ONF [93, 95], we do not expect to observe zero absorption, regardless of the QWP angle chosen. However, a minimum absorption should indicate that the polarization state at the waist is close to circular polarization in the transverse plane of the ONF[3].

We present the polarization tomography results in Fig. 5.10. The 22 measured Stokes vectors, presented in two groups of 11, are plotted in terms of their horizontal and vertical electric field components, E_x and E_y, respectively, for both the input and output beams (see Fig. 5.9). This representation helps to clearly visualize the ellipticity, orientation, and helicity of the measured beams. The first row for both groups of data shows the evolution of the polarization state of the input beam as the QWP is rotated from 0° to 180°. The direction of the arrow indicates the direction of rotation of the polarization vector, namely denoting left-handed polarization for a counter-clockwise rotation, and right-handed polarization for a clockwise rotation. The second row displays a series of bar charts representing the amplitude of the 795 nm fluorescence signal detected at SPCM1 for each polarization state of the input beam presented in the first row. Finally, the third row presents data for the output beam in a similar fashion to that of the first row.

The evolution of the peak height appears consistent with the changes made to the input beam polarization, though our input beam polarization control is not optimized. We note that the 795 nm emission is maximal when the input beam is linearly polarized and minimal when the input beam is close to circular polarization. However, the difference between these extremum should be more pronounced. While the peak height is never observed to be null, the relation between the input beam polarization and the observed emission signal has similarities with what was observed in the free-space experiment described in Section 5.2.4. In contrast, the output beam polarization appears to be almost always opposite to what would be expected from observing the 795 nm emission. Our results suggest that a large asymmetry exists between the two transformations T_1 and T_2, and that the effect of T_1 on the final polarization state is much weaker compared to that of T_2. Note that this is completely opposite to what our research unit has observed for nanofibers in air, where the down taper affects the polarization of the mode far more significantly than the up taper [116, 188], a phenomenon that was observed for numerous different fibers. Here, we are limited to a single ONF within the UHV system and it is likely that the feed-throughs have imposed a strain on the fiber causing this effect. This should be investigated further by combining the crossed-fiber polarization detection method with a fiber that passes through ferrules and Swagelock© to see if they affect the polarization changes. With only the single fiber at our disposal, an extensive description of the system is not possible. We will repeat this experiment in the future, using a HWP

[3]In fact, many laboratories report non-constant polarization along the entire length of the nanofiber. Here, we are effectively integrating along the interaction region to get an "average" polarization.

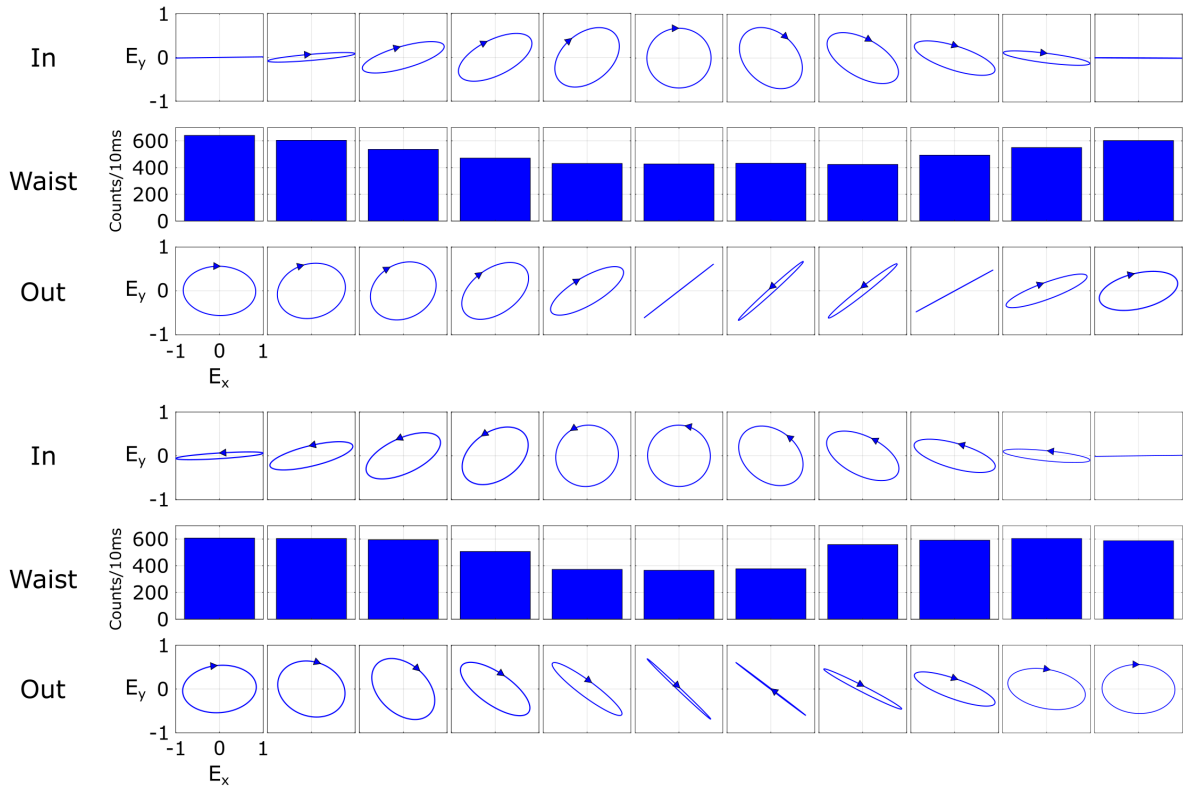

Figure 5.10: Polarization tomography results. The QWP is rotated from 0° to 180° over 22 steps. The results are presented in two groups of 11 for clarity. For each group, the first row shows the evolution of the input beam polarization state in terms of E_x and E_y, the second row shows the magnitude of the fluorescent peak at 795 nm collected at SPCM1 for a gate time of 10 ms, and the third row presents data similarly to the first row, but for the output beam.

in addition to the QWP in order to fully probe the Poincaré sphere, and thus completely characterize the system. This should allow us to find if local extrema exist for specific input polarization states, and establish a clear correlation between the input and waist, and between the waist and output. Accurate evaluation of the Mueller matrices associated with each transformation should then become possible.

5.4 Conclusion

We have demonstrated the $5S_{1/2} \rightarrow 6S_{1/2}$ one-color, two-photon transition in a hot Rb vapor at 993 nm. The effects of excitation laser power and beam polarization on the observed spectroscopy signals were investigated. The transition could be used as a reference at 993 nm as we have demonstrated frequency stabilization of the excitation laser to the spectroscopic peaks. The simple optical setup is easy to miniaturize and can be readily integrated into more complex experiments. The transition frequency is insensitive to stray magnetic fields and is, therefore, suitable for precision measurements and experimental setups where magnetic fields cannot be completely eliminated, e.g. in a MOT or a magnetically trapped Bose-Einstein condensate.

Driving the two-photon excitation using the evanescent field of a fundamental-mode ONF embedded in a cold atomic cloud led to evidence of strong-coupling between the atoms and guided modes of the ONF. A full theoretical description of the system is currently being developed in collaboration with Prof. J. Mompart (Universitat Autònoma de Barcelona) and should allow us to discover the nature of the strong-coupling effect reported.

Finally, we have exploited the selection rules associated with a two-photon transition between two S levels in order to evaluate the polarization state at the waist of the ONF. We have demonstrated that, even with a relatively small number of measurements, a link between input polarization state and polarization at the waist can be established. This method is of particular interest for improving ONF-based atom-trapping techniques, which have yet to be demonstrated for quasi-circularly polarized light. The 993 nm light could provide polarization calibration before being detuned by a few nm to create the red-detuned trapping beams required in a two-color ONF-based trapping scheme. Our technique relies solely on atoms trapped in a MOT and does not require extra imaging elements as is the case for Rayleigh scattering [7, 14, 32]. Further analysis of the presented data should also allow us to get insight on the transformations the guided light undergoes as it propagates through the ONF, an area in which our group has recently made some progress [189]. This is particularly valuable for the characterization of more complex experiments involving, for example, the HOMs of an ONF and their interaction with atoms in a MOT. Similar experiments will be repeated in the future, focusing on fully probing the system and evaluating the Mueller matrices associated with each transformation.

Chapter 6

Characterization of the Mode Excitation at a Nanofiber Waist

The work done on ONFs interfaced with atoms has been reviewed in previous chapters. The latest developments in the field include the probing of long-range dipole interactions via super-radiance [17], and the observation of large Bragg reflections [15] and heralded collective excitations [73] in ONF-based atom traps. Such fibers have also been engineered to form cavities, either by etching Bragg-gratings on either end of the waist [90, 190], or looping the fiber on itself to form a ring cavity [91]. Most of the work on nanofibers with atoms has exploited the fundamental mode, overlooking the higher order fiber-guided modes (HOMs) despite their potential [95, 98, 99, 102, 104]. To give but a few of the proposed applications, HOMs interfaced with cold atoms could be used for ONF-based atom traps [98, 99] with higher degrees of control than for the fundamental mode, to create tractor beams [102], and to drive quadrupole-allowed transitions [121]. In addition, the hybrid modes, namely the HE and EH modes, carry orbital angular momentum (OAM) [95], which could be tailored to exhibit superchiral properties [104]. To date, the only experiment that has ever reported on the interaction between the HOMs and cold atoms has been performed by our group [94].

This chapter is structured as follows. First, we give a brief introduction, motivating the project presented here, and highlighting the challenges and potential solutions associated with it. We then present the results obtained with initial designs of the experiment, illustrating the thought process and the modifications that led to the current experimental setup. We dedicate an entire section to some of the most important technical challenges when designing the experiment and the solutions we found. Finally, we present the latest design of the HOM experiment along with results obtained when attempting to precisely determine the mode excitation (i.e., for both the fundamental mode and the HOMs) at the waist of an HOM-ONF. Despite overcoming most of the earlier technical hurdles, we emphasize that the project reported here is still a work in progress. More work is needed to determine if our technique can be applied to accurately determine the modes excited at the waist of an HOM-ONF.

6.1 Introduction

One of the main challenges needing to be tackled before being able to exploit the HOMs for applications with atoms is to develop a way to reliably and controllably excite these modes at the waist of an ONF. Even when tailoring the ONF such that it only supports the first six modes, i.e., $HE_{11,e}$, $HE_{11,o}$, TE_{01}, TM_{01}, $HE_{21,e}$, and $HE_{21,o}$, cross-talk between them is unavoidable. In relation to potential applications, this poses a serious issue as, for example, only the hybrid modes carry OAM [95], and only a specific pair of modes should be excited to create an efficient atom trap using HOMs [99]. Aside from applications with atoms, HOMs have received much more interest, specifically for the creation of cylindrical vector beams (CVBs). These beams can be seen as the free-space equivalent of HOMs and have found a broad range of applications (for a review see, for example, [191]). In free-space, CVBs can be generated by combining two coaxial LG beams with orthogonal circular polarization [110], or by using a Q-plate [192]. Given their similarity to the HOMs, fibers have also been used to create CVBs at their output [112–114]. Volpe and Petrov demonstrated that, for a given input polarization, it was possible to selectively excite a pair of modes at the output of a straight, multimode fiber shielded from any external perturbation [112]. Later, experiments showed that the mode at the output of such fibers could be precisely controlled once a transfer matrix (TRM) of the system could be determined, thereby yielding a target mode at the output. Among the methods developed to evaluate the TRM of such a system, two were considered for the work in this chapter. In the first, the mode decomposition relied on interference between a reference plane wave and the output of a multimode fiber [114], whereas, in the second method, two SLMs placed at the input and output of a multimode fiber were used to calculate the coupling coefficients for each mode in the TRM of the whole system [113].

Unlike the aforementioned studies considering the output of a fiber, we are primarily interested in the mode at the *waist* of an ONF. Fatemi *et al.* [115] recently demonstrated that mode beating at the waist of a HOM-ONF could be detected by probing the evanescent field with a single-mode ONF. These results have significantly improved the precision of mode analysis via Rayleigh scattering reported by the same group [32]. However, these techniques are somewhat difficult to integrate within a cold atom setup. Therefore, we decided to test whether the cold atoms themselves could be used to probe the mode excitation at the waist, in a manner similar to the polarization tomography we presented in Section 5.3.2.

6.2 Initial Experiments

To achieve selective mode excitation at the waist of an HOM-ONF we first needed to answer two questions: (i) Since free-space generation of CVBs is achievable by exciting the HOMs of a multimode fiber [112, 113], is it possible to shape a CVB to look like a specific HOM and inject it into an HOM-ONF such that it excites the targeted mode? and (ii) Knowing that light injected into the HOM-ONF undergoes a series of transformations on propagation, is it possible to establish a correlation between the observed output profile and the mode at the waist? We aimed to answer these questions by designing the first generation of experiments, which, as will be detailed in Section 6.2.3, led to a partial

answer to question (ii).

6.2.1 Generation of cylindrical vector beams using a straight few-mode fiber

Our first attempt at creating CVBs in free-space followed the methods developed by Volpe and Petrov [112]. The selective excitation of pairs of HOMs cccurs when a circularly polarized LG_{01} beam is launched into a few-mode fiber (FMF). If the beam is σ^+-polarized, that is, the rotation of both the phase front and the polarization coincide, the expected output is a combination of TE_{01} and TM_{01}. Passing the output beam through a HWP allows one to generate either a TM_{01}-like or a TE_{01}-like free-space beam.

For the case of a σ^--polarized LG_{01} beam, the rotation of the phase and the polarization are opposite to each other, and the expected output should be a combination of a $HE_{21,e}$ and a $HE_{21,o}$ mode. Note that the HE_{21} modes are degenerate in their propagation constant, β, and thus should always combine to form a circularly polarized donut-shaped beam at the fiber output. Stress- or strain-induced birefringence can lift the degeneracy in β for these modes, allowing only one of them to be excited at a time.

Figure 6.1 shows the experimental setup used to reproduce the results reported in [112], and launch the resulting CVBs into the HOM-ONF installed in the UHV chamber (setup identical to that described in Chapter 3). A fiber-coupled ECDL (Toptica DL100 Pro) produces a 780 nm Gaussian beam that is incident on an SLM on which is displayed a fork hologram resulting from the superposition of a phase grating and a 2π phase dislocation. The resulting LG_{01} beam is passed through a QWP, before being injected into a $\sim$ 20 cm long FMF (FiberCore, SM1250 9/80) kept straight and shielded from air and vibrations by a Plexiglas cover. Note this fiber is identical to the FMF used to fabricate the HOM-ONF and supports up to the HE_{12} modes at 780 nm. The injection efficiency for the FMF is higher than 75% and no cross-talk with modes beyond the LP_{11} family is observed. The output beam is then passed through a HWP and a 90:10 BS (i.e., 90% of the power is transmitted and 10% is reflected). The transmitted beam is coupled into the HOM-ONF, while the reflected beam is passed through a linear polarizer before hitting a beam profiler (Thorlabs, BC106N-VIS). The output pigtail is kept as straight as possible to avoid any further transformation of the modes between the waist and the output. The beam coming out of the HOM-ONF is divided using another 90:10 BS, with 90% of the power being sent to a single photon counting module (SPCM) (Excelitas, SPCM-AQRH-FC), which is fiber-coupled to a FMF. The remaining 10% is passed through a rotating linear polarizer before being imaged by an actively cooled sCMOS camera (Andor, Zyla CMOS 4.2) for the polarization analysis necessary to identify the modes.

The CVBs, as imaged by the beam profiler, are displayed in Fig. 6.2. Without the linear polarizer, the resulting output beam is always donut-shaped, irrespective of the circular polarization chosen for the input beam. To determine the type of CVB produced, we rotate the linear polarizer (P1) placed in front of the beam profiler and observe the resulting profile. This produces a two-lobed pattern that either rotates in the same direction as the polarizer's axis in the case of TE_{01}-TM_{01} excitation, or opposite to it for HE_{21} excitation. Using a σ^+-polarized input beam, we rotate the fast-axis of the HWP in order to produce the expected TE_{01}-TM_{01} pair. This serves as a reference to

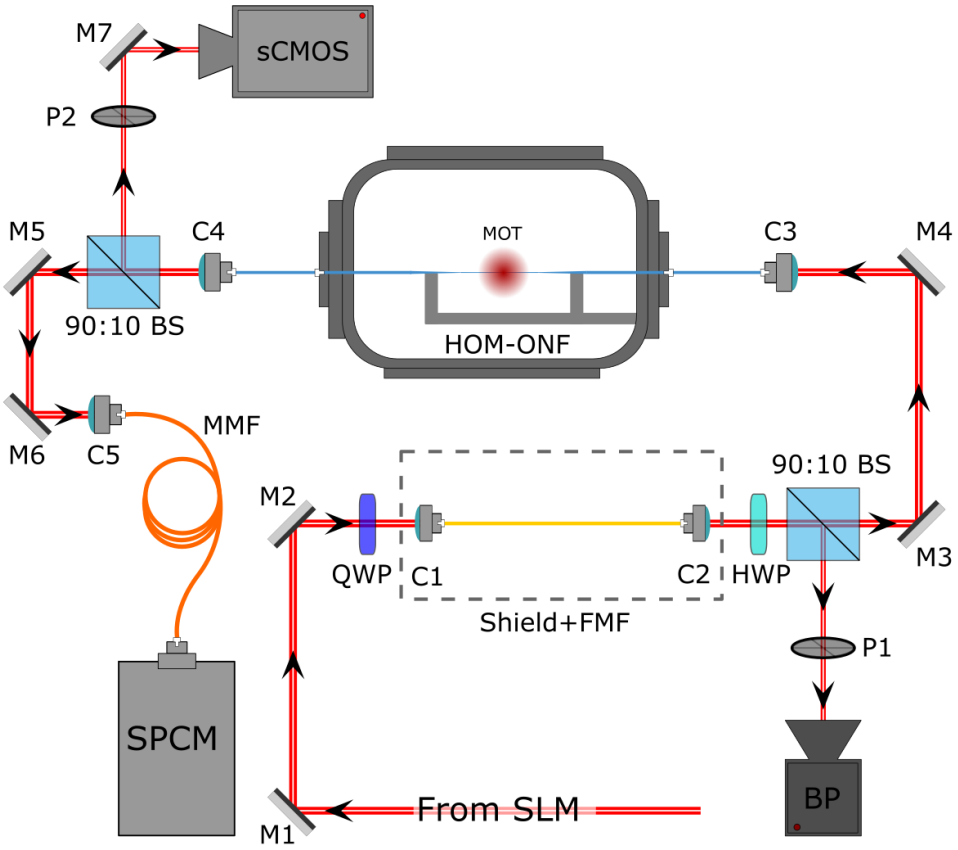

Figure 6.1: Schematic of the experimental setup for the CVB generation via an intermediate fiber. M1-M7: Mirrors, QWP: Quarter-wave plate, HWP: Half-wave plate, BS: Beam-splitter, P1-P2: Linear polarizers, C1-C5: Fiber collimators, FMF: Few-mode fiber, SPCM: Single-photon counting module, MMF: Multimode fiber, sCMOS: Scientific complementary metal oxyde semi-conductor camera, BP: Beam profiler.

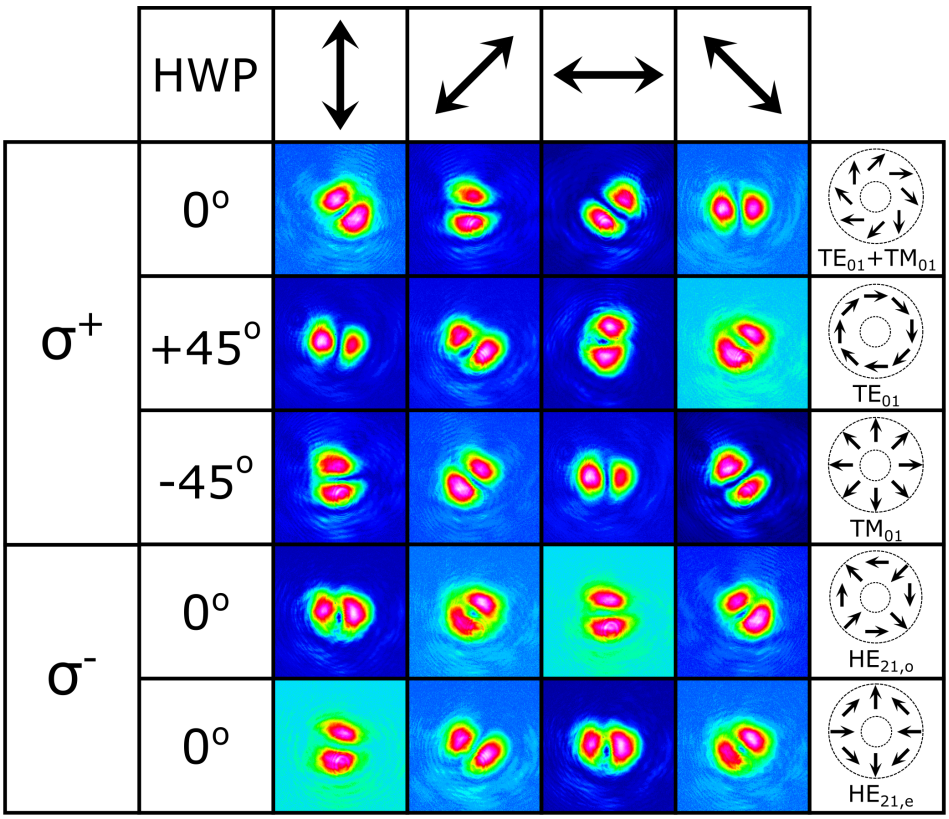

Figure 6.2: CVBs generated using the intermediate fiber method. A σ^+-polarized input beam leads to excitation of the TE_{01}-TM_{01} pair, which can be separated when the HWP is rotated by $\pm$ 45°. The evolution of the two-lobed pattern is plotted as the polarizer is rotated. The polarizer's axis is represented by the arrows at the top of the figure. Blue represents a low beam intensity and red a high beam intensity. The last column shows a diagram of the expected polarization profile.

subsequently produce the TE_{01}-like and TM_{01}-like CVBs by rotating the HWP by +45° and -45°, respectively. Due to imperfections in the coupling and probable asymmetries in the fiber, excitation of both HE_{21} modes at the same time was found to be very challenging, with only one of them being observed at a time. Adjusting the QWP to produce a σ^--polarized input beam would lead to a profile resembling that of a HE_{21} mode, but adjusting the coupling of the input beam using a pair of mirrors allowed us to get the desired output profiles. Here, the HWP is never rotated.

Injection of these CVBs into the HOM-ONF led to high power losses and output profiles showing evidence of cross-talk between modes of the LP_{01} and LP_{11} families. Bypassing the intermediate fiber and injecting LG_{01} or LG_{0-1} beams directly into the HOM-ONF was found to be easier and more efficient. We, therefore, abandoned this line of experiment and decided to change strategy to create HOM-like beams in free-space, the details of which are given in Section 6.4.1.

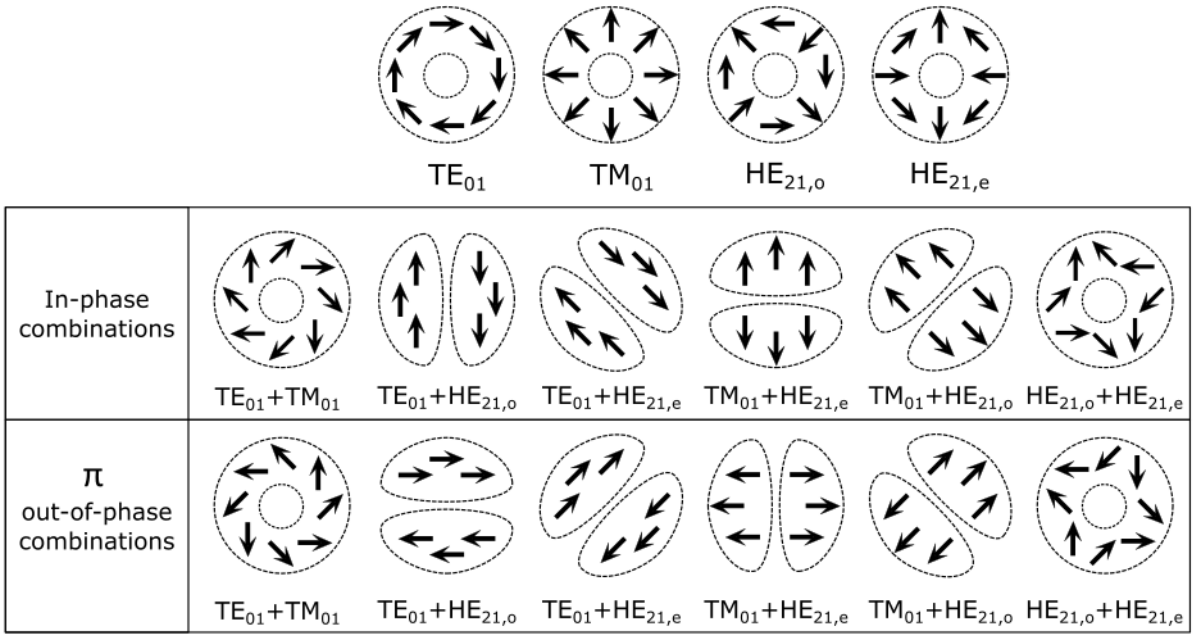

Figure 6.3: Identifiable combinations of HOMs. The first row shows the polarization distribution of individual, linearly polarized HOMs. The second row shows a list of in-phase combinations of pairs of modes that are distinguishable after polarization analysis. The third row shows how the pattern changes if the modes are π out-of-phase. In each case, the dashed pattern represents the beam shape as would be observed in free-space.

6.2.2 Twisting-induced nanofiber modes excitation

We had already developed a method to selectively excite specific HOMs at the output of a FMF during the fabrication of the HOM-ONF (see Section 2.4.1). As a reminder, we used stress-induced birefringence while launching an LG_{01} beam into a FMF to observe one of the HE_{21} modes at its output, so that its transmission during the pulling process could be monitored. In order to establish a link between the observed output and the mode at the waist, we decided to use the *twisting technique* once more. This time, the goal was to create not only the HE_{21} modes, but all of the modes in the LP_{11} family at the output of the nanofiber. As such, the earlier setup was adapted to lengthen the pigtail of the HOM-ONF and to accommodate the required polarization paddles (PP). The intermediate FMF used in the previous experiment was discarded and a $\sim$ 50 cm long FMF was spliced to the input pigtail of the ONF. Note that the FMF had identical specifications to that of the fiber used to fabricate the HOM-ONF (FiberCore SM1250 9/80) and was identical to the pigtail. The now elongated pigtail was then coiled around three PPs and its free end connected to a fiber collimator with an NA of 0.25 to maximize coupling of the free-space LG beam. We measured a coupling efficiency up to 85% in the fundamental mode (LG_{00} beam) at the output of the HOM-ONF and up to 60% for the LG_{01} beam. The experimental setup after the HOM-ONF was unchanged.

In most cases, this method produces output profiles that indicate significant mode mixing; simple polarization analysis does not provide enough information to accurately determine which modes have been mixed or in which proportion. In some cases, however,

an output profile can directly be identified as a specific combination of modes. These special cases are sketched in Fig. 6.3. The dashed lines indicate the pattern these modes, or combinations of modes, would produce at the output the HOM-ONF and the arrows represent polarization vectors. In the first row, we have sketched the polarization patterns of linearly polarized HOMs. We have already described how, in this case, the observation of a donut-shaped beam, along with the position and rotation of the two-lobed pattern produced after the beam is passed through a rotating linear polarizer, allows one to identify, with certainty, which mode was excited. In the second row, we show the six possible polarization profiles obtained when two in-phase HOMs are combined, each mode containing 50% of the total coupled beam power. This leads to characteristic patterns which, after polarization analysis, can be unequivocally identified[1]. For example, a donut-shaped beam either results from a single HOM excitation or an in-phase combination of either TE_{01} and TM_{01} or $HE_{21,o}$ and $HE_{21,e}$. Passing the beam through a linear polarizer, which rotates clockwise, will give a two-lobed pattern rotating with the linear polarizer in the case of a TE_{01}+TM_{01} combination, and opposite to the linear polarizer in the case of a $HE_{21,o}$+$HE_{21,e}$ combination. Furthermore, the initial position of these lobes when the linear polarizer's axis is, e.g., kept vertical, determines if the observed pattern is a pure mode or a combination of modes, as the lobes will be either vertical or horizontal in the case of a pure mode, or angled at $\pm$ 45° in the case of a combination. If a two-lobed pattern is observed before the beam is passed through the linear polarizer, polarization analysis reveals whether the combination involves either the TE_{01} mode or the TM_{01} mode with one of the two HE_{21} modes; Any TE_{01}+HE_{21} combination yields a polarization pattern **parallel** to the dark line between the two-lobes, and any TM_{01}+HE_{21} combination yields a polarization pattern **orthogonal** to the dark line between the two-lobes. As seen in the third row, these observations remain true even if the combined modes are π out-of-phase with respect to each other. The only difference is that the output profile is simply rotated by 90°. If the phase difference between the two modes is not an integer multiple of π, the polarization pattern becomes elliptical and the modal decomposition is no longer unique.

By adjusting the orientation of the PPs somewhat randomly, we were able to create beam profiles at the output of the HOM-ONF closely matching those of the specific mode combinations listed previously. These are presented in Fig. 6.4. It can be seen that the purity of the mode excitation is far from perfect; the resulting profiles are neither perfectly linearly polarized, nor are they resulting from the sole combination of two of the HOMs, each sharing half the total power.

6.2.3 Probing the waist using cold atoms

We created a cloud of cold ^{87}Rb atoms in a MOT, using the setup and methods described in Chapter 3. The center of the MOT was superimposed with the center of the nanofiber's waist and its position monitored using a pair of cameras imaging the top and side of the fiber. Although the cooling beams were aligned such that the center of the MOT coincided with the center of the waist, the atom cloud was initially formed at a small distance from the fiber. To do so, a pair of compensation coils (CC) in a Helmholtz configuration

[1]We emphasize that this approach is only valid if the mode mixing is the result of a combination of pure, linearly polarized modes. We only recently became aware of a more comprehensive polarization analysis method involving circular polarizers [193].

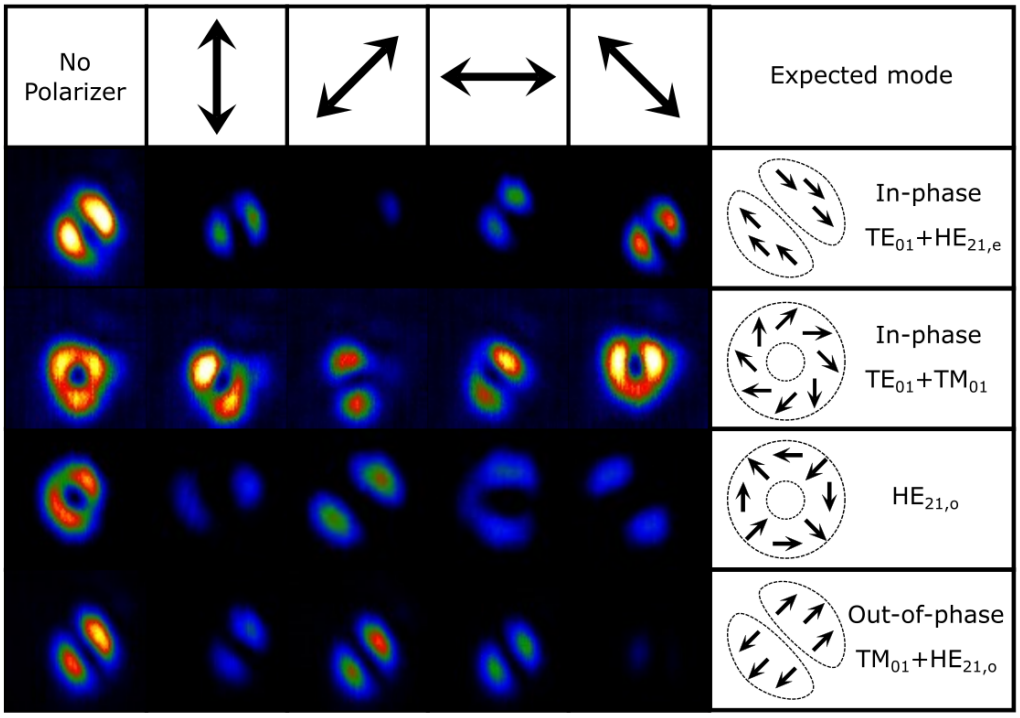

Figure 6.4: Experimentally obtained output profiles closely matching identifiable combinations of HOMs. The first column shows the beam profile when the polarizer was removed. Columns 2-5 show the evolution of the profile when the polarizer is rotated clockwise. The last column provides a sketch of the expected mode along with its description. The color-coding from black to white represents low to high intensity, respectively.

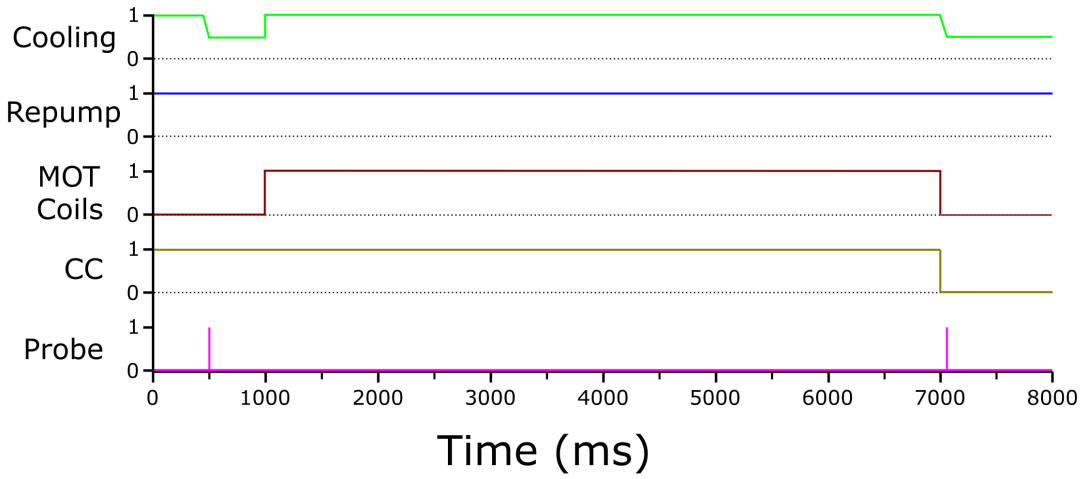

Figure 6.5: Diagram of the timing sequence for the absorption experiment.

shifted the magnetic center of the trap by a few millimeters in the horizontal plane and perpendicularly to the HOM-ONF's axis. The CCs were then quickly switched off using an insulated-gate bipolar transistor (IGBT) circuit, bringing the MOT back to the center of the fiber. This produced up to a 3-fold increase in the fluorescence signal collected at the HOM-ONF's output, likely translating to an increase in the number of atoms trapped in the MOT before its position was shifted. However, once overlapped with the fiber, the fluorescence signal decayed to a much lower value over the course of 1.5 s. We typically measured a maximum fluorescence signal of 32,000 counts/10 ms, decaying to 10,000 counts/10 ms. When optimized, the background signal from the cooling beams coupling into the HOM-ONF was $\approx$ 4,000 counts/10 ms.

A diagram of the experiment's timing sequence is given in Fig. 6.5. For the first 1,000 ms, the MOT coils were switched off so that a background measurement could be taken. The coils were then switched ON for the next 6,000 ms, allowing the cloud of atoms to form. The CCs, which initially shifted the MOT away from the fiber, were then switched off so that the center of the atom trap overlapped with the waist. The MOT coils were, once more, switched off, and the frequency of the cooling beams was ramped down to -45 MHz from the cooling transition over 50 ms, producing an optical molasses. The repump beam is always kept ON throughout the experiments. The probe beam was provided by a fiber-coupled ECDL (Toptica DL100 Pro) tuned to 780 nm. Prior to its injection in the HOM-ONF, the beam was double-passed through an AOM with a central frequency of 110 MHz (IntraAction ATM-1102DA2B). The frequency shift induced by the AOM was tuned such that the probe beam could be locked to the $5S_{1/2}F = 2 \rightarrow 5P_{3/2}F' = (1,3)_{co}$ crossover peak provided by a commercial saturation absorption spectroscopy system (Toptica, CoSy). During the experiment, the laser frequency was scanned from -20 MHz to +20 MHz in 2 ms by varying the voltage to the AOM. This frequency scan was repeated twice in one experimental cycle: once during the first 1,000 ms when the MOT coils were off to get a background signal, and once more as soon as the optical molasses regime was reached. The resulting signals were recorded by an SPCM set to record a signal every 20 μs.

The experimental cycle is repeated 100 times for each mode profile. The standard devi-

ation and average signal are evaluated for each point recorded by the SPCM. We present, in Fig. 6.6, the results obtained for each identifiable mode at the HOM-ONF's output. Figure 6.6(a) shows the polarization analysis of an output profile closely matching that of a circularly polarized HE_{11} mode which we choose as a reference. In the hypothetical case in which the output profile exactly matches that of the mode at the waist, the evanescent field would uniformly interact with atoms in the vicinity of the waist irrespective of the azimuthal angle around the fiber. Figures 6.6(b)-(f) show the results obtained for each output profile of interest. The inset shows the maximum absorption, evaluated after fitting the experimental data with a Lorentzian. The number in parentheses indicates the value of the ratio between the maximum absorption for the mode considered and that of the HE_{11} reference[2].

Using a finite element method (FEM) physics solver (COMSOL Multiphysics, RF module), we simulated the experiment to calculate the power in the evanescent field for the combinations of modes previously mentioned. In principle, the integrated power over the length of the waist should be directly correlated to the absorption in a specific combination of modes. More specifically, the absorption is directly proportional to the intensity of the guided field when operating below the saturation regime [186]. To minimize computational needs, we simulate a 100λ long waist, i.e., 78 μm, although the actual waist is 2 mm. The system is composed of two concentric, homogeneous, cylinders with refractive indices $n_1 = 1.455$ and $n_2 = 1$, representing the waist and vacuum. Although atoms in the vicinity would, in reality, lead to $n_2 > 1$, we assume the atomic gas is so dilute that the change in refractive index can be neglected. The radius of the waist is 350 nm and the vacuum cylinder's radius is chosen to be 10 times larger.

We first ran the mode solver to determine the effective refractive indices of the allowed modes. Once these were obtained, a full FEM simulation was run to evaluate the mode propagation and to calculate the power in the evanescent field integrated over the length of the simulated waist. For each simulation, we selected two modes at the input, both sharing 50% of the total input power, i.e., 1 nW for each case. The integrated power for each combination of modes was then compared to that of the reference circularly polarized HE_{11} mode. The results of these simulations are shown in Fig. 6.7. We note that the simulated profiles match those in Fig. 6.3, but are all rotated by 22.5° counter-clockwise. Another anomaly can also be seen: The TM_{01}-$HE_{21,o}$ pair yields a much larger ratio value than its TM_{01}-$HE_{21,e}$ counterpart for no apparent reason. The reasons for these two anomalies are not yet fully understood and currently under investigation. Nevertheless, a relative agreement between experimental and numerical ratios was observed.

In light of the reasonable match, we made the hypothesis that mode scrambling was taking place between the input pigtail of the HOM-ONF and its waist, probably in the down-taper. This contrasts with the results in Section 5.3.2, but matches what other researchers in our unit have observed for nanofibers in air [116]. This could be explained by the fact that the HOM-experiment was designed to minimize torsion on the tapered fiber during its installation in the UHV chamber, for example by precisely drilling the holes in the Teflon feed-throughs (see details in Section 2.5.3). As such, light propagating through the waist and the up-taper, assuming the latter to be fabricated adiabatically,

[2]The absorption of the fundamental mode was relatively low at the time. The current version of the HOM-experiment can yield typically $\sim 10\%$ absorption in the fundamental mode.

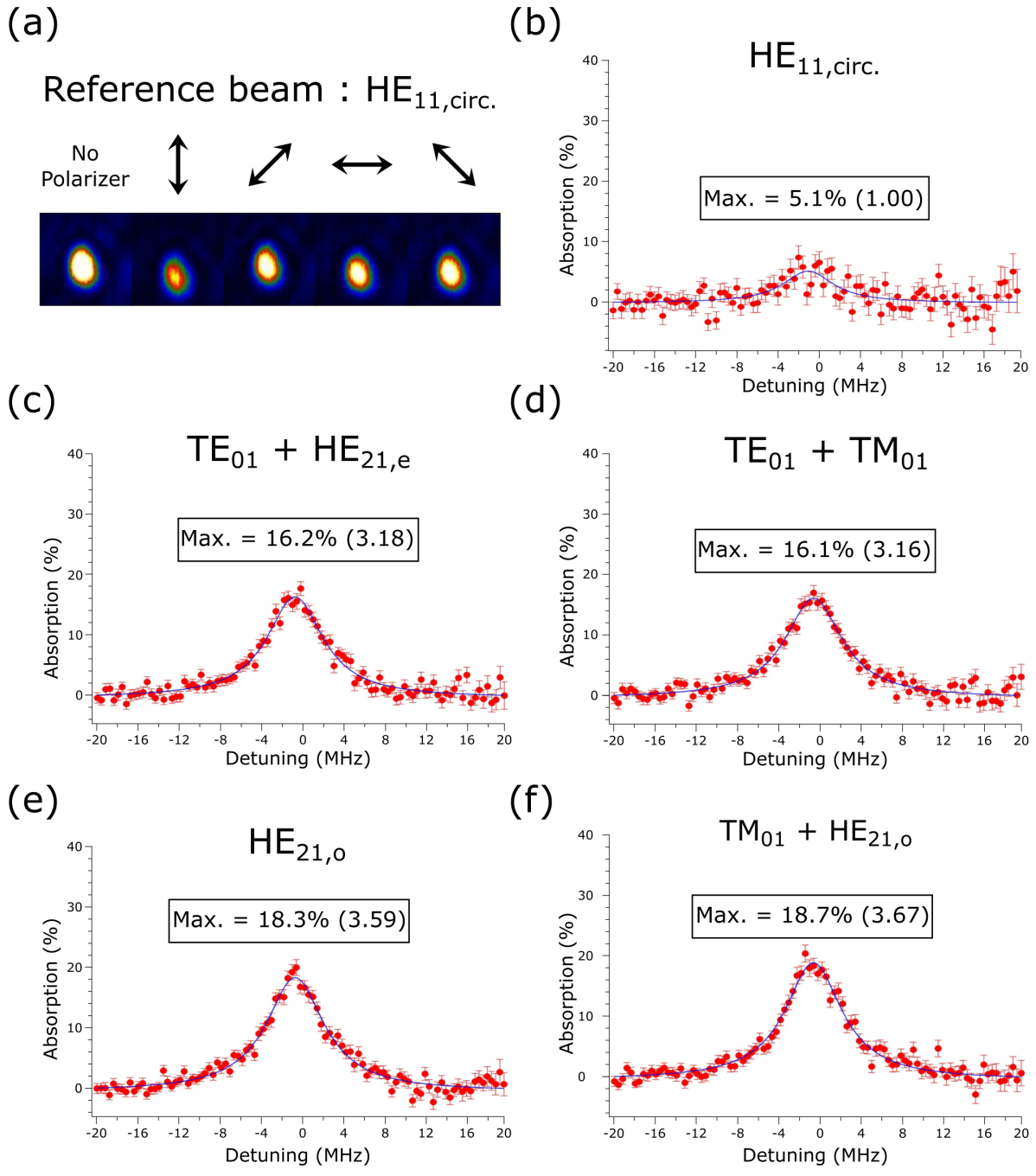

Figure 6.6: Results of the absorption experiment with identifiable modes at the output of the HOM-ONF. The framed inset indicates the maximum absorption along with its ratio to the reference beam absorption (number in parentheses).

Simulated output profile	Mode 1	Mode 2	Ratio to $HE_{11,circ.}$
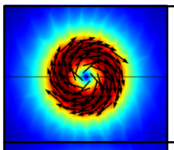	TE_{01}	TE_{01}	2.1798
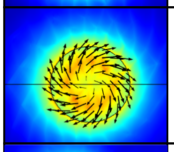	TE_{01}	TM_{01}	2.9527
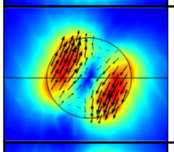	TE_{01}	$HE_{21,e}$	3.0568
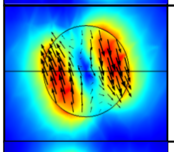	TE_{01}	$HE_{21,o}$	3.0651
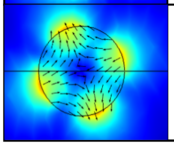	$HE_{21,e}$	$HE_{21,e}$	3.2652

Simulated output profile	Mode 1	Mode 2	Ratio to $HE_{11,circ.}$
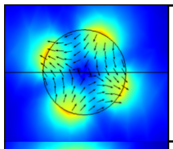	$HE_{21,o}$	$HE_{21,o}$	3.2818
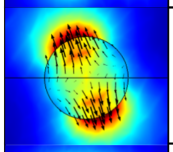	TM_{01}	$HE_{21,e}$	**3.8433**
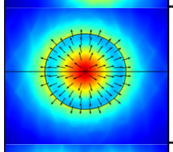	TM_{01}	TM_{01}	3.9875
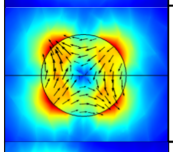	$HE_{21,e}$	$HE_{21,o}$	4.1737
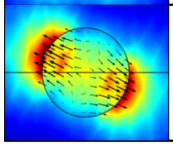	TM_{01}	$HE_{21,o}$	**4.3545**

Figure 6.7: FEM simulations of the relative power in the evanescent field for each combination of modes and single modes in the HOMs. For each case, the input power is distributed equally among the two modes. The color-coding from blue to red represents low to high intensity, respectively. The black arrows represent polarization vectors. There are anomalies in the highlighted values.

would remain mostly unaffected, thus resulting in an output mode profile that gives a relatively faithful representation of the modes at the waist. In practice, the mode cross-talk heavily depends on the fiber installed in the vacuum chamber. For every new nanofiber, this cross-talk needs to be characterized via, for example, calculation of a transfer matrix (TRM) of the system. To do so, we needed to be able to excite all the combinations of modes presented in Fig. 6.7, both reliably and efficiently. This led to an upgrade of the experiment in which we tackled several issues discussed in the next section.

6.3 Stability Issues

The first generation experiments had clear limitations. For example, an experiment could not be run for more than a few hours at a time as the anti-Helmholtz coils for the MOT would heat up the entire vacuum system and affect the modal excitation in the nanofiber. Adjusting mirrors or the polarization paddles to retain the desired mode profile caused the HOM-ONF to vibrate in the vacuum chamber, once more affecting the modes. In addition, randomly orienting the PPs to get the desired output profile made the acquisition of repeatable data challenging.

6.3.1 Heat-induced stretching of the optical nanofiber

One of the first issues encountered was caused by the anti-Helmholtz coils, which were heating by the Joule effect, and, by extension, were also heating the vacuum chamber[3]. As explained in Chapter 3, the coils are placed around the top and bottom viewports, in direct contact with the vacuum chamber. This also affects the U-mount supporting the HOM-ONF, as it directly connects to one of the science chamber's flanges. The aluminium mount thermally expands over time, i.e., an expansion of the order of 0.1 mm for a 25°C increase in temperature, whereas the nanofiber remains relatively unaffected by the change of temperature, i.e., an expansion of the order of 10^{-3} mm. This, in turn, causes the HOM-ONF to stretch, changing the mode excitation in the process and preventing us from running experiments over long periods of time. The drastic changes in the output modes caused by this heating issue were monitored over the course of an hour and are depicted in Fig. 6.8.

The heat-induced fiber stretching also caused several HOM-ONFs to break after their installation in the UHV chamber, even after passing the initial robustness test (see Section 2.5.4); a few mW of power coupled into the fiber combined with the thermal changes were enough to stretch the fiber beyond its limit and break it.

To control and, eventually, address this heating issue, we monitored the temperature of the flange on which the U-mount was attached, using a thermocouple wire (RS Components, RS PRO type-K) that was connected to a data acquisition card (National Instrument, DAQ). The change in temperature of the flange as it cooled naturally is shown in Fig. 6.9. Temperature was measured every second and the data stored over an arbitrary period of time. It can be seen that, in addition to the obvious threat this heating issue presented for reliably reproducing experimental results, the system has to

[3]Although not mentioned explicitly, the preliminary results presented in the previous section were obtained after adding cooling fans to tackle the heating issue described here.

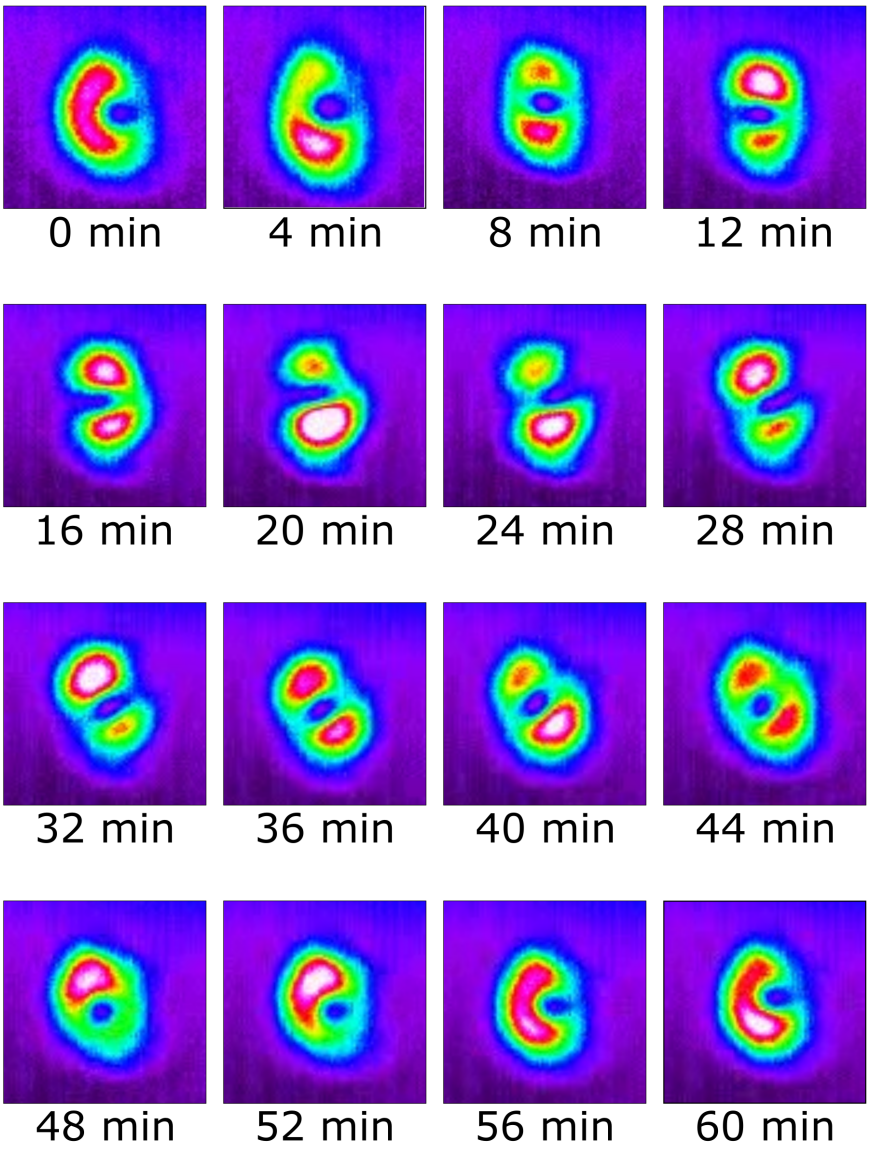

Figure 6.8: Time-lapse evolution of the output profile as the anti-Helmholtz coils heat up the chamber. An image of the output profile is taken every 4 minutes over the course of an hour. Blue represents a low beam intensity and red a high beam intensity.

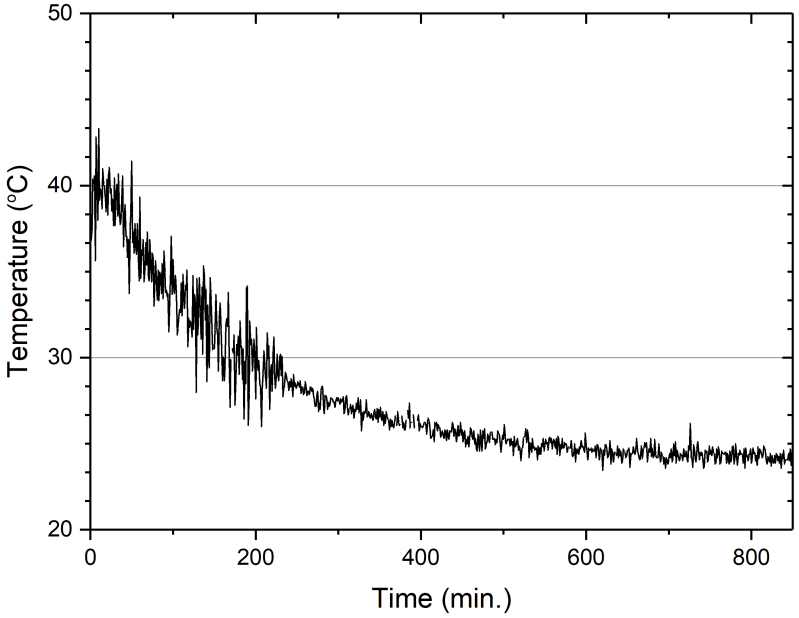

Figure 6.9: Temperature of the flange decreasing over time in the absence of external cooling mechansim.

be switched completely off for times ranging from 400 to 600 min before reaching room temperature in the absence of any active cooling method.

A simple and straightforward solution was to cool the coils using fans. The first attempt using fans designed to cool a CO_2 laser was a limited success; the coils and the flange were kept at temperatures below 30°C during the entire experiment, but vibrations in the HOM-ONF were observable even though the fans were mechanically decoupled from the optical table. In the current experimental setup, these large fans have been replaced by two smaller fans, also mechanically decoupled from the optical table. These are from the CPUs of two discarded computers. After all the components of the experiment have been switched on for a few hours, the vacuum chamber reaches a steady-state temperature of ∼35°C and no more vibrations of the HOM-ONF are observed. Although initially meant to be temporary, this simple and cheap solution was kept for the rest of the HOM-project. In the next upgrade of the experimental setup, however, the MOT coils should be removed from the vacuum chamber and cooled using a combination of heat sinks and water-cooling.

6.3.2 Transmission loss from Rubidium adsorption

Shortly after its installation, the transmission of the HOM-ONF was measured to be 90% in the fundamental mode. This transmission progressively degraded over time, although never to a detrimental level (i.e., from 90% to 85%). Changing the dispensers amplified this trend and the transmission in the fundamental mode dropped to 65%. We attribute this change in transmission to adsorption of Rb atoms onto the HOM-ONF's surface, as has been reported for ONFs embedded in hot atomic vapors [41, 44]. To prevent coating,

and even desorb most of the Rb atoms, we inject 500 μW of 1064 nm light into the HOM-ONF. This serves two purposes: (i) it heats up the fiber and prevents Rb atoms from adsorbing on the surface, preventing the loss of transmittance and (ii) it provides a red-detuned evanescent field which exerts an attractive force onto atoms in the vicinity of the HOM-ONF's waist, thus increasing the number of atoms interacting with a given guided mode. The transmission in the fundamental mode now reaches 80% after leaving the 1064 nm beam on for a few hours.

6.3.3 Fiber vibrations

Another issue encountered in early experimental designs was that of vibration. Inside the vacuum chamber, the U-mount that supports the nanofiber behaves as a cantilever. Since the whole vacuum chamber structure is fixed onto the optical table, any vibration of the optical table can, unfortunately, propagate to the U-mount and to the fiber itself, resulting in unwanted perturbations of the mode excitation. Although we could clearly observe the HOM-ONF vibrate on the front camera, the perturbations on the output profile were not as dramatic as those caused by heat-induced stretching. Nevertheless, this issue had to be addressed to establish a decent correlation between modes at the waist and the observed output profile. Aside from the large fans, adjusting optics on the optical table was found to be the main source of vibrations of the nanofiber. The transverse oscillatory motion would eventually dissipate after $\sim$20 min if the optical table was not touched. It was therefore crucial to avoid any further modifications to the optics prior to running an experiment. This was clearly an inconvenience when working with the twisted-input method of Section 6.2.2. This oversight in the U-mount design would have forced us to discard a perfectly good HOM-ONF if we were to rectify it. We circumvented the problem by redesigning the experiment to be computer-interfaced, with each of the essential components being remotely addressable. This led to the following considerations: (i) Discarding the polarization paddles and redesigning the experiment so that the mode excitation was controlled by the shape of the probe beam in free-space prior to its injection into the HOM-ONF, (ii) controlling the injection of the said probe beam without mechanically adjusting any of the optical components, (iii) switching the probe beam and the MOT on or off, on-demand, and (iv) doing a detailed analysis of the output profile without manually rotating a polarizer.

6.4 Mode Demultiplexing at the ONF Output

The experimental setup for the HOM-project in its current configuration is designed to be computer-controlled and remotely operable. Each essential element is interfaced via a home-written program coded in LabVIEW (2017-version, 64bit edition)[4]. A schematic of the general experimental setup is provided in Fig. 6.10. Three important areas, delimited by dashed lines, can be distinguished. Area A regroups all the optical components for the generation of HOM-like beams in free-space. The central element is a dual-hologram

[4]From this point onward, Simon P. Mekhail, another PhD student in the group, joined the project and wrote most of the LabVIEW code to control the experiment and to demultiplex the modes at the output of the nanofiber.

SLM (Meadowlark, 512 × 512 pixels, nematic liquid crystal, Analog SLM), connected to a computer and interfaced via the LabVIEW program. Fine-tuning of the probe beam injection is also possible using the SLM[5]. In Area B, the generated HOM-like beams are analyzed before being coupled to the HOM-ONF. Finally, in Area C, the beams produced at the output of the nanofiber are thoroughly analyzed via mode demultiplexing. The transmission of the probe beam is also monitored using a fiber-coupled SPCM (Excelitas, SPCM-AQRH-FC).

The HOM-ONF and the MOT are identical to what were described in previous chapters. The only modification is that the AOM of the repump beams is now connected to a data acquisition board (National Instrument X-series DAQ), for which the voltage delivered by each analog output port is computer-controllable. This allows us to switch the MOT on and off, on-demand, without affecting experimental parameters that could influence the modes at the waist. For example, doing the same procedure by turning off the magnetic coils would cool the vacuum-chamber, leading to a weakening of the initial stretch induced to the nanofiber.

6.4.1 Dual-hologram method for mode generation

To increase the chances of selectively exciting a single HOM in the fiber, we first generated CVBs in free space, the polarization profile of which were shaped to look like the fiber eigenmodes. This was done following a method similar to that developed by Maurer *et al.* [110], albeit with some minor modifications that make our setup more power efficient. This is the purpose of Area A in Fig. 6.10, which we now reproduce along with an annotated image of the experimental setup in Fig. 6.11.

As stated previously, the 780 nm probe beam is provided by a fiber-coupled ECDL (Toptica DL100 Pro) and its output is double-passed through an AOM, shifting the beam frequency by 220 MHz. The beam, which is now linearly polarized, is then injected into a polarization maintaining (PM) fiber, bringing it to the CVB-generation setup. A BS splits the power in half, sending the beam along two different paths. The reflected beam is further split with an adjustable ratio, using a combination of a HWP and a polarizing beam-splitter (PBS). Each of these beams is then injected into a PM fiber that eventually provides a reference beam when demultiplexing the probe beam, either before entering or after exiting the HOM-ONF. The beam in the transmitted path of the first BS is passed through a HWP with its fast-axis oriented such that the probe beam is now diagonally polarized. A D-shaped mirror (DSM) reflects the beam towards a beam displacer (BD1), which creates two orthogonal, linearly polarized beams at its output. After BD1, both beams propagate parallel to each other, before being incident on an SLM.

Given the preference in polarization imposed by the SLM (i.e., vertical polarization in this case), a half-inch HWP (HWP2) is inserted in the path of the horizontally polarized split beam to rotate it to the appropriate polarization. To generate the CVBs, we create two independently controllable holograms on the SLM display, with each hologram occupying one half of the display. Using a combination of a phase-dislocation pattern and a phase grating, we generate LG beams with an arbitrary topological charge. The

[5]This will be briefly described in Section 6.4.2. The interested reader will find more information in the PhD thesis of S.P. Mekhail, as he developed the gradient descent algorithm that led to a major improvement of the probe beam injection into the HOM-ONF.

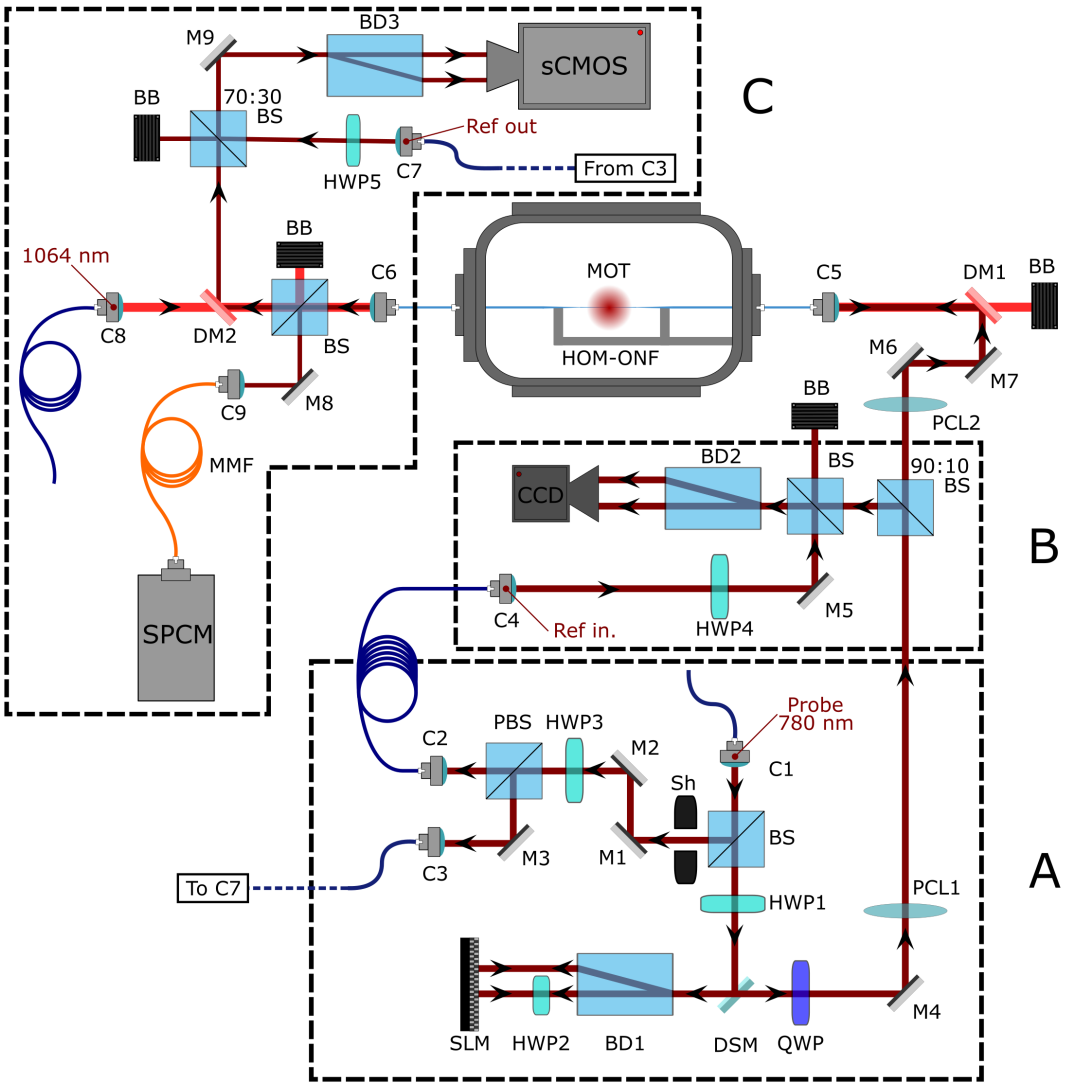

Figure 6.10: Schematic of the current experimental setup used for the HOM-project. The three major areas, central to the new experimental setup, are labeled A, B, and C, and are marked by dashed lines. Each of these are explained in detail in later sections. BB: Beam blocker, BD1-BD3: Beam displacers, BS: Beam-splitter (preceded by the transmission:reflection ratio, 50:50 if not explicitely stated), C1-C9:, Fiber collimators, CCD: Charge-coupled device camera, DM1-DM2: Dichroic mirror, DSM: D-shaped mirror, HWP1-HWP5: Half-wave plates, M1-M9: Mirrors, MMF: Multimode fiber, PBS: Polarizing beam-splitter, PCL1-PCL2: Plano-convex lenses, QWP: Quarter-wave plate, Sh: Shutter, SLM: Spatial light modulator, SPCM: Single-photon counting module, sCMOS: Scientific complementary metal-oxide semiconductor camera.

(a)

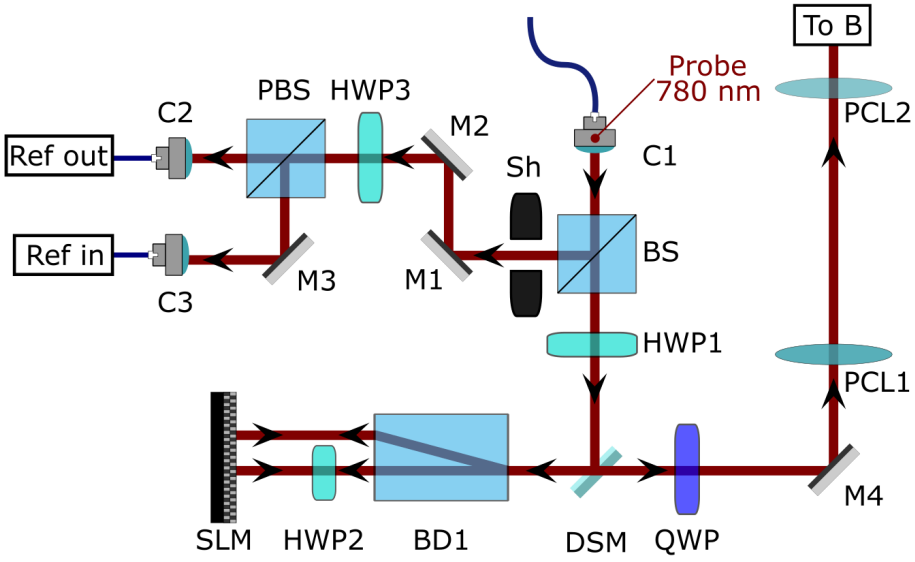

(b)

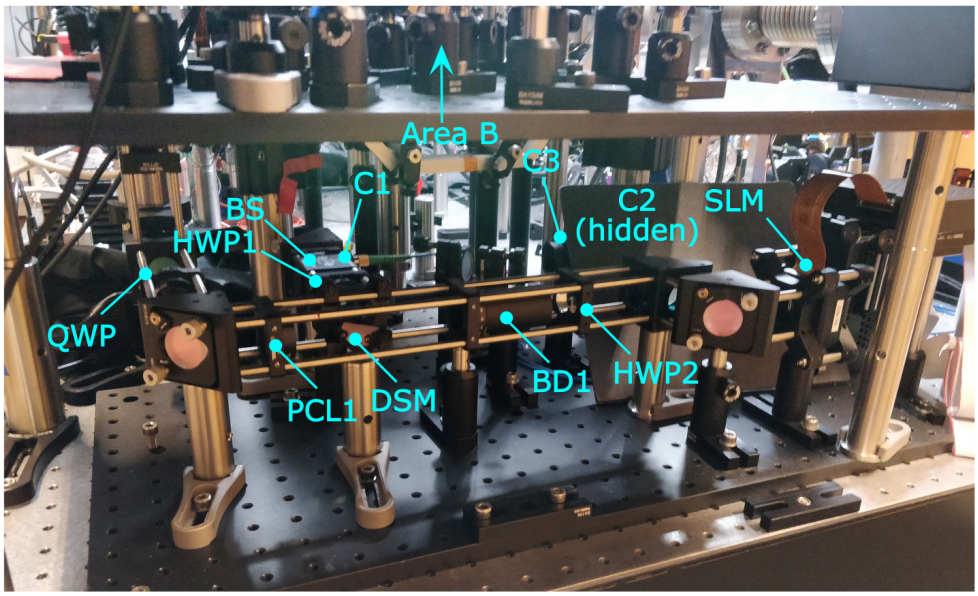

Figure 6.11: (a) Schematic and (b) image of the experimental setup used to generate HOM-like beams in free-space. Optical components are labeled as in Fig. 6.10.

first diffracted order produced by each hologram is reflected to almost retrace the original beam path and the two reflected, orthogonally polarized, beams recombine at the output of BD1. A small vertical tilt on the computer-controlled grating allows the recombined beam to propagate above the DSM and through a QWP with its fast-axis oriented at 45° with respect to the plane of the optical table, in order to convert the linear polarization of the beam's components into circular ones with opposite handedness [110]. To mimic the HOM-ONF's eigenmodes, the topological charge of the beam needs only be -1, 0, or +1. The combinations are summarized in Table 6.1. The beam is then sent to a second stage where two plano-convex lenses (PCL1 and PCL2) are positioned in a $4f$-telescope configuration to map the SLM holograms onto the focal plane of a coupling lens placed in front of the HOM-ONF. Both lenses have a focal length $f = 200$ mm and are positioned 400 mm apart, with the first lens positioned such that the SLM is at its focal point. The relay telescope prevents the beam from diffracting too much before it is injected into the nanofiber and allows us to finely tune the beam position, down to the nm-level, using the computer-controlled grating.

As shown in Fig. 6.11(b), the whole system is cage-mounted to prevent individual components from vibrating and inducing phase changes in the split beams. Area A is also modular, so that it can be removed and put back together quickly, without further adjustments, in the eventuality that the HOM-ONF would need to be replaced. As stated previously, our method for generating the CVBs in free-space differs slightly from that in [110], as we use a DSM where Maurer *et al.* used a BS. This provides a lot of power in the probe beam[6], but forces the retro-reflected LG beams to enter BD1 at a small angle (i.e., under 5°). However, in spite of this deviation, our setup produced high-quality CVBs.

The power in the probe beam can be further improved by finding the optimal grey-level offset and amplitude of the SLM for the 780 nm operating wavelength. To do so, we place an avalanche photodiode (APD) directly after M4 to monitor the power of the probe beam as both the offset and amplitude of the SLM are swept. The results of this optimization process are presented in Fig. 6.12, showing that an optimal value, marked by the white "X", was found for an offset of 52 and an amplitude of 32 on an 8-bit grey-scale.

[6]The HOM experiment was initially designed to trap atoms using specific combinations of modes in a two-color scheme. Conservation of optical power was crucial.

Table 6.1: Topological charges of the Laguerre-Gauss beams and phase difference required for the creation of the HOM-ONF's eigenmodes in free-space. L: Topological charge on the left hologram, R: Topological charge on the right hologram, $\Delta\varphi$: Phase difference between the beams.

L	R	$\Delta\varphi$	Mode produced
0	0	0	$HE_{11,v}$
0	0	π	$HE_{11,h}$
+1	-1	0	TE_{01}
+1	-1	π	TM_{01}
-1	+1	0	$HE_{21,o}$
-1	+1	π	$HE_{21,e}$

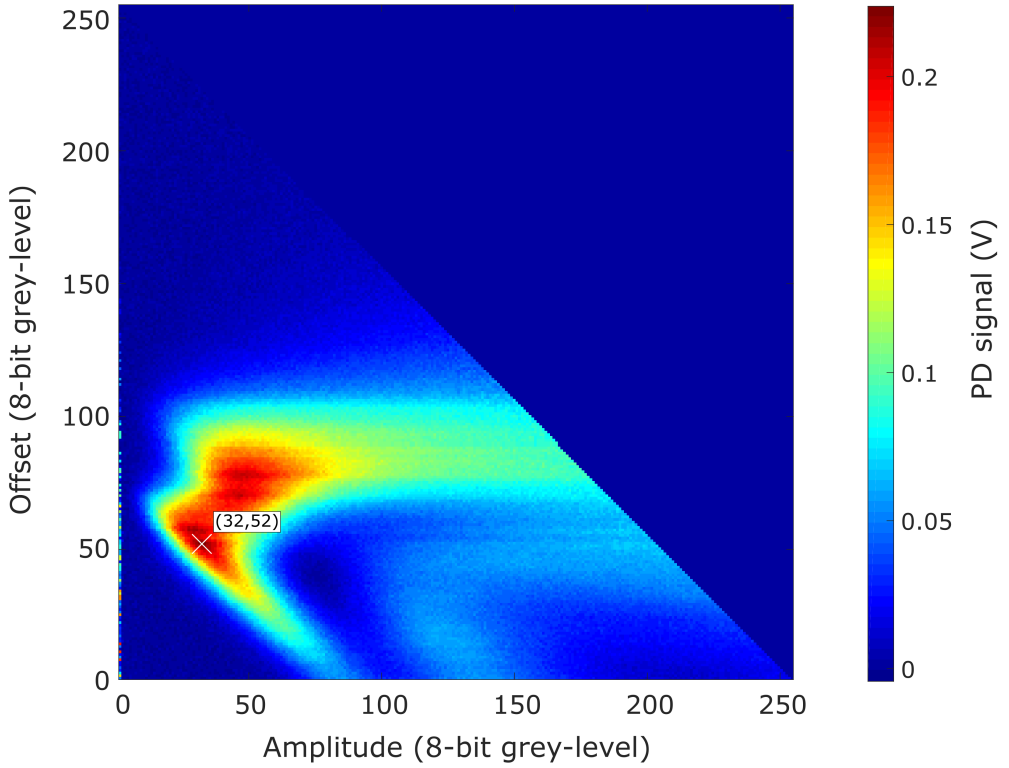

Figure 6.12: Optimization of the SLM at the 780 nm operating wavelength.

6.4.2 Fiber injection optimization

After generating the CVBs in free-space, their injection into the HOM-ONF is optimized. We first roughly adjust the injection of the beam via parallel transport, by mechanically adjusting the two mirrors before the fiber collimator at the input pigtail (i.e., M7 and DM1 in Fig. 6.10). Fine-tuning of the coupling is then performed by running an optimization algorithm that finds the best values of the vertical and horizontal tilt for both the left and right side of the SLM-generated gratings. The $4f$-telescope ensures that any change on the SLM is directly mapped onto the input end face of the HOM-ONF.

6.4.3 Input beam calibration

Small discrepancies between the optimal horizontal and vertical tilt values of the two beams are frequently found, leading to a change in the relative phase between the two recombined beams as their respective optical paths within BD1 are altered. Analysis and calibration of the probe beam after its optimization is the purpose of Area B. In Fig. 6.13(a), we have isolated the optical components depicted in Fig. 6.10 that were inside Area B, whereas Fig. 6.13(b) shows an image of the optics involved. The CVB to be analyzed is generated in Area A and split into two paths after entering a 90:10 BS. Most of the power is sent along the transmitted path to be injected into the HOM-ONF. The reflected beam first enters a BS whose only purpose is to combine the probe beam with a reference beam, also created in Area A. After passing through BD2, the

components of the shaped beam are split with respect to their polarization, yielding two well-separated polarization profiles on a CCD camera (Thorlabs, DCC3240N). The reference beam, exiting from C4 in the figure, passes through a HWP that rotates its linear polarization to 45°. This ensures the reference beam power is divided evenly after traveling through BD2, before impinging onto the camera.

To completely analyze, and eventually calibrate, the generated CVB, we use the so-called *interferometric decomposition into optical mode* (IDIOM) method, first developed by Fatemi and Beadie [114]. This method gives access to the phase and amplitude of an arbitrary electric field by interfering the flat phase-front of an off-axis homogeneous Gaussian reference beam with the beam to be analyzed. The complex coefficients of the generated CVBs can then be obtained from least-square fitting in the basis formed by the HOM-ONF's eigenmodes. Three measurements are necessary in order to unequivocally determine the phase and amplitude of the field: (i) the signal beam's intensity, I_{sig}, (ii) the reference beam's intensity, I_{ref}, and (iii) the combined intensities with the associated interference pattern, I_{tot}. An example of beam profiles obtained during such measurements is shown in Fig. 6.14.

We now mathematically demonstrate that the three aforementioned measurements are sufficient to determine the field of the probe beam in a manner similar to that in [114]. First, we know that I_{tot} is related to the signal and reference beams via the relation

$$\begin{aligned} I_{tot} &= |E_{sig}(\mathbf{r}) + E_{ref}(\mathbf{r})|^2 \\ &= I_{sig} + I_{ref} + 2\,\mathrm{Re}\left[E^*_{sig}(\mathbf{r})E_{ref}(\mathbf{r})\right], \end{aligned} \tag{6.1}$$

where E_{ref} and E_{sig} denote the electric fields of the reference and signal beams, and the star symbol represents the complex conjugate of the field. One can now isolate the intensity terms on one side of the equation to get the new relation:

$$I_{tot} - I_{sig} - I_{ref} = 2\,\mathrm{Re}\left[E^*_{sig}(\mathbf{r})E_{ref}(\mathbf{r})\right]. \tag{6.2}$$

The reference beam having a flat phase front can be expressed as the product of the field amplitude, $E_{0,ref}$ and a phase term relative to its tilt with the signal beam so that $E_{ref}(\mathbf{r}) = E_{0,ref}e^{i\mathbf{k}_{tilt}\cdot\mathbf{r}}$. To determine k_{tilt}, we take the Fourier transform of Eq.(6.2), for which two values[7] arise in k-space

$$\mathcal{F}\left(2\,\mathrm{Re}\left[E^*_{sig}(\mathbf{r})E_{0,ref}e^{i(\mathbf{k}_{tilt}\cdot\mathbf{r})}\right]\right) = g^*(\mathbf{k}-\mathbf{k}_{tilt}) + g(\mathbf{k}+\mathbf{k}_{tilt}), \tag{6.3}$$

with $g(\mathbf{k}) = \mathcal{F}[E^*_{sig}(\mathbf{r})E_{0,ref}]$. The two components are redundant of each other, allowing us to discard one by applying a digital mask in k-space. We experimentally measure k_{tilt} for both the horizontal and vertical polarization components, by calculating the center-of-mass of the beam in the Fourier-space. With k_{tilt} determined, we now take the inverse Fourier transform of the selected k-space component, which gives

$$\mathcal{F}^{-1}[g(\mathbf{k}+\mathbf{k}_{tilt})] = E^*_{sig}(\mathbf{r})E_{ref}(\mathbf{r})e^{i(\mathbf{k}_{tilt}\cdot\mathbf{r})}. \tag{6.4}$$

This unequivocally determines E_{sig}, since k_{tilt} has been evaluated, and we know E_{ref} from the measurement of I_{ref}, as the reference beam is assumed to have a flat, homogeneous phase front and a positive amplitude everywhere.

[7] Three values experimentally as a DC component is always present at the center of the k-space.

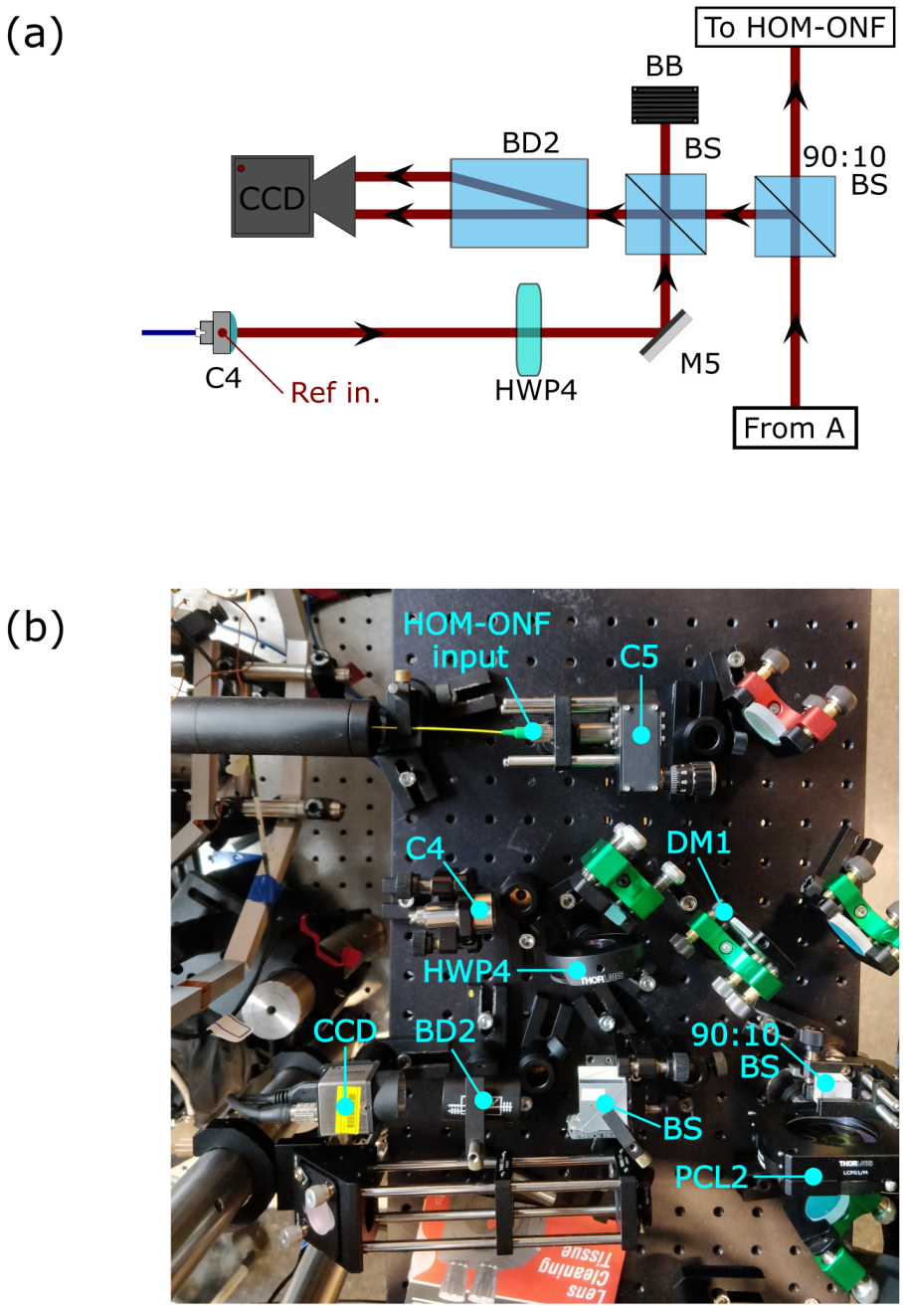

Figure 6.13: (a) Schematic and (b) photograph of the experimental setup used for the calibration of the input beam. Optical components are labeled as in Fig. 6.10.

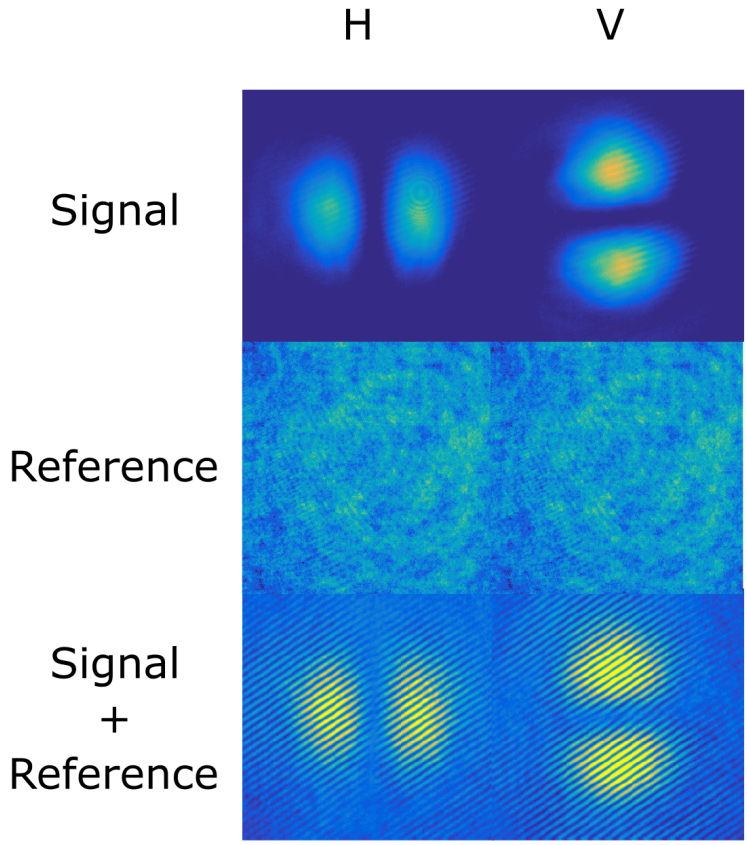

Figure 6.14: Intensity measurements necessary for the characterization of a generated CVB. The intensities of the signal and reference beams are first recorded, for both their horizontal and vertical polarization components. Their overlap leads to an interference pattern that helps determine the phase and amplitude of the signal beam.

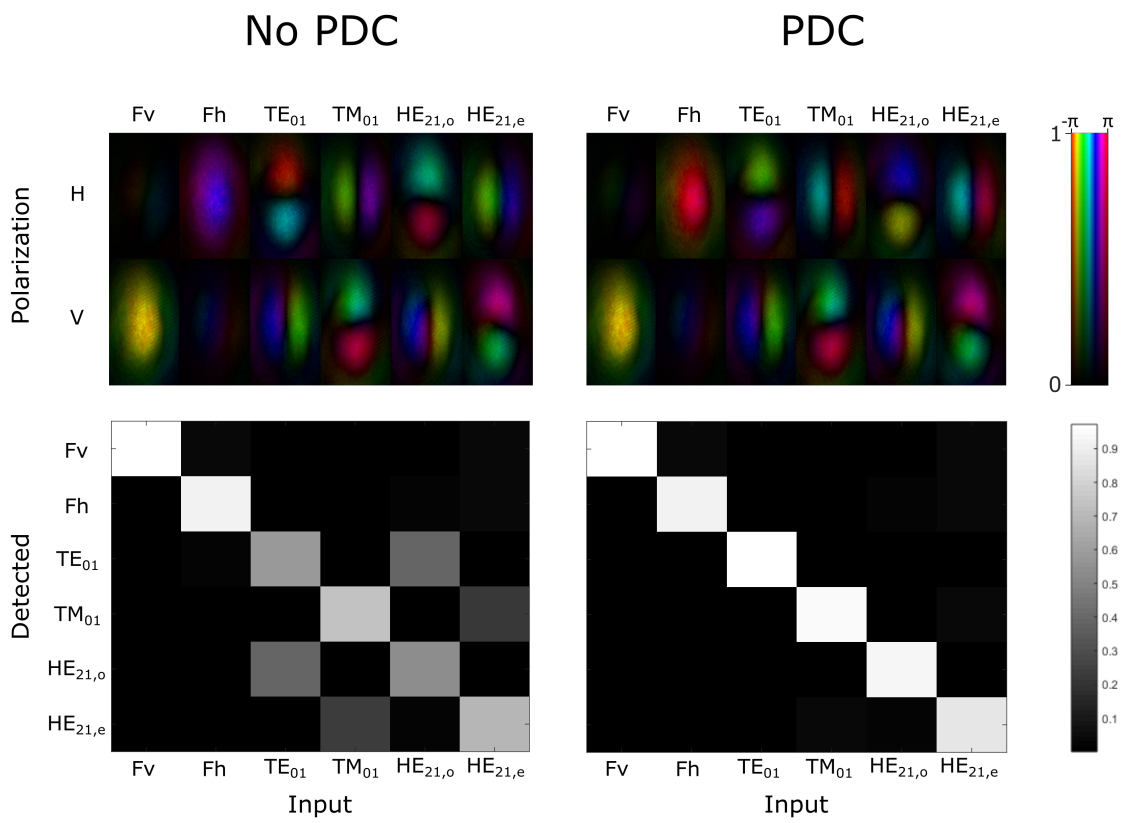

Figure 6.15: Effect of phase discrepancy correction (PDC) on the detected beam profile and associated transfer matrix (TRM). The left side of the figure shows the phase and amplitude of each mode of interest (top), and the computed TRM (bottom) without PDC. The right side of the figure shows the same items after PDC was applied.

As seen in the example presented in Fig. 6.14, CVBs are expected to display lobed profiles when split in polarization. These lobe profiles should always be perpendicular to each other and oriented vertically or horizontally if both the recombined LG beams are propagating in phase. We mentioned previously that a small difference in their relative phase could arise after optimizing the injection of the probe beam into the HOM-ONF. In this case, we observe lobes that are no longer aligned with the horizontal or vertical axes of the camera. This is easily corrected by adjusting the phase difference between the two holograms displayed on the SLM until the two lobes return to their expected positions. These ideal profiles can be used to evaluate the quality of the CVBs by proceeding with the mode decomposition and calculation of the transfer matrix (TRM) of the system.

Browsing through the available CVBs created by the SLM, we first align the imaged profile with a mode-dependent region of interest (ROI) on the camera, shaped to look like the target mode. This, essentially, tells the computer what to look for and where to look for it. In addition to the mode-dependent ROI, the mode-dependent phase profile is also encoded in the computer. This allows us to compute the coefficients in the TRM of the system for each CVB generated. We show the measured phases and amplitudes, along with the associated TRMs in Fig. 6.15. One can clearly see that the TRM on the left contrasts drastically with the expected diagonal matrix. This is due to a phase

discrepancy between the horizontal and vertical polarization components induced when beams are traveling through the BD, leading to a biased analysis of the CVB, which needs to be compensated for. A phase discrepancy compensation (PDC) algorithm developed by S.P. Mekhail[8] and integrated with the main LabVIEW program allows us to correct for this bias and compute the fields and TRM accurately. Moreover, the PDC algorithm was developed to be independent of the beam profile, meaning that it can also be applied when decomposing the modes excited at the output of the HOM-ONF.

6.4.4 Mode decomposition of the output profile and transfer matrix calculation

With the CVBs generated and calibrated, and after optimizing the injection of the probe beam into the HOM-ONF, we are now ready to decompose the mode excitation at the output of the fiber. This is the purpose of Area C, the optical components of which are schematized and pictured in Fig. 6.16. The setup can be subdivided into two parts: the top part is practically identical to the mode decomposition setup of Area B with the exception of the sCMOS camera (Andor, Zyla sCMOS 4.2), whereas the bottom part shows the coupling to an SPCM (Excelitas, SPCM-AQRH-FC), which allows us to monitor the transmission during experiments. The use of the sCMOS camera can be justified as experiments where atoms are involved require no more than a few nW of power. It was therefore crucial to make sure we could integrate the sCMOS camera within our setup and interface it with the LabVIEW program. A 1064 nm beam is also injected through the HOM-ONF to prevent adsorption of Rb atoms and to maintain the fiber at a controllable temperature.

To decompose the output profile in terms of the HOM-ONF eigenmodes, we used a similar approach to that presented in the previous section, measuring the signal, reference, and combined intensities, namely I_{sig}, I_{ref}, and I_{tot}. An example of such a measurement for an output profile is shown in Fig. 6.17. The reference beam is Gaussian, with a diameter exceeding that of the collimated output of the HOM-ONF.

These measurements are repeated 100 times for each of the six modes and an average TRM is calculated along with its standard deviation. We present a typical output profile decomposition and associated average TRM calculation in Fig. 6.18. The output fields' phases and amplitudes were reconstructed in each case, showing a Gaussian-looking output when the CVB mimics a fundamental mode and two-lobed profiles when the CVB mimics a HOM. The calculated transfer matrix is mostly block-diagonal, which indicates that cross-talk among the LP-families is minimal. Within each LP family, however, the mode coupling is found to be asymmetric. This asymmetry is generally expected with optical fibers [194], and stems from defects in the fiber, or twists and bends between input and output. For optical nanofibers, imperfect tapering might also play a role. It can also be seen that some of the HOMs (i.e., $HE_{21,e}$, and $HE_{21,o}$) couple to the fundamental modes. This is likely the result of either imperfect beam-shaping of these modes in free-space or imperfect coupling into the nanofiber and shall be corrected in future runs of the experiment. The associated standard deviation matrix shows that the system is relatively stable over the duration of the experiment. The data were acquired for an input probe

[8]The details of this algorithm can be found in S.P. Mekhail's PhD thesis.

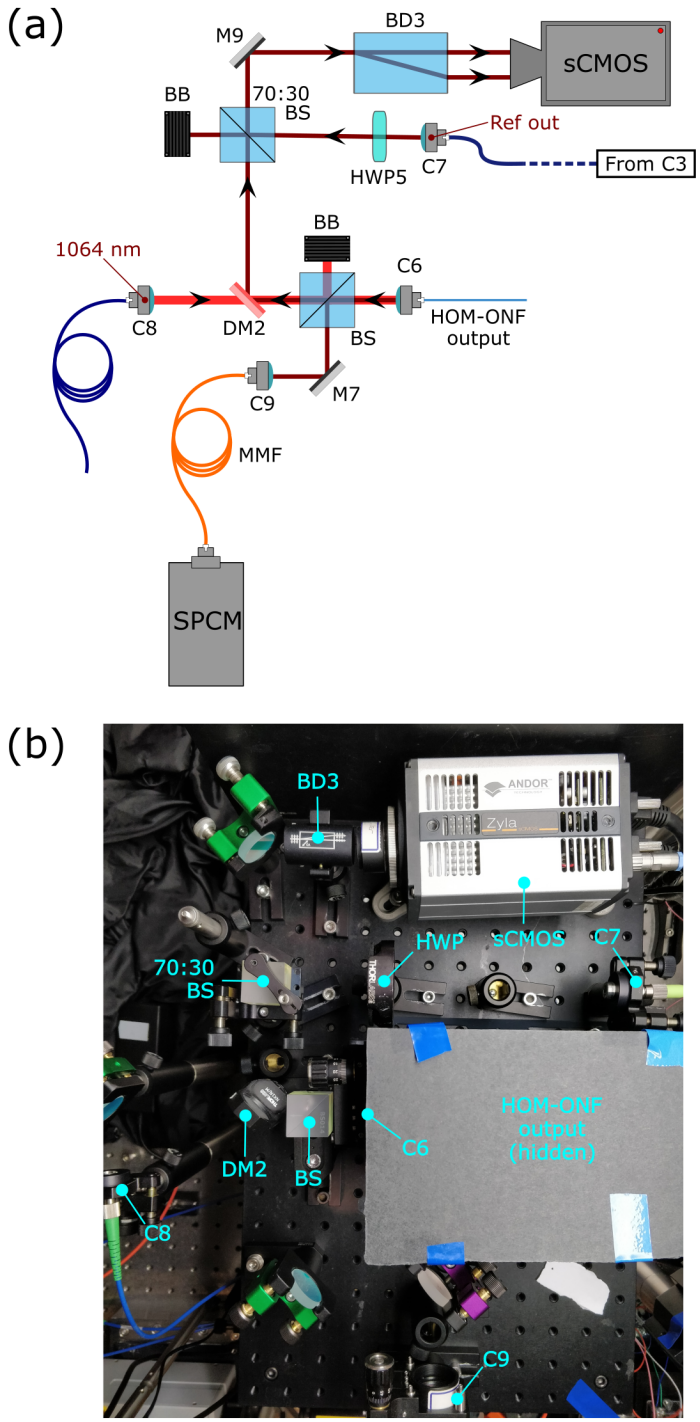

Figure 6.16: (a) Schematic and (b) image of the experimental setup used to decompose and monitor the transmission of the output beam. Optical components are labeled as in Fig. 6.10.

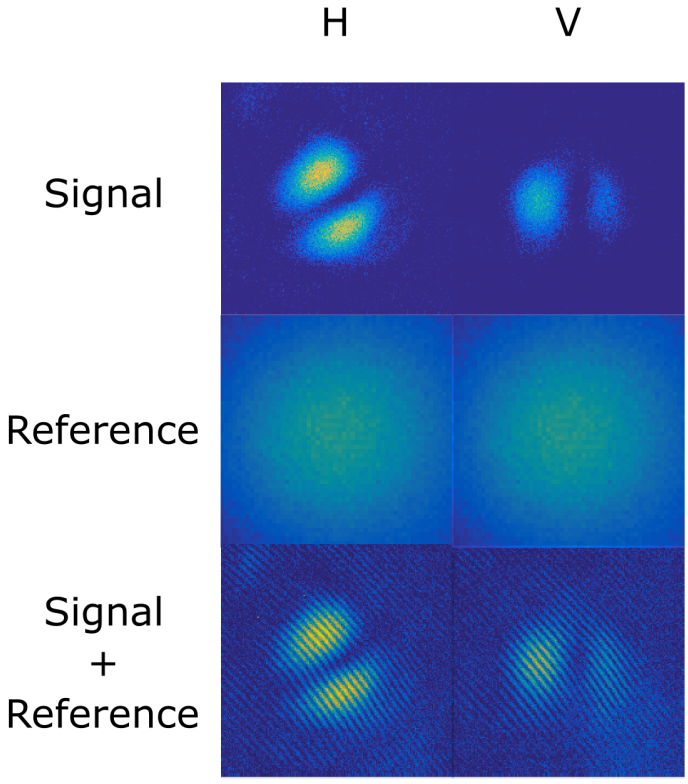

Figure 6.17: A typical intensity measurements for the characterization of the output profile.

beam power of 7.2 nW in the fundamental mode and for an exposure time of the sCMOS camera of 75 ms. We also injected 500 μW of 1064 nm light into the HOM-ONF.

6.5 Conclusion

Selective mode excitation at the waist of an HOM-ONF is desired for any HOM-based application and could serve as a powerful tool for nanofiber-based experiments with cold atoms, which have so far almost entirely relied on the fundamental mode alone. We presented a first generation of experiments aiming at measuring the correlation between the modes excited at the waist and the observed output profile. For these experiments, identifiable combinations of modes at the output of the HOM-ONF were selectively excited via twisting of the input pigtail. In each case, the absorption by atoms in a MOT overlapped with the waist was compared to results from FEM simulations of the system. This hinted that a direct correlation between mode excitation at the waist and the observed output profile may exist, leading to the hypothesis that mode mixing mainly occurs in the down-taper, whereas the up-taper does not affect the modes significantly. An overhaul of the experimental setup, in which every essential component could be remotely accessed and controlled, allowed us to perform mode demultiplexing on the beam profile produced at the output of a nanofiber after injecting it with shaped beams from free-space mimicking the HOMs. This, in turn, allowed us to precisely evaluate the transfer matrix of the system, constituting a major step forward for any future higher order mode experiments given the degree of precision required for such a project. The experimental setup now allows us to identify, both qualitatively and quantitatively, the mix of modes that forms any output profile. In the future, the transfer matrices of the system with and without atoms interacting with the evanescent field of the different modes in the nanofiber shall be compared in order to infer the modes at the waist. Moreover, inverting the transfer matrix of the system should allow us to correct for any mode scrambling in the down-taper of the fiber and to reconstruct any desired mode at the output of the HOM-ONF. This project will determine the validity of our hypothesis that mode scrambling does not occur to a detrimental level in the up-taper.

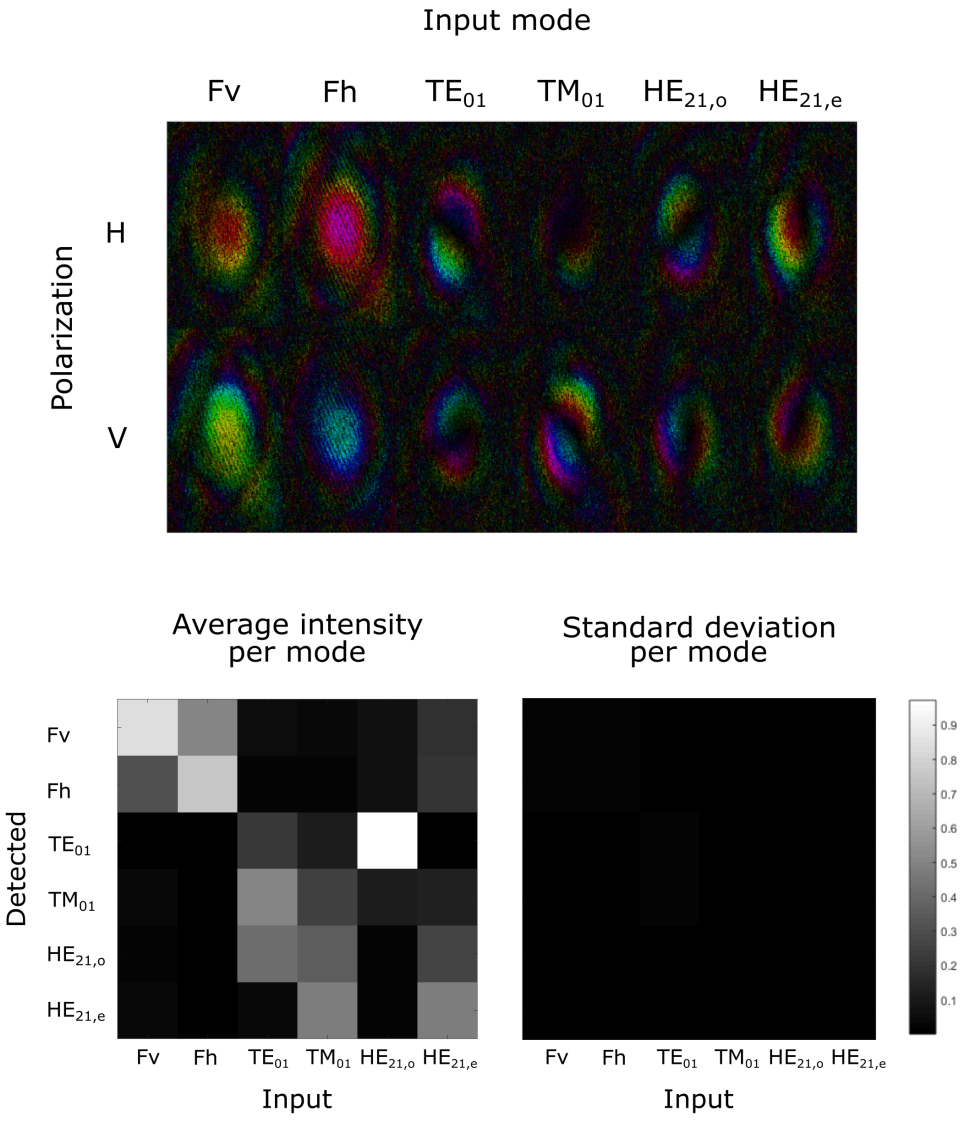

Figure 6.18: Field analysis of the output profile (top row) and associated average TRM with standard deviation (bottom row). The relevant experimental parameters are given in the text.

Chapter 7

Conclusion

The work carried out during this PhD project, and presented in this thesis, has been largely motivated by the development of methods to harness the full potential of HOMs in ONFs interfaced with cold atomic systems. This is valuable for fields of research aimed at creating atom-photon hybrid quantum systems, in particular for the development of new tools in nanofiber-based experiments, which have, so far, relied on exploiting the fundamental mode. The state-of-the-art of the ONF-cold atoms field of research was presented, showing the theoretical promises offered if one were to exploit HOMs in such systems, while also highlighting the lack of experimental work in this area of research.

The theory of HOM propagation in tapered fibers was provided, along with a detailed explanation of the fabrication methods employed to produce a high-transmission HOM-ONF, tailored to support up to the LP_{11} family of modes at 780 nm. A simple and cheap method to shield the fiber during installation inside an ultrahigh vacuum chamber was also described, with emphasis on the importance of cleanliness. The theory of atom cooling was also briefly presented before showing its experimental implementation in the cold atom setup used throughout this PhD project.

Chapter 4 summarized the results of our theoretical investigation into the quadrupole interaction between the evanescent field of a HOM-ONF and a single atom. These showed that nanofibers are excellent platforms to drive quadrupole-allowed transitions, in particular when compared to free-space beams. These results may find applications in future research on probing electric quadrupole transitions of atoms, molecules, and particles using the fundamental mode and HOMs of ONFs. Direct access to electric quadrupole transitions might be beneficial for fiber-based optical clocks [195]. Although the transition probability of such a transition is at its highest when driven by one of the fundamental modes, it remains significant when driven by a HE_{21} mode. This is of interest for the development of high-density information transfer protocols in atomic systems, as a photon in a combination of HE_{21} modes may carry OAM in addition to SAM [95, 135]. The theoretical study was done in the context of an experimentally addressable system: the dipole-forbidden, quadrupole-allowed $5S_{1/2} \rightarrow 4D_{5/2}$ transition in ^{87}Rb atoms. Initial experimental results obtained by other group members are already promising. The only dipole-allowed decay of this state to the ground state is via the intermediate level, $5P_{3/2}$, by cascaded emission of two photons at 1530 nm and 780 nm. The emitted photons are correlated and can be entangled [173, 196]. This could open up the possibility to develop a fiber-based source of entangled photon pairs at wavelengths relevant to telecommunica-

tions and atomic references.

Work on a two-photon transition at 993 nm was also discussed in Chapter 5. The first part of the project was done with a hot vapor of Rb atoms in order to confirm the selection rules associated with $S-S$ transitions, but also to study the effects of the probing beam power on the transition. It was found that this transition was well-suited as a frequency reference, as it is insensitive to stray magnetic fields, and frequency stabilization on the spectroscopic peaks is feasible. More work with the hot vapor could be envisaged; one could, for example, study whether the $S-S$ selection rules are modified when the exciting beams carry OAM in addition to SAM.

Experiments done with an ONF embedded in a cold atom cloud showed evidence of strong coupling, for which a theoretical model has yet to be developed. Exploiting the special selection rules associated with the transition, it was shown that cold atoms in a MOT could potentially be used to perform polarization tomography at the ONF's waist. The results are still preliminary, however, and more work is required before being able to fully characterize the system. Future experiments will be designed to probe a large portion of polarization states over the whole Poincaré sphere, thereby allowing one to establish a relationship between the polarization states at the input, waist, and output of an ONF. Calculation of Mueller matrices at each point of the system will enable a compensation scheme to be developed, thus leading to full control of the polarization state at the waist of the ONF. Members of our group have successfully achieved the latter in air, using a transverse optical fiber as a probe [116]. This is particularly valuable in the framework of selective mode excitation at the waist when considering HOMs, but also for fundamental mode based experiments where polarization is crucial.

The main project of this thesis, dedicated to the development of methods to selectively excite guided modes at the waist of a HOM-ONF, was presented in Chapter 6. Some of the preliminary results were shown, highlighting the technical challenges associated with such an experiment, but also hinting that the output profile may reflect the modes excited at the waist. The system overhaul that allowed us to remotely operate the experiment was described in detail. Our method for generating and calibrating CVBs that mimic HOMs in free-space was presented, demonstrating the close match between the generated polarization profiles and the modes supported by the nanofiber. The output was decomposed in terms of its components in the HOM-ONF's eigenmode basis, giving some interesting preliminary results. All the experiments on the HOM project done during this PhD have not yet yielded results that allow us to reliably determine the modes excited at the waist, but certainly provide advances in this area and give us plenty of ideas on future experiments.

Some experiments in which a MOT was overlapped with the waist of the HOM-ONF have already been done. A difference in transfer matrices, calculated with and without atoms near the fiber waist, was observed, potentially indicating a mode-dependent absorption of the probe beam. However, after careful analysis of the collected data, we found that the probe beam had been fluctuating between sets of experiments (experiments with the MOT were carried out a few weeks after obtaining the results presented in Section 6.4), and that the laser diode had to be replaced. This delayed the project and prevented us from doing additional experiments. In the future, these experiments will be redone along with the associated transfer matrix calculations. Differences between these transfer matrices, combined with theoretical simulations of the expected absorption from

different combinations of modes, should give us sufficient information to infer the modes excited at the waist of an HOM-ONF.

Another plan is to invert the transfer matrix of the system, calculated without atoms present near the waist, so that it can be used to reconstruct any desired mode profile at the output of the HOM-ONF. We have already performed some preliminary inversion of experimentally evaluated transfer matrices in MATLAB, using the Gerchberg–Saxton algorithm [197]. This has shown promising results, from which we were able to simulate the reconstruction of each mode supported by our fiber. The code has yet to be incorporated within the LabVIEW program that runs the HOM experiment. With this new tool at hand, and in addition to probing the waist with cold atoms, we shall be able to test our hypothesis that the down-taper constitutes the main cause of mode scrambling and that the up-taper does not affect the mode excitation between waist and output significantly. If these methods are found to be insufficient for selective mode excitation at the waist, the comparison of transfer matrices calculated in the presence and absence of atoms near the waist should still provide valuable information on the interaction between higher order fiber-guided modes and atoms. This has never been studied to this level of detail before.

Appendix A

HOM eigenvalue equations from Maxwell's equations

The results presented in what follows are exact solutions to Maxwell's equations for the guided modes. This is only valid in the so-called *strongly guiding* regime, in which the refractive index of the core, n_1, is much larger than the refractive index of the cladding, n_2. This regime directly applies to ONFs in which $n_1 \approx 1.45$ and $n_2 = 1$. For standard optical fibers, generally $n_1 - n_2 << 1$ and the resulting modal decomposition becomes degenerate in β to form the *linearly polarized* (LP) modes. The mathematical development for such modes has been covered elsewhere (see for example pp 66-73 of [92]) and shall not be developed here.

A.1 Maxwell's Equations for a Cylindrical Waveguide

The mathematical development presented in this section is largely based on Chapter 3 of [92]. Consider a cylindrical waveguide made out of non-magnetic and source free materials, with core radius, a, and cladding radius, b. This can be modeled by a step-index profile in a cylindrical coordinate system following

$$n(r) = \begin{cases} n_1, \text{ if } r < a \\ n_2, \text{ if } r > a \end{cases} \tag{A.1}$$

with $n_1 > n_2$. Since optical fibers generally have a cladding radius much larger than that of the core, it can be safely assumed that $b = \infty$ in what follows. Maxwell's equations for light propagating in such a waveguide, assumed to be isotropic and source free, are given by

$$\boldsymbol{\nabla} \times \mathbf{H} = \epsilon(r) \frac{\partial \mathbf{E}}{\partial t}, \tag{A.2}$$

$$\boldsymbol{\nabla} \times \mathbf{E} = -\mu_0 \frac{\partial \mathbf{H}}{\partial t}, \tag{A.3}$$

$$\boldsymbol{\nabla} \cdot (\epsilon(r)\mathbf{E}) = 0, \tag{A.4}$$

$$\boldsymbol{\nabla} \cdot \mathbf{H} = 0. \tag{A.5}$$

Taking the curl of Eq. A.4 and using the relation $\boldsymbol{\nabla} \times (\boldsymbol{\nabla} \times \mathbf{E}) = \boldsymbol{\nabla}(\boldsymbol{\nabla} \cdot \mathbf{E}) - \boldsymbol{\nabla}^2$, and then using Eq A.3 and Eq. A.5 to simplify the resulting expression, we get the wave equation for $\mathbf{E}$

$$\boldsymbol{\nabla}^2\mathbf{E} - \mu_0\epsilon(r)\frac{\partial^2\mathbf{E}}{\partial t^2} = -\boldsymbol{\nabla}\left(\frac{\mathbf{E}}{\epsilon(r)} \cdot \boldsymbol{\nabla}\epsilon(r)\right). \tag{A.6}$$

Replacing $\mathbf{E}$ by $\mathbf{H}$ in the previous expression gives a similar equation for the magnetic field.

A.2 Eigenvalue Equations

Due to the cylindrical symmetry of the waveguide, it is convenient to solve the wave equation in cylindrical coordinates with the z-axis pointing in the direction of the fiber axis. This allows one to solve for the field inside the core and the cladding separately. The full field is later obtained by applying boundary conditions and ensuring continuity at $r = a$. When solving Eq. A.6 inside either the core or the cladding, the right side vanishes as the term $\boldsymbol{\nabla}\epsilon(r)$ becomes 0 since the medium considered is homogeneous.

With the previous choice of $z-$axis, the wave propagating along the waveguide can be expressed as

$$\begin{bmatrix}\mathbf{E}(\mathbf{r},t)\\ \mathbf{H}(\mathbf{r},t)\end{bmatrix} = \begin{bmatrix}\mathbf{E}(r,\phi)\\ \mathbf{H}(r,\phi)\end{bmatrix}\exp(i(\omega t - \beta z)), \tag{A.7}$$

where β is the propagation constant of the wave, $\omega = 2\pi\nu$ is the angular frequency and ν the wave frequency. Before moving further, it is necessary to introduce the expression for the Laplace operator in cylindrical coordinates given by

$$\nabla^2_{\text{cyl}} = \partial_r^2 + \frac{1}{r}\partial_r + \frac{1}{r^2}\partial_\phi^2 + \partial_z^2, \tag{A.8}$$

where the shorthand notation for the partial derivative $\partial_m = \partial/\partial m$ with $m = r, \phi, z$, has been used. Introducing the expressions of Eqs. A.8 in their respective wave equation (Eqs. A.6), it can be shown [92] that each transverse component of a field can be written in terms of E_z and H_z as follow:

$$\begin{aligned} E_r &= \frac{-i\beta}{\omega^2\mu_0\epsilon - \beta^2}\left(\partial_r E_z + \frac{\omega\mu_0}{\beta}\frac{\partial_\phi}{r}H_z\right),\\ E_\phi &= \frac{-i\beta}{\omega^2\mu_0\epsilon - \beta^2}\left(\frac{\partial_\phi}{r}E_z - \frac{\omega\mu_0}{\beta}\partial_r H_z\right), \end{aligned} \tag{A.9}$$

for the components of the electric field in cylindrical coordinates, and similarly

$$\begin{aligned} H_r &= \frac{-i\beta}{\omega^2\mu_0\epsilon - \beta^2}\left(\partial_r H_z - \frac{\omega\epsilon}{\beta}\frac{\partial_\phi}{r}E_z\right),\\ H_\phi &= \frac{-i\beta}{\omega^2\mu_0\epsilon - \beta^2}\left(\frac{\partial_\phi}{r}H_z + \frac{\omega\epsilon}{\beta}\partial_r E_z\right), \end{aligned} \tag{A.10}$$

for the components of the magnetic field in cylindrical coordinates. Solving the wave equation for the axial components E_z and H_z is enough to determine all other components

of the light wave. Inserting the exponential term of Eq. A.7 into the wave equation A.6 gives

$$\left(\nabla^2_{\mathrm{T,cyl}} + (n^2k^2 - \beta^2)\right)\Psi_z = 0, \tag{A.11}$$

where we have introduced $\nabla^2_{\mathrm{T,cyl}} = \nabla^2 - \partial^2/\partial z^2$, which is the transverse Laplace operator in cylindrical coordinates, $\Psi_z = \{E_z, H_z\}$ represents the $z-$component of either the electric or magnetic field of the input light, respectively, and $k = \omega/c$ is the wave number defined with $c = 1/\sqrt{\epsilon_0\mu_0}$ the speed of light in vacuum. The solution to this equation can be expressed as the combination of a radial and an angular part and takes the form

$$\Psi_z = \Psi(r)\exp(\pm il\phi), \tag{A.12}$$

in which $l = 0, 1, 2, 3, \ldots$ is a positive integer called the *azimuthal mode order* [95], and $\Psi(r)$ is the radial field distribution. The sign inside the exponential term defines the polarization of the wave, namely, clockwise circular polarization if "+", and counter-clockwise circular polarization if "-". Inserting this into Eq. A.11 gives

$$\partial_r^2\Psi_z + \frac{1}{r}\partial_r\Psi_z + \left(n^2k^2 - \beta^2 - \frac{l^2}{r^2}\right)\Psi_z = 0. \tag{A.13}$$

This equation is the Bessel differential equation, for which the solutions are Bessel functions of order l. For either field in Ψ_z, the general solution to Eq. A.13 can take a different form depending on the sign of $n^2k^2 - \beta^2$. When $n^2k^2 - \beta^2 > 0$, the general solution to Eq. A.13 takes the form

$$\Psi(r) = c_1 J_l(hr) + c_2 Y_l(hr), \tag{A.14}$$

in which $\Psi(r) = \{e_z(r), h_z(r)\}$, $h^2 = n^2k^2 - \beta^2$, c_1 and c_2 are complex constants determined by the boundary conditions, and J_l, Y_l are Bessel functions of the first and second kind, respectively, of order l. When $n^2k^2 - \beta^2 < 0$, the general solution to Eq. A.13 takes the form

$$\Psi(r) = c_3 I_l(qr) + c_4 K_l(qr), \tag{A.15}$$

where $q^2 = \beta^2 - n^2k^2$, c_3 and c_4 are again complex constants determined by the boundary conditions, and I_l, K_l are modified Bessel functions of the first and second kind, respectively, of order l.

Application of the boundary conditions at the core-cladding transition to the solutions obtained above enables one to get the expression of the fields in the guided modes. For a guided mode to be transversely confined inside the waveguide, we have the condition

$$n_1k_0 > \beta > n_2k_0, \tag{A.16}$$

with k_0 the wave number in vacuum. This means that the mode in the core fulfills $h^2 = n_1^2k_0^2 - \beta^2 > 0$. Applying the condition to Eq. A.14 gives

$$r < a: \quad e_z(r) = AJ_l(hr), \quad \text{and} \quad h_z(r) = BJ_l(hr), \tag{A.17}$$

where A and B are complex coefficients, and the coefficients in front of the Y_l functions have been set to $c_2 = 0$ because Y_l diverges for $r \to 0$. In the cladding, we have $q^2 = \beta^2 - n_2^2k_0^2 > 0$ which applied to Eq. A.15 gives

$$r > a: \quad e_z(r) = CK_l(hr), \quad \text{and} \quad h_z(r) = DK_l(hr), \tag{A.18}$$

where C and D are complex coefficients, and the coefficients in front of the I_l functions have been set to $c_1 = 0$ because the function diverges for $r \to \infty$. Inserting these results in Eq. A.12 and subsequently in Eqs A.11 gives expressions for the guided fields in cylindrical coordinates.

For $r < a$ (core)

$$\begin{aligned} E_r(r) &= \frac{-i\beta}{h^2}\left[AhJ_l'(hr) + \frac{i\omega\mu_0 l}{\beta r}BJ_l(hr)\right]\exp[i(\omega t + l\phi - \beta z)] \\ E_\phi(r) &= \frac{-i\beta}{h^2}\left[\frac{il}{r}AJ_l(hr) - \frac{\omega\mu_0}{\beta}BhJ_l'(hr)\right]\exp[i(\omega t + l\phi - \beta z)] \\ E_z(r) &= AJ_l(hr)\exp[i(\omega t + l\phi - \beta z)] \end{aligned} \tag{A.19}$$

and

$$\begin{aligned} H_r(r) &= \frac{-i\beta}{h^2}\left[BhJ_l'(hr) - \frac{i\omega\epsilon_0 n_1^2 l}{\beta r}AJ_l(hr)\right]\exp[i(\omega t + l\phi - \beta z)] \\ H_\phi(r) &= \frac{-i\beta}{h^2}\left[\frac{il}{r}BJ_l(hr) + \frac{\omega\epsilon_0 n_1^2}{\beta}AhJ_l'(hr)\right]\exp[i(\omega t + l\phi - \beta z)] \\ H_z(r) &= BJ_l(hr)\exp[i(\omega t + l\phi - \beta z)] \end{aligned} \tag{A.20}$$

where $J_l' = dJ_l(hr)/d(hr)$, and for $r > a$ (cladding),

$$\begin{aligned} E_r(r) &= \frac{i\beta}{q^2}\left[CqK_l'(qr) + \frac{i\omega\mu_0 l}{\beta r}DK_l(qr)\right]\exp[i(\omega t + l\phi - \beta z)] \\ E_\phi(r) &= \frac{i\beta}{q^2}\left[\frac{il}{r}CK_l(qr) - \frac{\omega\mu_0}{\beta}DqK_l'(qr)\right]\exp[i(\omega t + l\phi - \beta z)] \\ E_z(r) &= CK_l(qr)\exp[i(\omega t + l\phi - \beta z)] \end{aligned} \tag{A.21}$$

and

$$\begin{aligned} H_r(r) &= \frac{i\beta}{q^2}\left[DqK_l'(qr) - \frac{i\omega\epsilon_0 n_2^2 l}{\beta r}CK_l(qr)\right]\exp[i(\omega t + l\phi - \beta z)] \\ H_\phi(r) &= \frac{i\beta}{q^2}\left[\frac{il}{r}DK_l(qr) + \frac{\omega\epsilon_0 n_2^2}{\beta}CqK_l'(qr)\right]\exp[i(\omega t + l\phi - \beta z)] \\ H_z(r) &= DK_l(qr)\exp[i(\omega t + l\phi - \beta z)] \end{aligned} \tag{A.22}$$

where $K_l' = dK_l(qr)/d(qr)$. The fields have to be continuous at the boundary between the core and the cladding, that is, at $r = a$. This leads to conditions on the constants $A, B, C,$ and$D$

$$\begin{aligned} AJ_l(ha) - CK_l(qa) &= 0, \\ A\left[\frac{il}{h^2 a}J_l(ha)\right] + B\left[\frac{-\omega\mu_0}{h\beta}J_l'(ha)\right] + C\left[\frac{il}{q^2 a}K_l(qa)\right] + D\left[\frac{-\omega\mu_0}{q\beta}K_l'(qa)\right] &= 0 \\ BJ_l(ha) - DK_l(qa) &= 0, \\ A\left[\frac{-\omega\epsilon_0 n_1^2}{h\beta}J_l'(ha)\right] + B\left[\frac{il}{h^2 a}J_l(ha)\right] + C\left[\frac{-\omega\epsilon_0 n_2^2}{q\beta}K_l'(qa)\right] + D\left[\frac{il}{q^2 a}K_l(qa)\right] &= 0 \end{aligned} \tag{A.23}$$

with the same use of the "prime" notation as in previous expressions. This leads to a nontrivial solution for the values of each constant, provided that the determinant of their coefficients in Eq. A.23 vanishes. This condition gives the eigenvalue equation

$$\left(\frac{J_l'(ha)}{haJ_l(ha)}+\frac{K_l'(qa)}{qaK_l(qa)}\right)\left(\frac{n_1^2J_l'(ha)}{haJ_l(ha)}+\frac{n_2^2K_l'(qa)}{qaK_l(qa)}\right)=l^2\left[\left(\frac{1}{qa}\right)^2+\left(\frac{1}{ha}\right)^2\right]^2\left(\frac{\beta}{k_0}\right)^2 \tag{A.24}$$

which allows to determine the value of the propagation constant β for each l. Noting that Eq. A.24 is quadratic in $J_l'(ha)/haJ_l(ha)$, and solving for this value yields two solutions, corresponding to two of the modes allowed to propagate in an ONF,

the EH-modes,

$$\frac{J_{l+1}(ha)}{haJ_l(ha)}=\frac{n_1^2+n_2^2}{2n_1^2}\frac{K_l'(qa)}{qaK_l(qa)}+\left(\frac{l}{(ha)^2}-R\right) \tag{A.25}$$

and the HE-modes,

$$\frac{J_{l-1}(ha)}{haJ_l(ha)}=-\left(\frac{n_1^2+n_2^2}{2n_1^2}\right)\frac{K_l'(qa)}{qaK_l(qa)}+\left(\frac{l}{(ha)^2}-R\right) \tag{A.26}$$

with

$$R=\left[\left(\frac{n_1^2-n_2^2}{2n_1^2}\right)^2\left(\frac{K_l'(qa)}{qaK_l(qa)}\right)^2+\left(\frac{l\beta}{n_1k_0}\right)^2\left(\frac{1}{q^2a^2}+\frac{1}{h^2a^2}\right)^2\right]^{1/2}. \tag{A.27}$$

These modes are usually defined for $l\neq 0$. One can use their characterizing conditions to obtain expressions for the constants $A, B, C,$ and$D$ in order to find the full expression of each component of their corresponding guided fields.

In the special case where $l=0$, two new families of solutions emerge. In the first case, setting $l=0$ in Eq. A.25 yields

$$\frac{J_1(ha)}{haJ_0(ha)}=-\frac{K_1(qa)}{qaK_0(qa)} \tag{A.28}$$

and in the second case, setting $l=0$ in Eq. A.26 yields

$$\frac{J_1(ha)}{haJ_0(ha)}=-\frac{n_2^2K_1(qa)}{qan_1^2K_0(qa)} \tag{A.29}$$

where special relation between Bessel functions and their derivatives have been used in both equations. With condition A.28 inserted in A.23, the constants A and C vanish. Substituting $A=C=l=0$ in Eqs. A.19 to A.22, shows that the only non-zero field components are H_r,H_z, and E_ϕ. Similarly, condition A.29 yields, $B=D=0$ which in turn gives the non-zero field components E_r,E_z, and H_ϕ. These modes are called transverse electric (TE) and transverse magnetic (TM), respectively.

Appendix B

Development of the Mathematical Expressions Relevant to a Quadrupole Interaction

B.1 Multipole Expansion and Associated Electric Interaction Energy

B.1.1 Multipole expansion

Let us assume a charge q is placed at a point defined by the vector $\mathbf{r}'$ within an appropriate frame of reference. We are interested in finding $\Phi(\mathbf{r})$, the Coulomb potential generated by this charge at a point $\mathbf{r}$. From electrostatic we know that we can write

$$\Phi(\mathbf{r}) = \frac{1}{4\pi\epsilon_0}\frac{q}{|\mathbf{r}-\mathbf{r}'|}, \tag{B.1}$$

in which ϵ_0 is the vacuum permittivity, and $|\mathbf{r}-\mathbf{r}'|$ is the norm of the $\mathbf{r}-\mathbf{r}'$ vector. We are particularly interested in expanding the $1/|\mathbf{r}-\mathbf{r}'|$ term. We can expand the norm of the vector subtraction as follow:

$$\begin{aligned} |\mathbf{r}-\mathbf{r}'| &= \sqrt{r^2 - 2\,\mathbf{r}\cdot\mathbf{r}' + r'^2} \\ &= r\sqrt{1 - 2\,\frac{\hat{\mathbf{r}}\cdot\mathbf{r}'}{r} + \left(\frac{r'}{r}\right)^2} \end{aligned} \tag{B.2}$$

in which $\hat{\mathbf{r}} = \mathbf{r}/r$, and we have assumed the frame of reference to be chosen such that $r \neq 0$ and is positive. We can now write the factor $1/|\mathbf{r}-\mathbf{r}'|$ as

$$\begin{aligned} \frac{1}{|\mathbf{r}-\mathbf{r}'|} &= \frac{1}{r}\frac{1}{\sqrt{1 - 2\,\frac{\hat{\mathbf{r}}\cdot\mathbf{r}'}{r} + \left(\frac{r'}{r}\right)^2}} \\ &= \frac{1}{r}\frac{1}{\sqrt{1+t}} \\ &= \frac{1}{r}(1+t)^{-1/2} \end{aligned} \tag{B.3}$$

where we have defined $t = -2\,\frac{\hat{\mathbf{r}}\cdot\mathbf{r}'}{r} + \left(\frac{r'}{r}\right)^2$. The last expression in Eq. B.3 can now be expanded in an infinite series of polynomials using the binomial theorem.

The binomial theorem states that any polynomial of the form $(1+x)^n$ can be expanded into an infinite series of powers of x following [198]

$$(1+x)^m = \sum_{m=0}^{\infty} \frac{m!}{n!(m-n)!} x^n \tag{B.4}$$

Its application to the last result of Eq.B.3 gives

$$\frac{1}{|\mathbf{r}-\mathbf{r}'|} = \frac{1}{r}\left(1 - \frac{t}{2} + \frac{3t^2}{8} - O(t^3)\right). \tag{B.5}$$

Inserting Eq. B.5 into Eq. B.1 and replacing t, we get the final expression

$$\Phi(\mathbf{r}) = \frac{q}{4\pi\epsilon_0 r}\left[1 - \frac{\hat{\mathbf{r}}\cdot\mathbf{r}'}{r} + \frac{1}{2r^2}(3(\hat{\mathbf{r}}\cdot\mathbf{r}')^2 - r'^2) + O\left(\frac{1}{r^3}\right)\right]. \tag{B.6}$$

Looking at each individual part of Eq. B.6, it is possible to identify several moments. The first term,

$$\Phi_{mon}(\mathbf{r}) = \frac{q}{4\pi\epsilon_0 r} \tag{B.7}$$

is the monopole potential, in which the scalar q is the monopole moment. The second term,

$$\Phi_{dip}(\mathbf{r}) = \frac{\hat{\mathbf{r}}}{4\pi\epsilon_0 r^2}(q\mathbf{r}') \tag{B.8}$$

is the dipole potential, in which the vector $\mathbf{D} = q\mathbf{r}'$ is the electric dipole moment.

To analyze the third term of Eq. B.6, it is essential to express $\hat{\mathbf{r}}$ and $\mathbf{r}'$ in Cartesian coordinates, as (r_1, r_2, r_3) and (x_1, x_2, x_3), respectively. Then, the term $(\hat{\mathbf{r}}\cdot\mathbf{r}')^2 = (r_i x_i)^2 = r_i r_j x_i x_j$. The dyad tensor $\hat{\mathbf{r}}\hat{\mathbf{r}}$ is thus given by

$$(\hat{\mathbf{r}}\hat{\mathbf{r}})_{ij} = r_i r_j \tag{B.9}$$

which helps define the quadrupole moment tensor

$$Q = q(3\mathbf{r}'\mathbf{r}' - r'^2) \tag{B.10}$$

and thus obtain the expression for the quadrupole electrical potential.

$$\Phi_{quad} = -\frac{\hat{\mathbf{r}}\hat{\mathbf{r}}}{4\pi\epsilon_0 r^3} Q \tag{B.11}$$

This easily links to Eq.B.31 presented in Ch. 3.

B.1.2 Quadrupole interaction energy

The expression for the quadrupole interaction energy shown in Eq. B.32 is derived in what follows, based on the expansion presented in [155].

Let us consider a localized charge q which is arbitrarily chosen to be positioned at the origin of a Cartesian frame of reference, under the influence of an external field $\mathbf{E}$. The field generates a potential $\Phi(\mathbf{r}')$. Then, the electrostatic energy of the system is given by

$$W = q\Phi(\mathbf{r}') \tag{B.12}$$

If the potential around q can be considered homogeneous, then it can be expanded in a Taylor series around the origin:

$$\Phi(\mathbf{r}') = \Phi(0) + \mathbf{r}' \cdot \boldsymbol{\nabla}\Phi(0) + \frac{1}{2}\sum_i \sum_j x_i x_j \frac{\partial^2 \Phi}{\partial x_i \partial x_j}(0) + \dots \tag{B.13}$$

in which the same notations as in the previous section for the Cartesian components of $\mathbf{r}'$ have been used. Since the external field $\mathbf{E} = -\boldsymbol{\nabla}\Phi$, Eq. B.13 can be rewritten

$$\Phi(\mathbf{r}') = \Phi(0) - \mathbf{r}' \cdot \mathbf{E}(0) - \frac{1}{2}\sum_i \sum_j x_i x_j \frac{\partial E_j}{\partial x_i}(0) + \dots \tag{B.14}$$

From Gauss' Law for the external field, we now that $\boldsymbol{\nabla} \cdot \mathbf{E} = 0$. Therefore, we can subtract $\frac{1}{6} r'^2 \nabla \cdot \mathbf{E}(0)$ from the last term of Eq. B.14, without any loss of generality to obtain the expression

$$\Phi(\mathbf{r}') = \Phi(0) - \mathbf{r}' \cdot \mathbf{E}(0) - \frac{1}{6}\sum_i \sum_j (3x_i x_j - r'^2 \delta_{ij}) \frac{\partial E_j}{\partial x_i}(0) + \dots \tag{B.15}$$

Inserting Eq. B.15into Eq. B.12 and remembering the definitions of the electric monopole, dipole, and quadrupole moments defined in the previous section, the final expression reads

$$W = q\Phi(0) - \mathbf{p} \cdot \mathbf{E}(0) - \frac{1}{6}\sum_i \sum_j Q_{ij} \frac{\partial E_j}{\partial x_i}(0) + \dots \tag{B.16}$$

where we clearly see appear the expression given in Eq.B.32 for the electric quadrupole interaction energy.

B.2 Matrix Elements of the Quadrupole Tensor Operators

We introduce the notations

$$\begin{aligned} x_{-1}^{(1)} &= \frac{x_1 - i x_2}{\sqrt{2}}, \\ x_0^{(1)} &= x_3, \\ x_1^{(1)} &= -\frac{x_1 + i x_2}{\sqrt{2}} \end{aligned} \tag{B.17}$$

for the spherical tensor components of the position vector $\mathbf{x} = (x_1, x_2, x_3)$. In terms of these components, we have

$$\begin{aligned} x_1 &= \frac{x_{-1}^{(1)} - x_1^{(1)}}{\sqrt{2}}, \\ x_2 &= i\frac{x_{-1}^{(1)} + x_1^{(1)}}{\sqrt{2}}, \\ x_3 &= x_0^{(1)}. \end{aligned} \tag{B.18}$$

We can write

$$x_i = \sum_q u_i^{(q)} x_q^{(1)}, \tag{B.19}$$

where $u_i^{(q)}$ with $i = 1, 2, 3$ are the components of the spherical basis vectors $\mathbf{u}^{(q)}$ in the Cartesian coordinate system $\{x_1, x_2, x_3\}$. The expressions for the vectors $\mathbf{u}^{(q)}$ are

$$\begin{aligned} \mathbf{u}^{(-1)} &= \frac{1}{\sqrt{2}}(1, i, 0), \\ \mathbf{u}^{(0)} &= (0, 0, 1), \\ \mathbf{u}^{(1)} &= -\frac{1}{\sqrt{2}}(1, -i, 0). \end{aligned} \tag{B.20}$$

We note that $\mathbf{u}^{(q)*} = (-1)^q \mathbf{u}^{(-q)}$, $\mathbf{u}^{(q)} \cdot \mathbf{u}^{(q')*} = \delta_{qq'}$, and $\sum_q u_i^{(q)} u_j^{(q)*} = \delta_{ij}$.

It follows from Eq. (B.19) that

$$x_i x_j = \sum_{M_1 M_2} u_i^{(M_1)} u_j^{(M_2)} x_{M_1}^{(1)} x_{M_2}^{(1)}. \tag{B.21}$$

In order to calculate the direct product $x_{M_1}^{(1)} x_{M_2}^{(1)}$, we use the formula [199]

$$x_{M_1}^{(1)} x_{M_2}^{(1)} = \sum_{Kq} T_q^{(K)} (-1)^q \sqrt{2K+1} \begin{pmatrix} 1 & 1 & K \\ M_1 & M_2 & -q \end{pmatrix}, \tag{B.22}$$

where $T_q^{(K)}$ with $q = -K, \ldots, K$ are the tensor elements of the irreducible tensor products $T^{(K)} = [x^{(1)} \otimes x^{(1)}]^{(K)}$ of rank $K = 0, 1, 2$. The expression for $T_q^{(K)}$ is

$$T_q^{(K)} = (-1)^q \sqrt{2K+1} \sum_{q_1 q_2} \begin{pmatrix} 1 & 1 & K \\ q_1 & q_2 & -q \end{pmatrix} x_{q_1}^{(1)} x_{q_2}^{(1)}. \tag{B.23}$$

We can show that

$$\begin{aligned} T_0^{(0)} &= -\frac{x_1^2 + x_2^2 + x_3^2}{\sqrt{3}}, \\ T_q^{(1)} &= 0, \end{aligned} \tag{B.24}$$

and

$$\begin{aligned} T_0^{(2)} &= \frac{2x_3^2 - x_1^2 - x_2^2}{\sqrt{6}}, \\ T_1^{(2)} &= -x_3(x_1 + ix_2), \\ T_{-1}^{(2)} &= x_3(x_1 - ix_2), \\ T_2^{(2)} &= \frac{1}{2}(x_1 + ix_2)^2, \\ T_{-2}^{(2)} &= \frac{1}{2}(x_1 - ix_2)^2. \end{aligned} \tag{B.25}$$

Note that $T_0^{(0)} = -R^2/\sqrt{3}$ and $T_q^{(2)} = 2(2\pi/15)^{1/2} R^2 Y_{2q}(\theta, \varphi)$, where $Y_{lq}(\theta, \varphi)$ are spherical harmonics with θ and φ being spherical angles.

We insert Eq. (B.22) into Eq. (B.21) and use Eq. (B.31). Then, we obtain

$$Q_{ij} \equiv e(3x_i x_j - R^2 \delta_{ij}) = 3e \sum_q u_{ij}^{(q)} T_q^{(2)}, \tag{B.26}$$

where

$$u_{ij}^{(q)} = (-1)^q \sqrt{5} \sum_{M_1 M_2} u_i^{(M_1)} u_j^{(M_2)} \begin{pmatrix} 1 & 1 & 2 \\ M_1 & M_2 & -q \end{pmatrix}. \tag{B.27}$$

The explicit expressions for the tensors $u_{ij}^{(q)}$ are

$$\begin{aligned} u_{ij}^{(2)} &= \frac{1}{2} \begin{pmatrix} 1 & -i & 0 \\ -i & -1 & 0 \\ 0 & 0 & 0 \end{pmatrix}, \\ u_{ij}^{(1)} &= \frac{1}{2} \begin{pmatrix} 0 & 0 & -1 \\ 0 & 0 & i \\ -1 & i & 0 \end{pmatrix}, \\ u_{ij}^{(0)} &= \frac{1}{\sqrt{6}} \begin{pmatrix} -1 & 0 & 0 \\ 0 & -1 & 0 \\ 0 & 0 & 2 \end{pmatrix}, \\ u_{ij}^{(-1)} &= \frac{1}{2} \begin{pmatrix} 0 & 0 & 1 \\ 0 & 0 & i \\ 1 & i & 0 \end{pmatrix}, \\ u_{ij}^{(-2)} &= \frac{1}{2} \begin{pmatrix} 1 & i & 0 \\ i & -1 & 0 \\ 0 & 0 & 0 \end{pmatrix}. \end{aligned} \tag{B.28}$$

Note that $u_{ij}^{(q)} = u_{ji}^{(q)}$, $u_{ij}^{(q)*} = (-1)^q u_{ij}^{(-q)}$, $\sum_{ij} u_{ij}^{(q)} u_{ij}^{(q')*} = \delta_{qq'}$, and $\sum_i u_{ii}^{(q)} = 0$.

The matrix elements of the tensor $T_q^{(2)}$ can be calculated using the Wigner-Eckart theorem [199]

$$\langle n'F'M'|T_q^{(2)}|nFM\rangle = (-1)^{F'-M'} \begin{pmatrix} F' & 2 & F \\ -M' & q & M \end{pmatrix} \langle n'F'\|T^{(2)}\|nF\rangle. \tag{B.29}$$

The invariant factor $\langle n'F'\|T^{(2)}\|nF\rangle$ is a reduced matrix element. The selection rules for F and F' are $|F'-F| \leq 2 \leq F'+F$. The selection rules for M and M' are $|M'-M| \leq 2$ and $M'-M=q$. When we use Eqs. (B.26) and (B.29), we obtain [139]

$$\langle n'F'M'|Q_{ij}|nFM\rangle = 3eu_{ij}^{(M'-M)}(-1)^{F'-M'} \times \begin{pmatrix} F' & 2 & F \\ -M' & M'-M & M \end{pmatrix} \langle n'F'\|T^{(2)}\|nF\rangle. \tag{B.30}$$

B.3 Quadrupole Interaction of an Atom with an Arbitrary Light Field

Consider an atom with a single valence electron interacting with an external optical field $\mathbf{E}$ through an electric quadrupole transition. We use Cartesian coordinates $\{x_1, x_2, x_3\}$ to describe the electric quadrupole and the internal states of the atom (see Fig. B.1(a)). We assume that the center of mass of the atom is located at the origin $\mathbf{x}=0$ of this coordinate system. Following a multipole expansion of the Coulombian potential generated by a single charge (see details of the multipole expansion in Section B.1.1), we define the electric quadrupole moment tensor Q_{ij} of the atom, with $i,j=1,2,3$, as

$$Q_{ij} = e(3x_ix_j - R^2\delta_{ij}), \tag{B.31}$$

where x_i is the ith coordinate of the valence electron of the atom and $R=\sqrt{x_1^2+x_2^2+x_3^2}$ is the distance from the electron to the center of mass of the atom. The electric quadrupole interaction energy is [155]

$$W = -\frac{1}{6}\sum_{ij} Q_{ij}\frac{\partial E_j}{\partial x_i}\Big|_{\mathbf{x}=0}, \tag{B.32}$$

where the spatial derivatives of the field components E_j with respect to the coordinates x_i are evaluated at the position $\mathbf{x}=0$ of the atom. For simplicity, we neglect the effect of the surface-induced potential on the atomic energy levels. This approximation is valid when the atom is not too close to the fiber surface [200].

We represent the field as $\mathbf{E}=(\boldsymbol{\mathcal{E}}e^{-i\omega t}+\boldsymbol{\mathcal{E}}^*e^{i\omega t})/2$, where $\boldsymbol{\mathcal{E}}$ is the field amplitude and ω the field frequency. Let $|e\rangle$ and $|g\rangle$ be upper and lower states of the atom, with energies $\hbar\omega_e$ and $\hbar\omega_g$, respectively. In the interaction picture and the rotating wave approximation, the interaction Hamiltonian of the system can be written as

$$H_I = -\hbar\sum_{eg}\Omega_{ge}e^{-i(\omega-\omega_{eg})t}\sigma_{eg} + \text{H.c.}, \tag{B.33}$$

where $\omega_{eg}=\omega_e-\omega_g$ is the atomic transition frequency, the σ_{eg} are the atomic transition operators and

$$\Omega_{ge} = \frac{1}{12\hbar}\sum_{ij}\langle e|Q_{ij}|g\rangle\frac{\partial\mathcal{E}_j}{\partial x_i} \tag{B.34}$$

is the Rabi frequency for the quadrupole transition between the states $|g\rangle$ and $|e\rangle$.

Consider the case of an alkali-metal atom with degenerate transitions between the magnetic sublevels $|g\rangle=|nFM\rangle$ and $|e\rangle=|n'F'M'\rangle$ (see Fig. B.1(b)). Here, n denotes the

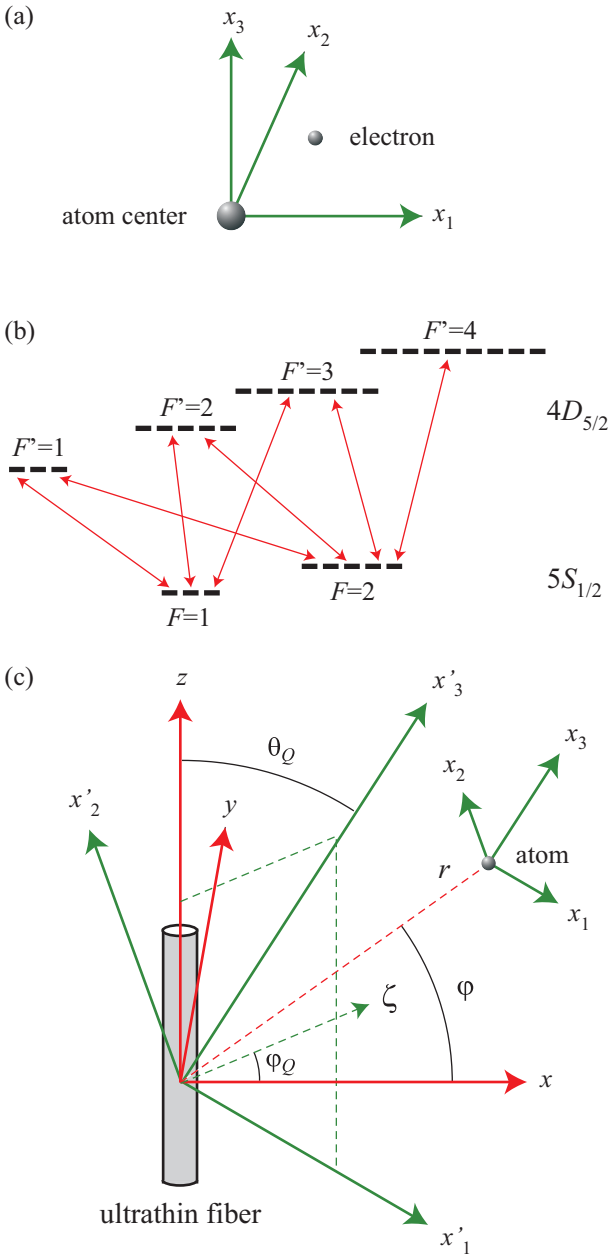

Figure B.1: (a) Local quantization coordinate system $\{x_1, x_2, x_3\}$ for an atom. (b) Schematic of the hyperfine split levels of the $4D_{5/2}$ and $5S_{1/2}$ states of a rubidium-87 atom. (c) Atom in the vicinity of an ONF with the fiber-based Cartesian coordinate system $\{x, y, z\}$ and the corresponding cylindrical coordinate system $\{r, \varphi, z\}$.

principal quantum number and also all additional quantum numbers not shown explicitly, F is the quantum number for the total angular momentum of the atom, and M is the magnetic quantum number. The matrix elements $\langle n'F'M'|Q_{ij}|nFM\rangle$ of the quadrupole

tensor operators Q_{ij} are, as shown in Appendix B.2, given as [139]

$$\langle n'F'M'|Q_{ij}|nFM\rangle = 3eu_{ij}^{(M'-M)}(-1)^{F'-M'} \times \begin{pmatrix} F' & 2 & F \\ -M' & M'-M & M \end{pmatrix} \langle n'F'\|T^{(2)}\|nF\rangle, \tag{B.35}$$

where the matrices $u_{ij}^{(q)}$ with $q = -2, -1, 0, 1, 2$ are given by Eqs. (B.28), the array in the parentheses is a $3j$ symbol, and the invariant factor $\langle n'F'\|T^{(2)}\|nF\rangle$ is the reduced matrix element of the tensor operators $T_q^{(2)} = 2(2\pi/15)^{1/2}R^2Y_{2q}(\theta,\varphi)$. Here, Y_{lq} is a spherical harmonic function of degree l and order q, and θ and φ are spherical angles in the spherical coordinates $\{R,\theta,\varphi\}$ associated with the Cartesian coordinates $\{x_1, x_2, x_3\}$.

It is clear from Eq. (B.35) that the selection rules for F and F' are $|F'-F| \leq 2 \leq F'+F$, and the selection rule for M and M' is $|M'-M| \leq 2$. Since the tensor operators $T_q^{(2)}$ do not act on the nuclear spin degree of freedom, the dependence of the reduced matrix element $\langle n'F'\|T^{(2)}\|nF\rangle$ on F and F' may be factored out as [199]

$$\langle n'F'\|T^{(2)}\|nF\rangle = (-1)^{J'+I+F} \times \sqrt{(2F+1)(2F'+1)} \begin{Bmatrix} F' & 2 & F \\ J & I & J' \end{Bmatrix} \langle n'J'\|T^{(2)}\|nJ\rangle, \tag{B.36}$$

where J is the quantum number for the total angular momentum of the electrons, I is the nuclear spin quantum number, and the array in the curly braces is a $6j$ symbol. The selection rules for J and J' are $|J'-J| \leq 2 \leq J'+J$.

Furthermore, since the tensor operators $T_q^{(2)}$ do not act on the electron spin degree of freedom, we have [199]

$$\langle n'J'\|T^{(2)}\|nJ\rangle = (-1)^{L'+S+J} \times \sqrt{(2J+1)(2J'+1)} \begin{Bmatrix} J' & 2 & J \\ L & S & L' \end{Bmatrix} \langle n'L'\|T^{(2)}\|nL\rangle, \tag{B.37}$$

where L is the quantum number for the total orbital angular momentum of the electrons and S the quantum number for the total spin of the electrons. It follows from the addition of angular momenta that the quadrupole matrix elements may be nonzero only if $|L'-L| \leq 2 \leq L'+L$. On the other hand, the parity of the tensor $T_q^{(2)} \propto Y_{2q}$ is even. Therefore, the quadrupole matrix elements may be nonzero only if L and L' have the same parity. Thus, the electric quadrupole transition selection rules for L and L' are $|L'-L| = 0, 2$ and $L'+L \geq 2$. We note that, in the special case where $L=0$ and $L'=2$, we have $\langle n', L'=2\|T^{(2)}\|n, L=0\rangle = \sqrt{2/3}\langle n', L'=2|R^2|n, L=0\rangle$.

We now calculate the quadrupole Rabi frequency $\Omega_{ge} = \Omega_{FMF'M'}$, defined by Eq. (B.34). When we insert Eq. (B.35) into Eq. (B.34), we obtain

$$\Omega_{FMF'M'} = \frac{e}{4\hbar}(-1)^{F'-M'} \begin{pmatrix} F' & 2 & F \\ -M' & M'-M & M \end{pmatrix} \times \langle n'F'\|T^{(2)}\|nF\rangle \sum_{ij} u_{ij}^{(M'-M)} \frac{\partial \mathcal{E}_j}{\partial x_i}. \tag{B.38}$$

In general, the Rabi frequency $\Omega_{FMF'M'}$ for the transition between the atomic states $|nFM\rangle$ and $|n'F'M'\rangle$ depends on the relative orientation of the quantization axis x_3 with respect to the electric field vector $\boldsymbol{\mathcal{E}}$.

The root-mean-square (rms) Rabi frequency $\bar{\Omega}_{FF'}$ is given by the rule [154]

$$\bar{\Omega}^2_{FF'} = \sum_{MM'} |\Omega_{FMF'M'}|^2. \tag{B.39}$$

We insert Eq. (B.38) into Eq. (B.39) and perform the summations over M and M'. Then, we obtain

$$\bar{\Omega}^2_{FF'} = \frac{e^2}{80\hbar^2} |\langle n'F' \| T^{(2)} \| nF \rangle|^2 \sum_q \left| \sum_{ij} u^{(q)}_{ij} \frac{\partial \mathcal{E}_j}{\partial x_i} \right|^2. \tag{B.40}$$

We note that Eqs. (B.38) and (B.40) can be used for a monochromatic light field with an arbitrary space-dependent amplitude $\boldsymbol{\mathcal{E}}$. In the particular case of standing-wave laser fields, Eqs. (B.38) and (B.40) reduce to the results of Ref. [139].

We assume that the field is near to resonance with the atom, that is, $\omega \simeq \omega_0$, where $\omega_0 \equiv \omega_{eg}$. The oscillator strength $f_{FF'}$ can be calculated from the rms Rabi frequency $\bar{\Omega}_{FF'}$ by using the relation [154]

$$\bar{\Omega}^2_{FF'} = \frac{e^2 |\mathcal{E}|^2}{8\hbar m_e \omega_0} (2F+1) f_{FF'}, \tag{B.41}$$

where m_e is the mass of an electron. This yields

$$\begin{aligned} f_{FF'} = {} & \frac{m_e \omega_0}{18\hbar e^2 (2F+1)} \\ & \times \sum_{MM'} \left| \sum_{ij} \langle n'F'M' | Q_{ij} | nFM \rangle \frac{1}{\mathcal{E}} \frac{\partial \mathcal{E}_j}{\partial x_i} \right|^2. \end{aligned} \tag{B.42}$$

Equation (B.42) can be used for a monochromatic light field with an arbitrary space-dependent amplitude $\boldsymbol{\mathcal{E}}$. In the particular case where $\boldsymbol{\mathcal{E}} = \boldsymbol{\mathcal{E}}_0 e^{i\mathbf{K}\cdot\mathbf{x}}$ with $\boldsymbol{\mathcal{E}}_0$ and $\mathbf{K}$ being constant real or complex vectors, Eq. (B.42) reduces to an expression that is in agreement with Refs. [143–145].

With the help of Eqs. (B.40) and (B.41), we find

$$f_{FF'} = \frac{m_e \omega_0}{10\hbar} \frac{|\langle n'F' \| T^{(2)} \| nF \rangle|^2}{2F+1} \sum_q \left| \sum_{ij} u^{(q)}_{ij} \frac{1}{\mathcal{E}} \frac{\partial \mathcal{E}_j}{\partial x_i} \right|^2. \tag{B.43}$$

We emphasize that Eq. (B.43) can be used for an arbitrary monochromatic light field. Due to the summation over M and M' in Eq. (B.39), the rms Rabi frequency $\bar{\Omega}_{FF'}$ and, consequently, the oscillator strength $f_{FF'}$ do not depend on the orientation of the quantization axis x_3. The quadrupole oscillator strength $f_{FF'}$, given by Eq. (B.43), is a measure that characterizes the proportionality of the rms Rabi frequency $\bar{\Omega}_{FF'}$ to the field magnitude $\mathcal{E}$ through Eq. (B.41). This measure depends not only on the quadrupole of the atom but also the normalized gradients of the field components. We note that, for atoms in free space, the oscillator strength can be interpreted as the ratio between the quantum-mechanical transition rate and the classical absorption rate of a single-electron

oscillator with the same frequency [154, 155]. However, this interpretation may not be valid for atoms in the vicinity of an object because the modifications of the transition rate are much more complicated than that of the Rabi frequency.

According to expressions (B.40) and (B.43), the dependencies of $\bar{\Omega}^2_{FF'}$ and $f_{FF'}$ on F and F' are included only in the factors $|\langle n'F'\|T^{(2)}\|nF\rangle|^2$ and $|\langle n'F'\|T^{(2)}\|nF\rangle|^2/(2F+1)$. These factors are determined by the internal atomic states. They do not depend on the center-of-mass position of the atom and the parameters of the fiber. They act as scaling factors for the dependencies on different F and F'. Consequently, the shapes of the dependencies of $\bar{\Omega}^2_{FF'}$ and $f_{FF'}$ on the position of the atom and the radius of the fiber do not depend on the quantum numbers F and F'.

We introduce the notations $\bar{\Omega}^{(0)}_{FF'}$ and $f^{(0)}_{FF'}$ for the rms Rabi frequency and oscillator strength of an atom interacting with a plane-wave light field in free space via an electric quadrupole transition. According to [138, 139, 145], we have

$$\bar{\Omega}^{(0)2}_{FF'} = \frac{e^2k^2|\mathcal{E}|^2}{160\hbar^2}|\langle n'F'\|T^{(2)}\|nF\rangle|^2 \tag{B.44}$$

and

$$f^{(0)}_{FF'} = \frac{m_e\omega_0^3}{20\hbar c^2}\frac{|\langle n'F'\|T^{(2)}\|nF\rangle|^2}{2F+1}. \tag{B.45}$$

The enhancements of the rms Rabi frequency and oscillator strength in arbitrary light are characterized by the factors

$$\begin{aligned}\eta_{\text{Rabi}} &= \frac{\bar{\Omega}_{FF'}}{\bar{\Omega}^{(0)}_{FF'}},\\ \eta_{\text{osc}} &= \frac{f_{FF'}}{f^{(0)}_{FF'}}.\end{aligned} \tag{B.46}$$

We find

$$\eta_{\text{osc}} = \eta^2_{\text{Rabi}} = \frac{2}{k_0^2|\mathcal{E}|^2}\sum_q\Big|\sum_{ij}u^{(q)}_{ij}\frac{\partial\mathcal{E}_j}{\partial x_i}\Big|^2. \tag{B.47}$$

It is clear from Eq. (B.47) that η_{Rabi} and η_{osc} are independent of the quantum numbers F and F'. Moreover, these factors do not depend on any characteristics of the atomic states except for the atomic transition frequency ω_0. They are determined by the normalized spatial variations of the mode profile function $\boldsymbol{\mathcal{E}}$ at the frequency ω_0.

We note that the oscillator strength $f_{JJ'}$ of the transition from a lower fine-structure level $|nJ\rangle$ to an upper fine-structure level $|n'J'\rangle$ of the atom may be obtained by summing up $f_{FF'}$ over all values of F'. The result is

$$f_{JJ'} = \frac{m_e\omega_0}{10\hbar}\frac{|\langle n'J'\|T^{(2)}\|nJ\rangle|^2}{2J+1}\sum_q\Big|\sum_{ij}u^{(q)}_{ij}\frac{1}{\mathcal{E}}\frac{\partial\mathcal{E}_j}{\partial x_i}\Big|^2. \tag{B.48}$$

In the case of an atom interacting with a plane-wave in free space, we have [138, 139, 145]

$$f^{(0)}_{JJ'} = \frac{m_e\omega_0^3}{20\hbar c^2}\frac{|\langle n'J'\|T^{(2)}\|nJ\rangle|^2}{2J+1}. \tag{B.49}$$

The relation between $f_{FF'}$ and $f_{JJ'}$ is [143, 144]

$$f_{FF'} = (2F'+1)(2J+1)\begin{Bmatrix}F' & 2 & F\\ J & I & J'\end{Bmatrix}^2 f_{JJ'}. \tag{B.50}$$

B.4 Quadrupole Interaction of an Atom with a Plane-Wave Light Field in Free Space

Assume that the field is a plane wave $\boldsymbol{\mathcal{E}} = \mathcal{E}\boldsymbol{\varepsilon}e^{i\mathbf{k}\cdot\mathbf{x}}$ in free space, where $\mathcal{E}$ is the amplitude, $\mathbf{k}$ is the wave vector, and $\boldsymbol{\varepsilon}$ is the polarization vector. In this case, the rms Rabi frequency $\bar{\Omega}^{(0)}_{FF'}$ is found from Eq. (B.40) to be

$$\bar{\Omega}^{(0)2}_{FF'} = \frac{e^2|\mathcal{E}|^2}{80\hbar^2}|\langle n'F'\|T^{(2)}\|nF\rangle|^2 \sum_q \Big|\sum_{ij} u^{(q)}_{ij} k_i \varepsilon_j\Big|^2. \tag{B.51}$$

Without loss of generality, we assume that the field propagates along the x_3 direction and is linearly polarized along the x_1 direction. Then, we have $\mathbf{k} = (0, 0, k)$ and $\boldsymbol{\varepsilon} = (1, 0, 0)$ in the Cartesian coordinate system $\{x_1, x_2, x_3\}$. These expressions lead to $k_i = k\delta_{i,3}$ and $\varepsilon_j = \delta_{j,1}$. Then, Eq. (B.51) gives

$$\bar{\Omega}^{(0)2}_{FF'} = \frac{e^2k^2|\mathcal{E}|^2}{80\hbar^2}|\langle n'F'\|T^{(2)}\|nF\rangle|^2 \sum_q |u^{(q)}_{31}|^2. \tag{B.52}$$

From Eqs. (B.28), we find $\sum_q |u^{(q)}_{31}|^2 = 1/2$. Hence, we obtain

$$\bar{\Omega}^{(0)2}_{FF'} = \frac{e^2k^2|\mathcal{E}|^2}{160\hbar^2}|\langle n'F'\|T^{(2)}\|nF\rangle|^2. \tag{B.53}$$

The oscillator strength $f^{(0)}_{FF'}$ is related to the rms Rabi frequency $\bar{\Omega}^{(0)}_{FF'}$ via the formula (B.41). With the help of this formula, we find

$$f^{(0)}_{FF'} = \frac{m_e\omega_0^3}{20\hbar c^2}\frac{|\langle n'F'\|T^{(2)}\|nF\rangle|^2}{2F+1}. \tag{B.54}$$

The oscillator strength $f^{(0)}_{JJ'}$ of the transition from a lower fine-structure level $|nJ\rangle$ to an upper fine-structure level $|n'J'\rangle$ of the atom in free space may be obtained by summing up $f^{(0)}_{FF'}$ over all values of F'. The result is [138, 139, 145]

$$f^{(0)}_{JJ'} = \frac{m_e\omega_0^3}{20\hbar c^2}\frac{|\langle n'J'\|T^{(2)}\|nJ\rangle|^2}{2J+1}. \tag{B.55}$$

The rate $\gamma_{F'F}$ of quadrupole spontaneous emission from an upper hyperfine-structure level $|n'F'\rangle$ to a lower hyperfine-structure level $|nF\rangle$ of the atom in free space is related to the oscillator strength $f^{(0)}_{FF'}$ as

$$\gamma^{(0)}_{F'F} = \frac{e^2\omega_0^2}{2\pi\epsilon_0 m_e c^3}\frac{2F+1}{2F'+1}f^{(0)}_{FF'}. \tag{B.56}$$

Hence, we find

$$\gamma^{(0)}_{F'F} = \frac{e^2\omega_0^5}{40\pi\epsilon_0\hbar c^5}\frac{|\langle n'F'\|T^{(2)}\|nF\rangle|^2}{2F'+1}. \tag{B.57}$$

The rate $\gamma^{(0)}_{J'J}$ of quadrupole spontaneous emission from an upper fine-structure level $|n'J'\rangle$ to a lower fine-structure level $|nJ\rangle$ of the atom in free space may be obtained by summing up $\gamma^{(0)}_{F'F}$ over all values of F. The result is [138, 139, 145]

$$\gamma^{(0)}_{J'J} = \frac{e^2\omega_0^5}{40\pi\epsilon_0\hbar c^5}\frac{|\langle n'J'\|T^{(2)}\|nJ\rangle|^2}{2J'+1}. \tag{B.58}$$

We have the relation

$$\gamma^{(0)}_{J'J} = \frac{e^2\omega_0^2}{2\pi\epsilon_0 m_e c^3}\frac{2J+1}{2J'+1} f^{(0)}_{JJ'}. \tag{B.59}$$

It follows from Eq. (B.36) that the relations between $\gamma^{(0)}_{F'F}$ and $\gamma^{(0)}_{J'J}$ and between $f^{(0)}_{FF'}$ and $f^{(0)}_{JJ'}$ are [143, 144]

$$\begin{aligned}
\gamma^{(0)}_{F'F} &= (2F+1)(2J'+1)\begin{Bmatrix} F' & 2 & F \\ J & I & J' \end{Bmatrix}^2 \gamma^{(0)}_{J'J}, \\
f^{(0)}_{FF'} &= (2F'+1)(2J+1)\begin{Bmatrix} F' & 2 & F \\ J & I & J' \end{Bmatrix}^2 f^{(0)}_{JJ'}.
\end{aligned} \tag{B.60}$$

B.5 Numerical Results (extended)

We plot in Fig. B.2 the absolute value of the Rabi frequency $\Omega_{FMF'M'}$ as a function of the radial distance r for the transitions between a lower sublevel $|FM\rangle$ and different upper sublevels $|F'M'\rangle$ via the interaction with different guided modes $N = \mathrm{HE}_{11}$, TE_{01}, TM_{01}, and HE_{21}. For the calculations shown in this figure, we chose the quantization axis to be $x_3 = z$. We observe that $|\Omega_{FMF'M'}|$ reduces almost exponentially with increasing r. The steep slope in the radial dependence of $|\Omega_{FMF'M'}|$ is a manifestation of the evanescent-wave behavior of the guided field outside the fiber. It is clear from Fig. B.2 that $|\Omega_{FMF'M'}|$ depends on the magnetic quantum numbers and the guided mode type. The dotted blue curve in Fig. B.2(b), which stands for the case of the upper sublevel $M' = 2$ and the TE mode, is zero. This means that the TE mode does not interact with the quadrupole transition between the sublevels $|5S_{1/2}, F = 2, M = 2\rangle$ and $|4D_{5/2}, F' = 4, M' = 2\rangle$ for the quantization axis $x_3 = z$. The vanishing of this interaction is a consequence of the properties of the TE mode, the quadrupole operator Q_{ij}, and the internal atomic states.

The Rabi frequency $\Omega_{FMF'M'}$ for the transition between the sublevels $|FM\rangle$ and $|F'M'\rangle$ depends on the relative orientation of the quantization axis x_3 with respect to the fiber axis z. In order to illustrate this dependence, we plot in Fig. B.3 the radial dependencies of the absolute value of the Rabi frequency $\Omega_{FMF'M'}$ for the quadrupole transition between the sublevels $|F = 2, M = 2\rangle$ and $|F' = 4, M' = 4\rangle$ for different choices of the quantization axis, namely $x_3 = z$, x, and y. We observe that $\Omega_{FMF'M'}$ strongly depends on the orientation of x_3. In the case of the HE_{11}, TM_{01}, and HE_{21} modes, the absolute value $|\Omega_{FMF'M'}|$ for $x_3 = y$ (see the dotted blue curves in Figs. B.3(a), B.3(c), and B.3(d)) is larger than for $x_3 = z$ and $x_3 = x$ (see the solid black and dashed red curves in Figs. B.3(a), B.3(c), and B.3(d)). However, in the case of the TE_{01} mode, we have $|\Omega_{FMF'M'}| = 0$ for $x_3 = y$ (see the dotted blue curve in Fig. B.3(b)). The vanishing of this interaction is a consequence of the properties of the TE mode, the quadrupole operator Q_{ij}, and the internal atomic states.

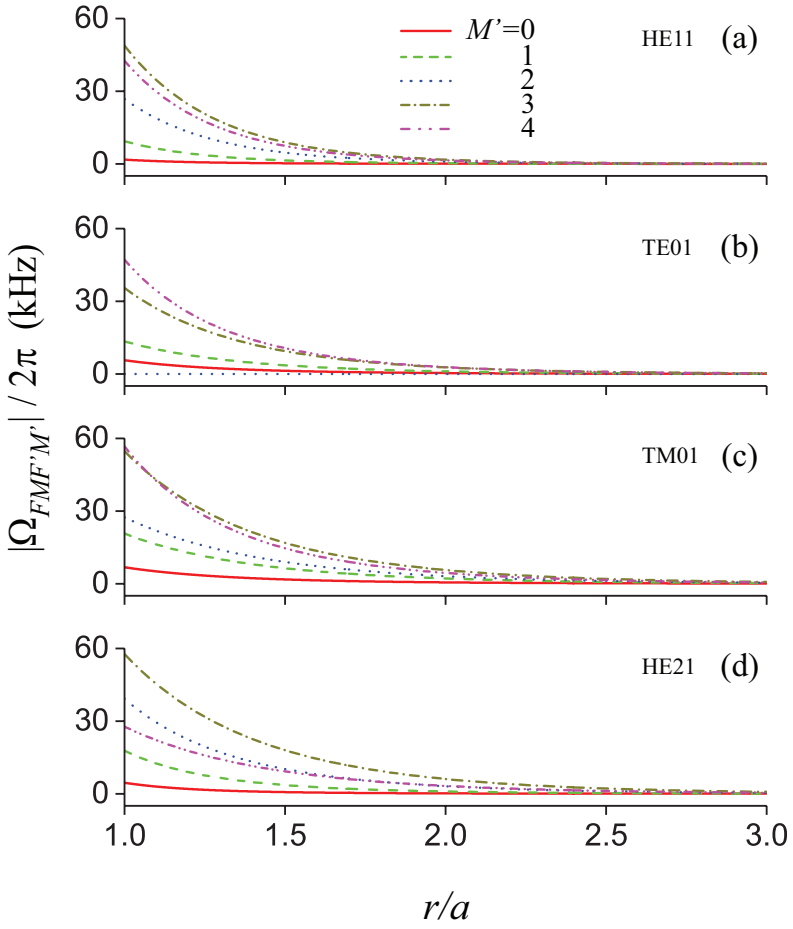

Figure B.2: Absolute value of the Rabi frequency $\Omega_{FMF'M'}$ for the quadrupole transition between the sublevel $M = 2$ of the level $5S_{1/2}F = 2$ and a sublevel M' of the level $4D_{5/2}F' = 4$ as a function of the radial distance r for different magnetic quantum numbers $M' = 0, 1, 2, 3, 4$ and different guided mode types $N = \mathrm{HE}_{11}$, TE_{01}, TM_{01}, and HE_{21}. The fiber radius is $a = 280$ nm. The wavelength of the atomic transition is $\lambda_0 = 516.5$ nm. The refractive indices of the fiber and the vacuum cladding are $n_1 = 1.4615$ and $n_2 = 1$, respectively. The power of the guided light field is 10 nW. The field propagates in the $+z$ direction. The hybrid modes are counterclockwise quasicircularly polarized. The quantization axis is $x_3 = z$. The azimuthal angle for the position of the atom in the fiber cross-sectional xy plane is arbitrary.

We plot in Figs. B.4 and B.5 the radial dependencies of $|\Omega_{FMF'M'}|$ for opposite phase circulation directions $p = \pm 1$ and opposite propagation directions $f = \pm 1$. These plots show that, given an orientation of the quantization axis, mode type, and transition type, $|\Omega_{FMF'M'}|$ may depend on p and f. The dependence of $|\Omega_{FMF'M'}|$ on f is related to the spin-orbit coupling of light [201–208]. Due to the spin-orbit coupling of light, spontaneous emission and scattering from an atom with a circular dipole near a nanofiber can be asymmetric with respect to the opposite propagation directions along the fiber axis[97, 103, 209–213]. We note that we have $|\Omega_{FMF'M'}| = 0$ for both directions $f = \pm 1$ in Figs. B.5(c) and B.5(f). The vanishing of the quadrupole transitions here is a consequence

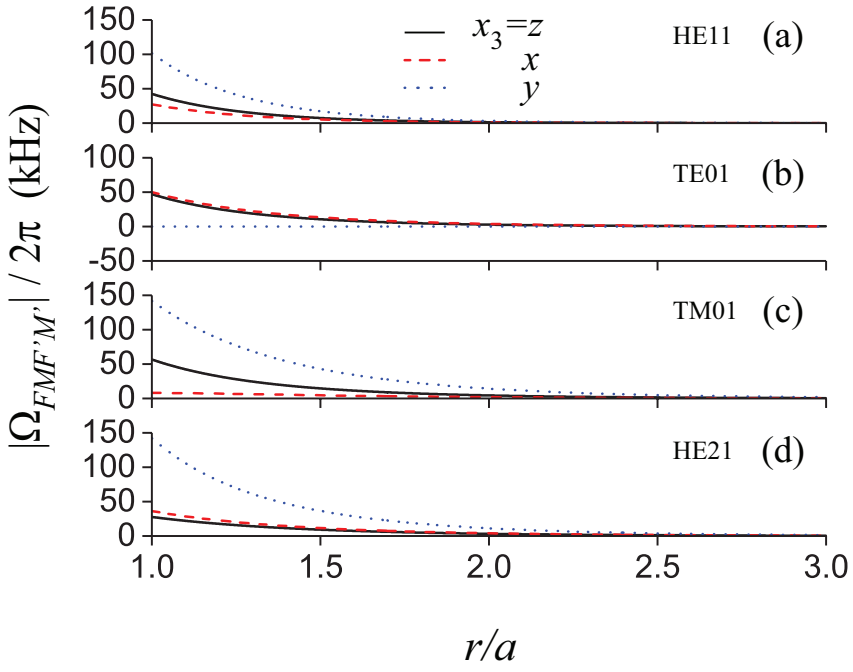

Figure B.3: Radial dependencies of the absolute value of the Rabi frequency $\Omega_{FMF'M'}$ for the quadrupole transition between the sublevels $|F = 2, M = 2\rangle$ and $|F' = 4, M' = 4\rangle$ for different choices of the quantization axis x_3 and different guided modes. The atom is positioned on the positive side of the x axis ($\varphi = 0$) and the hybrid modes are counterclockwise quasicircularly polarized. Other parameters are as for Fig. B.2.

of the properties of the guided field, the quadrupole operator, and the internal atomic states.

We plot in Figs. B.6 and B.7 the radial dependencies of the rms Rabi frequency $\bar{\Omega}_{FF'}$ and the oscillator strength $f_{FF'}$ of the atom. As already pointed out in Sec. **??**, due to the summation over transitions with different magnetic quantum numbers, $\bar{\Omega}_{FF'}$ and $f_{FF'}$ do not depend on the relative orientation of the quantization axis x_3 with respect to fiber axis z. Figs.B.6 and B.7 show that $\bar{\Omega}_{FF'}$ and $f_{FF'}$ achieve their largest values at $r/a = 1$, that is when the atom is directly placed on the surface of the ONF. We observe that $\bar{\Omega}_{FF'}$ reduces quickly and $f_{FF'}$ decreases slowly with increasing r. We note that the shapes of the curves in Figs. B.6(a) and B.7(a), where $F = 2$ and $F' = 4$, are the same as the shapes of the corresponding curves in Figs. B.6(b) and B.7(b), where $F = 2$ and $F' = 3$. These curves differ by a scaling factor (see Eqs. (B.40) and (B.43)).

Figs. B.6 and B.7 show that the rms Rabi frequency $\bar{\Omega}_{FF'}$ and the oscillator strength $f_{FF'}$ depend on the mode type. Comparison between the curves for different modes shows that, for the parameters of the figures, the oscillator strength $f_{FF'}$ for the fundamental mode HE_{11} (see the solid black curve in Fig. B.7) is the largest, while the corresponding rms Rabi frequency $\bar{\Omega}_{FF'}$ (see the solid black curve in Fig. B.6) is the smallest or the second smallest. The contrast between these relations is due to the fact that the rms Rabi frequency $\bar{\Omega}_{FF'}$ is proportional to the product of the oscillator strength $f_{FF'}$ and the electric field intensity $|\mathcal{E}|^2$ (see Eq. (B.41)).

We show in Figs. B.8 and B.9 the radial dependencies of the rms Rabi frequency $\bar{\Omega}_{FF'}$

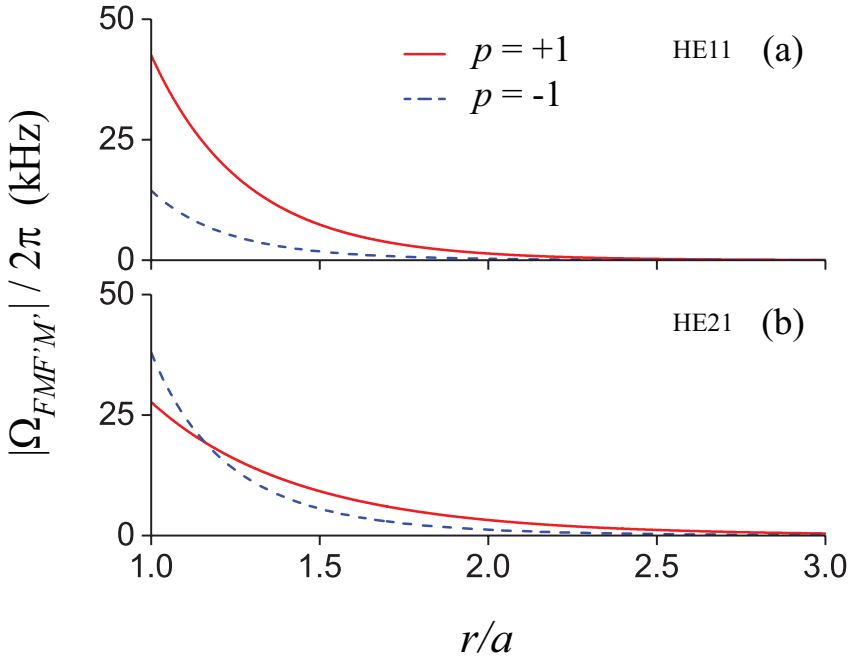

Figure B.4: Radial dependencies of the absolute value of the Rabi frequency $\Omega_{FMF'M'}$ for the opposite phase circulation directions $p = \pm 1$ of the circularly polarized hybrid modes HE_{11} and HE_{21}. The lower and upper levels of the transition are $|F = 2, M = 2\rangle$ and $|F' = 4, M' = 4\rangle$ and the quantization axis is $x_3 = z$. Other parameters are as for Fig. B.2.

and the oscillator strength $f_{FF'}$ of the atom interacting with the fundamental mode HE_{11} via the quadrupole transitions between different pairs of hfs levels F and F' of the ground state $5S_{1/2}$ and the excited stated $4D_{5/2}$. We observe from the figures that the curves for different pairs of F and F' have the same shape, that is, the curves for different pairs of F and F' differ only by a scaling factor (see Eqs. (B.40) and (B.43)). Comparison between the curves shows that the rms Rabi frequency and the oscillator strength are largest and smallest for the transitions between levels $F = 2$ and $F' = 4$ and between levels $F = 2$ and $F' = 1$, respectively. We note from Figs. B.8(a) and B.9(a) that the transitions between levels $F = 1$ and $F' = 1$ and between levels $F = 1$ and $F' = 3$ have almost the same $\bar{\Omega}_{FF'}$ and the same $f_{FF'}$.

We show in Figs. B.10 and B.11 the rms Rabi frequency $\bar{\Omega}_{FF'}$ and the oscillator strength $f_{FF'}$ as functions of the fiber radius a. We observe from Fig. B.10 that the rms Rabi frequency $\bar{\Omega}_{FF'}$ first increases and then decreases with increasing a. It is clear from this figure that $\bar{\Omega}_{FF'}$ for different guided modes have different maxima at different values of a. We observe from Fig. B.11 that, for the fundamental mode HE_{11}, the oscillator strength $f_{FF'}$ has a local minimum at $a \simeq 107$ nm. Meanwhile, for the higher-order modes, $f_{FF'}$ increases with increasing a. In the region $a < 498.2$ nm, $f_{FF'}$ for the HE_{11} mode is larger than that for higher-order modes. When a is in the region from 498.2 nm to 1000 nm, $f_{FF'}$ for the TM_{01} mode is lager than that for other modes. These regimes, however, are rarely reached in cold atom experiments where the fiber radius is usually

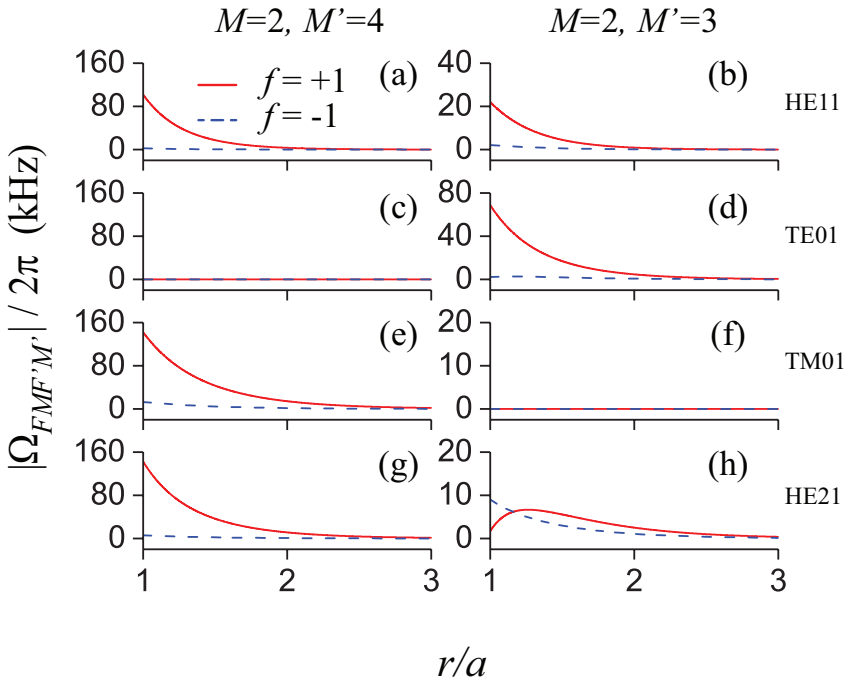

Figure B.5: Radial dependencies of the absolute value of the Rabi frequency $\Omega_{FMF'M'}$ for the opposite propagation directions $f = \pm 1$ of different guided modes. The lower and upper levels of the transition are $|F = 2, M = 2\rangle$ and $|F' = 4, M' = 4\rangle$ (left column) and $|F = 2, M = 2\rangle$ and $|F' = 4, M' = 3\rangle$ (right column). The quantization axis is $x_3 = y$, the atom is positioned on the positive side of the x axis, and the hybrid modes are counterclockwise quasicircularly polarized. Other parameters are as for Fig. B.2.

found in the range 200-400 nm.

The increase of $f_{FF'}$ for the HE_{11} and higher-order modes with increasing a in the region of large a is a consequence of the fact that expression (B.43) for $f_{FF'}$ contains the terms that are proportional to the gradients $\partial\mathcal{E}_{x,y,z}/\partial z$ of the field amplitudes $\mathcal{E}_{x,y,z}$ in the direction of the fiber axis z. These gradients are proportional to the propagation constant β, which increases with increasing fiber radius a [95, 214]. The decrease of $f_{FF'}$ with increasing a in the region of small a for the HE_{11} mode (see the solid black curve in Fig. B.11) is a result of the changes in the structure of the field and increase in mode volume contained outside the ONF. The initial decrease and the subsequent increase lead to the occurrence of a minimum in the dependence of $f_{FF'}$ on a in the case of the HE_{11} mode (see the solid black curve in Fig. B.11).

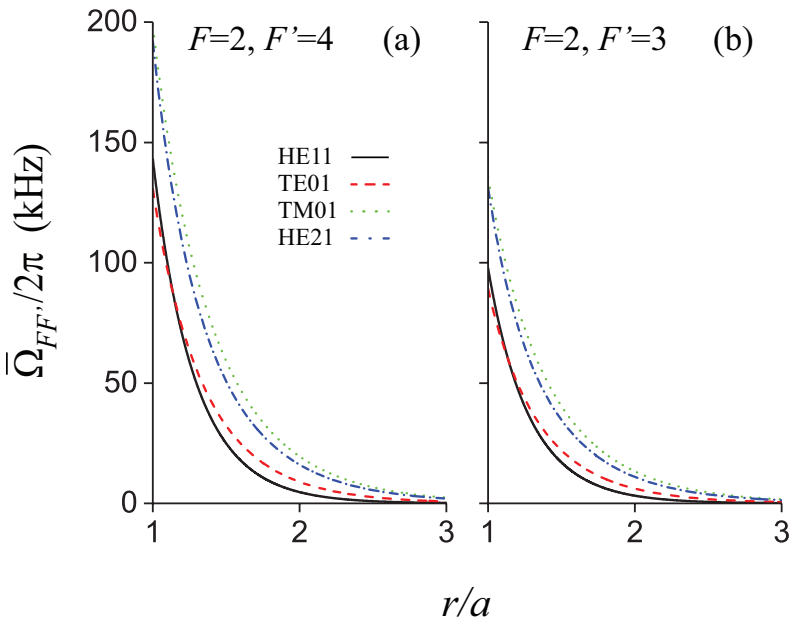

Figure B.6: Radial dependencies of the rms Rabi frequency $\bar{\Omega}_{FF'}$ for different guided modes. The hfs levels are $F = 2$ and $F' = 4$ in (a) and $F = 2$ and $F' = 3$ in (b). The hybrid modes are quasicircularly polarized and the quantization axis is arbitrary. Other parameters are as for Fig. B.2.

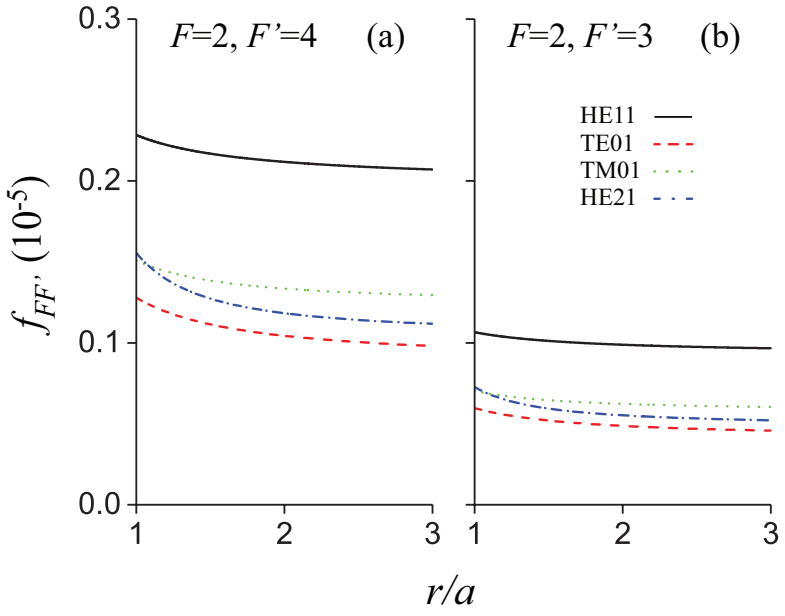

Figure B.7: Radial dependencies of the oscillator strength $f_{FF'}$ for different guided modes. Parameters used are as for Fig. B.6.

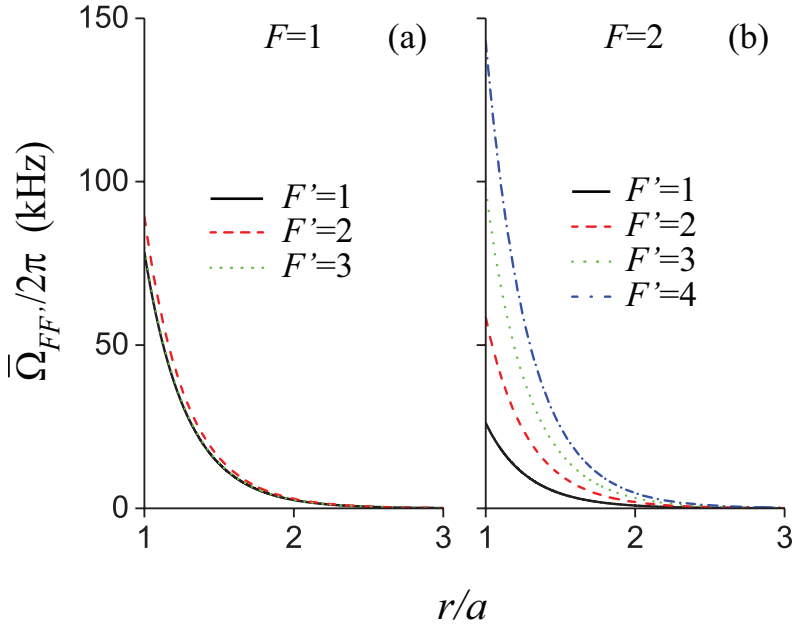

Figure B.8: Radial dependencies of the rms Rabi frequency $\bar{\Omega}_{FF'}$ of the atom interacting with the fundamental mode HE_{11} via the quadrupole transitions between different pairs of hfs levels F and F'. The hybrid modes are quasicircularly polarized and the quantization axis is arbitrary. Other parameters are as for Fig. B.2.

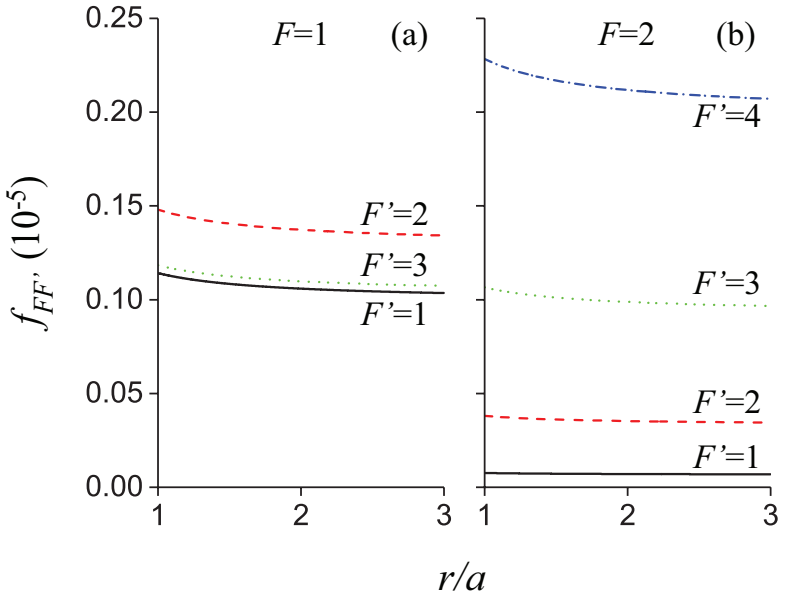

Figure B.9: Radial dependencies of the oscillator strength $f_{FF'}$ of the atom interacting with the fundamental mode HE_{11} via the quadrupole transitions between different pairs of hfs levels F and F'. Parameters used are as for Fig. B.8.

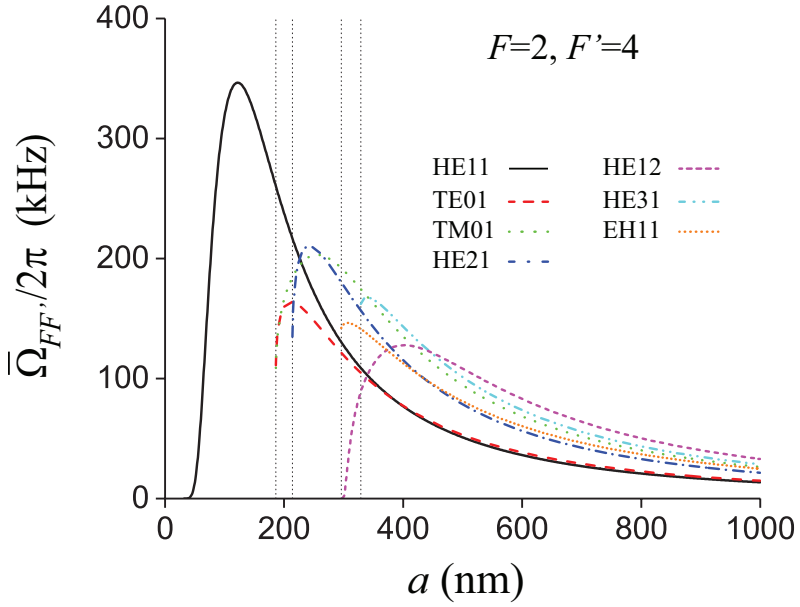

Figure B.10: Rms Rabi frequency $\bar{\Omega}_{FF'}$ as a function of the fiber radius a for different guided modes. The atom is positioned on the fiber surface. The hybrid modes are quasicircularly polarized and the quantization axis is arbitrary. Other parameters are as for Fig. B.2. The vertical dotted lines indicate the positions of the cutoffs for higher-order modes.

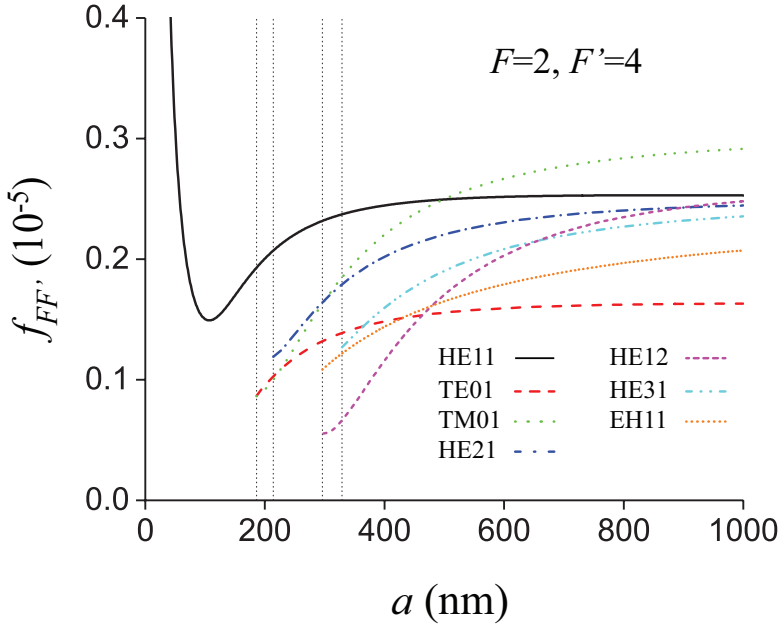

Figure B.11: Oscillator strength $f_{FF'}$ as a function of the fiber radius a for different guided modes. Parameters used are as for Fig. B.10.

Bibliography

[1] T. Nieddu, V. Gokhroo, and S. Nic Chormaic, J. Opt. **18**, 053001 (2016).

[2] L. Tong and M. Sumetsky, *Subwavelength and Nanometer Diameter Optical Fibers*, Springer (2009).

[3] L. Russell, D. Gleeson, V. Minogin, and S. Nic Chormaic, J. Phys. B: At. Mol. Opt. Phys **42**, 185006 (2009).

[4] L. Russell, K. Deasy, M. Daly, M. Morrissey, and S. Nic Chormaic, Meas. Sci. Technol. **23**, 015201 (2012).

[5] L. Russell, R. Kumar, V. Tiwari, and S. Nic Chormaic, Opt. Commun. **309**, 313 – 317 (2013).

[6] E. Vetsch, D. Reitz, G. Sagué, R. Schmidt, S. Dawkins, and A. Rauschenbeutel, Phys. Rev. Lett. **104**, 203603 (2010).

[7] A. Goban, K. Choi, D. Alton, D. Ding, C. Lacroûte, M. Pototschnig, T. Thiele, N. Stern, and H. Kimble, Phys. Rev. Lett. **109**, 033603 (2012).

[8] P. Schneeweiss, S. Dawkins, R. Mitsch, D. Reitz, E. Vetsch, and A. Rauschenbeutel, Appl. Phys. B **110**, 279–283 (2013).

[9] V. Minogin and S. Nic Chormaic, Laser Phys. **20**, 32–37 (2010).

[10] M. Frawley, S. Nic Chormaic, and V. Minogin, Phys. Scr. **85**, 058103 (2012).

[11] R. Kumar, V. Gokhroo, K. Deasy, and S. Nic Chormaic, Phys. Rev. A **91**, 053842 (2015).

[12] R. Kumar, V. Gokhroo, and S. Nic Chormaic, New J. Phys. **17**, 123012 (2015).

[13] C. Sayrin, C. Clausen, B. Albrecht, P. Schneeweiss, and A. Rauschenbeutel, Optica **2**, 353 (2015).

[14] B. Gouraud, D. Maxein, A. Nicolas, O. Morin, and J. Laurat, Phys. Rev. Lett. **114**, 180503 (2015).

[15] N. V. Corzo, B. Gouraud, A. Chandra, A. Goban, A. S. Sheremet, D. V. Kupriyanov, and J. Laurat, Phys. Rev. Lett. **117**, 133603 (2016).

[16] H. L. Sørensen, J.-B. Béguin, K. W. Kluge, I. Iakoupov, A. S. Sørensen, J. H. Müller, E. S. Polzik, and J. Appel, Phys. Rev. Lett. **117**, 133604 (2016).

[17] P. Solano, P. Barberis-Blostein, F. K. Fatemi, L. A. Orozco, and S. L. Rolston, Nat. Commun. **8**, 1857 (2017).

[18] J. Bures and R. Ghosh, J. Opt. Soc. Am. A **16**, 1992 (1999).

[19] L. Tong, R. Gattass, J. Ashcom, S. He, J. Lou, M. Shen, I. Maxwell, and E. Mazur, Nature **426**, 816–819 (2003).

[20] G. Brambilla, V. Finazzi, and D. Richardson, Opt. Express **12**, 2258 (2004).

[21] J. Ward, D. O'Shea, B. Shortt, M. Morrissey, K. Deasy, and S. Nic Chormaic, Rev. Sci. Instrum. **77**, 083105 (2006).

[22] L. Shi, X. Chen, H. Liu, Y. Chen, Z. Ye, W. Liao, and Y. Xia, Opt. Express **14**, 5055 (2006).

[23] L. Ding, C. Belacel, S. Ducci, G. Leo, and I. Favero, Appl. Opt. **49**, 2441 (2010).

[24] L. Tong, F. Zi, X. Guo, and J. Lou, Opt. Commun. **285**, 4641 – 4647 (2012).

[25] J. Ward, A. Maimaiti, V. Le, and S. Nic Chormaic, Rev. Sci. Instrum. **85** (2014).

[26] R. Nagai and T. Aoki, Opt. Express **22**, 28427–28436 (2014).

[27] H. Sorensen, E. Polzik, and J. Appel, J. Lightwave Technol. **32**, 1886 (2014).

[28] A. Petcu-Colan, M. Frawley, and S. Nic Chormaic, J. Nonlin. Opt. Phys. Mat. **20**, 293 (2011).

[29] M. Frawley, A. Petcu-Colan, V. Truong, and S. Nic Chormaic, Opt. Commun. **285**, 4648 (2012).

[30] S. Ravets, J. Hoffman, L. Orozco, S. Rolston, G. Beadie, and F. Fatemi, Opt. Express **21**, 18325 (2013).

[31] J. Hoffman, S. Ravets, J. Grover, P. Solano, P. Kordell, J. Wong-Campos, L. Orozco, and S. Rolston, AIP Adv. **4**, 067124 (2014).

[32] J. Hoffman, F. Fatemi, G. Beadie, S. Rolston, and L. Orozco, Optica **2**, 416–423 (2015).

[33] F. Le Kien, S. Gupta, K. Nayak, and K. Hakuta, Phys. Rev. A **72**, 063815 (2005).

[34] K. Nayak, P. Melentiev, M. Morinaga, F. Le Kien, V. Balykin, and K. Hakuta, Opt. Express **15**, 5431 (2007).

[35] A. Masalov and V. Minogin, J. Exp. Theor. Phys. **118**, 714 (2014).

[36] P. Solano, J. A. Grover, Y. Xu, P. Barberis-Blostein, J. N. Munday, L. A. Orozco, W. D. Phillips, and S. L. Rolston, Phys. Rev. A **99**, 013822 (2019).

[37] S. Scheel, S. Buhmann, C. Clausen, and P. Schneeweiss, Phys. Rev. A **92**, 043819 (2015).

[38] K. Nayak, F. Le Kien, M. Morinaga, and K. Hakuta, Phys. Rev. A **79**, 021801 (2009).

[39] F. Le Kien, V. Balykin, and K. Hakuta, Phys. Rev. A **74**, 033412 (2006).

[40] S. Spillane, G. Pati, K. Salit, M. Hall, P. Kumar, R. Beausoleil, and M. Shahriar, Phys. Rev. Lett. **100**, 233602 (2008).

[41] S. Hendrickson, T. Pittman, and J. Franson, J. Opt. Soc. Am. B: Opt. Phys. **26**, 267 (2009).

[42] S. Hendrickson, M. Lai, T. Pittman, and J. Franson, Phys. Rev. Lett. **105**, 173602 (2010).

[43] D. Jones, J. Franson, and T. Pittman, J. Opt. Soc. Am. B: Opt. Phys. **31**, 1997 (2014).

[44] M. Lai, J. Franson, and T. Pittman, Appl. Opt. **52**, 2595 (2013).

[45] T. Pittman, D. Jones, and J. Franson, Phys. Rev. A **88**, 053804 (2013).

[46] M. Morrissey, K. Deasy, W. Yuqiang, S. Chakrabarti, and S. Nic Chormaic, Rev. Sci. Instrum. **80**, 053102 (2009).

[47] K. Deasy, A. Watkins, M. Morrissey, R. Schmidt, and S. Nic Chormaic. *Few Atom Detection and Manipulation Using Optical Nanofibres*. In *Quantum Communication and Quantum Networking*, volume 36 of *Lecture Notes of the Institute for Computer Sciences, Social Informatics and Telecommunications Engineering*, pages 200–209. Springer Berlin Heidelberg, (2010).

[48] L. Russell, R. Kumar, V. Tiwari, and S. Nic Chormaic, Meas. Sci. Technol. **25**, 055203 (2014).

[49] J. Grover, P. Solano, L. Orozco, and S. Rolston, Phys. Rev. A **92**, 013850 (2015).

[50] T. Hennessy and T. Busch, Opt. Express **22**, 32509–32519 (2014).

[51] R. Cook and R. Hill, Opt. Commun. **43**, 258 – 260 (1982).

[52] V. Balykin, V. Letokhov, Y. Ovchinnikov, and A. Sidorov, Phys. Rev. Lett. **60**, 2137–2140 (1988).

[53] J. Hajnal, K. Baldwin, P. Fisk, H. Bachor, and G. Opat, Opt. Commun. **73**, 331 – 336 (1989).

[54] S. Féron, J. Reinhardt, S. Le Boiteux, O. Gorceix, J. Baudon, M. Ducloy, J. Robert, C. Miniatura, S. Nic Chormaic, H. Haberland, and V. Lorent, Opt. Commun. **102**, 83 – 88 (1993).

[55] S. Féron, J. Reinhardt, M. Ducloy, O. Gorceix, S. Nic Chormaic, C. Miniatura, J. Robert, J. Baudon, V. Lorent, and H. Haberland, Phys. Rev. A **49**, 4733–4741 (1994).

[56] M. Ol'Shanii, Y. Ovchinnikov, and V. Letokhov, Opt. Commun. **98**, 77 (1993).

[57] M. Renn, D. Montgomery, O. Vdovin, D. Anderson, C. Wieman, and E. Cornell, Phys. Rev. Lett. **75**, 3253 (1995).

[58] H. Ito, T. Nakata, K. Sakaki, M. Ohtsu, K. Lee, and W. Jhe, Phys. Rev. Lett. **76**, 4500 (1996).

[59] V. Balykin, K. Hakuta, F. Le Kien, J. Liang, and M. Morinaga, Phys. Rev. A **70**, 011401 (2004).

[60] C. Foot, *Atomic Physics*, Oxford University Press (2013).

[61] F. Le Kien, V. Balykin, and K. Hakuta, Phys. Rev. A **70**, 063403 (2004).

[62] N. Schlosser, G. Reymond, and P. Grangier, Phys. Rev. Lett. **89**, 023005 (2002).

[63] D. Reitz, C. Sayrin, R. Mitsch, P. Schneeweiss, and A. Rauschenbeutel, Phys. Rev. Lett. **110**, 243603 (2013).

[64] J. Lee, J. Grover, J. Hoffman, L. Orozco, and S. Rolston, J. Phys. B: At. Mol. Opt. Phys **48**, 165004 (2015).

[65] P. Schneeweiss, F. Le Kien, and A. Rauschenbeutel, New J. Phys. **16**, 013014 (2014).

[66] C. Lacroûte, K. Choi, A. Goban, D. Alton, D. Ding, N. Stern, and H. Kimble, New J. Phys. **14**, 023056 (2012).

[67] H. Katori, T. Ido, and M. Kuwata-Gonokami, J. Phys. Soc. Jpn. **68**, 2479 (1999).

[68] F. Le Kien, V. Balykin, and K. Hakuta, J. Phys. Soc. Jpn. **74**, 910 (2005).

[69] B. Arora and B. Sahoo, Phys. Rev. A **86**, 033416 (2012).

[70] H. Kimble, Nature **453**, 1023 (2008).

[71] L. Duan, M. Lukin, J. Cirac, and P. Zoller, Nature **414**, 413 (2001).

[72] A. Lvovsky, B. Sanders, and W. Tittel, Nature Photon. **3**, 706–714 (2009).

[73] N. V. Corzo, J. Raskop, A. Chandra, A. S. Sheremet, B. Gouraud, and J. Laurat, Nature **566**, 359–362 (2019).

[74] A. Gorshkov, A. André, M. Fleischhauer, A. Sørensen, and M. Lukin, Phys. Rev. Lett. **98**, 123601 (2007).

[75] K. Boller, A. Imamoğlu, and S. Harris, Phys. Rev. Lett. **66**, 2593 (1991).

[76] M. Fleischhauer, A. Imamoğlu, and J. Marangos, Rev. Mod. Phys. **77**, 633 (2005).

[77] L. Hau, S. Harris, Z. Dutton, and C. Behroozi, Nature **397**, 594–598 (1999).

[78] A. Patnaik, J. Liang, and K. Hakuta, Phys. Rev. A **66** (2002).

[79] F. Le Kien and K. Hakuta, Phys. Rev. A **79**, 013818 (2009).

[80] I. Cirac, P. Zoller, J. Kimble, and H. Mabuchi, Phys. Rev. Lett. **78**, 3221 (1997).

[81] A. Boozer, A. Boca, R. Miller, T. Northup, and H. Kimble, Phys. Rev. Lett. **98**, 193601 (2007).

[82] R. Miller, T. Northup, K. Birnbaum, A. Boca, A. Boozer, and H. Kimble, J. Phys. B: At. Mol. Opt. Phys **38**, S551 (2005).

[83] J. Busch and A. Beige, Phys. Rev. A **82**, 053824 (2010).

[84] E. Kyoseva, A. Beige, and L. Kwek, New J. Phys. **14**, 023023 (2012).

[85] F. Le Kien and K. Hakuta, Phys. Rev. A **79**, 043813 (2009).

[86] F. Le Kien and K. Hakuta, Phys. Rev. A **80**, 053826 (2009).

[87] F. Le Kien and K. Hakuta, Phys. Rev. A **83**, 043801 (2011).

[88] F. Le Kien and K. Hakuta, Phys. Rev. A **84**, 053801 (2011).

[89] K. Nayak, F. Le Kien, Y. Kawai, K. Hakuta, K. Nakajima, H. Miyazaki, and Y. Sugimoto, Opt. Express **19**, 14040 (2011).

[90] S. Kato and T. Aoki, Phys. Rev. Lett. **115**, 093603 (2015).

[91] S. K. Ruddell, K. E. Webb, I. Herrera, A. S. Parkins, and M. D. Hoogerland, Optica **4**, 576–579 (2017).

[92] A. Yariv, *Optical Electronics*, CBS College Publishing (1985).

[93] A. Snyder and J. Love, *Optical Waveguide Theory*, Kluwer Academic Publishers (2000).

[94] R. Kumar, V. Gokhroo, K. Deasy, A. Maimaiti, M. Frawley, C. Phelan, and S. Nic Chormaic, New J. Phys. **17**, 013026 (2015).

[95] F. L. Kien, T. Busch, V. G. Truong, and S. Nic Chormaic, Phys. Rev. A , 96 (2017).

[96] A. Masalov and V. Minogin, Las. Phys. Lett. **10**, 075203 (2013).

[97] F. Le Kien, S. S. S. Hejazi, T. Busch, V. G. Truong, and S. Nic Chormaic, Phys. Rev. A **96**, 043859 (2017).

[98] G. Sagué, A. Baade, and A. Rauschenbeutel, New J. Phys. **10**, 113008 (2008).

[99] C. Phelan, T. Hennessy, and T. Busch, Opt. Express **21**, 27093 (2013).

[100] J. Fu, X. Yin, N. Li, and L. Tong, Chin. Opt. Lett. **6**, 112–115 (2008).

[101] D. Reitz and A. Rauschenbeutel, Opt. Commun. **285**, 4705 (2012).

[102] M. Sadgrove, S. Wimberger, and S. Nic Chormaic, Sci. Rep. **6**, 28905 (2016).

[103] J. Petersen, J. Volz, and A. Rauschenbeutel, Science **346**, 67 (2014).

[104] F. L. Kien, T. Busch, V. G. Truong, and S. Nic Chormaic, Commun. Phys. **27**, 23 (2017).

[105] Y. Tang and A. E. Cohen, Science **332**, 333–336 (2011).

[106] A. Yao and M. Padgett, Adv. Opt. Photon. **3**, 161–204 (2011).

[107] M. J. Padgett, Opt. Express **25**, 11265–11274 (2017).

[108] C. Schulze, R. Brüning, S. Schröter, and M. Duparré, J. Lightwave Technol. **33**, 4488–4496 (2015).

[109] R. Brüning, Y. Zhang, M. McLaren, M. Duparré, and A. Forbes, J. Opt. Soc. Am. A **32**, 1678–1682 (2015).

[110] C. Maurer, A. Jesacher, S. Fürhapter, S. Bernet, and M. Ritsch-Marte, New J. Phys. **9**, 78 (2007).

[111] C. Rosales-Guzmán, B. Ndagano, and A. Forbes, J. Opt. **20**, 123001 (2018).

[112] G. Volpe and D. Petrov, Opt. Commun. **237**, 89 (2004).

[113] B. Ndagano, R. Brüning, M. McLaren, M. Duparré, and A. Forbes, Opt. Express **23**, 17330–17336 (2015).

[114] F. K. Fatemi and G. Beadie, Opt. Express **21**, 32291–32305 (2013).

[115] F. K. Fatemi, J. E. Hoffman, P. Solano, E. F. Fenton, G. Beadie, S. L. Rolston, and L. A. Orozco, Optica **4**, 157–162 (2017).

[116] F. Lei, G. Tkachenko, J. M. Ward, and S. Nic Chormaic, Phys. Rev. Applied **11**, 064041 (2019).

[117] T. A. Birks and Y. W. Li, J. Light. Tech. **10**, 432–438 (1992).

[118] E. R. Abraham and E. A. Cornell, Appl. Opt. **37**, 1762–1763 (1998).

[119] M. Anderson, J. Ensher, M. Matthews, C. Wieman, and E. Cornell, Science **269**, 198 (1995).

[120] H. Metcalf and P. van der Straten, *Laser Cooling and Trapping*, Springer (1999).

[121] F. Le Kien, T. Ray, T. Nieddu, T. Busch, and S. Nic Chormaic, Phys. Rev. A **97**, 013821 (2018).

[122] S. Franke-Arnold, L. Allen, and M. Padgett, Laser & Photon. Rev. **2**, 299 (2008).

[123] J. P. Torres and L. Torner, *Twisted Photons: Applications of Light with Orbital Angular Momentum*, Wiley-VCH (2011).

[124] G. Calvo, A. Picón, and E. Bagan, Phys. Rev. A **73**, 013805 (2006).

[125] L. Allen, M. Beijersbergen, R. Spreeuw, and J. Woerdman, Phys. Rev. A **45**, 8185–8189 (1992).

[126] A. Mair, A. Vaziri, G. Weihs, and A. Zeilinger, Nature **412**, 313–316 (2001).

[127] A. C. Dada, J. Leach, G. S. Buller, M. J. Padgett, and E. Andersson, Nat. Phys. **7**, 677–680 (2011).

[128] J. Leach, B. Jack, J. Romero, A. K. Jha, A. M. Yao, S. Franke-Arnold, D. G. Ireland, R. W. Boyd, S. M. Barnett, and M. J. Padgett, Science **329**, 662–665 (2010).

[129] S. Gröblacher, T. Jennewein, A. Vaziri, G. Weihs, and A. Zeilinger, New J. Phys. **8**, 75 (2006).

[130] J. Wang, J. Yang, I. Fazal, N. Ahmed, Y. Yan, H. Huang, Y. Ren, Y. Yue, S. Dolinar, M. Tur, and A. Willner, Nature Photon. **6**, 488 (2012).

[131] A. J. F. de Almeida, S. Barreiro, W. S. Martins, R. A. de Oliveira, D. Felinto, L. Pruvost, and J. W. R. Tabosa, Opt. Lett. **40**, 2545–2548 (2015).

[132] R. A. de Oliveira, G. C. Borba, W. S. Martins, S. Barreiro, D. Felinto, and J. W. R. Tabosa, Opt. Lett. **40**, 4939–4942 (2015).

[133] A. Nicolas, L. Veissier, L. Giner, E. Giacobino, D. Maxein, and J. Laurat, Nature Photon. **8**, 234 (2014).

[134] D.-S. Ding, W. Zhang, Z.-Y. Zhou, S. Shi, G.-Y. Xiang, X.-S. Wang, Y.-K. Jiang, B.-S. Shi, and G.-C. Guo, Phys. Rev. Lett. **114**, 050502 (2015).

[135] C. T. Schmiegelow, J. Schulz, H. Kaufman, T. Ruster, U. G. Poschinger, and F. Schmidt-Kaler, Nat. Commun. **7**, 12998 (2016).

[136] J. Nilsen and K. Niemax, J. Quant. Spectrosc. Radiat. Transf. **17**, 747 (1977).

[137] J. Nilsen and J. Marling, J. Quant. Spectrosc. Radiat. Transf. **20**, 327 (1978).

[138] H. S. Freedhoff, J. Chem. Phys. **22**, 435 (1989).

[139] D. V. James, Appl. Phys. B **66**, 181 (1998).

[140] P. K. Mondal, B. Deb, and S. Majumder, Phys. Rev. A **89**, 063418 (2014).

[141] E. A. Chan, S. A. Aljunid, N. I. Zheludev, D. Wilkowski, and M. Ducloy, Opt. Lett. **41**, 2005 (2016).

[142] M. Germann, X. Tong, and S. Willitsch, Nat. Phys. **10**, 820 (2014).

[143] S. Tojo, M. Hasuo, and T. Fujimoto, Phys. Rev. Lett. **92**, 053001 (2004).

[144] S. Tojo, T. Fujimoto, and M. Hasuo, Phys. Rev. A **71**, 012507 (2005).

[145] S. Tojo and M. Hasuo, Phys. Rev. A **71**, 012508 (2005).

[146] V. V. Klimov and V. S. Letokhov, Phys. Rev. A **54**, 4408 (1996).

[147] V. V. Klimov and M. Ducloy, Phys. Rev. A **62**, 043818 (2000).

[148] A. M. Kern and O. J. F. Martin, Phys. Rev. A **85**, 022501 (2012).

[149] K. Shibata, S. Tojo, and D. Bloch, Opt. Express **25**, 9476 (2017).

[150] L. Tong, R. R. Gattass, J. B. Ashcom, S. He, J. Lou, M. Shen, I. Maxwell, and E. Mazur, Nature **426**, 816 (2003).

[151] P. Solano, J. A. Grover, J. E. Homan, S. Ravets, F. K. Fatemi, L. A. Orozco, and S. L. Rolston, Adv. At. Mol. Opt. Phys. **66**, 439 (2017).

[152] L. Tong, J. Lou, and E. Mazur, Opt. Express **12**, 1025 (2004).

[153] F. L. Kien, J. Q. Liang, K. Hakuta, and V. I. Balykin, Opt. Commun. **242**, 445 (2004).

[154] B. W. Shore, *The Theory of Coherent Atomic Excitation*, Wiley, New York (1990).

[155] J. D. Jackson, *Classical Electrodynamics 3rd ed.*, Wiley, New York (1999).

[156] T. Nieddu, T. Ray, K. S. Rajasree, R. Roy, and S. Nic Chormaic, Opt. Express **27**, 6528–6535 (2019).

[157] K. Shimoda, *High-Resolution Laser Spectroscopy*, Springer Berlin Heidelberg (2014).

[158] L. S. Vasilenko, V. P. Chebotaev, and A. V. Shishaev, JETP Letters **12**, 113 – 115 (1970).

[159] B. Cagnac, G. Grynberg, and F. Biraben, Eur. Phys. J. **34**, 845–858 (1973).

[160] N. Bloembergen, M. D. Levenson, and M. M. Salour, Phys. Rev. Lett. **32**, 867–869 (1974).

[161] T. W. Hänsch, Rev. Mod. Phys. **78**, 1297–1309 (2006).

[162] S. Gulde, H. Häffner, M. Riebe, G. Lancaster, C. Becher, J. Eschner, F. Schmidt-Kaler, I. L. Chuang, and R. Blatt, Philos. Trans. Royal Soc. A **361**, 1363–1374 (2003).

[163] I. D. Abella, Phys. Rev. Lett. **9**, 453–455 (1962).

[164] F. Biraben, B. Cagnac, and G. Grynberg, Phys. Lett. A **49**, 71 – 72 (1974).

[165] D. Roberts and E. Fortson, Opt. Commun. **14**, 332 – 335 (1975).

[166] E. Campani, G. Degan, G. Gorini, and E. Polacco, Opt. Commun. **24**, 203 – 206 (1978).

[167] Y.-W. Liu and P. E. G. Baird, Meas. Sci. Technol. **12**, 740 (2001).

[168] B. A. Bushaw, W. Nörtershäuser, G. Ewald, A. Dax, and G. W. F. Drake, Phys. Rev. Lett. **91**, 043004 (2003).

[169] M.-S. Ko and Y.-W. Liu, Opt. Lett. **29**, 1799–1801 (2004).

[170] Y.-C. Lee, Y.-H. Chang, Y.-Y. Chen, C.-C. Tsai, and H.-C. Chui, J. Phys. B: At. Mol. Opt. Phys **43**, 235003 (2010).

[171] T. W. Hänsch, S. A. Lee, R. Wallenstein, and C. Wieman, Phys. Rev. Lett. **34**, 307–309 (1975).

[172] A. Matveev, C. G. Parthey, K. Predehl, J. Alnis, A. Beyer, R. Holzwarth, T. Udem, T. Wilken, N. Kolachevsky, M. Abgrall, D. Rovera, C. Salomon, P. Laurent, G. Grosche, O. Terra, T. Legero, H. Schnatz, S. Weyers, B. Altschul, and T. W. Hänsch, Phys. Rev. Lett. **110**, 230801 (2013).

[173] R. Roy, P. C. Condylis, Y. J. Johnathan, and B. Hessmo, Opt. Express **25**, 7960–7969 (2017).

[174] T. Chanelière, D. N. Matsukevich, S. D. Jenkins, T. A. B. Kennedy, M. S. Chapman, and A. Kuzmich, Phys. Rev. Lett. **96**, 093604 (2006).

[175] G. Grynberg, A. Aspect, C. Fabre, and C. Cohen-Tannoudji, *Introduction to Quantum Optics: From the Semi-classical Approach to Quantized Light*, Cambridge University Press (2010).

[176] K. D. Bonin and T. J. McIlrath, J. Opt. Soc. Am. B **1**, 52–55 (1984).

[177] A. Pérez Galván, Y. Zhao, and L. A. Orozco, Phys. Rev. A **78**, 012502 (2008).

[178] Grynberg, G., Biraben, F., Giacobino, E., and Cagnac, B., J. Phys. France **38**, 629–640 (1977).

[179] G. Grynberg and B. Cagnac, Rep. Prog. Phys. **40**, 791 (1977).

[180] E. Gomez, S. Aubin, L. A. Orozco, and G. D. Sprouse, J. Opt. Soc. Am. B **21**, 2058–2067 (2004).

[181] E. Gomez, F. Baumer, A. D. Lange, G. D. Sprouse, and L. A. Orozco, Phys. Rev. A **72**, 012502 (2005).

[182] C. S. Wood, S. C. Bennett, J. L. Roberts, D. Cho, and C. E. Wieman, Can. J. Phys. **77**, 7–75 (1999).

[183] J. Guéna, D. Chauvat, P. Jacquier, E. Jahier, M. Lintz, S. Sanguinetti, A. Wasan, M. A. Bouchiat, A. V. Papoyan, and D. Sarkisyan, Phys. Rev. Lett. **90**, 143001 (2003).

[184] R. T. Willis, F. E. Becerra, L. A. Orozco, and S. L. Rolston, Phys. Rev. A **82**, 053842 (2010).

[185] H. You, S. M. Hendrickson, and J. D. Franson, Phys. Rev. A **78**, 053803 (2008).

[186] G. Sagué, E. Vetsch, W. Alt, D. Meschede, and A. Rauschenbeutel, Phys. Rev. Lett. **99**, 163602 (2007).

[187] E. Hecht, *Optics, 4th Ed.*, Addison Wesley (2001).

[188] M. Joos, A. Bramati, and Q. Glorieux, Opt. Express **27**, 18818–18830 (2019).

[189] G. Tkachenko, F. Lei, and S. Nic Chormaic, arXiv **:1907.04533** (2019).

[190] W. Li, J. Du, V. G. Truong, and S. Nic Chormaic, Appl. Phys. Lett. **110**, 253102 (2017).

[191] Q. Zhan, Adv. Opt. Photon. **1**, 1–57 (2009).

[192] L. Marrucci, C. Manzo, and D. Paparo, Phys. Rev. Lett. **96**, 163905 (2006).

[193] M. Martinelli and P. Martelli, Adv. Opt. Photon. **9**, 129–168 (2017).

[194] J. Carpenter, C. Xiong, M. J. Collins, J. Li, T. F. Krauss, B. J. Eggleton, A. S. Clark, and J. Schröder, Opt. Express **21**, 28794–28800 (2013).

[195] S. Okaba, T. Takano, F. Benabid, T. Bradley, L. Vincetti, Z. Maizelis, V. Yampol'skii, F. Nori, and H. Katori, Nature Commun. **5**, 4096 (2014).

[196] T. Chanelière, D. N. Matsukevich, S. D. Jenkins, T. A. B. Kennedy, M. S. Chapman, and A. Kuzmich, Phys. Rev. Lett. **96**, 093604 (2006).

[197] R. Gerchberg and W. Saxton, Optik **35**, 237–246 (1972).

[198] G. Arfken and H. J. Weber, *Mathematical methods for physicists 6th ed., p.356*, Elsevier (1985).

[199] D. A. Varshalovich, A. N. Moskalev, and V. K. Khersonskii, *Quantum Theory of Angular Momemtum*, World Scientific Publishing, Singapore (2008).

[200] F. L. Kien and K. Hakuta, Phys. Rev. A **75** (2007).

[201] A. V. Dooghin, N. D. Kundikova, V. S. Liberman, and B. Y. Zeldovich, Phys. Rev. A **45**, 8204 (1992).

[202] V. S. Liberman and B. Y. Zeldovich, Phys. Rev. A **46**, 5199 (1992).

[203] M. Y. Darsht, B. Y. Zeldovich, I. V. Kataevskaya, and N. D. Kundikova, JETP **80**, 817 (1995).

[204] K. Y. Bliokh, A. Aiello, and M. A. Alonso, *The Angular Momentum of Light, edited by D. L. Andrews and M. Babiker, p.174*, Cambridge University Press, New York (2012).

[205] K. Y. Bliokh, J. Dressel, and F. Nori, New J. Phys. **16**, 093037 (2014).

[206] K. Y. Bliokh, A. Y. Bekshaev, and F. Nori, Nature Commun. **5**, 3300 (2014).

[207] A. Aiello, P. Banzer, M. Neugebauer, and G. Leuchs, Nature Photon. **9**, 789 (2015).

[208] K. Y. Bliokh and F. Nori, Phys. Rep. **592**, 1 (2015).

[209] F. L. Kien and A. Rauschenbeutel, Phys. Rev. A **90**, 023805 (2014).

[210] R. Mitsch, C. Sayrin, B. Albrecht, P. Schneeweiss, and A. Rauschenbeutel, Nature Commun. **5**, 5713 (2014).

[211] F. L. Kien and A. Rauschenbeutel, Phys. Rev. A **90**, 063816 (2014).

[212] C. Sayrin, C. Junge, R. Mitsch, B. Albrecht, D. O'Shea, P. Schneeweiss, J. Volz, and A. Rauschenbeutel, Phys. Rev. X **5**, 041036 (2015).

[213] P. Lodahl, S. Mahmoodian, S. Stobbe, P. Schneeweiss, J. Volz, A. Rauschenbeutel, H. Pichler, and P. Zoller, Nature **541**, 473 (2017).

[214] D. Marcuse, *Light Transmission Optics*, Krieger, Malabar, FL (1989).